

# Scanning tunneling microscopy and spectroscopy of topological insulators

Dissertation  
zur Erlangung des akademischen Grades  
Doctor rerum naturalium  
(Dr. rer. nat.)

vorgelegt von  
**Vladislav Nagorkin**  
geboren am 29.07.1992 in Miass

Fakultät für Mathematik und Naturwissenschaften  
Bergische Universität Wuppertal

2024

Eingereicht am 26.09.2024

1. Gutachter: Prof. Dr. Christian Hemker-Heß
2. Gutachter: Prof. Dr. Dirk Lützenkirchen-Hecht

# Abstract

The aim of this work is to investigate the electronic properties of the conventional (non-magnetic) and magnetic topological insulators at the atomic scale with the use of low-temperature scanning tunneling microscopy and spectroscopy (STM/STS). In particular, the STM/STS measurements have been performed on one of the prototypical topological insulators  $\text{Bi}_2\text{Te}_3$  and recently synthesized intrinsic magnetic topological insulators  $\text{MnBi}_2\text{Te}_4$  and  $\text{MnBi}_4\text{Te}_7$ .

The high-resolution differential conductance maps were measured on  $\text{Bi}_2\text{Te}_3$  single crystals and allowed to reveal quasiparticle interference in this material. The latter was used for studying electron scattering processes of both surface and bulk origin at different energies. For that the quasiparticle interference patterns were modeled with the use of the spin-selective joint density of states approach including the intricate three-dimensional spin texture of this material. Based on that, the topological properties are clearly demonstrated by the linear energy dispersion of the dominant scattering vector and completely suppressed backscattering. Apart from that, non-dispersive scattering modes are resolved and interpreted by scattering involving both surface and bulk states which allows to approximate the bulk energy gap range. These findings are shown to be robust against the external magnetic field of magnitude up to 15 T.

Atomically resolved STM data acquired on the single crystals of  $\text{MnBi}_2\text{Te}_4$  exhibit noticeable electronic modulations related to the Mn/Bi antisite intermixing. The zero differential conductance was measured in the tunneling spectra, which is, most probably, one of the very first indication of the magnetic exchange gap in magnetic topological insulators detected by STS. The gap size of around 25 meV is in a reasonable agreement with the surface band structure calculations on this material including the cation intermixing. The STM/STS data provide an evidence of the chemically inhomogeneous surface showing both gapped and gapless tunneling spectra. From the STM data acquired on the other intrinsic magnetic topological insulator,  $\text{MnBi}_4\text{Te}_7$ , two kinds of surfaces were identified in accordance with its crystal structure suggesting two possible surface terminations. However, the quality of the measured crystals (cation intermixing) did not allow to obtain reliable spectroscopic data.

# Contents

<b>1. Introduction</b>	<b>1</b>
<b>2. Introduction to the materials</b>	<b>3</b>
2.1. Topological insulators	3
2.1.1. Quantum Hall state and quantum spin Hall state	3
2.1.2. Three-dimensional topological insulators: overview	6
2.1.3. Three-dimensional topological insulators: experimental dis- covery	9
2.1.4. $\text{Bi}_2\text{Te}_3$ : crystal and electronic structure	12
2.1.5. STM and STS of $\text{Bi}_2\text{Te}_3$	15
2.2. Magnetic topological insulators	17
2.2.1. Theoretical background	17
2.2.2. Possible realizations in materials	19
2.2.3. Actual results	21
2.3. MnBiTe-family of compounds	23
2.3.1. $\text{MnBi}_2\text{Te}_4$	26
2.3.2. $\text{MnBi}_4\text{Te}_7$	32
<b>3. Experimental technique: STM and STS</b>	<b>41</b>
3.1. Tunneling current	42
3.2. STM measurement modes	45
3.2.1. Topography	45
3.2.2. Single point spectroscopy	46
3.2.3. $dI/dU$ maps	47
3.3. Quasiparticle interference	48
3.4. Experimental setup	49
<b>4. Experimental results</b>	<b>55</b>
4.1. $\text{Bi}_2\text{Te}_3$	55
4.1.1. Topography	55
4.1.2. STS	61

## CONTENTS

---

4.1.3. $dI/dU$ maps in zero-field . . . . .	62
4.1.4. QPI analysis of the zero-field $dI/dU$ maps . . . . .	68
4.1.5. Magnetic field measurements . . . . .	79
4.1.6. Conclusions . . . . .	90
4.2. $\text{MnBi}_2\text{Te}_4$ . . . . .	91
4.2.1. Topography . . . . .	91
4.2.2. STS . . . . .	96
4.2.3. $dI/dU$ mapping . . . . .	101
4.2.4. Conclusions . . . . .	107
4.3. $\text{MnBi}_4\text{Te}_7$ . . . . .	108
4.3.1. Topography . . . . .	108
4.3.2. Temperature-dependent STS . . . . .	115
4.3.3. Conclusions . . . . .	118
<b>5. Summary . . . . .</b>	<b>119</b>
<b>A. Additional experimental and simulated QPI data on <math>\text{Bi}_2\text{Te}_3</math> . .</b>	<b>121</b>
<b>B. Symmetrization procedure of the FT-QPI patterns . . . . .</b>	<b>129</b>
<b>C. Program codes . . . . .</b>	<b>133</b>
<b>D. Additional STS data on <math>\text{MnBi}_4\text{Te}_7</math> . . . . .</b>	<b>159</b>
<b>Bibliography . . . . .</b>	<b>160</b>

## CONTENTS

---

# Chapter 1

## Introduction

Since ancient times, human society has been in a continuous accumulation of knowledge, developing and modernizing scientific theories, methods and technologies for their subsequent practical applications. More specifically, modern experimental physics strictly depends on novel materials and the development of the experimental research methods. One of the examples of new materials that have substantially changed the research direction in the field of condensed matter physics, are three-dimensional topological insulators which are literally extremely prospective for the future of humankind. These materials were first discovered around 15 years ago and display plenty of unusual electronic properties such as Dirac energy dispersion with spin-momentum locking, insulating bulk, robust surface states against non-magnetic perturbations, high surface conduction [1–8]. The interplay of the non-trivial topology and magnetism induced a tremendous growth of research in this field which, in particular, has recently (in 2019) led to the discovery of intrinsic magnetic topological insulators combining the inverted electronic band structure with long-range magnetic order [9–11]. These materials are expected to reveal a magnetic exchange energy gap in the surface electronic band structure and to exhibit a long-sought quantum anomalous Hall effect as well as quantized magnetoelectric phenomena [12, 13]. These materials along with the non-magnetic topological insulators present a fertile platform for the study of new quantum states of matter. Furthermore, they are considered promising candidates for technological applications in low-power consumption electronics and quantum computing which can potentially work above cryogenic temperatures up to room temperature.

To investigate the physical aspects of these emergent materials a crucial step is to have an acceptable level of the development of the experimental methods. In this regard, scanning tunneling microscopy and spectroscopy (STM/STS) manifests itself as the unique and powerful technique which allows probing electronic density of states of solids (generally, also in liquid and gaseous environments) locally with subatomic spatial resolution [14, 15]. In addition, the STM technique allows to shed

more light on the electronic band structure of different materials by studying electron scattering processes through quasiparticle interference (QPI). Another important extension of STM such as spin-polarized scanning tunneling microscopy provides possibilities to visualize spin structures and study magnetic phenomena at the single-atom scale [16].

The aim of the current work is to contribute to the ongoing investigation of the electronic properties of the prototypical topological insulator  $\text{Bi}_2\text{Te}_3$  and its magnetic related compounds  $\text{MnBi}_2\text{Te}_4$  and  $\text{MnBi}_4\text{Te}_7$ , which were recently found to be the first intrinsic magnetic topological insulators, by low-temperature STM/STS. This doctoral thesis is organized in the following way:

Chapter 2 consists of the general introduction to the material classes of topological insulators and magnetic topological insulators. In addition, the main crystal, electronic and magnetic properties of the compounds  $\text{Bi}_2\text{Te}_3$ ,  $\text{MnBi}_2\text{Te}_4$ ,  $\text{MnBi}_4\text{Te}_7$  investigated in this thesis are presented in that chapter.

The basics of the experimental technique STM/STS (including QPI) starting from the quantum tunneling phenomenon are discussed in Chapter 3. This chapter introduces different measurement modes usually exploited in the experiments. In addition, it provides also a detailed description of the experimental setup and its repair.

Chapter 4 is the main part of this thesis and presents the experimental results obtained by low-temperature STM measurements (topography, STS and differential conductance maps with the QPI) on three different materials  $\text{Bi}_2\text{Te}_3$ ,  $\text{MnBi}_2\text{Te}_4$ ,  $\text{MnBi}_4\text{Te}_7$  with the discussion for each of the compounds. The main results are the QPI data acquired on  $\text{Bi}_2\text{Te}_3$  single crystals in a relatively wide energy range which allow imaging the Dirac cone (linear energy dispersion) of the surface state. The absence of the backscattering in the experiment and the evidence of the bulk involved scattering revealed by the QPI simulations are discussed in this chapter. Magnetic field measurements were carried out but did not reveal new scattering channels caused by Zeeman field. The most important result obtained by STM/STS measurements on the magnetic topological insulator  $\text{MnBi}_2\text{Te}_4$  is one of the first detection of the magnetic exchange energy gap in the tunneling spectra. Despite a strong disorder and rather poor quality of the crystals, the measured STM/STS data on the related compound  $\text{MnBi}_4\text{Te}_7$  allow to distinguish two surface terminations as expected from the crystal structure.

The main conclusions of this dissertation are presented in Chapter 5.

# Chapter 2

## Introduction to the materials

### 2.1. Topological insulators

#### 2.1.1. Quantum Hall state and quantum spin Hall state

Topology being originally a branch of mathematics was firmly embedded in physics with the discovery of quantum Hall effects (integer and fractional) in the early 1980s [17, 18] after some theoretical predictions in 1970s [19, 20]. In general, topological phases of matter are different from ordinary phases in the sense that as long as they do not demonstrate broken symmetries, some fundamental properties (quantized Hall conductance, number of gapless boundary modes) remain robust under smooth changes in material parameters unless a quantum phase transition occurs [21]. Electrons in the quantum Hall state are confined to two dimensions and are exposed to a strong external magnetic field which forces them to move in cyclotron orbits. Unlike normal insulators, the drift of the cyclotron orbits caused by an electric field results in the quantized Hall conductivity

$$\sigma_{xy} = Ne^2/\hbar, (N = 1, 2, 3, \dots), \quad (2.1.1)$$

which is a precisely measured physical quantity (accuracy is  $\sim 10^{-9}$  [22]) and independent of the materials, geometry and temperature ( $e$  is the elementary charge and  $\hbar$  is the Planck constant). This integer number  $N$  is indeed a topological invariant of the quantum Hall state. According to the TKNN (Thouless, Kohmoto, Nightingale, and den Nijs) theory [23], two-dimensional gapped band structures can be classified topologically by an integer  $n$  (Chern invariant), to the equivalence classes of the Bloch Hamiltonian that can be continuously deformed into one another without gap closing. The Chern invariant can be understood physically as the total Berry flux associated with the Bloch wave functions  $|u_m(\mathbf{k})\rangle$  ( $m$  is the index of the occupied

band,  $N$  is their total number) in the Brillouin zone

$$n = \frac{1}{2\pi} \int F d^2\mathbf{k}, \quad (2.1.2)$$

$$F = \sum_{m=1}^N [\nabla_{\mathbf{k}} \times \langle u_m(\mathbf{k}) | i\nabla_{\mathbf{k}} | u_m(\mathbf{k}) \rangle]. \quad (2.1.3)$$

The TKNN theory also showed that the Chern number  $n$  is identical to the integer  $N$  in the Hall conductivity, thus, making  $N$  the topological invariant of the quantum Hall state [23].

Lorentz force caused by the external magnetic field makes electrons moving in cyclotron orbits but the sample boundaries interrupt this motion (leading to skipping orbits) which results in the unidirectional propagation of the electronic states along the edge (dubbed "chiral") because their backward motion is not possible (see Fig. 2.1.1). These chiral edge states are protected against disorder by the bulk topology of the quantum Hall state.

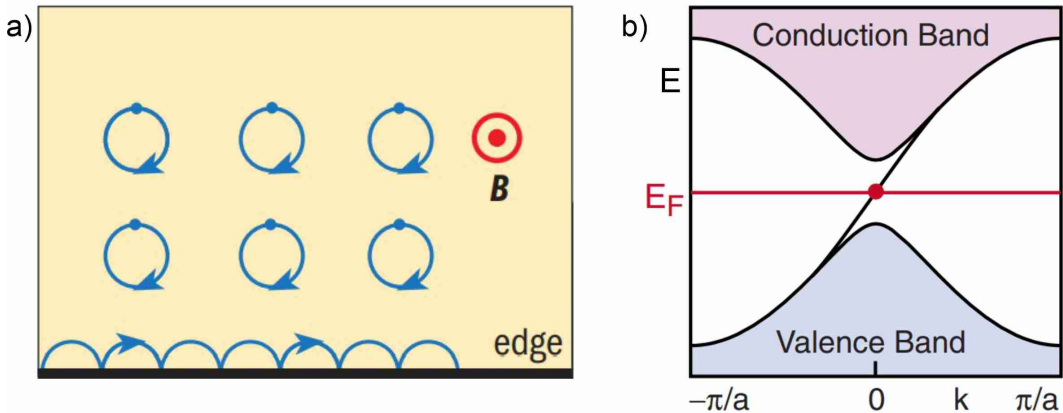


**Fig. 2.1.1** a) Illustration of the cyclotron orbits in the quantum Hall state. Adapted from [24]. b) Electronic band structure of the quantum Hall state with the chiral edge state connecting the valence band with the conduction band. Adapted from [25].

However, this quantum Hall state can be realized only in an external magnetic field. Later, in 2005 a new state of matter was predicted theoretically [21, 26, 27] known as the quantum spin Hall state, or two-dimensional topological insulator, for which no external field is required. In such a system strong interaction of the electron spin with the orbital motion of electrons (strong spin-orbit coupling (SOC)) serves as an effective spin-dependent magnetic field which is opposite for spin-up and spin-down electrons. The quantum spin Hall state can be naively understood as a superposition of two quantum Hall systems with opposite spins. This quantum spin Hall state is time-reversal symmetry invariant since both magnetic field and spin are odd under the time-reversal symmetry. The quantum spin Hall state consists of a

pair of edge states which move in opposite directions with opposite spins as shown in Fig. 2.1.2 [26]. This pair of edge states is termed "helical", since the spin is always correlated with the direction of the propagation. As in the quantum Hall state, the backscattering is also suppressed but due to a different reason, in particular, the time-reversal symmetry. Since in the quantum spin Hall state an electron has to flip its spin for backscattering, the time-reversal symmetry would be broken. As long as the time-reversal symmetry is preserved (there are no magnetic impurities), the backscattering is forbidden. In other words, the pair of gapless edge states is robust due to the time-reversal symmetry against backscattering.

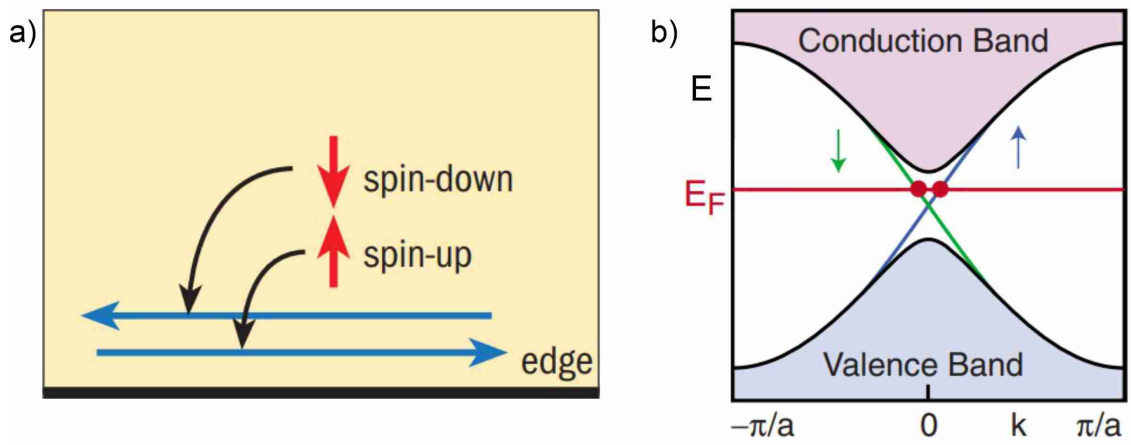


**Fig. 2.1.2** a) Illustration of the quantum spin Hall state in the real space. Adapted from [24]. b) Electronic band structure of the quantum spin Hall state with the pair of gapless edge states between the valence and the conduction bands. Adapted from [25].

For such a quantum spin Hall state the total Hall conductance is zero (and the Chern number  $n = 0$ ) since the spin-up and spin-down electrons contribute to it equally but with the opposite sign. However, for these time-reversal symmetry invariant systems a new topological invariant  $\mathbb{Z}_2$  was constructed which can take only one of two values  $\nu = 1$  or  $\nu = 0$  for the topologically non-trivial quantum spin Hall insulators and conventional insulators, respectively [21].

This  $\mathbb{Z}_2$  topological invariant can be interpreted by considering a Kramers pair of the edge states. According to the quantum-mechanical Kramers' theorem, all the eigenstates of a time-reversal symmetry invariant Hamiltonian are at least twofold degenerate. In the case of a quantum spin Hall insulator, two edge states at momenta  $k$  and  $-k$  form a Kramers pair. Given the  $2\pi/a$  ( $a$  is the lattice constant) periodicity of the crystal, momenta  $k = 0$  and  $k = \pi/a$  will be special time-reversal invariant momenta which are invariant under  $k$  reversal. So the edge states have to be twofold degenerate at  $k = 0$  and  $k = \pi/a$  (the same for  $k = -\pi/a$ ) if they exist, while the spin-orbit interaction splits the degeneracy away from those special points. Therefore, the time-reversal symmetry guarantees the topological protection

of the edge states by crossing of two branches at  $k = 0$  [21]. Fig. 2.1.3 shows two possible ways of how the states at  $k = 0$  and  $k = \pi/a$  can connect [1]. In the first case presented in Fig. 2.1.3a the edge states connect the valence and conduction bands in a zigzag way, thereby intersect the Fermi level  $E_F$  an odd number of times which corresponds to the quantum spin Hall state with topologically protected edge states. In contrast, Fig. 2.1.3b illustrates an ordinary insulator in which the edge states connect pairwise and can be destroyed by pushing all of the bound states out of the gap, so the bands cross the Fermi level an even number of times.

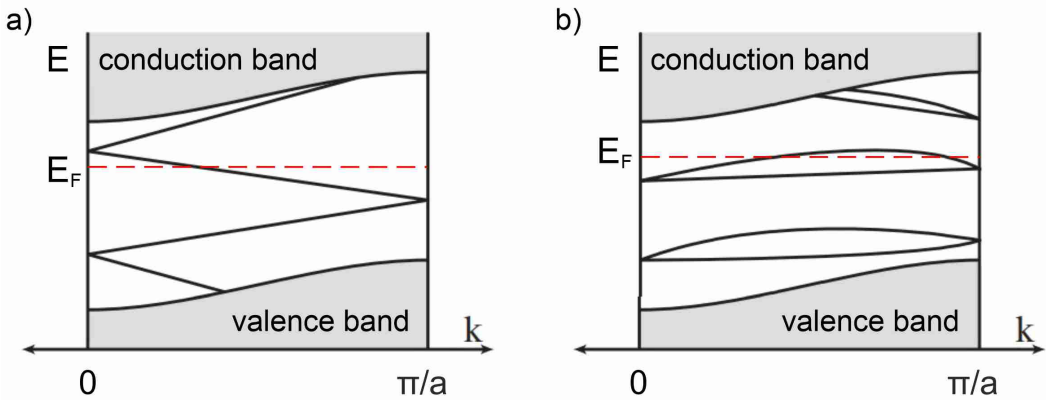


**Fig. 2.1.3** Electronic dispersion between two boundary Kramers degenerate points  $k = 0$  and  $k = \pi/a$ . a) Odd number of edge states intersecting the Fermi level. b) Even number of edge states crossings at the Fermi energy. Adapted from [1].

## 2.1.2. Three-dimensional topological insulators: overview

Finally, the existence of a three-dimensional topological insulator was theoretically predicted in 2006 [1–3]. Such a three-dimensional topological insulator is characterized by the inverted and gapped bulk band structure due to the strong SOC with the existence of unique gapless nondegenerate surface states arising from the bulk topological order [1]. According to [1], electrons in the surface bands of a three-dimensional topological insulator behave like two-dimensional Dirac fermions and obey the two-dimensional Dirac equation [28]. These surface states resemble the edge states of two-dimensional topological insulators in that sense that electrons can propagate in any direction on the surface (one certain direction for two-dimensional topological insulators) but their spin is always perpendicular to their linear momentum (spin-momentum locking) as shown in Fig. 2.1.4.

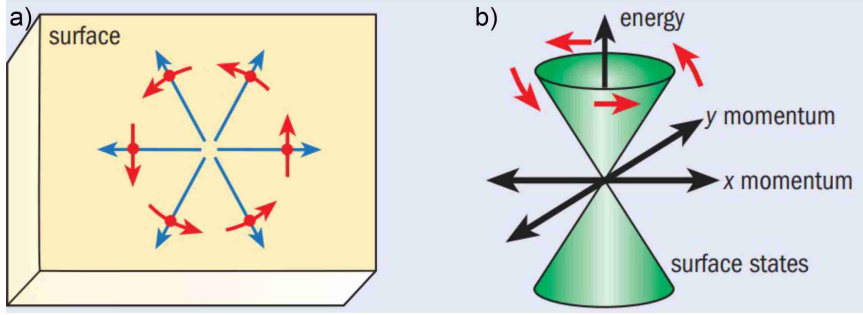


**Fig. 2.1.4** a) Spin-momentum locking on the surface of a three-dimensional topological insulator. b) Energy-momentum dispersion (Dirac cone) of the surface states of a three-dimensional topological insulator. Adapted from [24].

Unlike two-dimensional topological insulators, the three-dimensional topological insulators are characterized by four  $\mathbb{Z}_2$  topological invariants ( $\nu_0; \nu_1, \nu_2, \nu_3$ ), and there are four independent time-reversal invariant momenta  $\Gamma_{1,2,3,4}$  in the surface Brillouin zone. The surface states must be Kramers degenerate at these special points, forming two-dimensional Dirac points in the surface band structure (see Fig. 2.1.5). There are two ways of surface band connectivity for two-dimensional topological insulators as shown in Fig. 2.1.3, but four bulk  $\mathbb{Z}_2$  topological invariants for three-dimensional topological insulators change the picture [4]. The most important one among the four invariants,  $\nu_0$ , identifies two distinct subclasses of topological insulators. When  $\nu_0 = 0$ , the system is a weak topological insulator with an even number of Dirac points enclosed by the surface Fermi circle as shown in Fig. 2.1.5a. When  $\nu_0 = 1$ , the system is a strong topological insulator with an odd number of Dirac points enclosed by the surface Fermi circle (see Fig. 2.1.5b). In the simplest case of a strong topological insulator the Fermi surface encloses one single Dirac point (see Fig. 2.1.5c) leading to a non-trivial  $\pi$  Berry phase which was found to be a universal feature of the strong topological insulators and protects electrons from being localized in the presence of disorder as long as the bulk energy gap remains unchanged [29].

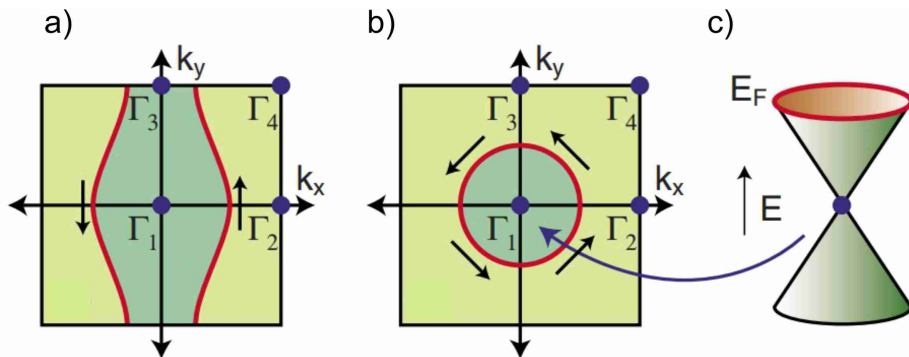


**Fig. 2.1.5** a) The surface Fermi circle for a weak topological insulator. b) The surface Fermi circle for a strong topological insulator. c) In the simplest strong topological insulator the Fermi circle encloses a single two-dimensional Dirac point. Adapted from [4] and [25].

There are several approaches for the mathematical definition of the  $\mathbb{Z}_2$  topological invariant [2, 4, 26, 30–32]. One of them [1, 30], which is known as the Fu-Kane method, is based on considering a unitary matrix  $w_{mn}(\mathbf{k}) = \langle u_m(\mathbf{k}) | \Theta | u_n(-\mathbf{k}) \rangle$  of the time-reversal operator  $\Theta \equiv e^{i\pi S_y/\hbar} K$  ( $\Theta^2 = -1$  for spin- $\frac{1}{2}$  electrons,  $S_y$  is the spin operator, and  $K$  is the complex conjugate operator) in the Bloch state basis. The Bloch Hamiltonian is time-reversal symmetric at 8 specific points in the three-dimensional Brillouin zone. For each of these time-reversal invariant momenta one can define [1]

$$\delta_{\Gamma_a} = \sqrt{\det[w(\Gamma_a)]} / Pf[w(\Gamma_a)] = \pm 1, \quad (2.1.4)$$

where the Pfaffian

$$Pf[w(\Gamma_a)]^2 = \det[w(\Gamma_a)]. \quad (2.1.5)$$

This allows to define four topological indices  $(\nu_0; \nu_1, \nu_2, \nu_3)$  as following:

$$(-1)^{\nu_0} = \prod_{n_j=0,\pi} \delta_{n_1 n_2 n_3} \quad (2.1.6)$$

which has the only difference from the  $\mathbb{Z}_2$  invariant for the two-dimensional case in the number of the time-reversal momenta (8 unlike 4 for the two-dimensional topological insulators), and

$$(-1)^{\nu_{i=1,2,3}} = \prod_{n_j \neq i = 0,\pi; n_i = \pi} \delta_{n_1 n_2 n_3}, \quad (2.1.7)$$

where  $n_j = 0, \pi$  set the time-reversal invariant vectors in the primitive reciprocal lattice.

According to [1], for crystals with inversion symmetry the  $\mathbb{Z}_2$  invariant calculations can be simplified to

$$\delta_{\Gamma_a} = \prod_m \xi_m(\Gamma_a) \quad (2.1.8)$$

where the Bloch states  $|u_m(\Gamma_a)\rangle$  are also parity eigenstates with eigenvalue  $\xi_m(\Gamma_a) = \pm 1$ , thereby, the product has to be taken over the Kramers pairs of the occupied bands.

Usually three-dimensional weak topological insulators can be formed by stacking layers of a two-dimensional quantum spin Hall insulator, but the resultant surface states are unstable to disorder because crystal dislocations are associated with the one-dimensional helical edge states [33]. However, a three-dimensional strong topological insulator is not layered and is topologically non-trivial. It has time-reversal symmetry protected gapless surface states and this is normally meant by the term

"topological insulator".

Importantly, some of the topological insulators (e.g.  $\text{Bi}_2\text{Se}_3$ ,  $\text{Bi}_2\text{Te}_3$ ,  $\text{Sb}_2\text{Te}_3$ ) exhibit a large 150–300 meV energy gap, i.e. much larger than the room temperature thermal fluctuations [6–8, 34, 35]. Given these unique properties (no backscattering, robust topological surface states in the absence of the magnetic field, large bulk bandgap) topological insulators may be of a great importance for potential applications in room-temperature spintronic devices, high-performance electronics, dissipationless transistors for quantum computing and, of course, for the study of new quantum phases of matter.

### 2.1.3. Three-dimensional topological insulators: experimental discovery

The search for topological insulators was carried out among materials consisting of heavy elements with strong SOC (e.g. Bi, Sb, Te, Hg,...). The quantum spin Hall state was theoretically proposed to be realized in  $\text{CdTe}/\text{HgTe}/\text{CdTe}$  quantum wells in 2006 [36]. Later this prediction was successfully confirmed by transport measurements in such heterostructures [37].

Soon after the theoretical prediction [4] the first three-dimensional topological insulator was experimentally discovered in 2008 which is the semiconducting  $\text{Bi}_{1-x}\text{Sb}_x$  alloy. Bi is a semimetal with strong SOC and a bulk energy gap at the L point [38] with a Dirac-like dispersion near the L point, according to band structure calculations [39]. Sb substitution of Bi ( $0.07 < x < 0.22$ ) leads to the bulk band inversion with the occurrence of a massless Dirac point. The non-trivial topology of  $\text{Bi}_{0.9}\text{Sb}_{0.1}$  was verified by angle-resolved photoemission spectroscopy (ARPES) where the measured electronic band structure features a bulk energy gap at the L point and 5 surface bands crossings [40] as shown in Fig. 2.1.6a. The odd number of band crossings between time-reversal invariant points  $\Gamma$  and M evidences the topologically protected surface states in this material. The non-trivial topology of the surface states of  $\text{Bi}_{0.9}\text{Sb}_{0.1}$  was also revealed by spin-resolved ARPES measurements of the surface states [41] which were found to be nondegenerate and strongly spin-polarized. Mapping of the spin texture of the Fermi surface of this compound evidences for the  $\pi$  Berry phase characteristic for topological insulators [41].

In addition, the topological nature of the surface states in topological insulators can be probed locally with atomic resolution by scanning tunneling microscopy (STM) which will be described in Chapter 3. According to the STM studies on  $\text{Bi}_{0.92}\text{Sb}_{0.08}$  [42], the absence of backscattering which is characteristic for topological insulators was clearly proved due to the suppressed intensity in the  $\Gamma$ -M direction in the Fourier-transformed quasiparticle interference (FT-QPI) patterns (which will

be discussed in Chapters 3, 4) indicating the chiral nature of the topological surface states (see Fig. 2.1.6b).

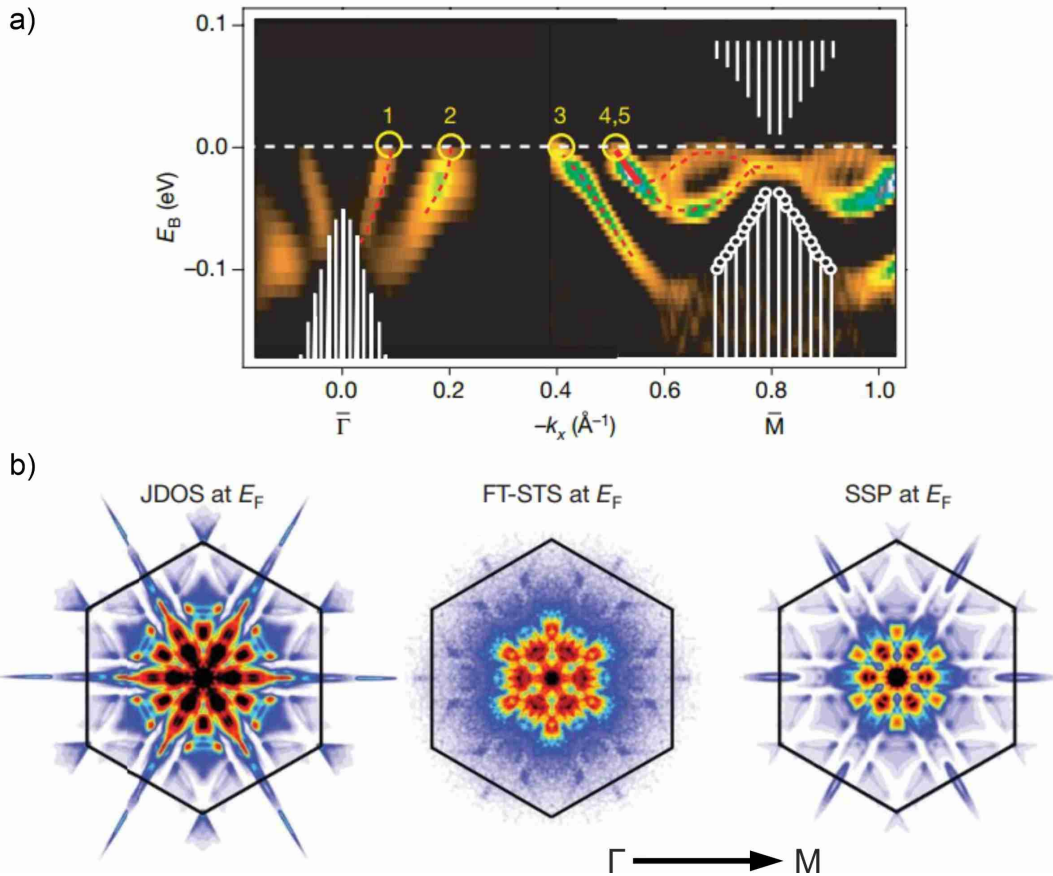


**Fig. 2.1.6** a) Experimental band structure of  $\text{Bi}_{0.9}\text{Sb}_{0.1}$  measured by ARPES. The surface band dispersion second-derivative image (for better representation of dispersive features) along  $\Gamma$ -M direction is plotted. Five Fermi level crossings between  $\Gamma$  and M are denoted by yellow circles with the doubly degenerate band near  $-k_x \approx 0.5 \text{ \AA}^{-1}$ . The red lines are guides to the eye. The shaded white area shows the projection of the bulk bands, b) Quasiparticle interference pattern (in the middle) detected by STM on  $\text{Bi}_{0.92}\text{Sb}_{0.08}$  is in a better agreement with the calculations based on the spin-selective scattering than the spin-independent calculations. This is due to the suppressed intensity of the outer intensity peaks corresponding to the backscattering (the right figure) when backscattering was not taken into account and, in contrast, the pronounced outer peaks (the left figure) when backscattering was involved in the calculations. Adapted from [40] and [42].

However, the  $\text{Bi}_{1-x}\text{Sb}_x$  compound has strong drawbacks as its complicated surface band structure along with a relatively small bulk band gap of around 38 meV [43]. This required the search for better materials which were later called "second generation" of three-dimensional topological insulators [5]. These are stoichiometric binary compounds  $\text{Bi}_2\text{Se}_3$ ,  $\text{Bi}_2\text{Te}_3$  and  $\text{Sb}_2\text{Te}_3$  [6, 7] which were widely studied before mainly due to their peculiar thermoelectric properties. Theoretical calculations [6] predicted a rather simple surface electronic structure with only a single Dirac cone as depicted in Fig. 2.1.7a which was confirmed by ARPES experi-

ments [7,8,34,35] where the helical spin texture of the surface Dirac electrons and the spin-momentum locking were also directly observed (see Fig. 2.1.7b). These semiconductors with strong SOC exhibit much larger bulk energy gap than  $\text{Bi}_{1-x}\text{Sb}_x$ , in particular,  $\sim 300$  meV for  $\text{Bi}_2\text{Se}_3$  [6, 7, 34] and  $\sim 150$  meV for  $\text{Bi}_2\text{Te}_3$  [8, 34, 35] which are one order of magnitude larger than the thermal energy at room temperature, making them potentially usable in room temperature electronic devices with topological protection.

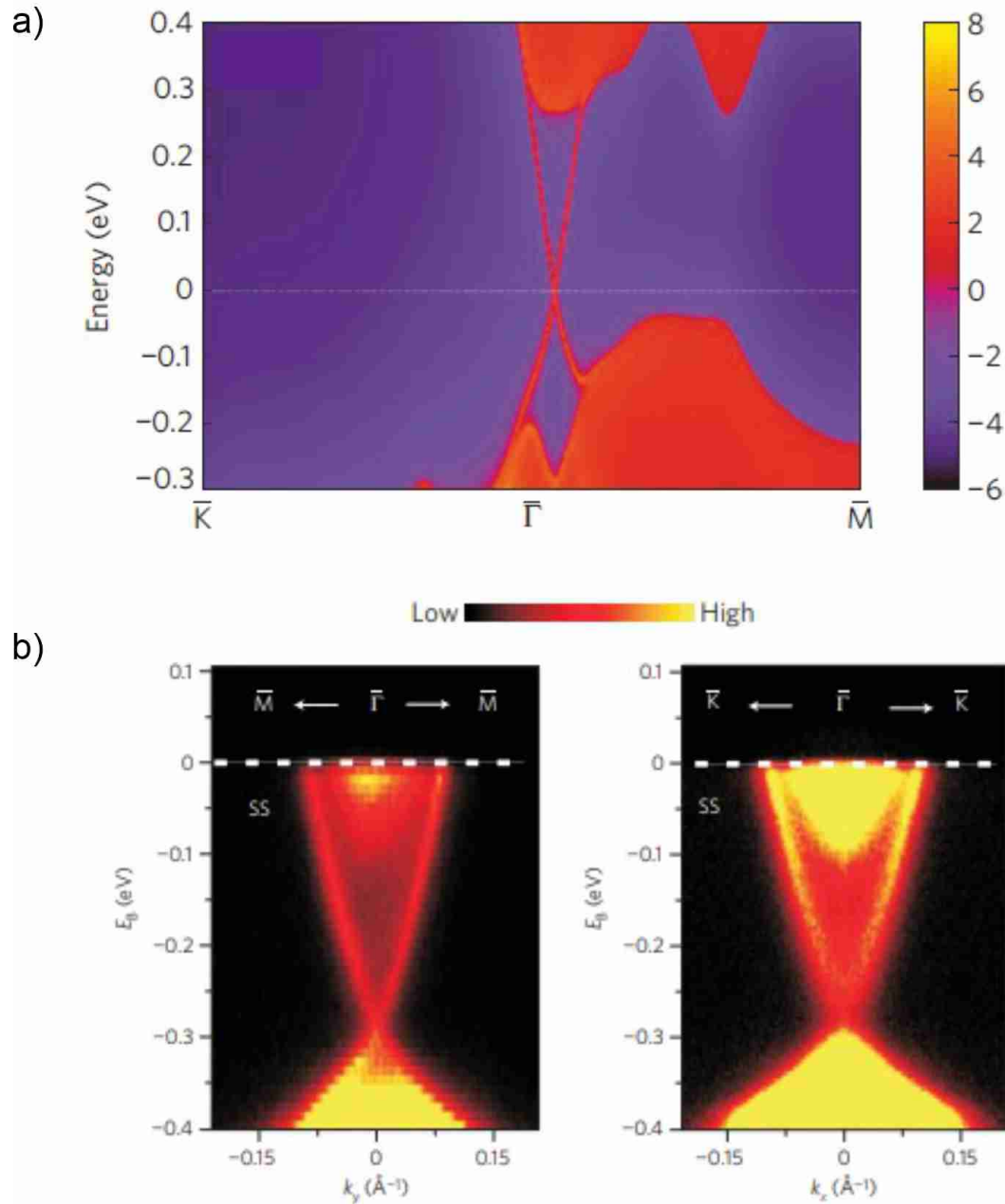


**Fig. 2.1.7** a) Calculated electronic band structure of  $\text{Bi}_2\text{Se}_3$ . b) Experimental band structure of  $\text{Bi}_2\text{Se}_3$  measured by ARPES in the  $\Gamma$ -M and  $\Gamma$ -K high-symmetry directions. X-shaped bands indicate the Dirac cone of the surface states. Adapted from [6] and [7].

## 2.1.4. $\text{Bi}_2\text{Te}_3$ : crystal and electronic structure

$\text{Bi}_2\text{Te}_3$  is one of the second generation three-dimensional topological insulators and serves as a base for  $\text{MnBi}_2\text{Te}_4$  and  $\text{MnBi}_4\text{Te}_7$  compounds also studied in this work.  $\text{Bi}_2\text{Te}_3$  has a rhombohedral crystal structure with the primitive unit cell consisting of Bi atoms with chemically inequivalent Te(1) and Te(2) sites. The structure of this compound is more conveniently described by the hexagonal unit cell composed of 3 so-called quintuple layers, where each of them is formed by 5 atomic layers in the sequence Te(1)-Bi-Te(2)-Bi-Te(1) stacked along the  $c$ -axis as shown in Fig. 2.1.8 [44]. The lattice constant  $a \approx 4.38 \text{ \AA}$  and the height of one quintuple layer is around  $10 \text{ \AA}$ . The quintuple layers are bonded by van der Waals forces which are weaker than the interatomic covalent and ionic bonds in each of the quintuple layers [45], making the crystal predominantly being cleaved on a Te(1) terminated (111) surface and accessible for surface-sensitive characterization by means of ARPES and STM.

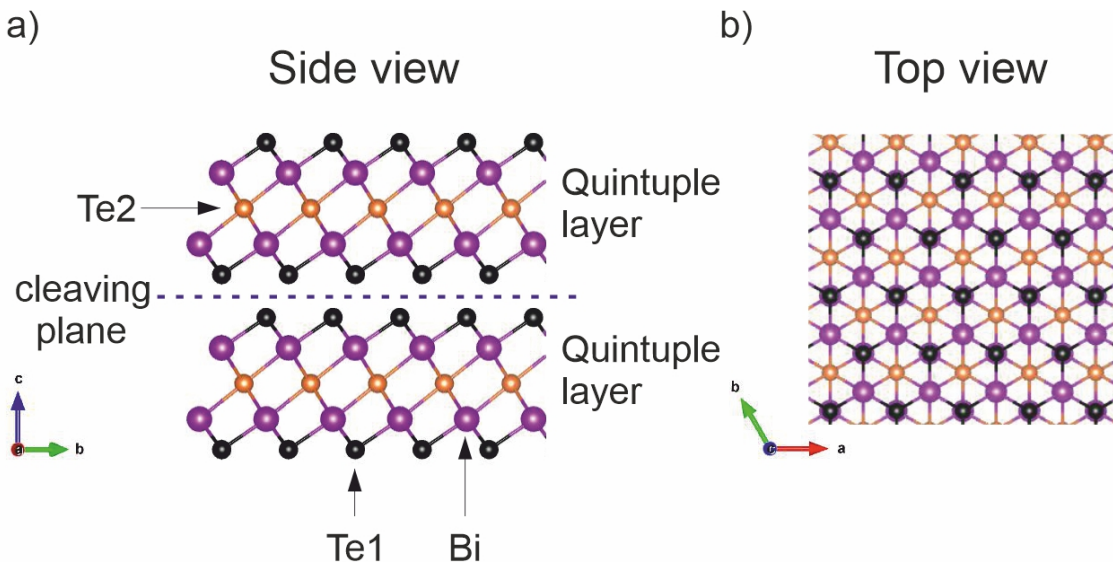


**Fig. 2.1.8** Crystal structure of  $\text{Bi}_2\text{Te}_3$  with a) side view of two quintuple layers and b) top view along the  $c$ -axis.

The electronic band structure calculations of  $\text{Bi}_2\text{Te}_3$  predicted the presence of a single Dirac cone of the surface state [6] which was later experimentally observed by ARPES where a distinct single V-shaped band centered at the  $\Gamma$ -point of the surface Brillouin zone appears in the bulk band gap of the material (see Fig. 2.1.9) [8, 34, 35]. This band existing for both  $\Gamma$ -K and  $\Gamma$ -M high-symmetry directions is unambiguously associated with the Dirac cone of the surface states which possess helical spin texture with spin-momentum locking. It is worth to note that the Dirac point in  $\text{Bi}_2\text{Te}_3$  is energetically located inside its bulk valence band unlike for many other three-dimensional topological insulators as, for example,  $\text{Bi}_2\text{Se}_3$ ,  $\text{Sb}_2\text{Te}_3$ ,  $\text{Bi}_x\text{Sb}_{1-x}$ .

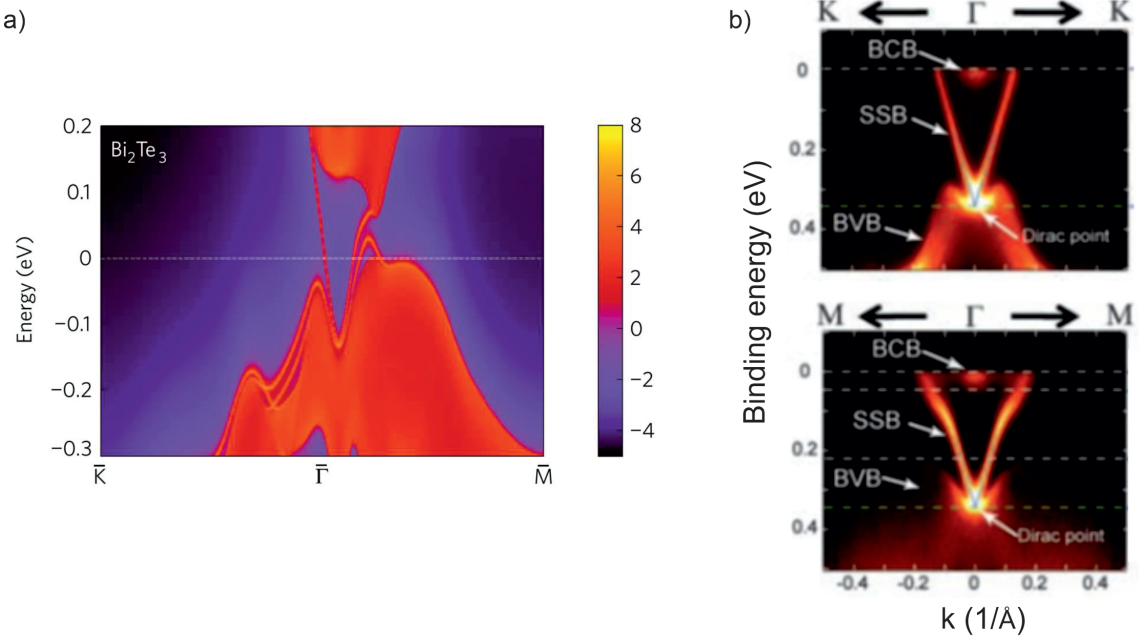


**Fig. 2.1.9** a) Calculated band structure of  $\text{Bi}_2\text{Te}_3$ , b) Experimental band structure from the ARPES measurements. Adapted from [6,8].

In addition, according to the very first ARPES measurements on  $\text{Bi}_2\text{Te}_3$  [8] the measured surface band structure, the Dirac cone is different for  $\Gamma$ -K and  $\Gamma$ -M high-symmetry directions. This deviation starts from around 200 meV above the Dirac point as shown in Fig. 2.1.9b and Fig. 2.1.10a. It results in changes of the shape of the surface states constant-energy contour as a function of energy as Fig. 2.1.10b illustrates: the experimental ARPES measured constant-energy contour at some energies becomes not circular anymore but looks like a snowflake, concave hexagram with relatively sharp tips extending along the  $\Gamma$ -M direction, and curves inward in between. This Fermi surface anisotropy is called hexagonal warping and was theoretically explained by introducing an additional, cubic in  $k$  term into the surface Dirac Hamiltonian

$$H(\mathbf{k}) = k^2/(2m) + v_k(k_x\sigma_y - k_y\sigma_x) + \frac{\lambda}{2}(k_+^3 + k_-^3)\sigma_z, \quad (2.1.9)$$

( $v_k = v(1 + \alpha k^2)$  is the Dirac velocity with a second-order correction,  $\sigma_{x,y,z}$  are the Pauli matrices,  $\lambda$  is the hexagonal warping parameter,  $k_{\pm} = k_x \pm ik_y$ ) due to the existing crystal and time-reversal symmetries in the rhombohedral system [46]. The first-principles calculations of the hexagonally warped Dirac cone [47] are presented in Fig. 2.1.11b where the Fermi surface shape transforms from a circle at the energies near the Dirac point to a hexagon and then appear as a warped hexagon further away from the Dirac point as shown in Fig. 2.1.11. The hexagonal warping itself induces an out-of-plane spin component  $s_z$  [46]. Fig. 2.1.12 illustrates the intricate three-dimensional spin texture of  $\text{Bi}_2\text{Te}_3$ , which was confirmed experimentally by

spin-resolved ARPES [34, 48].

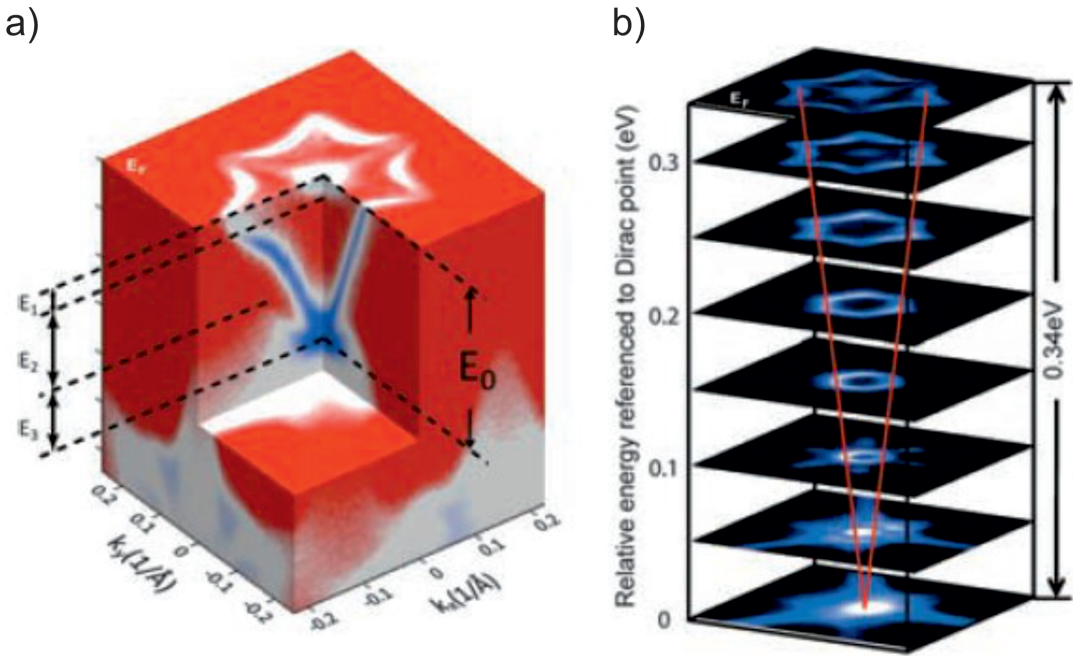


**Fig. 2.1.10** a) A three-dimensional illustration of the electronic band structure of  $\text{Bi}_2\text{Te}_3$ . b) Constant-energy contours and their energy evolution. Red lines indicate the Dirac cone. Adapted from [8].

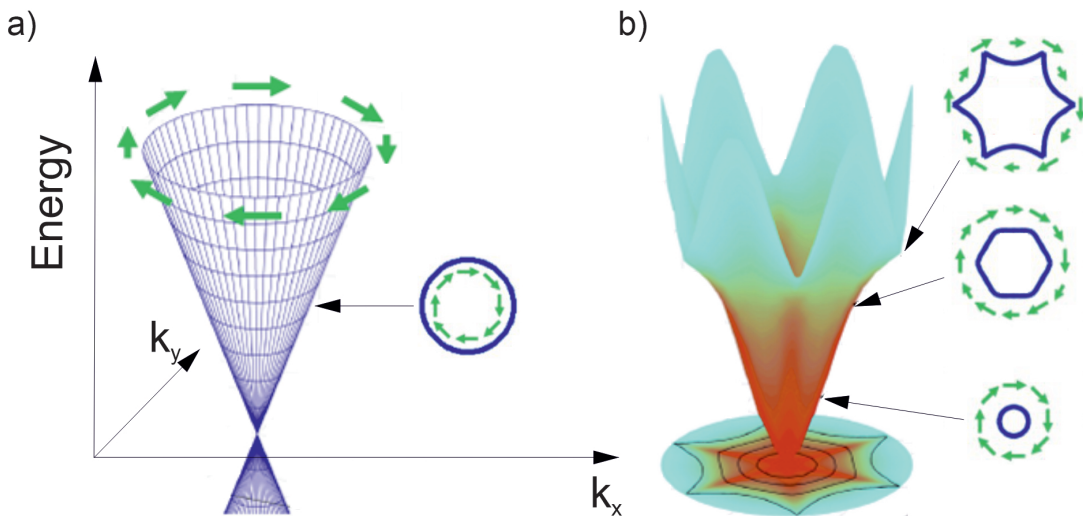


**Fig. 2.1.11** Calculated Dirac cone of the surface states in  $\text{Bi}_2\text{Te}_3$  with corresponding constant-energy contours in  $(k_x, k_y)$ -planes: a) ideal cone of  $\text{Bi}_2\text{Te}_3$  with only circular Fermi surfaces, b) warped cone with the constant-energy contours evolving from a circle to a snowflake. Spin directions marked by green arrows are perpendicular to linear momenta at each point demonstrating the helical in-plane spin texture. Adapted from [47].

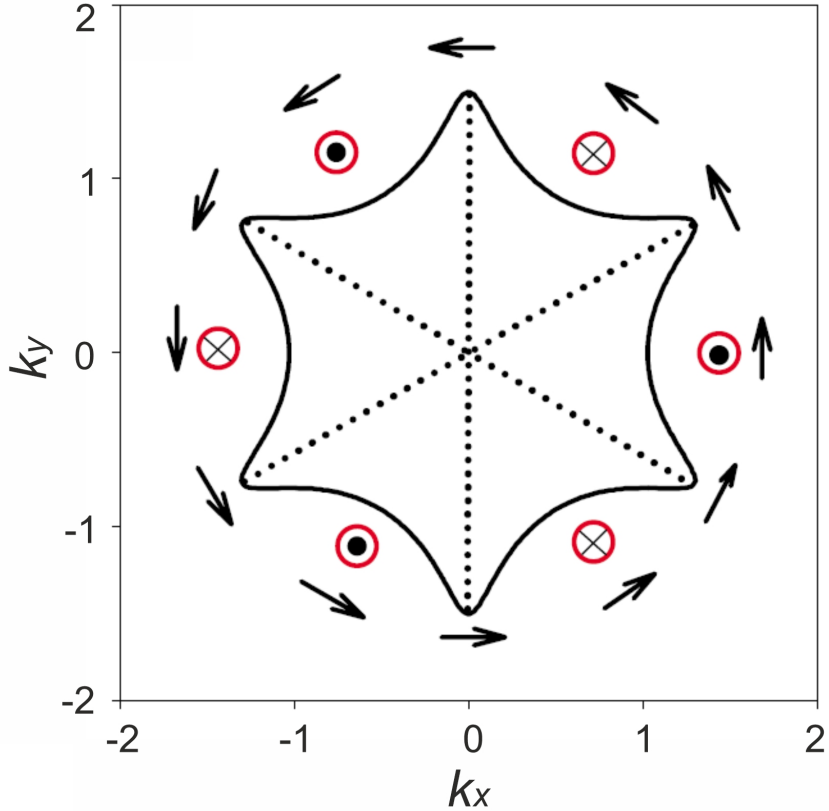


**Fig. 2.1.12** The three-dimensional spin texture of  $\text{Bi}_2\text{Te}_3$  for the hexagonally warped Dirac cone. The spin orientation in the  $xy$  plane is shown by the black arrows, and the solid dots/crosses indicate the out-of-plane component  $s_z$ .  $k_x$  and  $k_y$  values are presented in relative units.  $s_z = 0$  at the corners of the warped hexagon, while it reaches the largest magnitude exactly between them with staggered signs. Adapted from [49].

### 2.1.5. STM and STS of $\text{Bi}_2\text{Te}_3$

Local electronic properties of  $\text{Bi}_2\text{Te}_3$  were investigated by STM at cryogenic temperatures [50–58]. The STM topography data of the pristine stoichiometric compound reveal an atomically corrugated  $\text{Te}(1)$ -terminated surface with the presence of various native defects arising from  $\text{Bi}_{\text{Te}}$  (Bi on a Te site) or  $\text{Te}_{\text{Bi}}$  (Te on a Bi site) substitutions, vacancies ( $\text{V}_{\text{Te}}$ ), and interstitial defects inside the van der Waals gaps between adjacent quintuple layers or adatoms. The identification of the observed defect types was made with the use of density functional theory (DFT)-based calculations in [50] which is illustrated in Fig. 2.1.13 for the filled states with the large filled-states topography image.

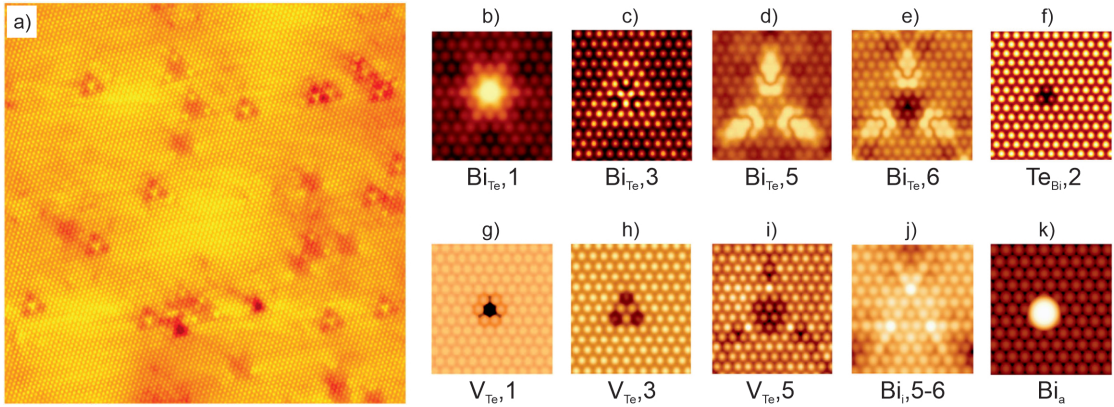


**Fig. 2.1.13** a)  $40 \text{ nm} \times 40 \text{ nm}$  topography of stoichiometric  $\text{Bi}_2\text{Te}_3$  at  $U_{bias} = -0.4 \text{ V}$ ,  $T = 4.5 \text{ K}$ . STM simulations for filled states for  $\text{Bi}_{\text{Te}}$  defects located in the b) first ( $\text{Bi}_{\text{Te}},1$ ), c) third ( $\text{Bi}_{\text{Te}},3$ ), d) fifth ( $\text{Bi}_{\text{Te}},5$ ), and e) sixth ( $\text{Bi}_{\text{Te}},6$ ) atomic layer, f)  $\text{Te}_{\text{Bi}}$  defects located in the second ( $\text{Te}_{\text{Bi}},2$ ) atomic layer, (g)  $\text{V}_{\text{Te}}$  defects located in the first ( $\text{V}_{\text{Te}},1$ ), h) third ( $\text{V}_{\text{Te}},3$ ), and i) fifth ( $\text{V}_{\text{Te}},5$ ) atomic layer, and (j)  $\text{Bi}_i$  defects located in between the fifth and sixth ( $\text{Bi}_i,5-6$ ) atomic layer and k) on top of the first ( $\text{Bi}_a$ ) atomic layer. The notation  $A(V)_{B,n}(i,a)$  ( $A$  – substituting atom on a  $B$  site in the  $n^{th}$  atomic layer,  $V$  – vacancy,  $i$  – interstitial,  $a$  – adatom) will be also used further, in section 4.1. Adapted from [50].

The hexagonal warping effect in  $\text{Bi}_2\text{Te}_3$  plays an important role in electron scattering processes which were explored by QPI on the crystalline defects or atomic step edges in the STM experiments on this material [50, 52, 53, 55, 56]. In particular, since the backscattering is suppressed by the time-reversal symmetry, relatively weak interference effects would be expected. However, the warping of the Fermi surface leads to the opening up of different scattering channels enhancing the QPI signal [46, 47, 53] which will be discussed later, in section 4.1. All the abovementioned QPI studies on  $\text{Bi}_2\text{Te}_3$  clearly demonstrate the linear energy-momentum dispersion of the dominant scattering vector in the six-fold symmetric FT-QPI patterns with the absence of backscattering channel (see Fig. 2.1.14) confirming the topological protection of the surface states in this material.

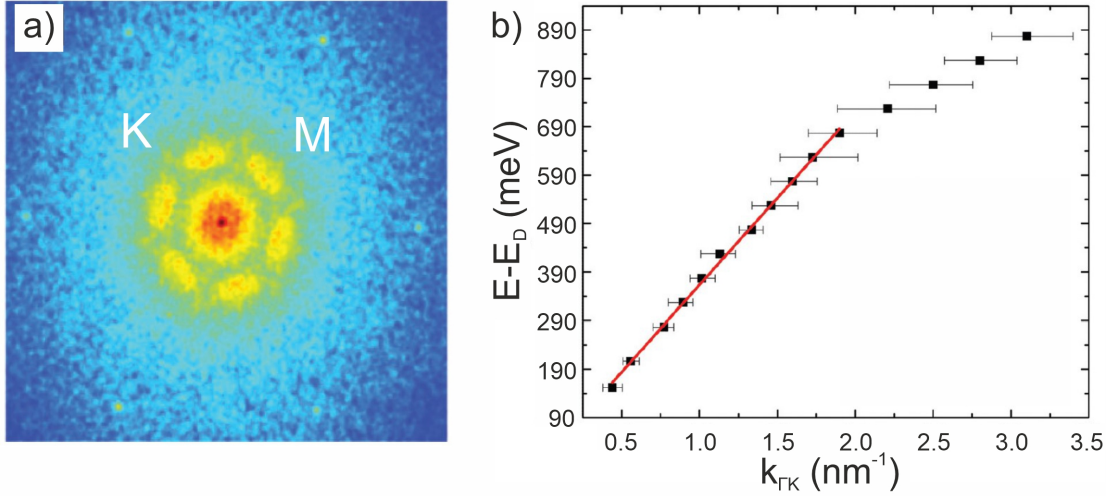


**Fig. 2.1.14** a) Example of the six-fold symmetric FT-QPI pattern measured in the warped energy region,  $E = 540$  meV counted from the Dirac point,  $I = 50$  pA,  $T = 4.8$  K. b) Energy dispersion of the topological surface states with the linear fit (red line). Adapted from [52].

## 2.2. Magnetic topological insulators

### 2.2.1. Theoretical background

Shortly after the theoretical prediction and the experimental observation of the time-reversal symmetry protected three-dimensional topological insulators the natural question arose that how magnetism can interact with conventional topological insulators. One can expect that since magnetism lifts the time-reversal symmetry, the topological surface states would be destroyed. In fact, an indirect magnetic exchange mediated by the topological surface states results in a Zeeman-like energy gap opening at the Dirac point as shown in Fig. 2.2.1.

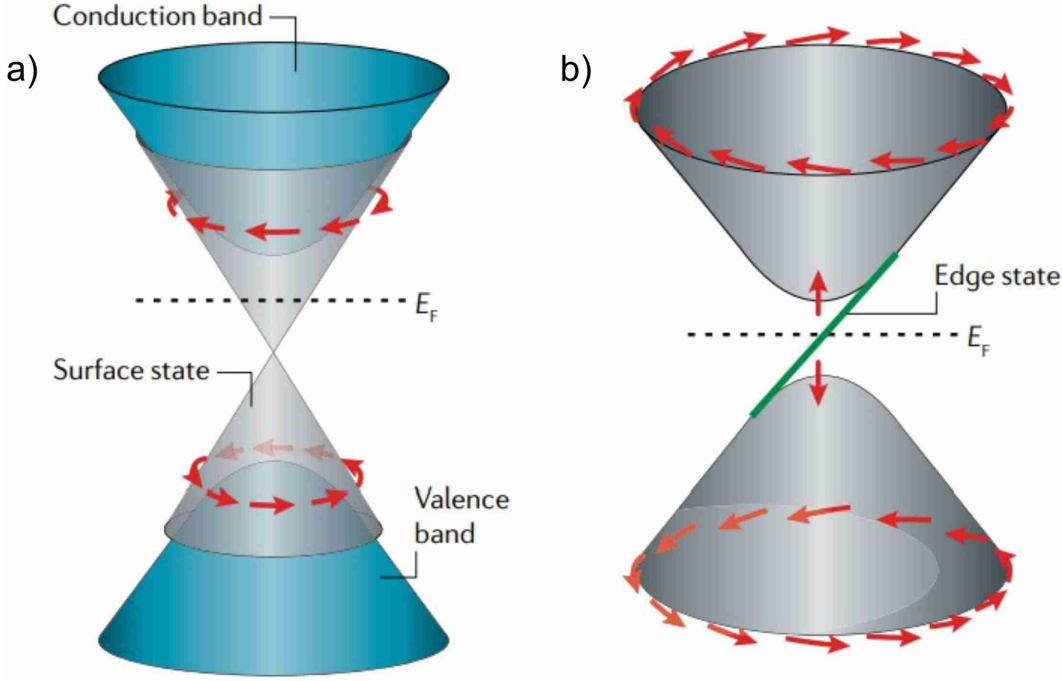


**Fig. 2.2.1** a) Massless and b) gapped Dirac cones of the surface states with spin-momentum locking in a topological insulator and in a magnetic topological insulator, respectively. Similar to the integer quantum Hall systems (see 2.1.1), the chiral edge state in b) hosts electrons which conduct electricity with no dissipation in the direction of the sample boundary. Adapted from [12].

One important example of magnetic topological insulators, i.e. materials combining both long-range magnetic ordering with the topological electronic structure, which is, in particular, relevant to the present work is given by antiferromagnetic topological insulators. According to a theoretical paper [59], introducing antiferromagnetic order into a topological insulator leads to the following: although both time-reversal symmetry  $\Theta$  and primitive-lattice translational symmetry  $T_{1/2}$  are broken, their combination  $S = \Theta T_{1/2}$  symmetry is preserved leading to the  $\mathbb{Z}_2$  topological classification. As a consequence, an exchange gap in the surface states is induced on the symmetry-breaking surface, while the symmetry-preserving surface hosts massless Dirac states as nonmagnetic  $\mathbb{Z}_2$  topological insulators do.

Magnetic topological insulators provide a great opportunity to realize exotic quantum phenomena, in particular, quantum anomalous Hall effect at zero external magnetic field [60] as well as topological magnetoelectric and quantized magneto-optical effects [31, 61, 62]. These effects arise from considering the surface Hall current leading to non-trivial electrodynamics of topological insulators similar to axion electrodynamics [31]. This makes a remarkable relation between the solid state physics and the elementary particle physics. The axion is a hypothetical elementary particle which is expected to be a possible component of cold dark matter [63, 64]. Modified Maxwell equations in topological insulators give rise to a peculiar axion-

type coupling between magnetization  $\mathbf{M}$  and electric field  $\mathbf{E}$  [31, 61]:

$$\mathbf{M} = \frac{e^2}{2h\pi} \theta \mathbf{E} = \sqrt{\frac{\epsilon_0}{\mu_0}} \alpha \frac{\theta}{\pi} \mathbf{E}, \quad (2.2.1)$$

where  $\theta = \pi$  in  $\mathbb{Z}_2$  topological insulators,  $\theta = 0$  in ordinary insulators,  $e$  is the elementary charge,  $h$  is the Planck constant,  $\epsilon_0$  and  $\mu_0$  are the electric and magnetic constants, respectively.

Therefore, the magnetoelectric susceptibility in topological insulators is quantized in units of  $\alpha$  (fine structure constant). For example, at the interface between a topologically trivial material ( $\theta = 0$ ) and a thin film of a magnetic topological insulator with collinear magnetizations on both top and bottom surfaces of the film, if the Fermi energy lies inside the exchange gap, then the spatial change of  $\theta = \pm\pi$  through the interface. This results in a quantum anomalous Hall effect with an integer quantized in units of  $e^2/h$  Hall conductivity  $\sigma_{xy}$  in absence of an external magnetic field (see Fig. 2.2.2a). In the other case with anticollinear magnetizations the axion insulator state emerges which is characterized by vanishing longitudinal conductivity  $\sigma_{xx} = 0$  with simultaneous zero Hall-conductivity  $\sigma_{xy} = 0$  as illustrated in Fig. 2.2.2b. All these effects have a great potential for the low-power-consumption electronics and, especially, for spintronics.

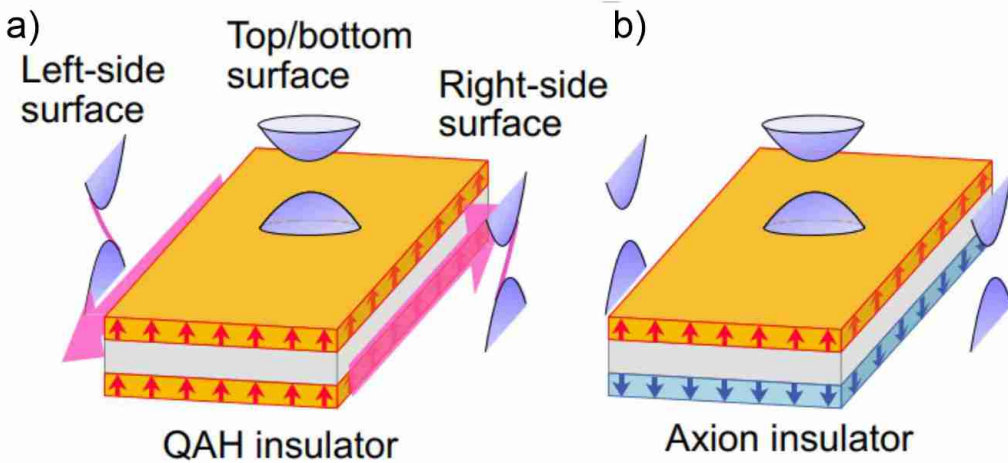


**Fig. 2.2.2** Schematic representation of the a) quantum anomalous Hall and b) axion insulator states. Magnetization opens a gap in the top and bottom surface states. One-dimensional chiral edge channels (pink arrows) are formed on the side surface in a) when the magnetizations (red arrows) are collinear. The energy gap opens also on the side surface in b) when the magnetizations are anticollinear. Adapted from [65].

## 2.2.2. Possible realizations in materials

The general routes to introduce magnetism into topological insulators and create a magnetic topological insulator are the following: magnetic doping with magnetic

$3d$  or  $4f$  elements [13, 60, 66–74], proximity effect by interfacing a topological insulator with ferromagnetic/antiferromagnetic insulators [31, 75–82], magnetic extension of the topological insulator crystal structure [83–85], and construction of intrinsic magnetic topological insulators [83–86].

The first and the most widely applied way to get a magnetic topological insulator was to dope a normal non-magnetic topological insulators with magnetic atoms. For instance, one of the first attempts was undertaken with Mn-doped  $\text{Bi}_2\text{Te}_3$  which showed a clear surface state gap measured by ARPES and the ferromagnetic order below 12 K [68]. However, as inferred from the STM measurements on that material, there are Mn-atoms substituting Bi-sites on the topmost layer and they are not clustered and distributed randomly on the surface, not forming a periodic sublattice. This would increase inhomogeneities in the electronic structure and magnetic properties which have not been avoided so far, thereby, it substantially reduces the temperature for the realization of the quantum anomalous Hall effect. For this reason, the idea of magnetic doping turned out to be not viable for searching the real candidates for magnetic topological insulators.

Another strategy to create a magnetic topological insulator is to make a direct contact between an ordinary topological insulator and a magnetic material via the interfacial exchange coupling, when a ferromagnetic/antiferromagnetic material (or even a layer) is placed near the topological insulator in order to induce the magnetization into the region of the topological insulator. However, the best so far obtained results (not clear quantum anomalous effect, a small exchange gap) by such a magnetic proximity are not appropriate for the final goal of the dissipationless spin-based electronics at ambient conditions and leave a lot of uncertainties for the heterostructure engineering [75, 76, 78, 79, 82].

Unlike the magnetic proximity approach, the so-called magnetic extension of the surface of the topological insulator implies that the topological states strongly penetrate into the magnetic film, when a ferromagnetic insulator film is deposited on top of the topological insulator, which is structurally exactly the same as the magnetic insulator, yielding an increase of the Dirac point gap size up to  $\sim 100$  meV [83–85]. Nevertheless, the observation of the quantum anomalous Hall effect in these heterostructures has not been demonstrated so far.

The next idea is to implement an ideal, intrinsic magnetic topological insulator, i.e. a material with both magnetic order and topologically non-trivial electronic structure. Thereby, the main obstacle in raising the critical temperature of the quantum anomalous Hall effect – inhomogeneous distribution of magnetic atoms inside a topological insulator – is expected to be overcome. This long-sought search has recently provided several magnetic topological insulator candidates in Mn-Bi-Te family of materials [9–11].

### 2.2.3. Actual results

The expected gapped Dirac cone was experimentally verified on different compounds. For example, Fig. 2.2.3a illustrates the ARPES measured massive Dirac cone on magnetic Fe(Mn)-doped  $\text{Bi}_2\text{Se}_3$  [13], and Fig. 2.2.3b shows the magnetism-induced zero conductance gap of approximately 30 meV detected by STS on Cr-doped  $(\text{Bi}_{0.1}\text{Sb}_{0.9})_{1.92}\text{Te}_3$  [87]. However, its existence in real intrinsic magnetic topological insulators is still under debate and will be discussed in next chapters.

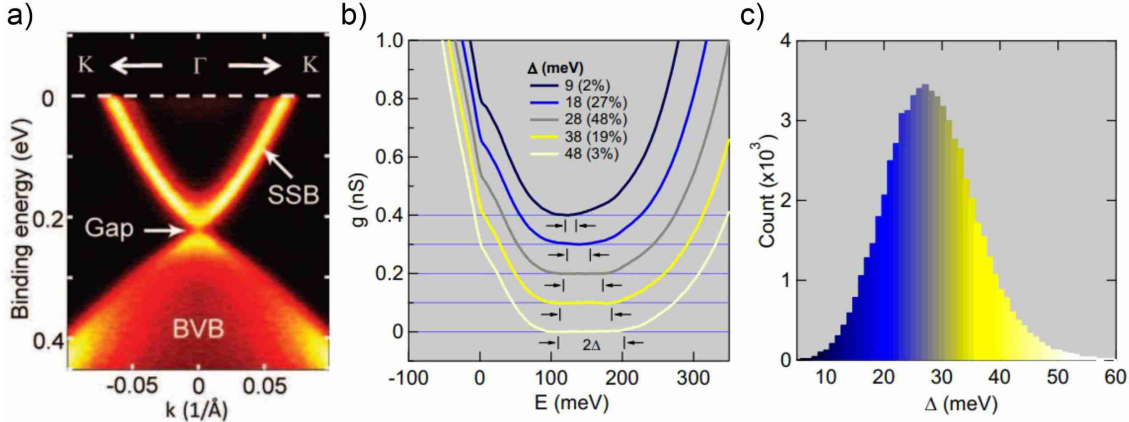


**Fig. 2.2.3** a) ARPES measured electronic band structure of 16% Fe-doped  $\text{Bi}_2\text{Se}_3$  with a gap formation at the Dirac point. Adapted from [13]. b) Gapped differential conductance spectra of Cr-doped  $(\text{Bi}_{0.1}\text{Sb}_{0.9})_{1.92}\text{Te}_3$  and c) histogram of the gap size measured at different surface locations by STS. Adapted from [87].

The STM studies on magnetically doped topological insulators, e.g. Mn, Fe, Cr-doped  $\text{Bi}_2\text{Te}_3$ ,  $\text{Bi}_2\text{Se}_3$ , provide a proof of their non-trivial topology [87–89]. Absence of the backscattering revealed from the FT-QPI patterns (see section 3.3) indicates the helical spin texture of the topological surface states even in the presence of magnetic impurities. Similar to the undoped  $\text{Bi}_2\text{Te}_3$  (see section 2.1.4), the energy evolution of the FT-QPI patterns corresponding to the hexagonally warped Dirac cone of the surface states was observed in the Mn-doped  $\text{Bi}_2\text{Te}_3$  which further supports the topological nature of the surface states (see Fig. 2.2.4). However, the influence of the broken time-reversal symmetry on the electronic structure was demonstrated by opening of new scattering channels in addition to that observed in time-reversal symmetry invariant topological insulators [89].

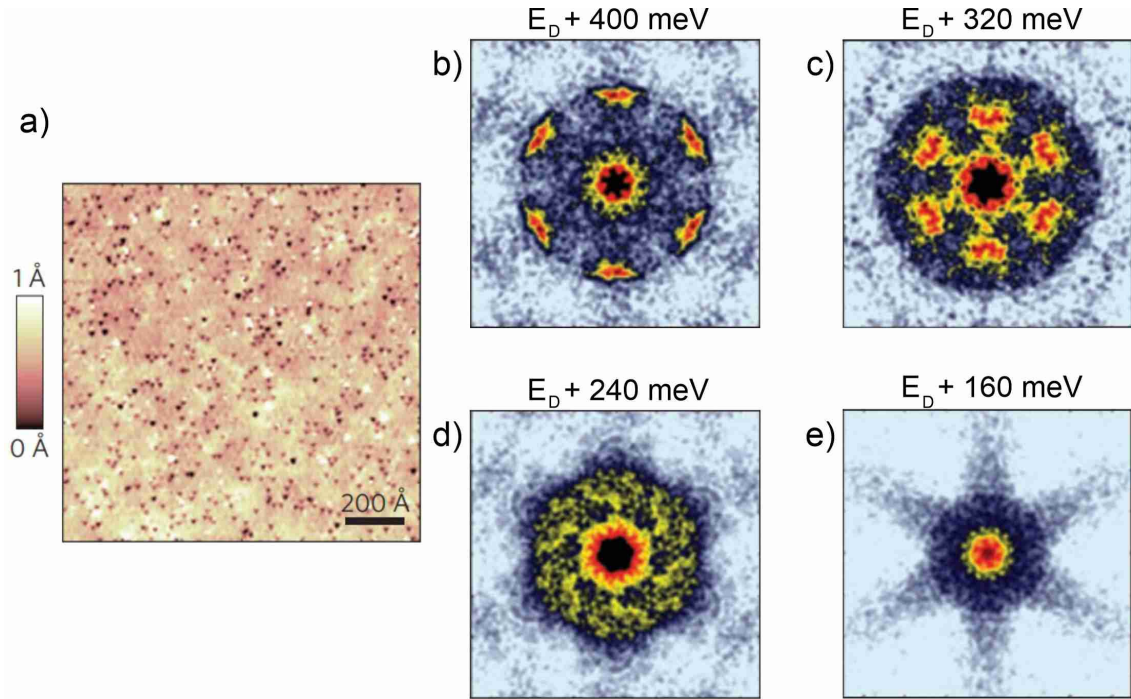


**Fig. 2.2.4** Mn-doped  $\text{Bi}_2\text{Te}_3$ : a) STM topography, b)–e) FT-QPI patterns at different energies with respect to the Dirac point detected by STM. Adapted from [88].

Concerning the expected quantum anomalous Hall and axion insulator states, both they have been reported in Cr- and V-doped topological insulators (see Fig. 2.2.5) but only in the millikelvin temperature range [65–67, 90–98]. The latter was caused by the inhomogeneous magnetic doping which affects the local magnetism reducing the observing quantization temperature and impeding the applications of these effects in room temperature electronic devices.

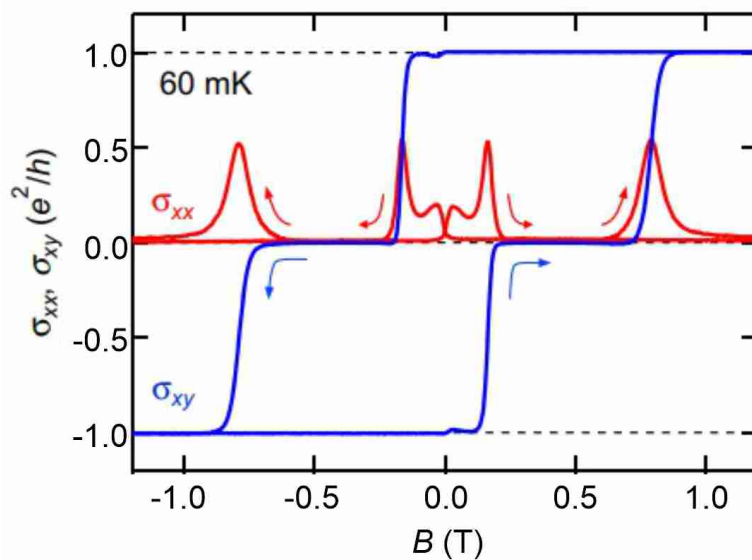


**Fig. 2.2.5** Magnetic field dependence of Hall conductivity ( $\sigma_{xy}$ ) and longitudinal conductivity ( $\sigma_{xx}$ ) of the Cr-V doped  $(\text{Bi},\text{Sb})_2\text{Te}_3$  film at  $T = 60$  mK. Adapted from [65].

In addition, quantum anomalous Hall and axion insulator states have been reported in odd- (5 septuple layers [99]) and even numbers (6 septuple layers [100]), respectively, of Te-Bi-Te-Mn-Te-Bi-Te septuple layers flakes of the intrinsic magnetic topological insulator  $\text{MnBi}_2\text{Te}_4$  which will be described more in detail in next chapters. In those transport experiments an axion insulator state was revealed at  $T = 1.6$  K [100], a zero-field quantum anomalous Hall was achieved at  $T = 1.4$  K and the quantization temperature reached 6.5 K at the external field  $H = 7.6$  T [99].

## 2.3. MnBiTe-family of compounds

Eventually, the search of intrinsic magnetic topological insulators has been succeeded in the  $\text{MnBi}_{2n}\text{Te}_{3n+1}$  ( $n = 1, 2, 3, \dots$ ) series of materials. Apart from the previously found  $\text{MnBi}_2\text{Te}_4$  [101], novel compounds  $\text{MnBi}_4\text{Te}_7$  and  $\text{MnBi}_6\text{Te}_{10}$  [102, 103] were very recently derived from  $\text{Bi}_2\text{Te}_3$  with Mn-Te bilayer intercalation. All the materials in this  $\text{MnBi}_{2n}\text{Te}_{3n+1}$  family are layered van der Waals magnets, consisting of non-magnetic  $\text{Bi}_2\text{Te}_3$  quintuple layer and magnetic  $\text{MnBi}_2\text{Te}_4$  (so-called septuple layer) blocks stacking along the  $c$ -axis and coupled by van der Waals bonds. Each quintuple (septuple) layer represents Te-Bi-Te-Bi-Te(Te-Bi-Te-Mn-Te-Bi-Te) atomic stacking, respectively. Unlike for  $\text{MnBi}_2\text{Te}_4$ , which is assembled by only magnetic septuple layers with the length of  $\approx 1.37$  nm,  $\text{MnBi}_4\text{Te}_7$  has an additional quintuple layer between each neighboring septuple layer and the other compounds host more extra quintuple layers between the septuple layers (see Fig. 2.3.1).

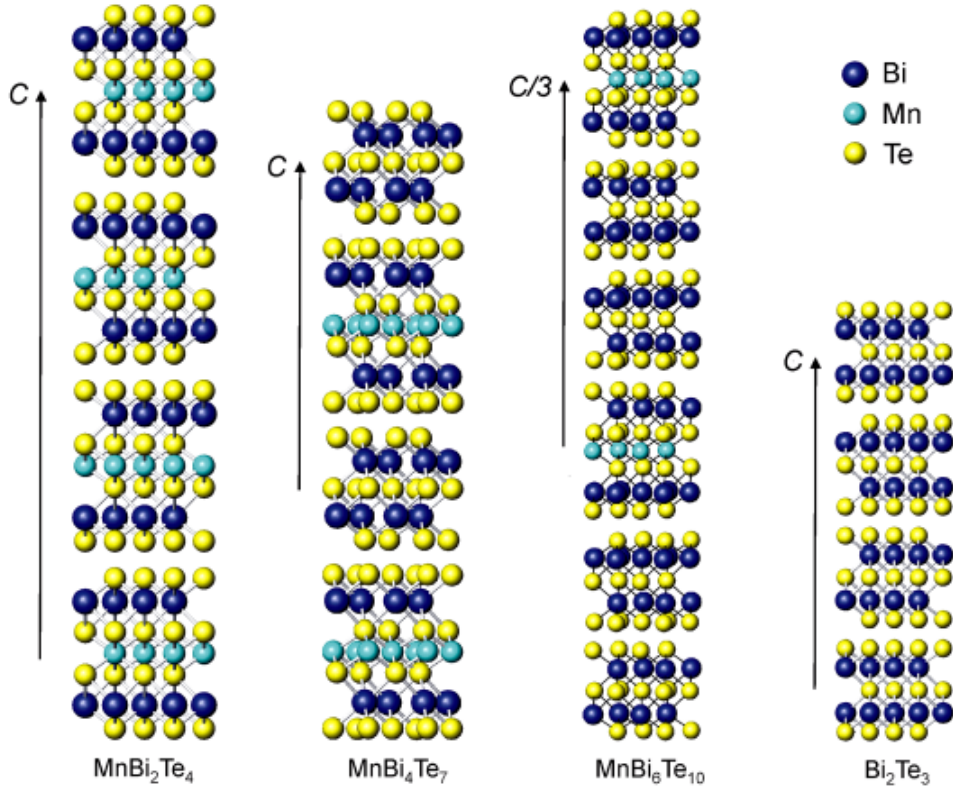


**Fig. 2.3.1** Crystal structures of  $\text{MnBi}_2\text{Te}_4$ ,  $\text{MnBi}_4\text{Te}_7$ ,  $\text{MnBi}_6\text{Te}_{10}$  and  $\text{Bi}_2\text{Te}_3$ . Adapted from [102].

The first unique property of such materials is that magnetic Mn-atoms obey structural ordering, implying that they are positioned on the crystallographic sites in an atomic sheet in the middle of each septuple layer. The second essential property is that these compounds demonstrate magnetic order.  $\text{MnBi}_2\text{Te}_4$  undergoes an antiferromagnetic phase transition at  $T \approx (24-25)$  K, while  $\text{MnBi}_4\text{Te}_7$  is an antiferromagnet between  $\sim 5$  K and  $\sim 13$  K, and there are signatures of the ferromagnetic order below  $\sim 5$  K.  $\text{MnBi}_6\text{Te}_{10}$  has a distinct antiferromagnetic phase as  $\text{MnBi}_2\text{Te}_4$  but below  $\approx 11$  K which can be tuned into a ferromagnetic phase below 12 K upon delicate defect engineering, as recently reported [104, 105]. Therefore, to observe quantum anomalous Hall effect in these magnetically coupled systems, strong external magnetic field exceeding the saturation field is required. Indeed, the quantum anomalous Hall effect and axion insulator state have been reported on  $\text{MnBi}_2\text{Te}_4$  thin flakes but only at  $T \approx 1.4$  K [99, 100], though the more recent data on this compound are controversial since the quantum anomalous Hall state was observed in both 5-septuple layer and 6-septuple layer flakes which points to material related issues [106].

The bulk of these materials orders into an A-type AFM structure which means that magnetic moments experience ferromagnetic exchange within each of the septuple layers and antiferromagnetic exchange along the crystallographic  $c$ -axis with the out-of-plane orientation of the magnetization easy axis [9, 10]. Given that the

distances between magnetic Mn-containing layers become larger upon increasing  $n$ , thus, the antiferromagnetic interlayer exchange coupling as well as the saturation field is getting smaller. In contrast to the examples of the  $\text{MnBi}_{2n}\text{Te}_{3n+1}$  series ( $n = 1, 2$ ),  $\text{MnBi}_8\text{Te}_{13}$  (the first reported intrinsic robust ferromagnetic topological insulator) has a ferromagnetic order with  $T_C \sim 10.5$  K since the interlayer ferromagnetic exchange becomes energetically more favorable than the antiferromagnetic one [107].

Therefore, one can argue that the larger the number of quintuple layer spacers between the adjacent septuple layers, the more pronounced the ferromagnetic properties of the compound which may facilitate the observation of quantum anomalous Hall effect and other intriguing associated phenomena [107]. Moreover, even the so-called single-layer magnets, where the interlayer exchange coupling vanishes, have been theoretically predicted and experimentally observed in the  $\text{MnBi}_{2n}\text{Te}_{3n+1}$  materials ( $n \geq 3-4$ ) [108]. However, in reality, due to the special requirements of the crystal growth technique (a few °C temperature window between the melting points of  $\text{Bi}_2\text{Te}_3$  and  $\text{MnBi}_{2n}\text{Te}_{3n+1}$ ), it becomes gradually much more difficult to grow single crystals upon going from  $\text{MnBi}_2\text{Te}_4$  to the higher numbers  $n$  [109, 110]. Furthermore, it appears to be much more complicated to perform surface-sensitive experiments such as ARPES and STM where it is necessary to identify all the possible surface terminations.

First-principles DFT calculations performed on  $\text{MnBi}_2\text{Te}_4$ ,  $\text{MnBi}_4\text{Te}_7$  and  $\text{MnBi}_6\text{Te}_{10}$  with the assumed A-type antiferromagnetic order predict that these compounds are, indeed, antiferromagnetic topological insulators since the obtained band inversion stems from the hybridization between Te-5p and Bi-6p bands only when SOC is taken into account [9, 11, 110–115]. The  $\mathbb{Z}_2 = 1$  topological invariant was, also, confirmed by calculations, which allows to propose that these materials are intrinsic antiferromagnetic topological insulators. A direct proof of the antiferromagnetic topological insulator would be the presence of a gap in the surface states at the Dirac point in the band structure measured in the antiferromagnetic phase on the symmetry-breaking (001) surface which is a natural cleavage plane in all these materials.

However, although there are some clear signatures of the gapped Dirac cone observed by ARPES in  $\text{MnBi}_2\text{Te}_4$ ,  $\text{MnBi}_4\text{Te}_7$ , and  $\text{MnBi}_6\text{Te}_{10}$  [9, 11, 109, 114–120], gapless surface states are, also, present [110, 114, 115, 120–122], therefore, the fundamental puzzle of the surface electronic structure in these materials requires a more thorough exploration.

### 2.3.1. $\text{MnBi}_2\text{Te}_4$

As reported in [9],  $\text{MnBi}_2\text{Te}_4$  was proved to be the first antiferromagnetic topological insulator by band structure calculations and ARPES measurements [9, 10].

$\text{MnBi}_2\text{Te}_4$  as the simplest example of Mn-Bi-Te material family is composed of a sequence of septuple layers consisting of Te-Bi-Te-Mn-Te-Bi-Te atomic planes. This compound possessing trigonal symmetry crystallizes in a  $R\bar{3}m$  space group (lattice parameters  $a \approx 4.33$  Å,  $c \approx 40.9$  Å) [102, 109, 123]. The main advantage of  $\text{MnBi}_2\text{Te}_4$  with respect to the other candidates for magnetic topological insulators is that the former material exhibits both structural and magnetic order [124, 125]. Mn-atoms are arranged periodically at the corresponding crystallographic sites forming a ferromagnetic layer in the middle of each septuple layer. Magnetic properties [9, 109, 117, 123, 126–128], neutron diffraction [123, 127, 129], X-ray magnetic dichroism measurements [9, 109] and first-principles calculations [9, 111] reveal that  $\text{MnBi}_2\text{Te}_4$  has a magnetic ground state of A-type antiferromagnetic order mentioned above. However, the single-crystal X-ray diffraction, transmission electron microscopy and STM experiments revealed a considerable amount (several percents) of cation intermixing in the Mn and Bi sites (and, also, Bi and Te sites) which may result in a non-stoichiometry of the compound [109, 123] as shown in its crystal structure in Fig. 2.3.2. It is worth to note that this cation disorder is ubiquitous in  $\text{TtBi}_2\text{Te}_4$  ( $\text{Tt} = \text{Ge, Pb, Sn}$ ) crystals [109, 130].

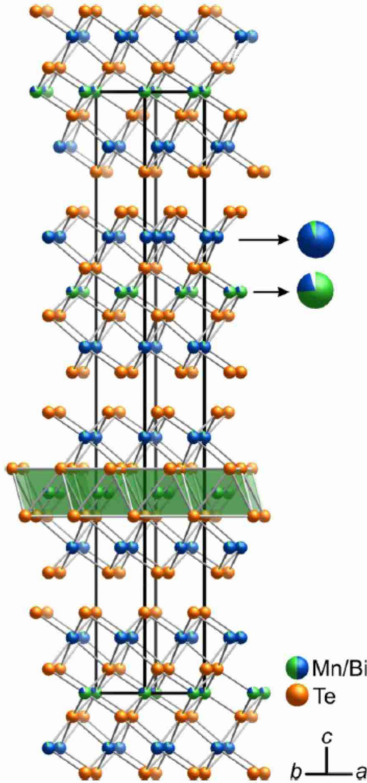


**Fig. 2.3.2** Crystal structure of  $\text{Mn}_{0.85(3)}\text{Bi}_{2.10(3)}\text{Te}_4$  with mixed site occupancies. Adapted from [109].

Magnetic properties of  $\text{MnBi}_2\text{Te}_4$  crystals were scrutinized by different research groups and bear mostly similar characteristics. The most significant of them are listed here. Anisotropic magnetic susceptibility obtained in its temperature dependence measured both at  $H \parallel c$  and  $H \perp c$  which evidences in favor of A-type antiferromagnetic order establishing below  $T_N = (24-25)$  K (see Fig. 2.3.3a) while the paramagnetic phase follows Curie-Weiss law [9, 109, 114, 117, 123, 126-128]. Apart from that, magnetization curve  $M(H)$  exhibits a clear metamagnetic spin-flop transition (canted antiferromagnetic state [117]) at  $T = 2$  K at  $H = (3.5-3.7)$  T shown in Fig. 2.3.3b when  $H \perp (001)$  in accordance with the easy axis of magnetization directed along the surface normal [9, 109, 114, 117, 123, 126]. It is also worth to mention that  $\text{MnBi}_2\text{Te}_4$  may become a magnetic Weyl semimetal under a moderate external magnetic field parallel to the  $c$ -axis, according to the band structure calculations [111, 112, 124]. The occurrence of the long-range antiferromagnetic ordering is, also, supported by electrical resistivity and specific heat measurements with the indicative peak at around  $T_N$  as presented in Figs. 2.3.3c,d. The resistivity shows nearly linear behavior as typical metals but has a sharp cusp at around  $T_N$  implying a strong spin scattering due to spin fluctuations near the paramagnetic-antiferromagnetic phase transition [9, 109, 117, 123]. A steep anomaly was found in both electrical and Hall resistivity at  $H = 7.8$  T ( $H \parallel c$ ),  $T = 2$  K where Mn spins

are supposed to be fully polarized (Fig. 2.3.4) [123, 126]. The negative sign of the Hall coefficient derived from the field dependence of the Hall resistivity explicitly indicates an electron type of carriers [9, 117, 123, 128].

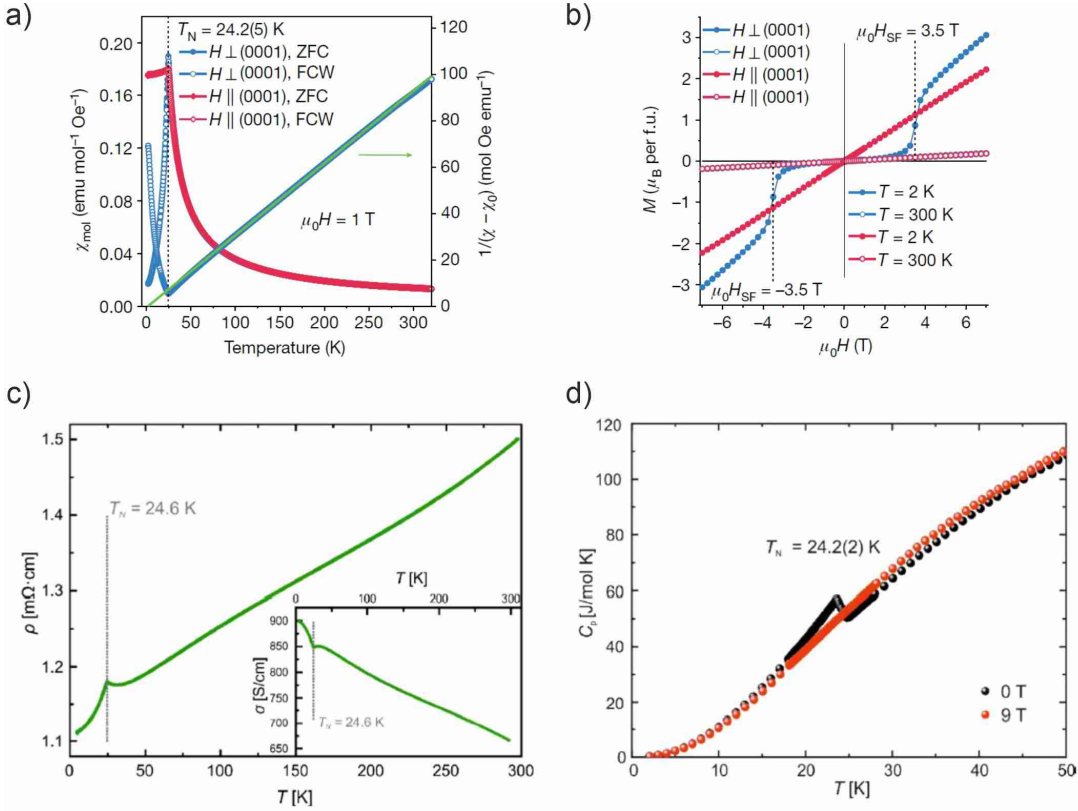


**Fig. 2.3.3** MnBi<sub>2</sub>Te<sub>4</sub> single crystals: a) magnetic susceptibility, b) field-dependent magnetization curves ( $H_{SF}$  – spin-flop magnetic field), c) in-plane electrical resistivity, d) specific heat. Adapted from [9, 109].

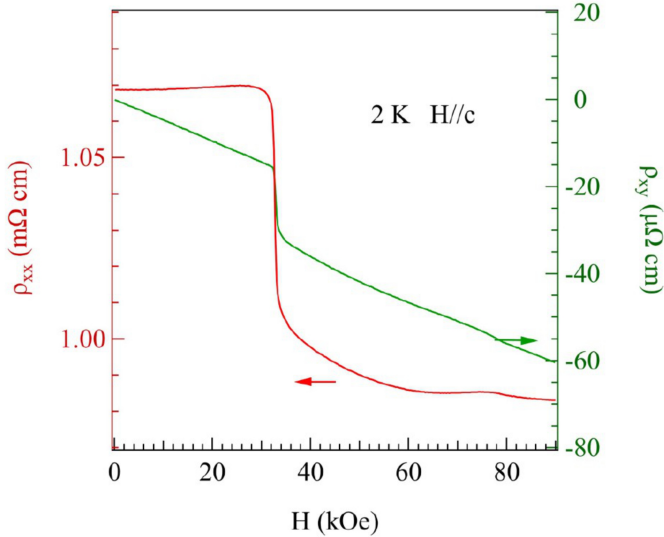


**Fig. 2.3.4**  $\rho_{xx}$  and  $\rho_{xy}$  as a function of magnetic field in MnBi<sub>2</sub>Te<sub>4</sub> single crystals. Adapted from [123].

However, the saturation magnetization at  $H \approx 7.8$  T is around  $4\mu_B$  per Mn, unlike the expected value of  $(4.5\text{--}5)\mu_B$  suggesting a  $\text{Mn}^{2+}$  high-spin configuration  $S = 5/2$  which was also derived from neutron scattering studies [123]. As found recently in [131], the high-field magnetization data reveal two plateaus with the latter one occurring at around 50 T with the full magnetic moment of  $4.6\mu_B$  per Mn (see Fig. 2.3.5). In other words, the full saturation of magnetization requires such high fields due to the antiferromagnetic coupling of the Mn/Bi (Mn on a Bi-site) ions and Mn/Mn (Mn on its expected site), leading to a ferrimagnetic structure of the septuple layers with reduced net magnetization as found by neutron diffraction experiments [129, 132].

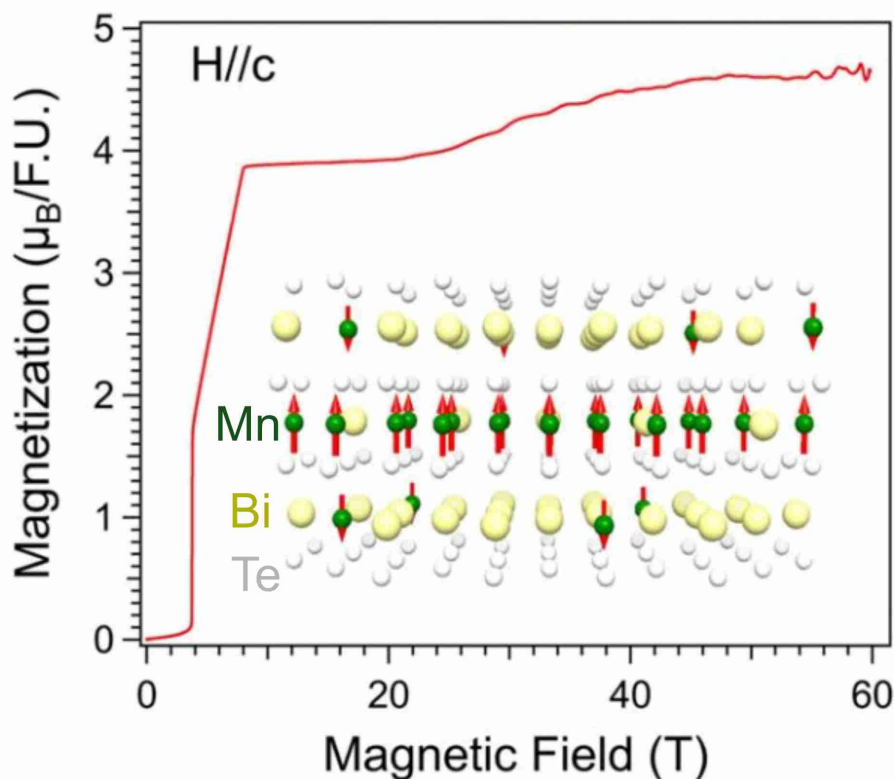


**Fig. 2.3.5** Magnetization as a function of magnetic field parallel to the crystallographic  $c$ -axis. The spin arrangement in the ferrimagnetic septuple layer is shown in the inset. Adapted from [133].

The out-of-plane orientation of magnetization is supported by X-ray magnetic circular and linear dichroism (XMCD, XMLD) measurements at the Mn  $\text{L}_{2,3}$  absorption edge performed at  $T = 2$  K, where the residual XMCD signal was detected only in the normal light incidence, unlike grazing light incidence, after the external magnetic field was turned off [9, 109]. The probing depth was a few nanometers which entails that the first septuple layer was explored primarily as well as that out-of-plane magnetism extends very close to the surface. Although no strong difference in the surface and bulk magnetic states was found and the residual signal

was reported to be consistent with the ferromagnetic intralayer coupling, mesoscopic domains are supposed to appear on the topmost layer [9,134]. The XLD signal was detected only in grazing (not in normal) light incidence geometry at  $T = 2$  K and was absent at  $T = 40$  K (above  $T_N$ ), indicating its magnetic nature [109].

According to the first-principles calculations considering the A-type antiferromagnetism with the out-of-plane magnetization in  $\text{MnBi}_2\text{Te}_4$  the natural cleavage plane (001) inevitably gives rise to gapped surface states with the gap size of (50–90) meV [9,111–113]. Nevertheless, this prediction was not confirmed in several independent ARPES experiments. The discrepancy can be reconciled with different assumptions which will be discussed further in this work. The calculated topologically non-trivial energy gap size was found to be around (160–200) meV [9,111,112] which is in agreement with the ARPES measurements [9,113,116,118,122,134–137]. The fundamental energy gap was shown to be inverted by varying the SOC constant in the density of states (DOS) calculations indicating a non-trivial topology of  $\text{MnBi}_2\text{Te}_4$  [9] as plotted in Fig. 2.3.6.

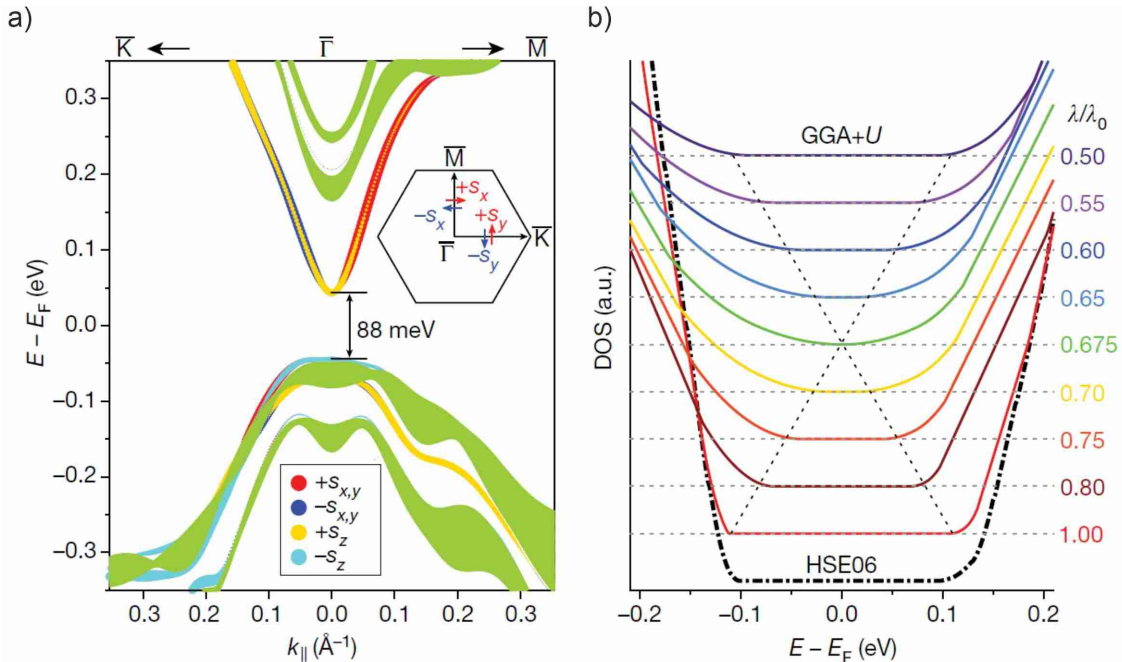


**Fig. 2.3.6** a) Spin-resolved electronic structure of the  $\text{MnBi}_2\text{Te}_4$  (001) surface. The green areas correspond to the bulk band structure projected onto the surface Brillouin zone. The red, blue, yellow and cyan circles correspond to positive and negative in-plane and out-of-plane components of the spin vector  $\mathbf{s}$ . The surface Brillouin zone is shown in the inset. b) Total DOS of bulk  $\text{MnBi}_2\text{Te}_4$  calculated for the interlayer antiferromagnetic state for different values of the SOC constant  $\lambda$ . The horizontal dashed lines indicate a zero DOS level for each value of  $\lambda$ , and their intersections with the inclined lines mark the bulk band gap edges. Adapted from [9].

Aiming to resolve the most important issue on the interplay between intrinsic magnetism and topology in  $\text{MnBi}_2\text{Te}_4$  numerous ARPES experiments have been

performed on the (001) surface which is its natural cleavage plane. However, the results seem to be rather contradictory so far. ARPES measurements on  $\text{MnBi}_2\text{Te}_4$  crystals revealed bulk conduction and valence bands where the conduction band exhibits an exchange splitting below  $T_N$  [119, 134, 135]. Based on the results of band structure calculations [9, 112, 113, 124], one can expect a gap-like feature inside the bands with linear dispersion (gapped Dirac cone) inside the bulk band gap in the electronic band structure measurements. In fact, the first ARPES experiments on  $\text{MnBi}_2\text{Te}_4$  crystals unveiled gapped Dirac surface states with a sizeable exchange gap of 50–100 meV at the  $\Gamma$ -point in both high-symmetry directions  $\text{K}-\Gamma-\text{K}$  and  $\text{M}-\Gamma-\text{M}$  [9, 109, 116–119]. The surface state nature of the observed cone was confirmed by the absence of any photon energy dependence in the ARPES measurements [9]. It is very striking that while this energy gap in the topological surface states shows some variations, it persists even in the paramagnetic phase up to room temperature as shown in Figs. 2.3.7a,b [9, 116, 117]. It could be caused by an instantaneous out-of-plane spin polarization existing both below and above  $T_N$  as inferred by spin-resolved ARPES, XMCD, XMLD and electron spin resonance measurements [9, 109, 134, 138] or due to spin fluctuations in the magnetically disordered phase [117, 134]. The surface electronic structure is influenced by strong spin-orbit interaction as evidenced by spin-resolved ARPES experiments where Rashba-type spin polarization was observed [116, 119]. At the same time, one evidence of the influence of the antiferromagnetic-paramagnetic transition on the electronic structure was demonstrated by the temperature evolution of the intensity of the topological surface states across  $T_N$  [119, 134]. It experiences a sharp reduction upon approaching  $T_N$  from the ordered phase and remains almost constant in the paramagnetic phase.

However, more recent ARPES experiments unexpectedly demonstrated gapless surface states on the (001) surface of  $\text{MnBi}_2\text{Te}_4$  crystals which made the investigations of this material much more complicated [113, 122, 135–137]. For instance, X-shaped bands centered at the  $\Gamma$ -point with clear linear dispersion were observed inside the bulk band gap on  $\text{MnBi}_2\text{Te}_4$  crystals by ARPES displaying a little  $k_z$ -dispersion pointing towards their surface character [113]. This finding could be explained by several reasons which will be discussed in more detail in section 4.2.2. Such ungapped Dirac surface states were found to be robust across  $T_N$  as shown [113, 122, 135] where the time-reversal symmetry gets restored (see Figs. 2.3.7c,d). On the other hand, a diminished gap (15–18) meV in both antiferromagnetic and paramagnetic phases was also observed which is associated with the persisting spin fluctuations above  $T_N$ .

The existing STM and STS data measured on  $\text{MnBi}_2\text{Te}_4$  crystals [139–142] will be presented and discussed in section 4.2.

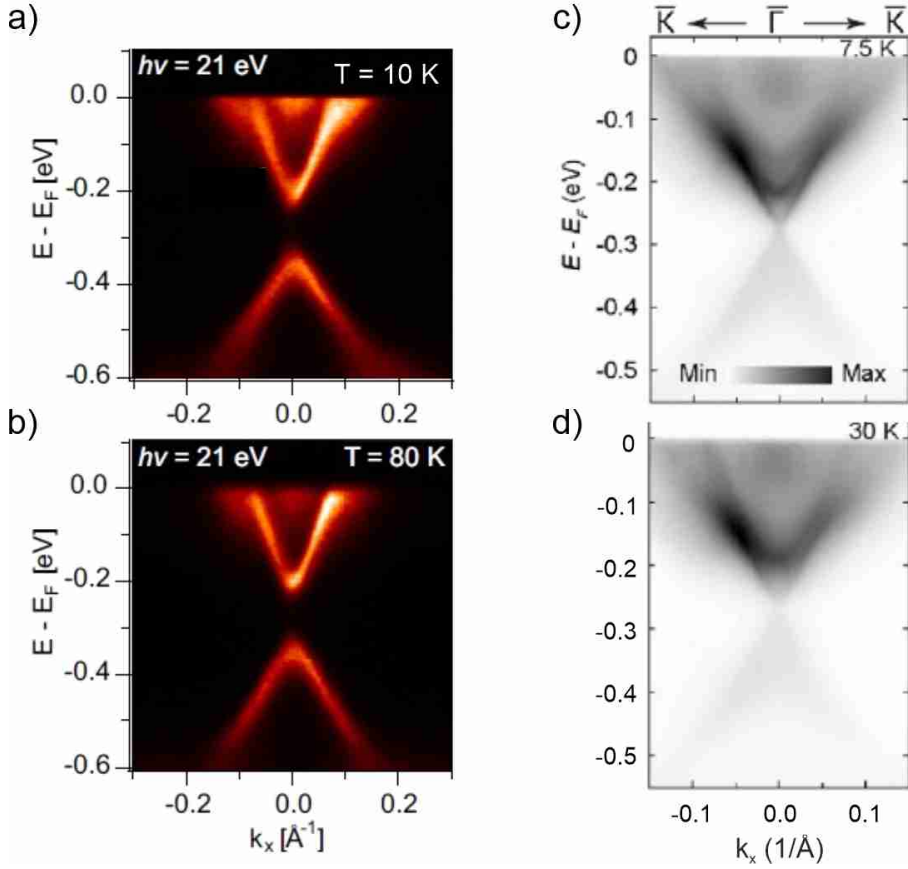


**Fig. 2.3.7** Gapped surface states in ARPES band structures of  $\text{MnBi}_2\text{Te}_4$  measured at a)  $T = 10\text{ K}$  and b)  $T = 80\text{ K}$ . Adapted from [116]. c), d) Gapless ARPES measured surface band structures at  $T = 7.5\text{ K}$  and  $T = 30\text{ K}$ , respectively. Adapted from [135].

### 2.3.2. $\text{MnBi}_4\text{Te}_7$

$\text{MnBi}_4\text{Te}_7$  is another member of the Mn-Bi-Te family consisting of the alternate stacking of quintuple layers and magnetic septuple layers separated by van der Waals gaps (see Fig. 2.3.8) and were first synthesized by Z. Aliev *et al.* [102]. Similar to  $\text{MnBi}_2\text{Te}_4$ , the lattice symmetry of  $\text{MnBi}_4\text{Te}_7$  is trigonal (but space group  $P\bar{3}m1$ ), the in-plane lattice parameter does not alter significantly:  $a \approx 4.36\text{ \AA}$  ( $c \approx 23.8\text{ \AA}$ ) as determined by X-ray diffraction and transmission electron microscopy experiments which, also, confirm the presence of cationic disorder (mixed Mn and Bi occupancies) as in the case of  $\text{MnBi}_2\text{Te}_4$  [11, 102, 103, 123]. These antisite defects and Mn vacancies appear only in the septuple layer blocks and were not found in quintuple layers [11].

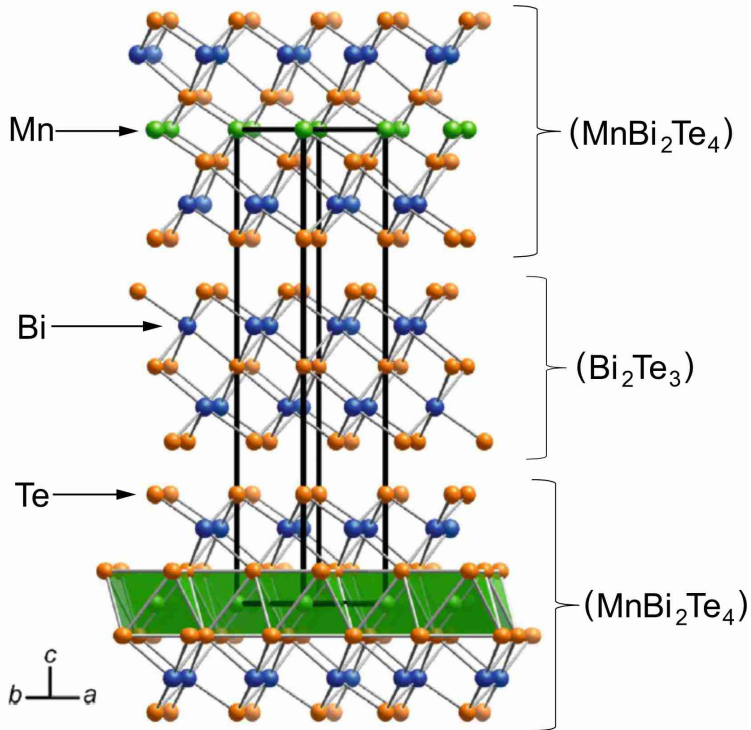


**Fig. 2.3.8** Crystal structure of  $\text{MnBi}_4\text{Te}_7$  with the unit cell marked by thick black lines. Adapted from [11].

Compared to  $\text{MnBi}_2\text{Te}_4$ , the  $\text{MnBi}_4\text{Te}_7$  compound demonstrates more complex magnetic phases. All the temperature-dependent resistivity and magnetization measurements on  $\text{MnBi}_4\text{Te}_7$  crystals revealed two anomalies associated with increased electron scattering due to a modification of the magnetic structure as shown in Fig. 2.3.9. The most pronounced one appeared at  $T_N = (12-13)$  K and corresponds to the antiferromagnetic phase transition, and the other anomaly, as seen from the ferromagnetic hysteresis-like  $M(H)$  curves, indicates a ferromagnetic ordering at  $T < 7$  K [11] while the resistivity bears a jump at  $T = 5$  K [11, 110, 114, 143]. The observed  $T_N$  is considerably smaller than that for  $\text{MnBi}_2\text{Te}_4$  which is in line with the reduced antiferromagnetic exchange interaction due to the increased spacing between adjacent Mn magnetic layers in  $\text{MnBi}_4\text{Te}_7$ . Apart from that, while  $M(H)$  curves acquired at  $T = 10$  K show a typical metamagnetic spin-flop transition [11], in other reports a spin-flip transition at  $H = 0.15$  T at  $T = 2$  K ( $H \parallel c$ ) and a saturation field  $H = 0.22$  T were observed [114, 136, 143, 144]. Lower transition and saturation fields than in  $\text{MnBi}_2\text{Te}_4$  are, also, in agreement with the weaker interlayer antiferromagnetism in  $\text{MnBi}_4\text{Te}_7$ . It is worth to note that an external magnetic field-induced Weyl state in  $\text{MnBi}_4\text{Te}_7$  single crystals has been recently experimentally observed through the detection of an intrinsic anomalous Nernst effect [145]. Hall resistivity measurements indicating anomalous contribution below  $T_N$  support the long-range antiferromagnetic order and reveal another metamagnetic transition

at low fields  $H \leq 300$  Oe at  $T \leq 7$  K [11]. The negative sign of the Hall coefficient points towards n-type conductivity [11, 114, 143, 144].

As in  $\text{MnBi}_2\text{Te}_4$ , magnetization (and resistivity as well) exhibits a strong anisotropy since the magnetic moments measured at  $H \parallel c$  are much larger than for  $H \perp c$  which indicates a preferable orientation of the net magnetization in the ordered phase perpendicular to the layers [11, 110]. Such observations are consistent with the A-type antiferromagnetic order predicted by DFT calculations and confirmed by neutron diffraction measurements [127, 144]. The ordered moment was found to be in the range  $(5.1\text{--}5.6)\mu_B$  which is in a rough agreement with the  $S = 5/2$   $\text{Mn}^{2+}$  high-spin configuration [11, 114, 143]. The latter is endorsed by the electron spin resonance measurements on  $\text{MnBi}_4\text{Te}_7$  which, also, evidence in favor of essentially ferromagnetic coupling inside magnetic septuple layers which persists up to  $T = 30$  K (correlated paramagnetic state) [11, 146].

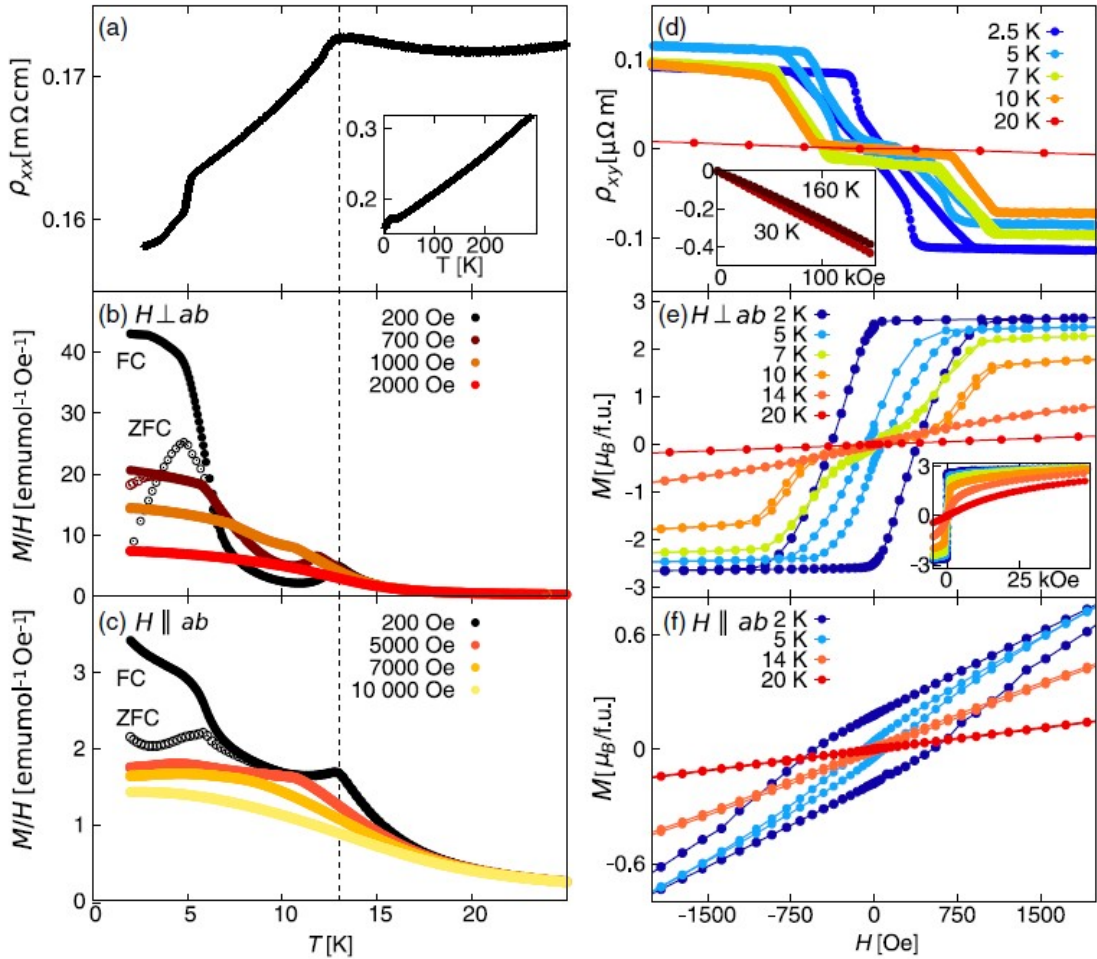


**Fig. 2.3.9** Magnetic and transport properties of  $\text{MnBi}_4\text{Te}_7$ : a) in-plane electrical resistivity as a function of temperature. b), c) Normalized magnetization as a function of temperature for fields applied both perpendicular and parallel to the  $ab$  directions. d), e) Hall resistivity and magnetization as a function of the field applied perpendicular to the  $ab$  planes. f) Magnetization as a function of the field applied parallel to the  $ab$  planes. Adapted from [11].

Magnetic properties of  $\text{MnBi}_4\text{Te}_7$  were further explored by XMCD and XMLD measurements at the Mn  $\text{L}_{2,3}$  absorption edge performed at  $T = (2\text{--}40)$  K [11]. The XMCD data corroborate the out-of-plane orientation of the net magnetization. The remanent XMLD signal was detected only in the normal light incidence, unlike grazing light incidence, and is monotonically decreasing with increasing temperature as for the transition from magnetically ordered state to a paramagnetic one.

Electronic band structure calculations on the easy-cleaved (001) plane of  $\text{MnBi}_4\text{Te}_7$  considering A-type antiferromagnetism were performed by several groups but gave controversial results [11, 110, 114, 115, 147]. Although, the fundamental band gap was found to be inverted leading to the non-trivial topology and  $\mathbb{Z}_2 = 1$  antiferromagnetic topological insulator state, its width varies from 75 meV [11] to 247 meV [110]. Furthermore, unlike gapless surface states in  $\text{Bi}_2\text{Te}_3$ , and as expected for the symmetry-breaking (001) surface, the quintuple layer terminated surface exhibits a massive Dirac cone with a surface states gap of  $\sim 60$  meV [114, 115] or a diminished gap (less than 30 meV) [11, 110, 147]. Such a gap reduction could be due to a predominant localization of the topological surface states in the quintuple layer and weaker interaction with the Mn-containing septuple layer [147]. In similar way, assuming A-type antiferromagnetic configuration for the septuple layer termination both gapped and gapless surface states have been reported. While sizeable gaps ( $\sim 60\text{--}70$  meV) were obtained in [11, 110, 115, 147], nearly gapless surface states were unexpectedly found in [114].

Experimentally acquired electronic band structures of  $\text{MnBi}_4\text{Te}_7$  are controversial as well. As in  $\text{MnBi}_2\text{Te}_4$ , the characteristic n-doping of the samples was observed in all ARPES measurements [11, 110, 114, 115, 121, 122, 147, 148], which is consistent with the Hall resistivity data on  $\text{MnBi}_4\text{Te}_7$  [11, 114, 143, 144]. The Dirac point is located at the binding energy  $\sim(270\text{--}300)$  meV below the chemical potential reminiscent to that in  $\text{MnBi}_2\text{Te}_4$ . The bulk band gap width was found to be (100–225) meV [114, 121, 147] which is in a rough agreement with the first-principles calculations [11, 110]. The Dirac surface states exhibit a distinct energy gap of (50–100) meV on the quintuple layer surface termination [11, 114, 115, 148] or remain gapless as in three-dimensional  $\text{Bi}_2\text{Te}_3$  [121, 122] which could be caused by a strong suppression of the magnetization across the topmost quintuple layer. As for the septuple layer terminated surface, in most ARPES studies the surface states are X-shaped (ungapped) [114, 115, 121, 122], while the gapped Dirac cone was also observed [11]. Such a frequently observed magnetic gap disappearance is supposed to be explained by the same mechanism as in  $\text{MnBi}_2\text{Te}_4$  [113, 122, 135–137] reflecting the proposed deviation of the A-type antiferromagnetic order on the cleaved surface to a spin disorder or an average effect of different antiferromagnetic domains. At the same time, one has to note that in some early ARPES experiments where a strongly gapped (90

meV) Dirac cone was obtained, it was not possible to distinguish between two possible surface band structures due to the size of the laser beam spot (20–50)  $\mu\text{m}$  which is much larger than the quintuple/septuple layers surface domain size [110, 136]. Concerning the temperature evolution of the topological surface states, they appear to be temperature independent as evidenced by a non-vanishing magnetic gap in the paramagnetic phase (at  $T = 80$  K) [11] (see Fig. 2.3.10), a slightly diminished gap at  $T = 300$  K [110] due to persisting spin fluctuations even far above  $T_N$ , or a gapless Dirac cone for both quintuple- and septuple layer terminations [121, 122] as shown in Fig. 2.3.11.

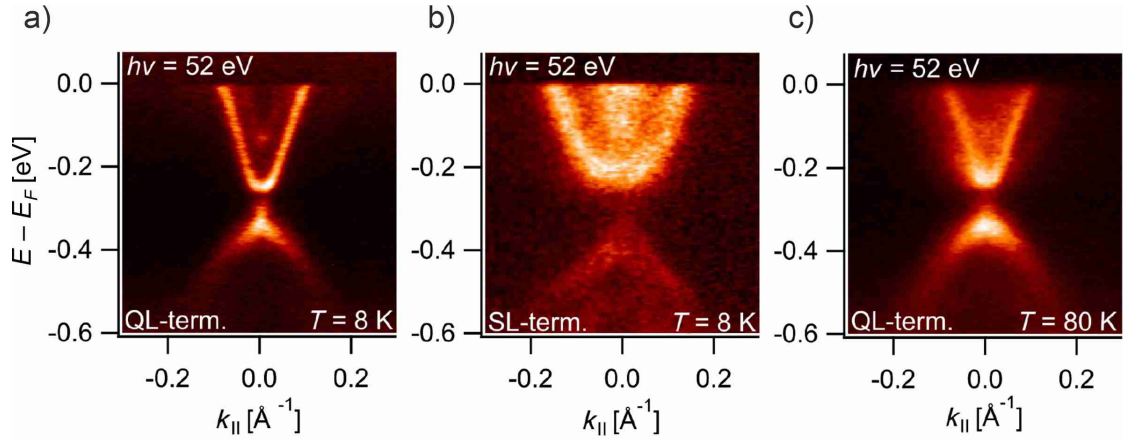


**Fig. 2.3.10** Gapped electronic structure of  $\text{MnBi}_4\text{Te}_7$  measured by ARPES (along the  $\Gamma$ -M-direction): a) quintuple layer termination at 8 K, b) septuple layer termination at 8 K, c) quintuple layer termination at 80 K. Adapted from [11].

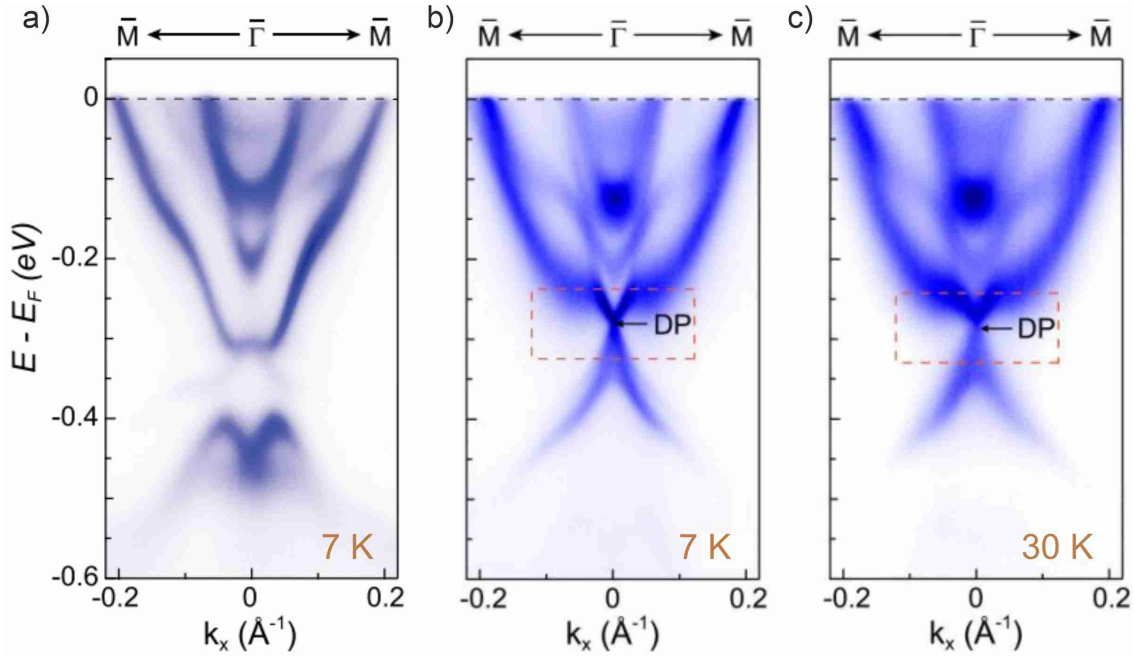


**Fig. 2.3.11** Gapped and gapless ARPES data on  $\text{MnBi}_4\text{Te}_7$ : a) quintuple layer termination at 7 K. b) Septuple layer termination at 7 K. c) Septuple layer termination at 30 K. Adapted from [122].

The STM/STS investigations of  $\text{MnBi}_4\text{Te}_7$  single crystals reveal two atomically resolved (001) surfaces in agreement with the crystal structure containing alternate quintuple and septuple layers. The observed atomic steps identified two possible surface terminations explicitly [115, 140, 149]. The septuple layer termination hosts Bi/Te-antisite defects (bright spots) and Mn/Bi-antisites which are present on the quintuple layer terminated surface and appeared as dark triangles for both surfaces which can be seen in Fig. 2.3.12.

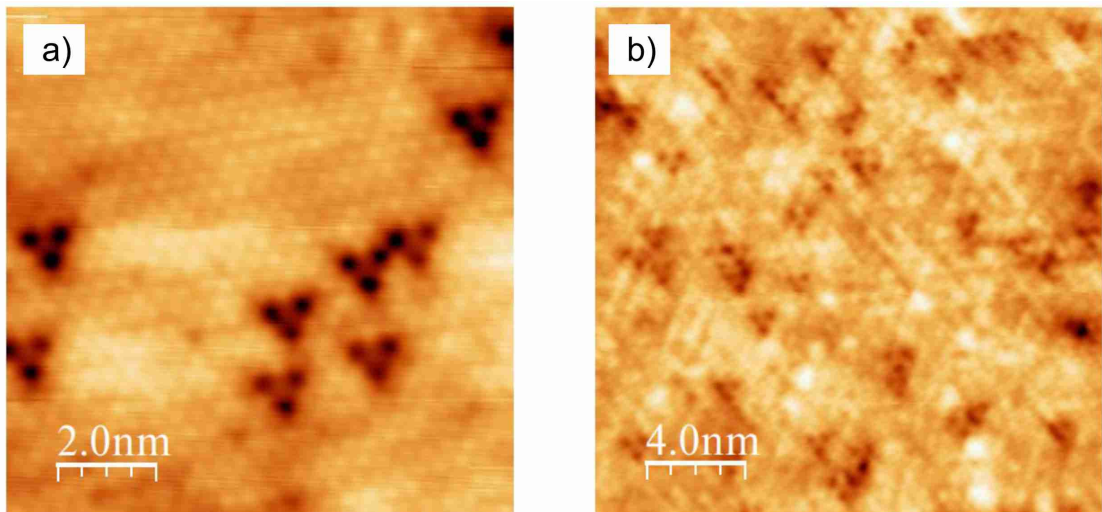


**Fig. 2.3.12** STM topography of  $\text{MnBi}_4\text{Te}_7$ : a) quintuple layer terminated surface,  $U_{bias} = 0.5$  V,  $I_T = 1$  nA and b) septuple layer terminated surface at  $U_{bias} = 0.5$  V,  $I_T = 200$  pA. Adapted from [115].

Fig. 2.3.13 illustrates the  $dI/dU$  tunneling spectra recorded on defect free areas of the quintuple layer surface showing a suppression of DOS near the Dirac point in contrast to the V-shaped dip at the Dirac point on the septuple layer surface which is consistent in all the STS data on this compound [115, 140, 149]. It was shown by DFT-calculations in [115] that a gapped Dirac cone on the quintuple layer termination is created by the hybridization effect between the orbitals of the top quintuple layer and its adjacent septuple layer. The absence of the gap on the septuple layer terminated surface is explained by a possible spin disorder unlike the bulk A-type antiferromagnetic order. In addition, the very recent temperature-dependent STS studies on  $\text{MnBi}_4\text{Te}_7$  reveal the presence of the electronic state at the septuple layer step edge which vanishes above  $T_N$  and does not exist at the quintuple layer step edge (see Fig. 2.3.14). Therefore, this edge state appears to be induced by the intrinsic magnetism of the material [149]. In the other STM/STS work on  $\text{MnBi}_4\text{Te}_7$  QPI data were obtained at  $T = 4.5$  K [115]. Given the discrepancies in the observed FT-QPI patterns from the calculated joint DOS (JDOS) and taking into account the hybridization between septuple and quintuple layers, Rashba bands observed by spin-ARPES, the spin-selective JDOS was calculated. Its comparison with the observed FT-QPI patterns yielded the following spin textures: spin-helical Dirac state with hexagonal warping for the quintuple layer termination, a pair of Rashba-split states from the 2<sup>nd</sup> quintuple layer and a strongly canted helical state from the surface sandwiched in between – for the septuple layer terminated surface.

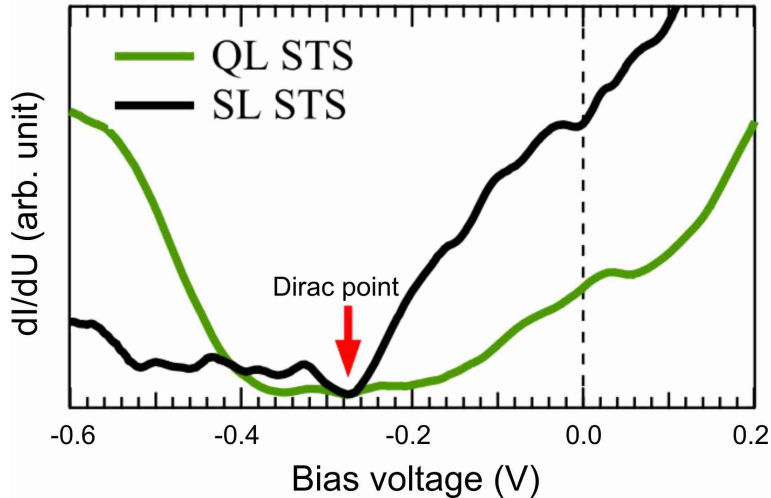


**Fig. 2.3.13** Averaged STS spectra taken at defect free areas of quintuple layer- (green curve) and septuple layer (black curve) terminations of  $\text{MnBi}_4\text{Te}_7$ .  $U_{bias} = 0.5$  V,  $I_T = 500$  pA,  $T = 4.5$  K. The dashed line indicates the position of the Fermi level. Adapted from [115].

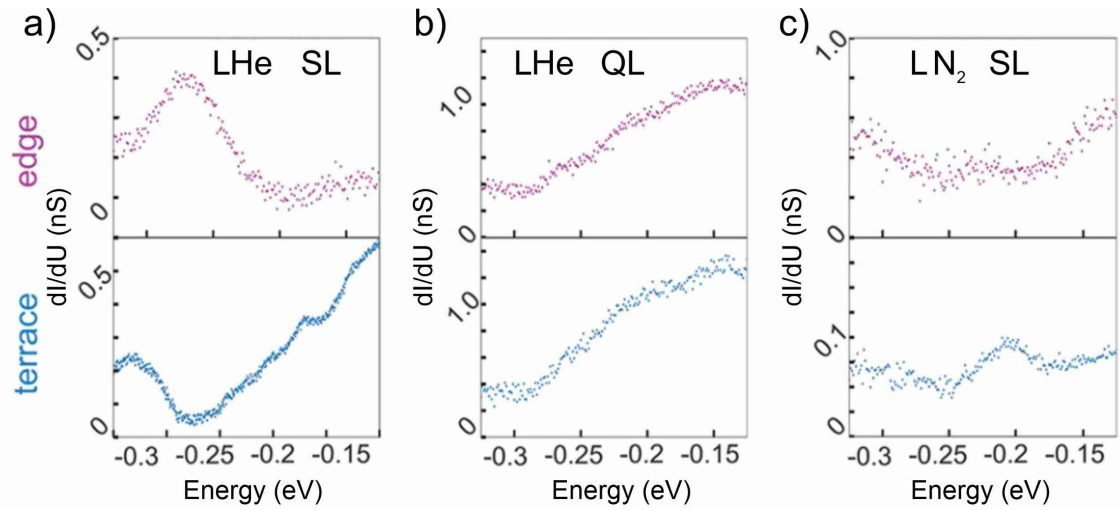


**Fig. 2.3.14**  $dI/dU$  spectra at the step edge (upper panel) and terrace (lower panel) measured on a) septuple layer surface at 4.5 K, b) quintuple layer surface at 4.5 K, and c) septuple layer surface at 77 K. Adapted from [149].



# Chapter 3

## Experimental technique: STM and STS

The first scanning tunneling microscope was invented in 1981 by G. Binnig and H. Rohrer [150, 151]. Nowadays the STM has established itself as a powerful tool for local characterization of electronic properties of surfaces of various solids (and also molecular nanostructures) with atomic fidelity.

Fig. 3.0.1 illustrates the underlying idea of this experimental technique. In general, an atomically sharp tip usually made of conducting materials (metals like W, Pt/Ir alloy, Au,...) is attached to a piezosscanner (a tube configuration is mostly used for achieving better lateral resolution [15]) and brought very close to the investigated material's surface. Typically this distance  $d$  amounts to a few Ångströms. The movement of the piezosscanner with the tip in 3 directions  $x$ ,  $y$ ,  $z$  is controlled by applying voltage to the scanner's electrodes  $x+$ ,  $x-$ ,  $y+$ ,  $y-$  (on the outside) and  $z$  (on the inside) as shown in Fig. 3.0.1. A bias voltage  $U_{bias}$  applied to the sample (which is always the case in the present work) leads to the shift of the Fermi level of the sample with respect to that of the tip. Therefore, it becomes possible to detect the tunneling current flowing in the formed tunneling junction. Depending on the polarity of the bias voltage, the tunneling current can flow from the sample to the tip or vice versa. For negative  $U_{bias}$  on the sample the current will flow from the occupied states of the sample into the tip, while for positive  $U_{bias}$  the direction of the current is opposite, thereby, the unoccupied states of the sample can be probed. Normally the tunneling current is kept constant during scanning with the use of the feedback loop that transforms the deviations of the current from the set point value into variations of the tip height to get a topography of the surface.

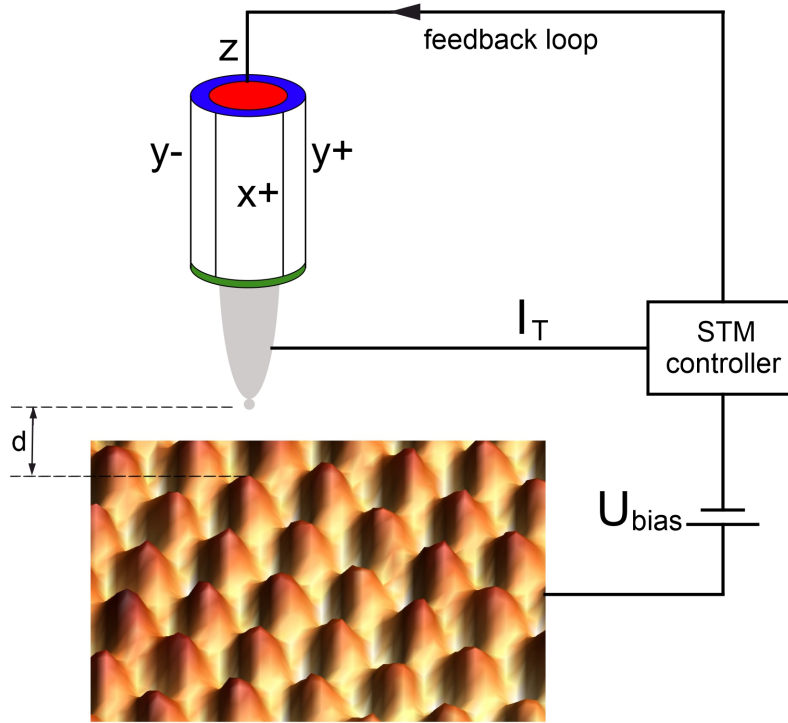


**Fig. 3.0.1** General principle of the STM. An atomically sharp tip is scanning on an atomically corrugated surface of  $\text{Bi}_2\text{Te}_3$  measured in this work. The tunneling current  $I_T$  is measured from the tip which is fixed at the end of the scanner tube, its relative height  $d$  is controlled by the feedback loop.

### 3.1. Tunneling current

In order to understand the factors affecting the tunneling current in the STM one has to describe the STM operation involved quantum mechanics. Considering a tunneling junction formed by a sample and a tip which are separated by vacuum as a potential barrier of a rectangular shape with a height  $U_0$  and a width  $d$ , a simple time-independent Schrödinger equation can be solved. It turns out that an electron has a non-zero probability to penetrate through the barrier with the energy  $E < U_0$ , unlike that in classical mechanics. The corresponding wave functions for the regions 1 (before the barrier), 2 (within the barrier) and 3 (after tunneling) are shown in Fig. 3.1.1. The most important is that they oscillate outside of the barrier, while the wave function in the barrier region decays exponentially. The transmission factor for this barrier calculated based on the boundary conditions is the following (assuming a strongly attenuating barrier with  $\frac{\sqrt{2m(U_0-E)}}{\hbar}d \gg 1$  typical for STM [14]):

$$T \approx \frac{16E(U_0 - E)}{U_0^2} \exp\left(-\frac{2d}{\hbar} \sqrt{2m(U_0 - E)}\right), \quad (3.1.1)$$

where  $m$  is the free electron mass and  $\hbar$  is the Planck constant.

This equation reflects also the exponential dependence of the tunneling current

in the STM experiment on the tip-sample distance. In practice, every 1 Å change of the tip height results in approximately one order of magnitude change of the tunneling current. This extremely high sensitivity is the main reason of the high spatial resolution of the STM.

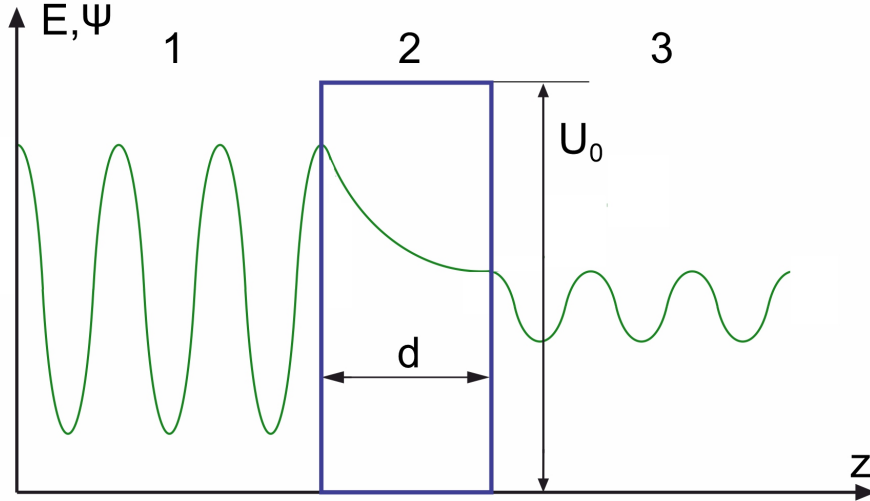


**Fig. 3.1.1** Electron tunneling schematic representation for a rectangular barrier of the width  $d$  and the height  $U_0$ . The green curves are sketches of the wave functions in the regions 1, 2 and 3.

The next approach which considers the DOS of the sample and the tip was done by J. Bardeen [152], where the tunneling process was considered as a transition from the initial state to the final state (from the tip to the sample for positive bias voltage, for example, as shown in Fig. 3.1.2) by means of the time-dependent perturbation theory. In this case the transition probability per unit of time from the tip to the sample is given by the Fermi's golden rule:

$$w_{fi} = \frac{2\pi}{\hbar} \sum_{i,f} |M_{fi}|^2 \delta(E_f - E_i), \quad (3.1.2)$$

where  $M_{fi}$  is the tunneling matrix element from the initial state to the final state and  $\delta(E_f - E_i)$  is the Dirac delta function.

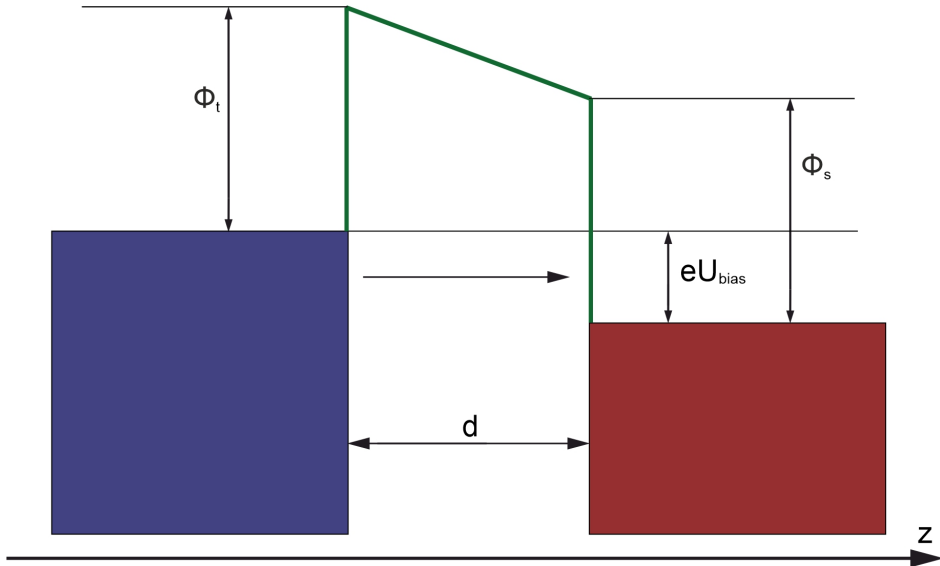


**Fig. 3.1.2** Energy diagram of electron tunneling from the tip (blue colored) to the sample (red colored) in STM. Positive  $U_{bias}$  is applied to the sample and shifts its Fermi level down.  $\Phi_t$  and  $\Phi_s$  denote the work functions of the tip and sample materials, respectively.

In its turn, the tunneling matrix element is expressed through the wave functions of the sample and the tip as

$$M_{fi} = \frac{\hbar^2}{2m} \int_S (\psi_{t,i} \nabla \psi_{s,f}^* - \psi_{s,f}^* \nabla \psi_{t,i}) dS, \quad (3.1.3)$$

where  $S$  is the surface of the region between the tip and the sample. Given the electron spin degeneracy as a factor of 2 for the transition rate  $w_{fi}$ , the tunneling current can be written as the following:

$$I_T = \frac{4\pi e}{\hbar} \sum_{i,f} |M_{fi}|^2 \delta(E_f - E_i). \quad (3.1.4)$$

The equation 3.1.4 can be modified moving on to the DOS of the sample  $\rho_s$  and the tip  $\rho_t$  and also taking into account the Fermi-Dirac distribution of the electrons:

$$I_T = \frac{4\pi e}{\hbar} \int_0^{eU_{bias}} \rho_t(\epsilon - eU_{bias}) \rho_s(\epsilon) f_t(\epsilon - eU_{bias}) (1 - f_s(\epsilon)) |M(\epsilon)|^2 d\epsilon, \quad (3.1.5)$$

where  $\epsilon$  is the energy counted from the Fermi level, and

$$f(\epsilon) = \frac{1}{1 + \exp\left(\frac{\epsilon}{k_B T}\right)}. \quad (3.1.6)$$

which leads to a small thermal smearing ( $\sim k_B T$ ) of the  $I_T$  and, thus becomes important usually for relatively high temperatures comparable with (or larger than) the size of the investigated spectroscopic features.

The tunneling matrix element is affected by many factors, for example, the tip geometry and its electronic structure which can not be known explicitly. However, it can be determined in terms of the semiclassical WKB-approximation (assuming  $eU_{bias}$  negligible compared to the work functions of the tip and the sample which are normally in the range 3-4 eV) [153]:

$$|M(\epsilon)|^2 \propto \exp\left(-\frac{2d}{\hbar}\sqrt{2m\Phi}\right), \quad (3.1.7)$$

where  $\Phi$  is the half sum of the work functions of the tip and the sample. Under this approximation the tunneling current becomes

$$I_T = \frac{4\pi e}{\hbar} \exp\left(-\frac{2d}{\hbar}\sqrt{2m\Phi}\right) \int_0^{eU_{bias}} \rho_t(\epsilon - eU_{bias})\rho_s(\epsilon)f_t(\epsilon - eU_{bias})(1 - f_s(\epsilon))d\epsilon, \quad (3.1.8)$$

Looking at this equation the most essential parts are the exponential dependence of the tunneling current on the tip-sample distance and the convolution of the sample's and the tip's DOS. To get rid of the latter the tips for the STM experiment are normally made of materials with approximately energy-independent DOS (in the relevant energy window) such as metals W, Pt/Ir alloy, Au and others. Within this simplification, the tunneling current is considered to be proportional to the integrated DOS of the sample for very low temperatures.

Another approximation was obtained by Tersoff and Hamann [154], where the wave function of the tip was assumed as a spherically symmetric *s*-wave orbital. For small bias voltages it also results in a direct proportionality of the differential conductance to the local DOS (LDOS) of the sample.

## 3.2. STM measurement modes

### 3.2.1. Topography

Given the exponential dependence of the tunneling current  $I_T$  on the distance  $d$  between the tip and the sample, one can scan over the surface with the tip and measure the sample's surface topography. In general, it can be done by two different methods. One of them, which is the most widely exploited, is called constant current mode.  $I_T$  is kept constant with the use of the feedback loop at a specified set point value, while the tip is scanning over the investigated surface (see Fig. 3.0.1). The resulting variations of the  $z$ -position of the tip as a function of the  $(x, y)$ -coordinates represents the map of the sample LDOS integrated within the energy range from  $-eU_{bias}$  to  $E_F$ . In practice, the real topography can not be detected due to local

variations of the surface electronic structure caused, for example, by impurities, defects or charge density waves [155, 156]. Alternatively, one can maintain the distance  $d$  constant and measure the variations of  $I_T$  on the surface. Although this method dubbed constant-height mode works faster than the constant-current mode with the feedback loop involved, the former one needs very flat surfaces to avoid possible crashes of the tip on the sample. Usually atomically resolved surfaces are studied by STM, one example of which is shown in Fig. 3.2.1.

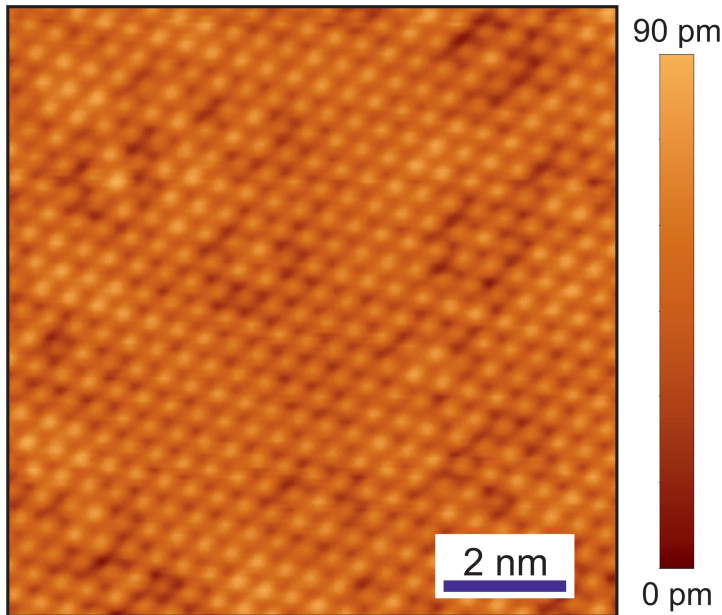


**Fig. 3.2.1** Constant current topography acquired on  $10 \text{ nm} \times 10 \text{ nm}$  surface area of a  $\text{Bi}_2\text{Te}_3$  single crystal at  $U_{bias} = 300 \text{ mV}$ ,  $I_T = 500 \text{ pA}$ ,  $T = 6.9 \text{ K}$  showing clearly an atomic corrugation along with surface defects.

### 3.2.2. Single point spectroscopy

By disabling the feedback loop in the STM experiment, which means fixing the  $z$ -position ( $x, y$ -positions are also fixed) of the tip,  $I_T$  can be measured when  $U_{bias}$  is swept. Looking again at the equation 3.1.8, one can notice that for the temperatures close to 0 K the differential conductance  $dI/dU(x, y, U_{bias})$  turns out to be proportional to the sample DOS at any location  $(x, y)$  on the surface. This provides a unique opportunity to measure electronic properties of various materials locally at the atomic scale, unlike other spectroscopy methods. In principle, the differential conductance spectra can be obtained by numerical derivation of the  $I(U)$  spectra. However, the resulting  $dI/dU$  spectra become more noisy than that measured directly with a commonly used lock-in amplifier by applying a small modulation voltage (typically, of the order of a few mV or even  $\mu\text{V}$ ). The lock-in amplifier includes a phase-sensitive detector which effectively singles out only the first harmonic of the tunneling current at the frequency of the modulation. This component is pro-

portional to the  $dI/dU$  and can be also averaged, whereas all the other harmonics are cut off resulting in a tremendously high signal-to-noise ratio. However, the STS has two main limitations. In particular, the energy resolution is affected by thermal broadening of the Fermi-Dirac distribution ( $3.5 k_B T \approx 1.5$  meV for the STM used in the present work at  $T = 5$  K,  $k_B$  is the Boltzmann constant) and, on the other hand, by the modulation voltage ( $2.5 eU_{mod}$ ) [157]:

$$\Delta E = \sqrt{(3.5k_B T)^2 + (2.5eU_{mod})^2}. \quad (3.2.1)$$

One example of the  $dI/dU$  spectrum measured on a  $\text{Bi}_2\text{Te}_3$  crystal in the present work can be found in Fig. 3.2.2.

### 3.2.3. $dI/dU$ maps

Besides measuring single point spectra, the STM allows recording  $dI/dU$  maps on selected energies and areas in the  $(x, y)$ -plane. One option is to measure the maps at a certain bias voltage when scanning the surface with the closed feedback loop, applying a small modulation voltage. This is usually called  $dI/dU$  mapping and requires a time spent on each pixel during scanning larger (by one order of magnitude) than the bias modulation period. Nevertheless, this is a less time-consuming way to obtain the  $dI/dU$  maps (typical time  $\sim$  several hours) than another one which is called full spectroscopy mapping. This measurement mode allows measuring  $dI/dU$  maps at different energies in the selected energy range and provides not only topography data and differential conductance maps with high resolution for different energies, but also the  $dI/dU$  spectra at each selected location on the surface at the same time. This is a rather demanding method since it requires to open the feedback loop at each point of the map. For that one needs an ideal stability of the tunneling junction during the whole measurement time which usually takes from several days up to around one week (limited by the liquid helium evaporation rate in the experimental setup) for high spatial and energy resolution data.

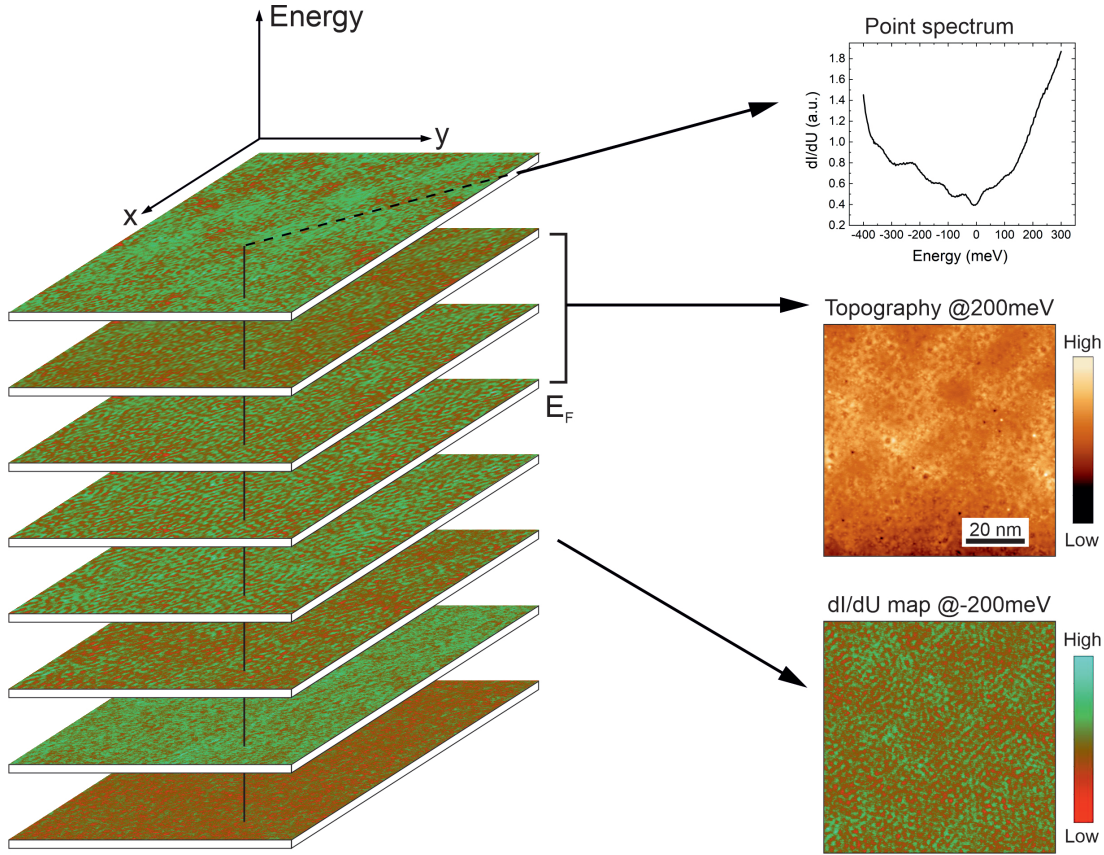


**Fig. 3.2.2** 4-dimensional full spectroscopy map  $dI/dU(x, y, U)$  representation. Examples of single point spectra, topography and differential conductance maps measured at different energies on single crystals of  $\text{Bi}_2\text{Te}_3$  are plotted.

### 3.3. Quasiparticle interference

In simple metals with parabolic energy dispersion in presence of disorder created by point-like impurities or step edges the charge density oscillates as a function of distance from impurity. According to [158, 159], it can be written as

$$\rho_S(E, x) \propto 1 - J_0[2q(E)x] \quad (3.3.1)$$

for the step edge, and

$$\rho_S(E, r) \propto 1 + \frac{2}{\pi qr} [\cos^2(qr - \frac{\pi}{4} + \eta_0) - \cos^2(qr - \frac{\pi}{4})] \quad (3.3.2)$$

for the point-like impurity, where  $E$  is the energy,  $x$  and  $r$  are the distances from the step edge and the impurity, respectively,  $q$  is the amplitude of the scattering vector at the energy  $E$ ,  $J_0$  is the 0<sup>th</sup>-order Bessel function,  $\eta_0$  is the phase shift.

This is called Friedel oscillations [160] which were directly observed by STM in the real space [158, 161, 162] and became one of the very remarkable discoveries of the STM. Fig. 3.3.1a illustrates the Cu(111) surface [163]. One can clearly see mod-

ulations of the LDOS which arise from elastic electron scattering (which for such a simple one free-electron band material is backscattering with  $\mathbf{q} = 2\mathbf{k}$  as shown in Fig. 3.3.1b) resulting in the interference pattern of incoming ( $\mathbf{k}_i$ ) and outgoing ( $\mathbf{k}_f$ ) electrons with  $\mathbf{q} = \mathbf{k}_f - \mathbf{k}_i$ . That is why it is called quasiparticle interference (QPI) in relation to materials with more intricate electronic band structure like superconductors, heavy fermion materials, topological materials... The natural method to get the information on scattering processes is Fourier transform (see Fig. 3.3.1c) of the real-space STM data which allows to extract both the length and the direction of the scattering vectors [164]. For materials with more complicated electronic band structures, like topological insulators (which will be discussed in more detail in section 4.1.4), the relation  $\mathbf{q} = 2\mathbf{k}$  is not true anymore, so one can not explicitly extract the electron wave vector  $\mathbf{k}$  (and, thus, the electronic band dispersion) from the STM data. Nevertheless, the QPI allows investigating different scattering processes and serves as a complementary tool to ARPES with the advantage of having access to the unoccupied electronic states.

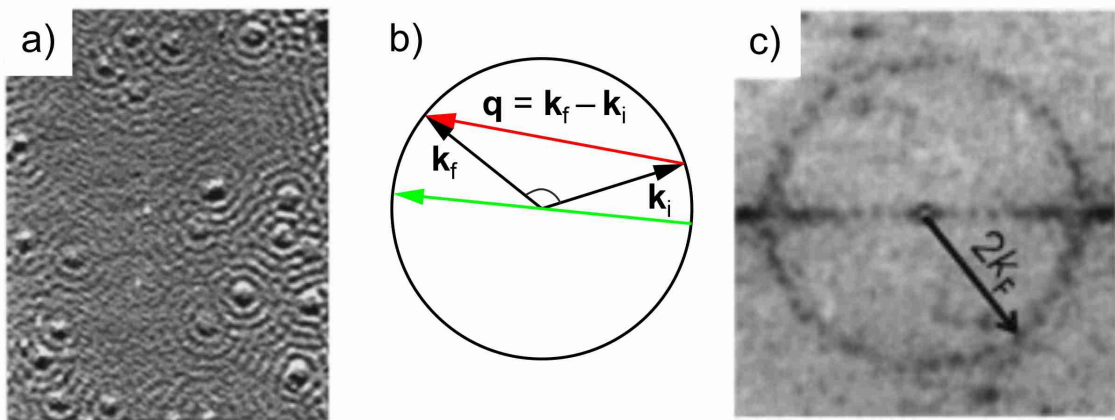


**Fig. 3.3.1** a) Constant current STM image of Cu(111). Circular wave-like pattern originates from scattering around point-like defects. Adapted from [163]. b) Sketch of the circular constant-energy contour corresponding to the band structure of Cu(111). The red vector  $\mathbf{q}$  indicates the scattering from  $\mathbf{k}_i$  to  $\mathbf{k}_f$ , the green vector is the backscattering vector. c) Two-dimensional Fourier transform of a). Adapted from [163].

### 3.4. Experimental setup

All the experimental data presented in this work were measured with the home-built STM called "Dip-stick STM" [165]. This STM is based on a tube design of  $\approx 2$  m height (see Fig. 3.4.1) and can be immersed into usual liquid  ${}^4\text{He}$  magnet cryostats. By that the cryogenic vacuum is created inside the STM, which has to be evacuated to a pressure  $\sim 10^{-5}$  mbar before inserting it into the cryostat. All the data were obtained with the Oxford Instruments magnet cryostat [166] which has a maximal perpendicular field 15 T at 4.2 K and is lifted by a damping system for

the vibration isolation. This STM system is considered as a variable-temperature STM since it allows doing measurements from the base temperature of  $\sim 5$  K up to the room temperature with the use of the heating cup covering the whole STM head. The normal time for cooling down the STM from the room temperature to the base temperature is around 17 hours. The total measurement time at the base temperature can take up to 11 days between the consecutive refills of the liquid helium. It is also possible to increase the measurement time up to 8 weeks by using a liquid  $^4\text{He}$  dewar with 220 liters of volume. However, this is not the option for measurements in magnetic fields. The Dip-stick STM in this work was operated by different commercially available STM controllers Nanonis Specs [167] and RHK R9 [168].

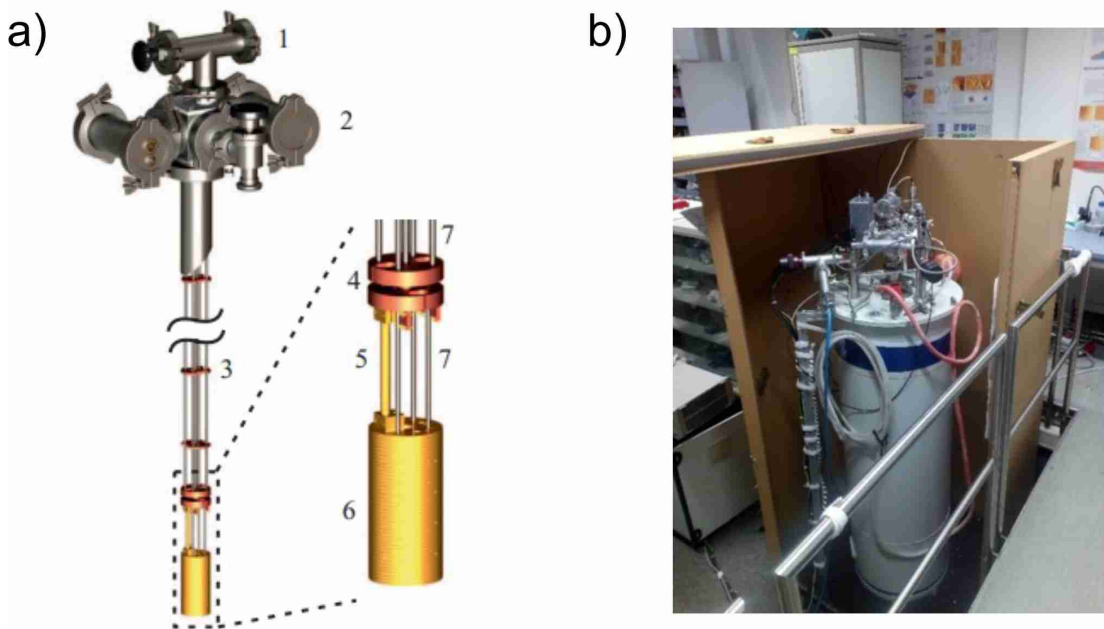


**Fig. 3.4.1** a) Design of the Dip-stick STM with a section through the stainless steel tube. The middle part of the tube is not shown for better visualization. The magnified image shows the STM head covered by the heating cup. (1) Cleaving mechanism control, (2) connections for electrical wiring and pumping, (3) stainless steel capillary tubes with heat radiation baffles, (4) copper disks for thermal coupling to the helium volume, (5) thermal connection to the STM head, (6) STM head with the heating cup, and (7) stainless steel capillary tubes. Adapted from [165]. b) Photography of the STM system inside the magnet cryostat.

The STM head was designed in the Pan style [169] and is mounted at the end of the stainless steel capillary tubes as shown in Fig. 3.4.1a. All the components of the STM head are made of non-magnetic materials to exclude their influence on the measurements with an external magnetic field and minimize magnetic stray fields at the sample. The most crucial part of the STM head (see Fig. 3.4.2) is the scanner unit which consists of the sapphire prism (6), the scanner tube holder (5), and the

scanner tube (10) which is mounted inside the sapphire prism. The piezoelectric scanner tube [170] has five electrodes (see Fig. 3.0.1) with four  $x/y$ -electrodes on the outside of the tube and the  $z$ -electrode on the inside. The full scanning range at 5 K (300 K) is around 2.4  $\mu\text{m}$  (600 nm) and 600 nm (250 nm) for the  $x/y$  and  $z$ -directions, respectively. The tip is mounted at the end of the scanner tube with the use of a Macor socket and a molybdenum spring. In this STM system configuration the bias voltage is applied to the sample, and tunneling current is measured from the tip. The sapphire prism is clamped inside the STM body by six piezoelectric walker stacks (8). Each of the stacks consists of four piezoplates glued to each other by conductive glue [171]. A polished  $\text{Al}_2\text{O}_3$  plate is glued on top of each of the piezoelectric stacks and provides the coarse approach motion by the slip-stick-method [172]. Four of the stacks are glued to the STM body, while the other two are glued to the counterpart plate (7) which is pressed against the sapphire prism by a molybdenum spring (9). By changing the spring force, one can adjust the friction between the sapphire prism and the  $\text{Al}_2\text{O}_3$  plates for achieving a reasonable approach time. For instance, at the room temperature it takes  $\approx 80$  s at 120 V to move the tip from the full retract position to a distance of  $< 1$  mm from the sample when the automatic approach can be run which takes a few minutes (usually, less than 30 minutes) more. For the base temperature the approach procedure takes several times (normally, around 3–4) longer due to the lower value of the piezo constant of the material from which the piezoelectric stacks are made.

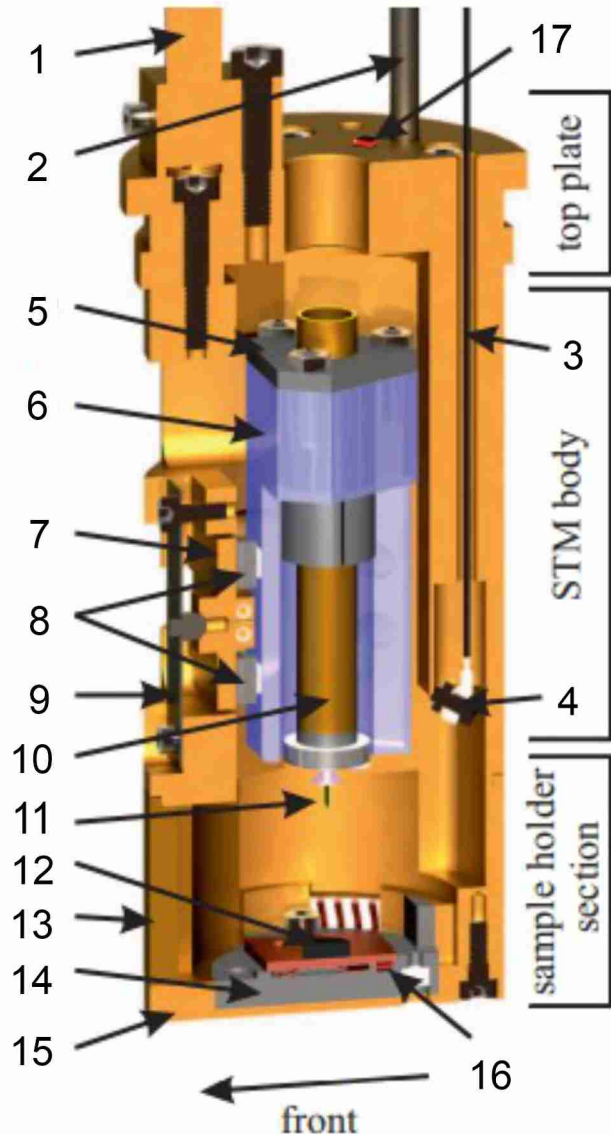


**Fig. 3.4.2** Schematic section of the STM head which can be divided into three parts: top plate, STM body, and sample holder section: (1) thermal connection, (2) stainless steel capillary tube, (3) cleaving wire, (4) cleaving stamp, (5) tube scanner holder (Macor [173]), (6) sapphire prism, (7) counterpart plate, (8) shear-piezo stacks, (9) molybdenum leaf spring, (10) tube scanner, (11) tip holder with tip, (12) sample, (13) front panel, (14) Macor part for bias insulation, (15) bottom plate, (16) Cernox sample temperature sensor, and (17) Cernox STM body temperature sensor. Adapted from [165].

In general, the surface-sensitive STM technique requires perfectly clean and flat surfaces. The Dip-stick STM has a cleaving mechanism installed on top of it (see Fig. 3.4.1a) which allows cleaving the investigated crystals *in situ* just before approaching the tip to the surface being already in the cryogenic vacuum conditions. The cleaving procedure is demonstrated in Fig. 3.4.3. Each new measured sample has to be glued with the conductive glue [171] onto a metallic sample holder (1), then a metallic cleaving stamp (3) is glued on top of the sample (2) with the same

glue. The cleaving wire (6) with the insulating eye (4) at its end is attached to the cleaving stamp by the screw nut (7). The tip quality can be checked on the test sample (5), and the tip has to be fully retracted for cleaving. The freshly cleaved surface occurs after pulling the cleaving wire from top of the STM in such a way that the cleaving stamp goes into the parking position (I) and can not affect the experiment. This Dip-stick STM allows also to prepare and mount air-sensitive samples inside a special Argon glovebox where the whole STM can be placed.

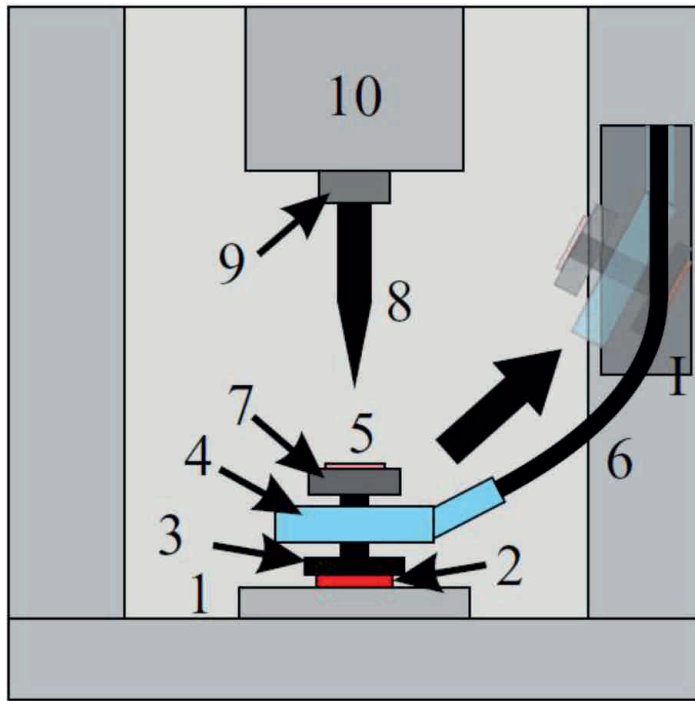


**Fig. 3.4.3** Sketch of the sample cleaving procedure. The movement of the cleaving stamp during the cleaving is indicated by the broad arrow. (1) Sample holder, (2) sample, (3) cleaving stamp with a screw thread on one end, (4) insulating eye, (5) test sample (e.g. gold on mica), (6) cleaving wire, (7) screw nut, (8) tip, (9) tip holder, (10) scanner unit, (I) parking position of the cleaving stamp. The insulating eye is made of copper, covered by an insulating varnish, and soldered to the cleaving wire. A coating of the insulating varnish (GE-Varnish [174]) prevents short-circuiting  $U_{bias}$  and ground. Adapted from [165].

The most commonly used ways for the STM tips preparation are electrochemical etching of W-wires and mechanical cutting of Pt/Ir-wires which were both used in this work. The W wires were electrochemically etched by 8 % NaOH solution with the usual formation of tungsten oxide layer on the tip. Therefore, they were further annealed by electron beam heating at  $\sim 2000$  °C at high vacuum ( $\sim 10^{-7}$  mbar) in a special flashing chamber to remove the tungsten oxide by evaporation. Some of the experiments were performed with the tips made by simple mechanical cutting of Pt/Ir-wires at ambient conditions since the Pt/Ir alloy is not air-sensitive.

During the current work all the parts of the STM-head (including the analogous Dip-stick STM setup) were repaired. Since each sudden breakdown of the setup

components (especially, piezoelectric materials) required quite thorough repair work, very accurate handling with the STM-head is necessary. For example, after the breakage of the scanner electrodes, they were glued and fixed, and the STM has been put into the operation. The latter is proved by the observed atomic corrugation both at ambient conditions on a standard STM material highly oriented pyrolytic graphite (HOPG) and, later, at the base temperature on  $\text{MnBi}_2\text{Te}_4$  as shown in Fig. 3.4.4. However, it turned out that the piezo constant of the tube scanner was reduced with a factor of  $\approx 1.67$ . Therefore, the correct scanner's calibration was performed based on the atomically resolved topographic data and yielded the values of the full range of the scanner mentioned above. The long-term QPI measurements on  $\text{Bi}_2\text{Te}_3$  (see sections 4.1.3 and 4.1.4), for example, further prove the successful repair of the Dip-stick STM.

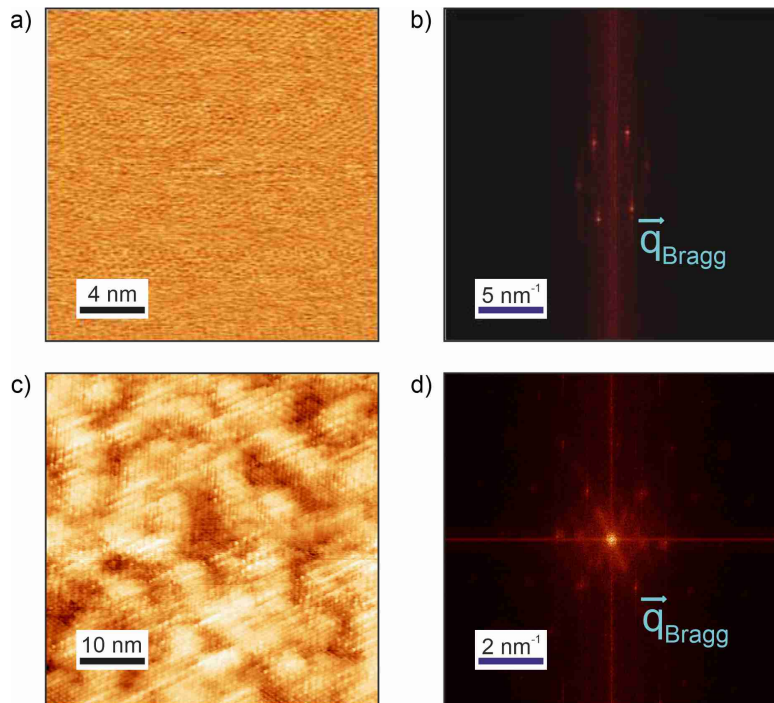


**Fig. 3.4.4** a) Topography scan of HOPG at  $T = 298$  K on air,  $U_{bias} = 200$  mV,  $I_T = 100$  pA. b) Fast Fourier transform (FFT) of the image a) with the marked Bragg reflection vector  $\frac{4\pi}{\sqrt{3}a}$  corresponding to atomic corrugation which allows to estimate the lattice constant  $a$  of the material and compare it with its literature value for the calibration of the scanner. Note that the Bragg peaks in one direction (corresponding to the slow scanning direction in a)) look less clear than the others due to the unavoidable thermal drift at room temperature. The average value of the extracted Bragg vectors was used for the estimation of the correction factor of the tube scanner's piezo constant. c) Topography of  $\text{MnBi}_2\text{Te}_4$  measured at  $T = 6$  K,  $U_{bias} = -300$  mV,  $I_T = 50$  pA. d) FFT of c) with the Bragg vectors (recognized as the most distinct six-fold symmetric spots) extracted in the same way as for HOPG in b). The correction factor of the scanner's piezo constant was found to be nearly the same as in b) pointing towards the right calibration.

# Chapter 4

## Experimental results

The STM data measured in this work were analyzed with WSxM [175]. In addition, other different software were intentionally developed in Python for the  $dI/dU$  maps analysis (see program codes in Appendix C) and spin-selective joint density of states calculations which will be discussed in section 4.1.4.

### 4.1. $\text{Bi}_2\text{Te}_3$

In this section the following manuscript is reproduced:

V. Nagorkin, S. Schimmel, P. Gebauer, A. Isaeva, D. Baumann, A. Koitzsch, B. Büchner and C. Hess, *Bulk and surface electron scattering in disordered  $\text{Bi}_2\text{Te}_3$  probed by quasiparticle interference*, submitted to Phys. Rev. B, arXiv:2409.04294v1 [cond-mat.mes-hall] (2024) (available at <http://arxiv.org/abs/2409.04294>).

All the crystals of the  $\text{Bi}_2\text{Te}_3$  compound were cleaved in cryogenic vacuum at the base temperature  $T \sim (6-7)$  K just before the measurements in the Dip-stick STM presented in section 3.4 with the Nanonis Specs STM-controller. Bias voltage modulation was provided externally by the SR 830 lock-in amplifier with  $U_{mod} = (2-10)$  mV RMS and  $f_{mod} = 0.667$  kHz.

#### 4.1.1. Topography

Fig. 4.1.1a depicts an overview of the surface of the measured samples in a field of view of  $50 \times 50$  nm $^2$ . This topography image represents an atomically corrugated hexagonal Te-terminated surface with a characteristic line profile taken along the unit cell vector  $a$  or  $b$  (which are indistinguishable) and shown in Fig. 4.1.1d, where 43 peaks on 20 nm length scale provide the oscillation period of around 4.65 Å. Fig. 4.1.1c shows the FFT of the topography with very distinct Bragg reflection spots indicating a hexagonal lattice and an additional six-fold symmetric pattern

inside. The half-distances between the opposite Bragg spots measured in 3 directions provide the values of  $q_{Bragg}$ : 1.52 1/Å, 1.54 1/Å and 1.56 1/Å. Hence, the average value of  $q_{Bragg} = 1.54$  1/Å and the corresponding lattice constant (as for hexagonal HOPG in section 3.4  $a = \frac{4\pi}{\sqrt{3}q_{Bragg}}$ )  $a = 4.7 \pm 0.1$  Å which is consistent with the oscillation period derived from the topography line profile in Fig. 4.1.1d and is in a reasonable agreement with the literature value of  $a \approx 4.38$  Å (see section 2.1.4). Although this discrepancy which was in the range 2–7 % in the whole experiment might come from the STM scanner artifacts, it is not essential for the QPI data presented in sections 4.1.3, 4.1.4, 4.1.5 due to larger errors in those data. The line profile in Fig. 4.1.1d exhibits another modulation arising from the surface defects which is also revealed in the FFT in Fig. 4.1.1c. This inner long-wavelength six-fold symmetric structure corresponds to the energy integrated QPI and will be discussed further.

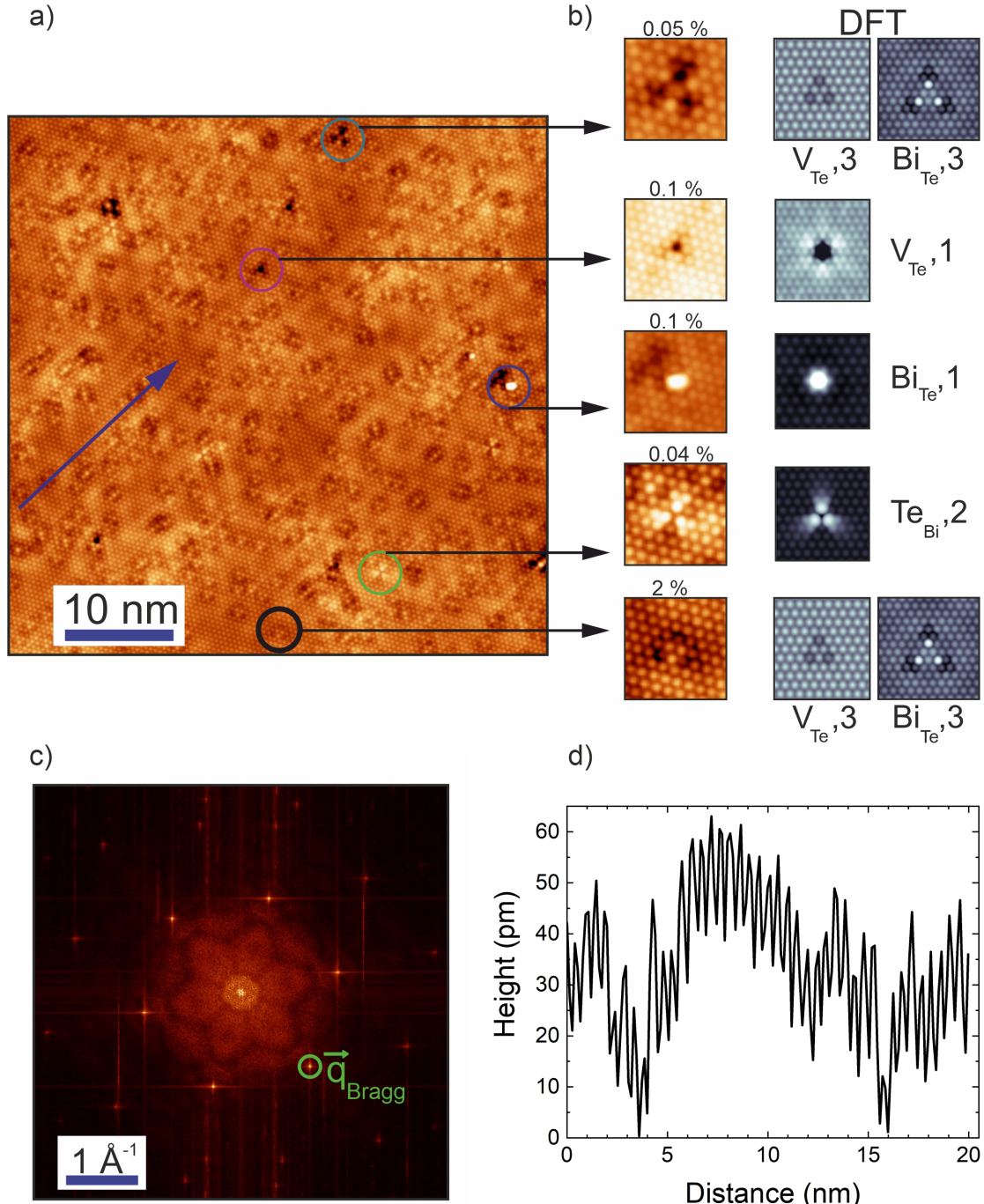


**Fig. 4.1.1** a) Representative topography of  $\text{Bi}_2\text{Te}_3$  measured at  $U_{\text{bias}} = 100$  mV,  $I_T = 100$  pA,  $T = 6.9$  K. Examples of various defects are marked with circles of different colours. b) The observed defect types on the left column with their corresponding DFT-based calculations adapted from [50]. Numbers above the figures denote the densities of the defects as the percentage of atomic sites occupied by them. The notation of the defects is the same as in Fig. 2.1.13. c) FFT of the image a). d) Line profile of the topography made across two defects and indicated with the blue arrow in a).

The topography image in Fig. 4.1.1a reveals numerous defects of different origin plotted in the left column of Fig. 4.1.1b. They can be grouped into different types, according to the former experimental STM defect studies and DFT-based

calculations of the defects in  $\text{Bi}_2\text{Te}_3$  [50,51] shown in the right column of Fig. 4.1.1b (see also the calculations for occupied states presented in a different colorscale in Fig. 2.1.13). The comparison was based on counting the number of atoms giving the contrast in the topography of the defects (selected fields of view of  $\sim 100 \times 100 \text{ nm}^2$ ) and taking into account the bias voltage dependence of the defects measured in the current work (see Fig. 4.1.2). In particular, the defects appearing as three-fold symmetric dots of bright contrast arising from the crystal symmetry can be identified as Te/Bi-antisites in the second atomic layer from top. The dark triple dots are, most likely, Te-vacancies or Bi substitutions in the third layer of the topmost quintuple layer (see Fig. 4.1.1b). Meanwhile, these three-fold symmetric defects (triple dots of both dark and bright contrast) show almost no dispersion in contrast to the data in [50]. The single dark dots can be identified as the Te-surface vacancies in the first Te-layer. In addition, the observed single bright spots in the topography are, most likely, Bi/Te antisite defects occurring in the first Te layer rather than Bi adatoms since they do not show any migration while scanning on the same surface spot. All these defects have relatively small density of  $\leq 0.1 \%$ , unlike the most abundant defect type marked with the black circle in Fig. 4.1.1a which has a density of around 2 defects per 100 surface atoms (2 %). One can even notice that these defects are mixed, overlap with each other. For comparison with the literature, the density of the dominant defects does not exceed 1 %, as, for example, in [55]. Although there is no perfect correspondence of the dominant defect in the current work with the former DFT studies in [50], it could be potentially assigned to the Te-vacancy or Bi substitution in the third (Te) atomic layer inside the topmost quintuple layer. Note that its three-fold symmetry suggests a three-fold symmetric scattering potential [52,55,88]. The latter affects the QPI data and will be discussed in section 4.1.3.

It is worth to mention that the STM appearance of the abovementioned dominant defects changes with the bias voltage as illustrated in Fig. 4.1.2 where topography images were obtained on the same  $30 \text{ nm} \times 30 \text{ nm}$  surface region containing different kinds of defects. In particular, the dominant defect looks as a triangle formed by 3 atoms of bright contrast at positive bias voltages (empty states) as shown in Fig. 4.1.2i. At negative bias voltages (occupied states) it becomes dimmer and gets surrounded by atoms of more dark contrast as depicted in Fig. 4.1.2k which does not look very similar to the theoretical calculations (see Figs. 4.1.2j,l) for any kinds of defects studied in [50].

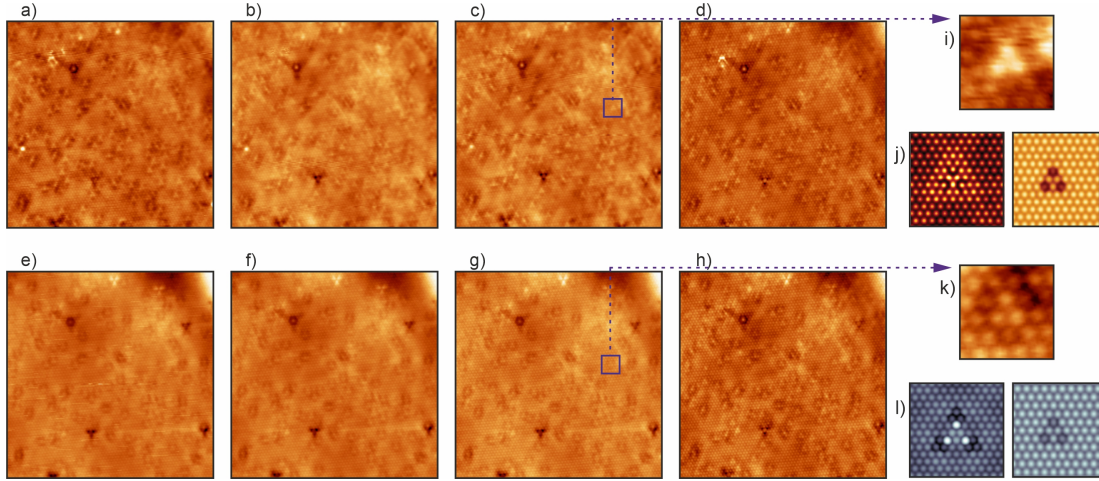


**Fig. 4.1.2** a)–d) Topography images of  $\text{Bi}_2\text{Te}_3$  measured at  $U_{bias} = -700$  mV,  $-500$  mV,  $-400$  mV,  $-100$  mV, respectively. e)–h) Topographies at  $U_{bias} = 700$  mV,  $500$  mV,  $400$  mV,  $100$  mV, respectively. i), k) Zoom-in view of the defect marked in c) and g) with their corresponding DFT-based calculations for  $\text{BiTe}_3$  (on the left) and  $\text{VTe}_3$  (on the right) in j) and l) taken from [50], respectively. The scanned area size  $30$  nm  $\times$   $30$  nm,  $I_T = 1$  nA.

This deviation of the shape of the most abundant defect from both experimental and theoretical literature data on  $\text{Bi}_2\text{Te}_3$  could suggest possible extrinsic doping of the crystals. To verify it, they were transferred for X-ray photoelectron spectroscopy (XPS) measurements (at first, they were cleaved) performed by Dr. A. Koitzsch at IFW Dresden. The XPS analysis reveals the absence of extrinsic dopants (which confirms the intrinsic origin of the defects) and no deviation from the stoichiometry of this compound [176]. Note that there are relatively small contents of oxygen and carbon contaminants (see Fig. 4.1.3) which are often observed in XPS experiments, also copper and silver peaks in the spectrum are related to the sample holder and the component of the conducting glue, respectively. At first glance, no strong differences were recognized in the obtained spectrum compared to the previously measured XPS spectra on  $\text{Bi}_2\text{Te}_3$  [177]. However, a closer look at the relatively narrow Bi  $4f$  peak reveals slight deviations from its ideal shape. In order to fit the photoemission spectrum by Voigt profiles, a second component of the Bi  $4f$  peak needs to be taken into account, as shown in Fig. 4.1.3. This suggests modified chemical environments of Bi atoms, which can be evidenced by the disorder in the STM topographic data (see the data above). Meanwhile, the additional contribution to the Bi  $4f$  peak was also detected by XPS in [178] where it was caused by Bi surface oxides, the latter could occur in the crystals used in the current work as well due to their exposure to air prior to the STM measurements.

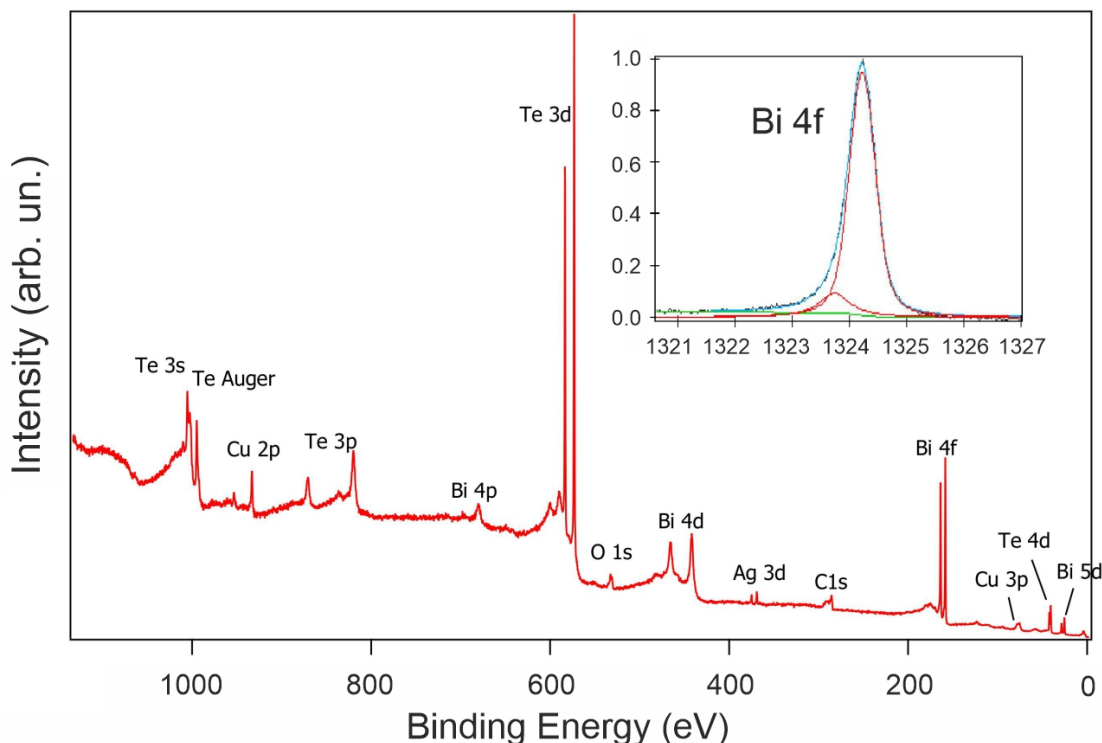


**Fig. 4.1.3** XPS spectra of  $\text{Bi}_2\text{Te}_3$  measured by Dr. A. Koitzsch at IFW Dresden. The inset shows two components of the  $\text{Bi} 4f$  peak (red curves) derived from the fitting of the experimental data (black curve). The cyan curve is the sum of the two red curves. Note that the energy scale in the inset displays the kinetic energy of electrons and is different from the one shown in the main spectrum.

### 4.1.2. STS

Fig. 4.1.4 shows differential conductance spectra measured on  $\text{Bi}_2\text{Te}_3$  which bear no strong variations. These  $dI/dU$  tunneling spectra were measured as spectroscopy maps on the surface grids across the defects as well. For example, in the spectra taken on the three-fold symmetric defect (which is not the dominant one), as shown in Fig. 4.1.4, one would not see detectable differences in the STS even with the spectroscopy resolution of 3 mV.

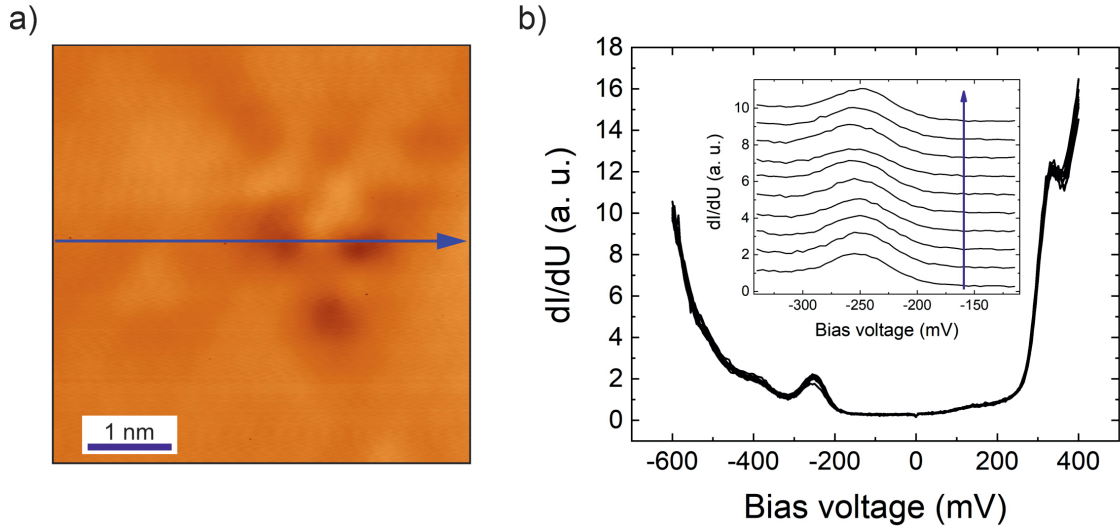


**Fig. 4.1.4** a) Topography of a  $5 \text{ nm} \times 5 \text{ nm}$  area where the STS map on a  $10 \times 10$  grid was measured on  $\text{Bi}_2\text{Te}_3$  across one of the non-dominant three-fold symmetric defects.  $U_{bias} = 400 \text{ mV}$ ,  $I_T = 350 \text{ pA}$ . b) Tunneling spectra measured along the blue arrow shown in a) with their waterfall representation in the inset.

However, on larger lengthscales as, for example, on a  $30 \text{ nm} \times 30 \text{ nm}$  surface area with the most abundant defects shown in Fig. 4.1.5 one can see more variations, which may be a signature of the possible quasiparticle interference. Therefore, it is especially important to investigate these changes by measuring the  $dI/dU$  maps at different energies.

It is worth to note that the tip-induced band bending phenomenon which was observed in semiconductors and insulators and even in topological insulators as, for example,  $\text{Bi}_2\text{Se}_3$  [179], was not found in the measured samples. To illustrate, the Fig. 4.1.6 depicts an example of the  $dI/dU$  spectra measured at different bias voltages of 100 mV and  $-350 \text{ mV}$  and  $-400 \text{ mV}$  at the same location which lie on top of each other.

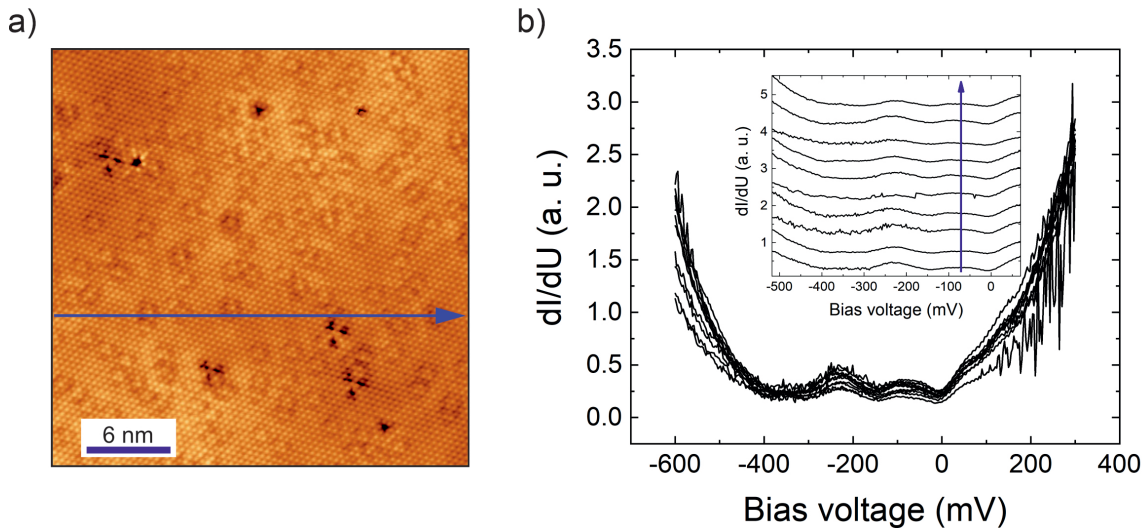


**Fig. 4.1.5** a) Surface topography of the area where the STS map on a  $10 \times 10$  grid was measured across the dominant defects at  $U_{bias} = 300$  mV,  $I_T = 500$  pA. b)  $dI/dU$  spectra measured along the blue arrow shown in a) with their waterfall representation in the inset.

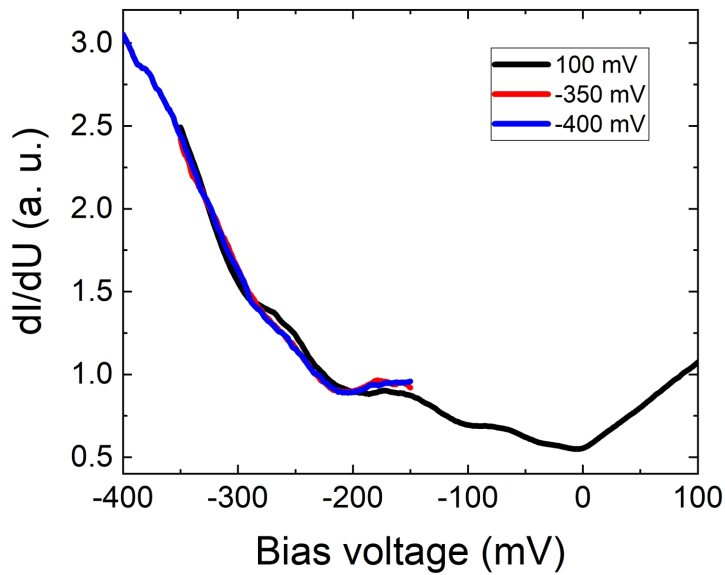


**Fig. 4.1.6**  $dI/dU$  spectra measured at the same surface position at 100 mV, -350 mV and -400 mV bias voltages with  $I_T = 1$  nA.

### 4.1.3. $dI/dU$ maps in zero-field

The most important data acquired in this work are the differential conductance maps measured in a relatively large energy range from -800 meV to 500 meV with respect to the Fermi level. The main goal of this experiment was to track the evolution of the FFT patterns of the  $dI/dU$  maps (FT-QPI) as a function of the energy (i.e. applied bias voltage). These FT-QPI patterns (see section 3.3) arise

from scattering of electrons on surface step edges or defects (the latter case was realized in the experiment) and, thus, provide information on the electronic band structure of the sample. In general, these measurements require both rather wide fields of view ( $> 40$  nm for  $512 \times 512$  pixels images) to gain a sufficient resolution in the momentum space and a close to perfect stability of the STM during the whole experiment.

The  $dI/dU$  maps were measured on the same surface spot of  $80$  nm  $\times$   $80$  nm size (see Fig. 4.1.7a) consisting of many defects which are conceivably identified as  $\text{Bi}_{\text{Te},3}$  or  $\text{V}_{\text{Te},3}$  (see section 4.1.1) in accordance with Fig. 4.1.1 and Fig. 4.1.2. The tunneling current set point was deliberately set to a new value at each next energy to keep the tunneling resistance ( $U_{\text{bias}}/I_T$ ) constant for 19 values of the bias voltage between  $300$  mV and  $-600$  mV. In other words, since reducing the bias voltage makes the tip-sample distance smaller, the tunneling current set point can be decreased at the same time to lift the tip further away from the sample and avoid the set point effect. The  $dI/dU$  maps shown in Fig. 4.1.8 demonstrate nicely an energy dependent spatial modulation of the differential conductance with a period of (2–4) nm which is a hallmark of the QPI. In particular, one can clearly see a continuous increase in the modulation period in real space with reducing the bias voltage from  $300$  mV down to  $-70$  mV. At lower energies the patterns become more blurred, and one has to rely on the FT-QPI data in order to infer the energy dependence (see Fig. 4.1.9). For better illustration, these data are plotted in Fig. 4.1.10 as a stack, where the linear dispersion is shown by the red dotted lines with a node at about  $-355$  mV. The image size of  $80$  nm  $\times$   $80$  nm allows to observe both the QPI in the differential conductance maps and the Bragg peaks as shown in Fig. 4.1.7b which is important for the correct determination of the QPI scattering vectors directions and lengths. The maps were measured on different samples at different conditions and gave nearly identical FT-QPI patterns (see section 4.1.4 and Appendix A) which unambiguously indicates reliability and reproducibility of the obtained data.

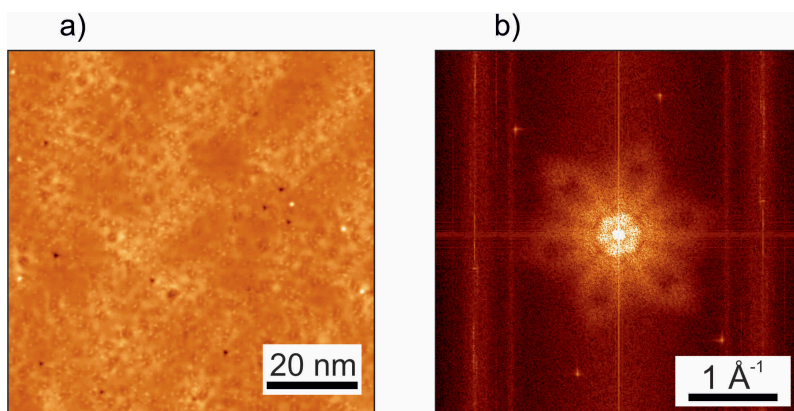


**Fig. 4.1.7** a) Topography of the surface area where  $dI/dU$  maps were measured,  $U_{\text{bias}} = -120$  mV,  $I_T = 400$  pA with its FFT in b).

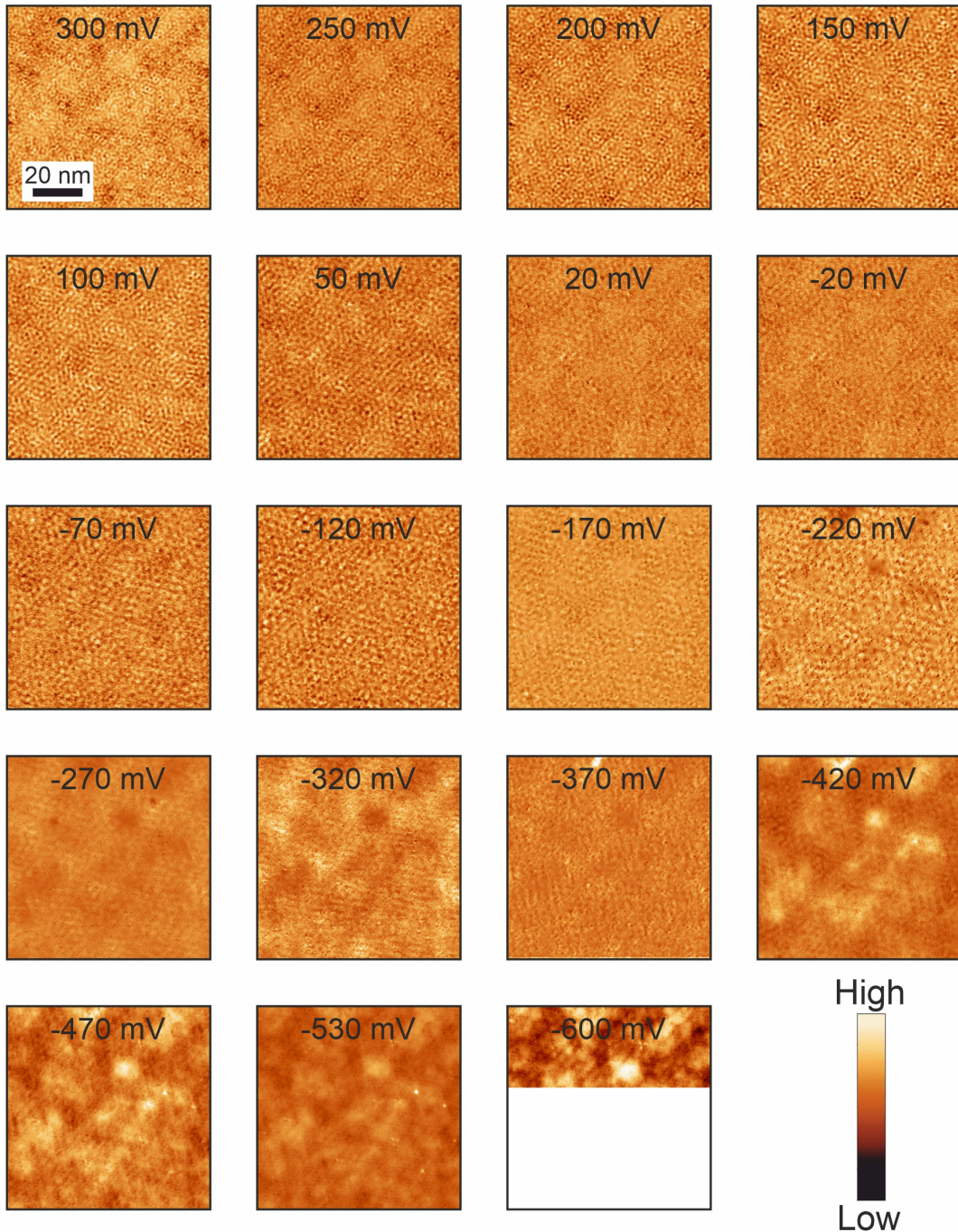


**Fig. 4.1.8** Series of the  $dI/dU$  maps measured at the energies from 300 mV to  $-600$  mV on the same surface area. The scalebar is the same for each of the maps.

The corresponding Fourier transforms of the data shown in Fig. 4.1.8 are plotted in Fig. 4.1.9. All the FT-QPI patterns were symmetrized according to the six-fold symmetric crystal structure in order to achieve better signal-to-noise ratio (see more details in Appendix B).

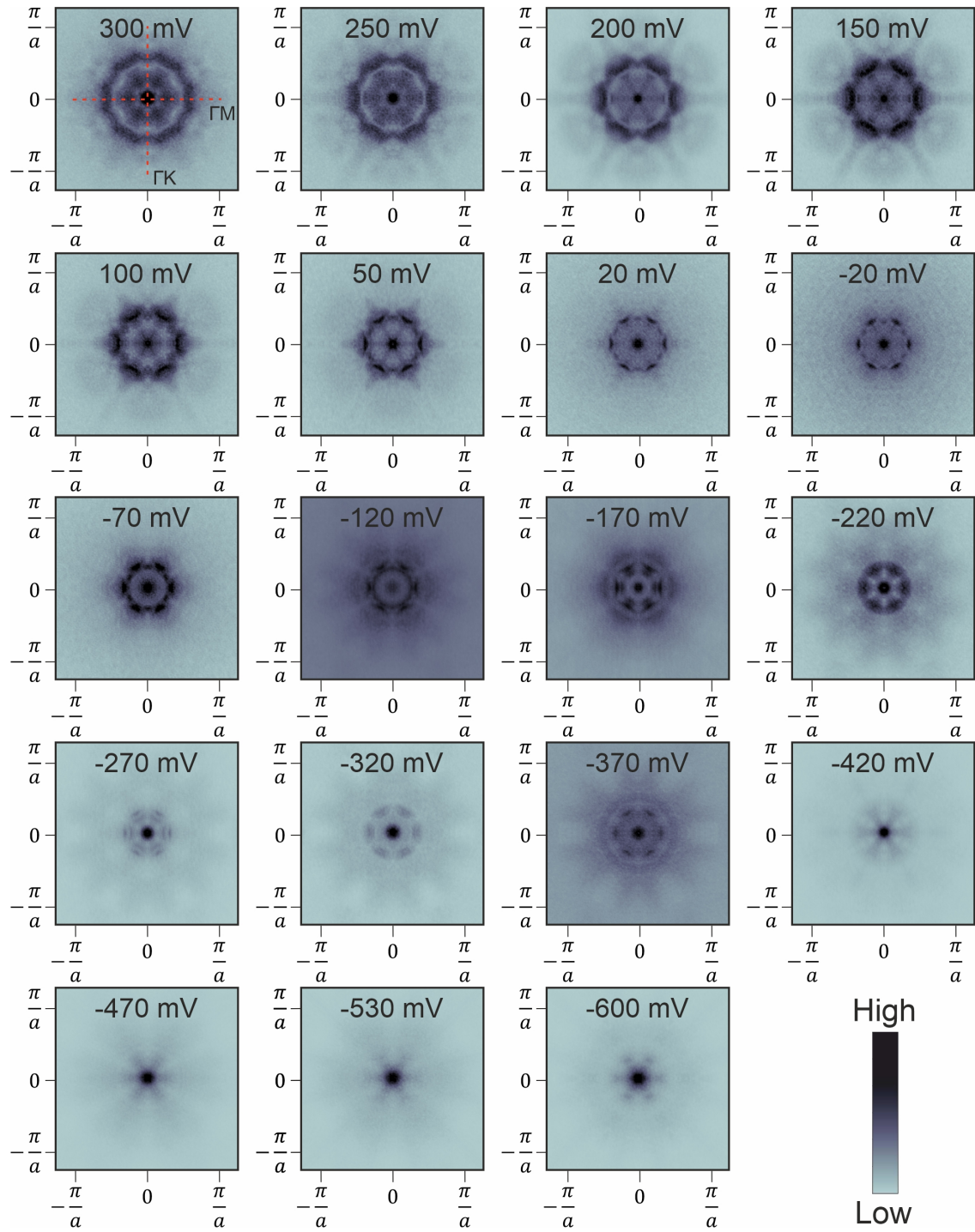


**Fig. 4.1.9** Series of the symmetrized FT-QPI patterns measured at the bias voltages from 300 mV to  $-600$  mV on the same surface area. The lattice constant value  $a = 4.7$  Å as mentioned in section 4.1.1.

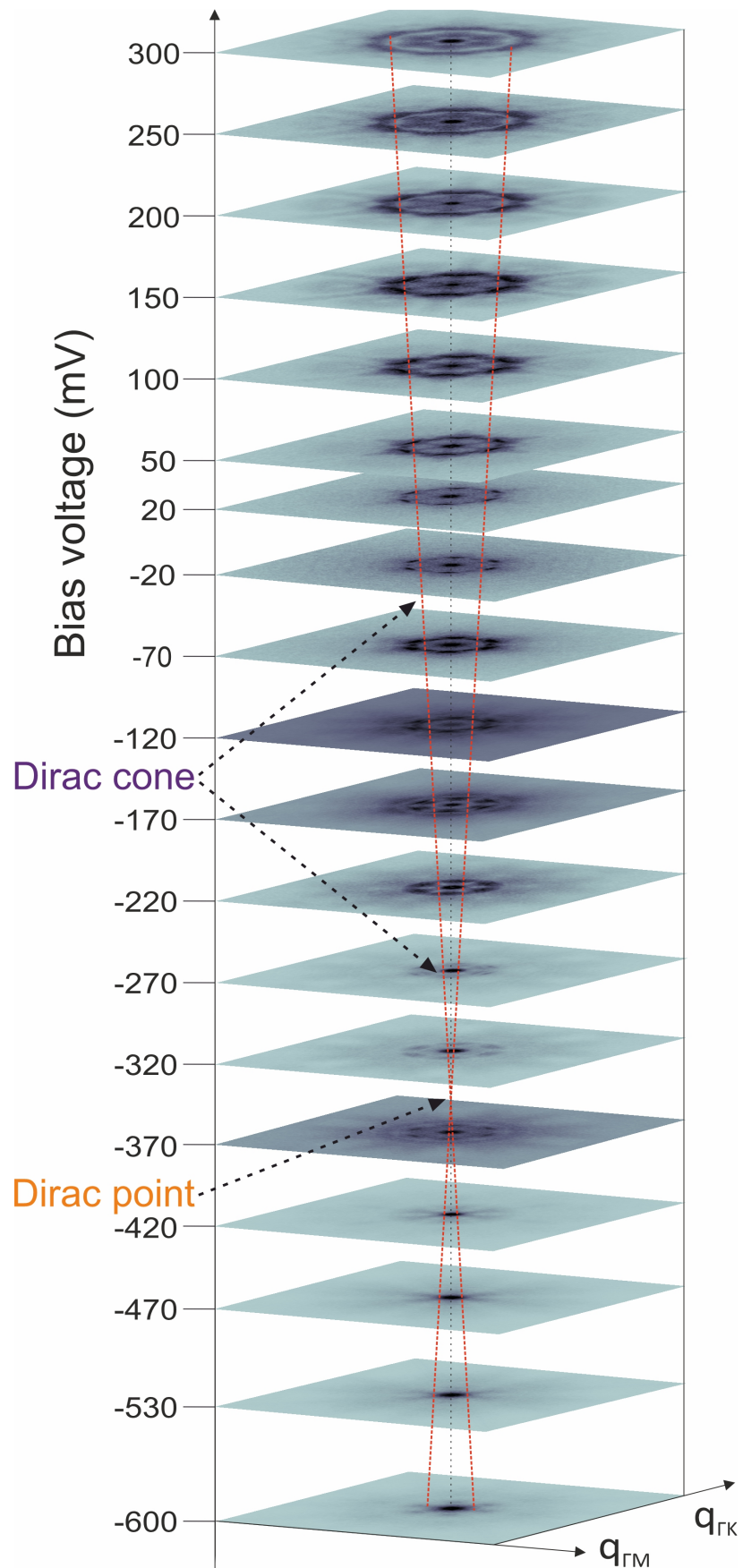


**Fig. 4.1.10** Stack of the FT-QPI patterns measured at  $B = 0$  T. High-symmetry directions  $\Gamma$ -M and  $\Gamma$ -K are labelled as  $q_{\Gamma M}$  and  $q_{\Gamma K}$ , respectively.

At first glance, the FT-QPI data obtained at 19 bias voltages in the range from  $-600$  mV to  $300$  mV, which is presented in Fig. 4.1.9, can be classified into 5 types according to characteristic observed structures in the FFT as illustrated in Fig. 4.1.11.

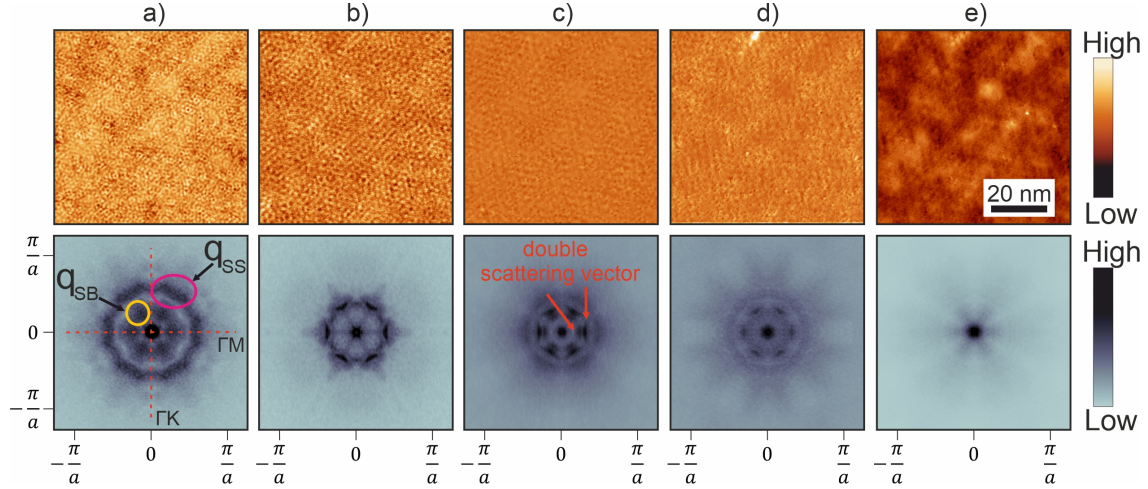


**Fig. 4.1.11** a)–e)  $dI/dU$  maps (top) with corresponding FT-QPI patterns (bottom) at specific energies of  $300$  mV,  $50$  mV,  $-170$  mV,  $-370$  mV,  $-470$  mV, respectively, measured on the surface shown in Fig. 4.1.7. High-symmetry crystallographic directions are labelled in a). Two distinguishable sets of scattering vectors  $q_{SS}$  and  $q_{SB}$  are marked by magenta and yellow ellipses, respectively. The in-plane lattice constant value  $a$  was derived from topographic data.

To be more precise, the maps shown at high bias voltages from  $300$  mV to  $150$  mV as in Fig. 4.1.11a exhibit six arc-shaped structures of high intensity in the  $\Gamma$ -M crystallographic direction, characteristic for a Dirac surface state in  $\text{Bi}_2\text{Te}_3$  and denoted as  $q_{SS}$  in Fig. 4.1.11a. Note that the Bragg peaks are not visible in Fig. 4.1.11 and further in this chapter since they appear at significantly larger values of the scattering vector, so the presented FFTs were obtained by cutting edges from the raw FFTs (the same dimensions for each energy) for better demonstration of the FT-QPI features (see an example of raw FT-QPI patterns in Appendix A). Apart from that, another six-fold symmetric structure of weaker intensity (labelled as  $q_{SB}$  in Fig. 4.1.11a) collinear with the abovementioned one is clearly visible in Fig. 4.1.11a but does not exist in Fig. 4.1.11b, i.e. at lower energies. At those energies in the range  $[-70; 100]$  mV the FT-QPI patterns only consist of the spots that can be assigned to  $q_{SS}$ . With decreasing bias voltage the scattering vectors shorten (see Figs. 4.1.9 and 4.1.10) and become more clearly defined and sharper than those at higher energies. Going further to lower bias voltages from  $-120$  mV down to  $-320$  mV the scattering vector experiences a splitting into two distinct vectors of nearly the same intensities (see Fig. 4.1.11c). In this energy range the dispersion becomes weaker, i.e., the QPI peak position becomes nearly energy independent (see Fig. 4.1.11). At the bias voltage of  $-370$  mV the scattering vector is again single, not

splitted (see Fig. 4.1.11d), while at further lower bias voltages the FT-QPI pattern becomes less clear with significantly weaker intensity (see Fig. 4.1.11e).

All the FT-QPI patterns in Fig. 4.1.9 reveal an enhanced intensity in the  $\Gamma$ -M direction, while one can notice a less pronounced intensity in the  $\Gamma$ -K direction as well (for more details see the next section 4.1.4 and Appendix A).

#### 4.1.4. QPI analysis of the zero-field $dI/dU$ maps

For the analysis of the FT-QPI data traces along the  $\Gamma$ -M directions (where the intensity is the highest) were taken for each of the used bias voltages, these intensity profiles are plotted in Fig. 4.1.12c. For example, at  $U_{bias} = 300$  mV in Fig. 4.1.12a there are 2 dominant scattering vectors corresponding to 2 kinds of the intensity peaks in Fig. 4.1.12b with the peak positions labelled as  $q_{SS}$  and  $q_{SB}$ . The central peak arises due to the inevitable constant component of the tunneling current and low-frequency noise due to mechanical vibrations of the STM, thus, it is not relevant. The background of the intensity profiles including the central peak was subtracted as shown in Fig. 4.1.12b for  $U_{bias} = 300$  mV. Gaussian fits of the peaks (see Fig. 4.1.12b) of the curves plotted in Fig. 4.1.12c allowed to extract the values of  $q_{SS}$  and  $q_{SB}$  which are displayed on the intensity graph in Fig. 4.1.12d as circles: black – the outer, dominant vector, red and magenta – 2 components of the double scattering vector. The black circles were fitted by the black straight line resembling the Dirac cone of the surface states measured by ARPES in the same  $\Gamma$ -M direction on  $\text{Bi}_2\text{Te}_3$  (see Fig. 2.1.9). The observed linear dispersion confirms the relativistic Dirac nature of the surface state in  $\text{Bi}_2\text{Te}_3$ .

The described analysis was made for all the used energies, and the extracted data are plotted on the two-dimensional graph in Fig. 4.1.13 where as in Fig. 4.1.12 the black squares correspond to the main vector, red and blue squares – double vector, green squares are the inner peaks in the FFT existing only at high energies with no certain energy dispersion which can be associated with the bulk scattering, as will be discussed further below. The most remarkable result is the clear linear energy dispersion which starts from 300 mV, at least, and breaks down below 100 mV. In order to make a linear fit of the energy dispersive QPI scattering vector  $q_{SS}$ , the energy range from 100 mV to 300 mV was chosen, at which the Dirac velocity derived from the slope of the linear fit of the energy dispersion, as shown in Fig. 4.1.13,  $v_D = (4.3 \pm 0.3) \times 10^5$  m/s is in a good agreement with the existing data on this compound [8, 50, 52, 56, 57]. The extrapolation of the linear fit of  $q_{SS}$  at bias voltages from 300 mV to 100 mV allows to estimate the Dirac point energy to  $-355$  meV at which  $q = 0$  (see Fig. 4.1.13).

The lengths of the dominant scattering vectors extracted from the FT-QPI data

on 5 measured samples and, in addition, on different surface areas of the same samples are plotted in Fig. 4.1.14. From that one can clearly argue that the data are sample independent within the batch under investigation. The linear fit for the dominant scattering vector for 5 samples is marked by the red line resulting in the Dirac point energy of  $-360 \pm 40$  mV and  $v_D = (4.3 \pm 0.4) \times 10^5$  m/s. The vertical black line indicates the non-dispersive scattering mode with the average  $q \approx 0.21$   $1/\text{\AA}$ .

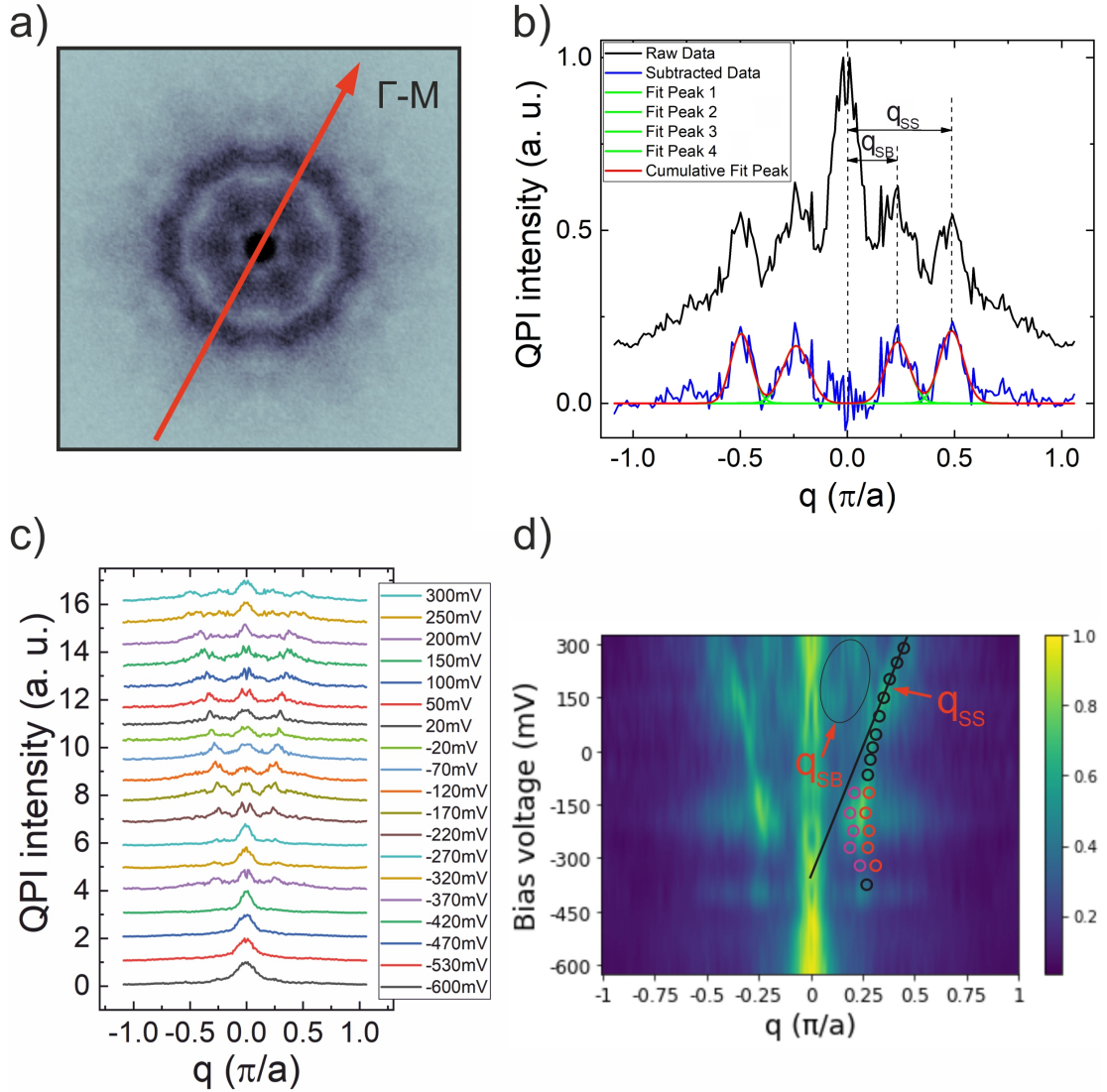


**Fig. 4.1.12** a) QPI pattern obtained at  $U_{bias} = 300$  mV. b) Intensity profile of the QPI pattern in a) taken along the  $\Gamma$ -M direction marked with the red arrow in a).  $q_{SS}$  and  $q_{SB}$  are the peak positions corresponding to the outer and the inner scattering vectors in a). Gaussian fitting of the observed peaks was performed after subtraction of the background with the central peak. c) QPI intensity profiles along the  $\Gamma$ -M direction at bias voltages from 300 mV down to  $-600$  mV. d) Intensity graph of the QPI energy dispersion obtained from c). The data extracted from Gaussian fit of the curves in c) are plotted as circles: black – the outer, dominant vector  $q_{SS}$ , red and magenta – double scattering vector. The black line is the linear fit made for biases above 100 mV. The inner scattering vector  $q_{SB}$  is indicated by the black ellipse.

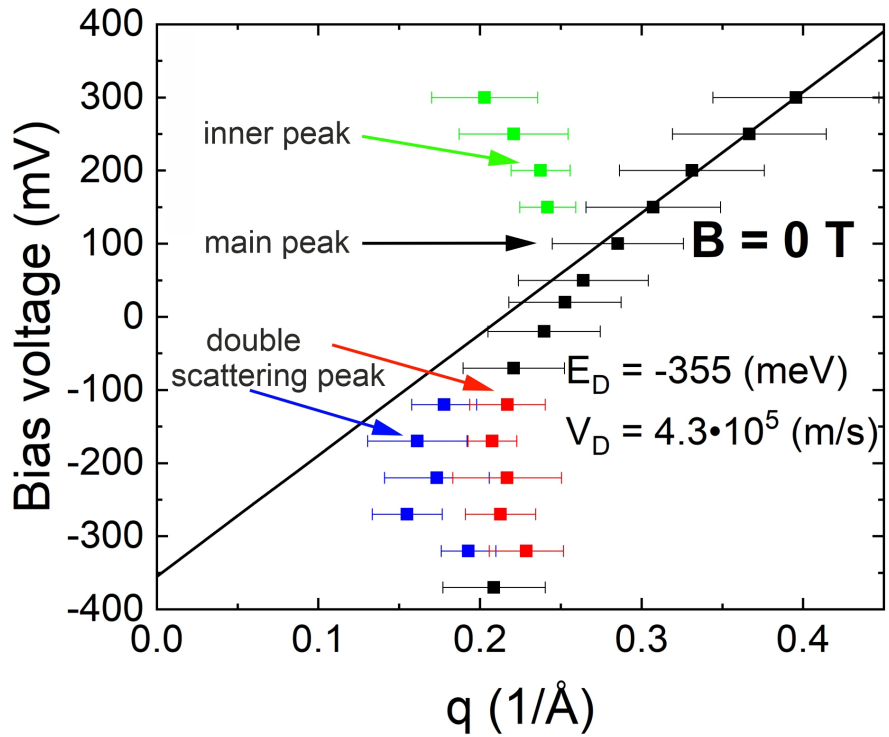


**Fig. 4.1.13** QPI energy dispersion in the  $\Gamma$ -M direction measured at  $B = 0$  T. The data corresponding to the main  $q_{SS}$ , the inner  $q_{SB}$  and the double scattering vectors are plotted in black, green and red/blue colours, respectively. The black line shows the linear fit to the data points in the bias voltage range from 300 meV to 100 meV.

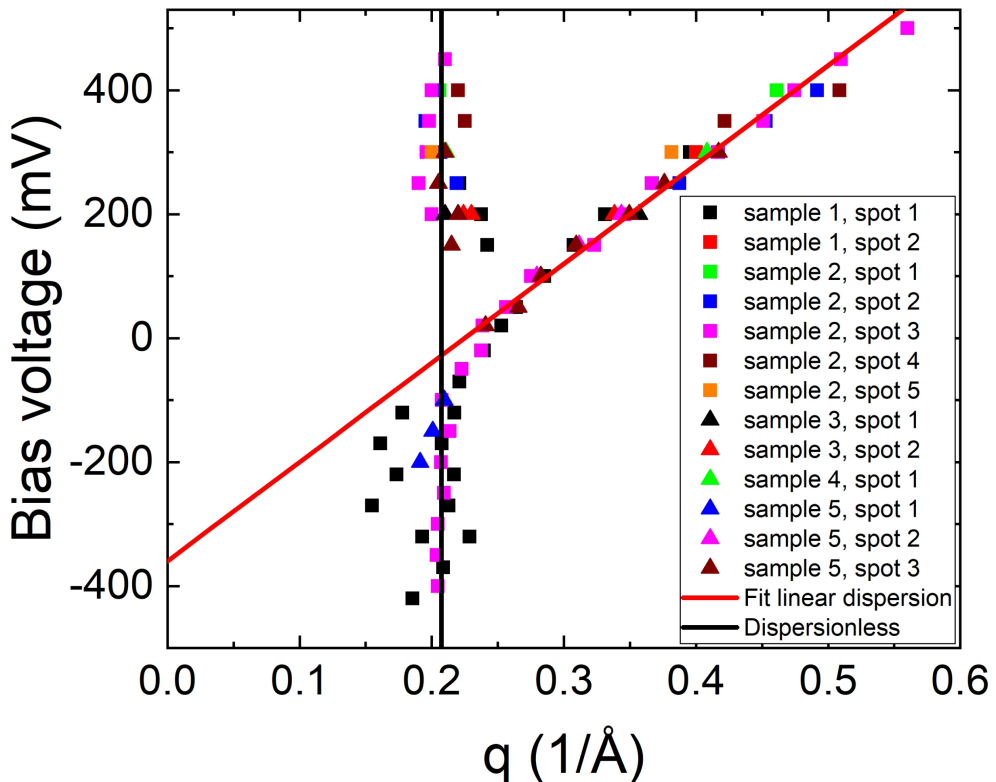


**Fig. 4.1.14** QPI energy dispersion in the  $\Gamma$ -M direction obtained at  $B = 0$  T on different samples and different surface areas on the same samples.

For further analysis of the experimental FT-QPI data one needs to make their comparison with the known surface band structure data on  $\text{Bi}_2\text{Te}_3$  [8, 46, 47, 53]. For that one should consider the energy evolution of the constant-energy contours in this material which were measured by ARPES [8, 53] along with the electronic band structure calculations [46, 47]. According to those studies the circular shape of the constant-energy contour transforms into a hexagon which further becomes a concave hexagram like a snowflake due to the hexagonal warping effect in  $\text{Bi}_2\text{Te}_3$  upon increasing the energy starting from the Dirac point. Since the surface state in this material is protected by time-reversal symmetry from backscattering one would expect to see rather faint QPI signals. However, different scattering channels can be opened up due to the hexagonal warping of the constant-energy contours of the surface state [47].

A simplified first-order approach to model the FT-QPI patterns is provided by joint density of states (JDOS) calculations for the surface electrons (and bulk electrons as well in the present work) based on the corresponding band structure data. According to this method, which was first proposed for topological insulators by P. Roushan *et al.* [42, 180], one should consider JDOS which is a function of the momentum difference  $\mathbf{q}$  (i.e. scattering vector) between initial and final scattering states on the same constant-energy contour:

$$JDOS(\mathbf{q}) = \int I(\mathbf{k})I(\mathbf{k} + \mathbf{q})d^2\mathbf{k}, \quad (4.1.1)$$

where  $I(\mathbf{k})$  is the momentum dependent DOS, which can e.g., be approximated from ARPES intensity data (see Fig. 4.1.15a). Therefore, one needs to compute the autocorrelation of the DOS in the initial and final states integrated over the first Brillouin zone. This calculation does not consider the spin selection rules and allows scattering in any directions with several scattering vectors as shown in Fig. 4.1.15b which was not observed in the experimental QPI data (see Fig. 4.1.9). In order to take into account the helical in-plane [180] and the warping induced out-of-plane spin texture [34, 46, 48], the spin-dependent scattering matrix element  $T(\mathbf{q}, \mathbf{k})$  (which characterizes the scattering probability as a function of the scattering vector and spins of the initial and final states) can be introduced as follows:

$$T(\mathbf{q}, \mathbf{k}) \propto (1 + \cos(\theta_f - \theta_i)) + a^2(1 + \cos(3(\theta_f - \theta_i))), \quad (4.1.2)$$

where  $\theta_f$  and  $\theta_i$  are the angles that define  $\mathbf{k}_f$  and  $\mathbf{k}_i$  in reciprocal space,  $a$  is the maximal value of the ratio between the out-of-plane and the in-plane spin components [34, 46, 48]. From this one can calculate spin-dependent scattering probability patterns:

$$SSP(\mathbf{q}) = \int V(\mathbf{k})I(\mathbf{k})T(\mathbf{q}, \mathbf{k})V(\mathbf{k} + \mathbf{q})I(\mathbf{k} + \mathbf{q})d^2\mathbf{k}. \quad (4.1.3)$$

It is clear from the equations 4.1.2 and 4.1.3 that scattering with opposite spins is effectively cancelled. The spin-selective scattering probability mainly results in the suppressed intensity for the backscattering processes which appear as the outer structure in the JDOS patterns. This is remarkably demonstrated in Fig. 4.1.15, where the spin-dependent scattering probability in Fig. 4.1.15c reveals significantly weaker backscattering intensity than in the corresponding JDOS calculations plotted in Fig. 4.1.15b. Additionally, the three-fold symmetric scattering potential  $V$  [52, 55, 88] related to the dominant defect type (see section 4.1.1) was also utilized in the current work. More detailed information concerning the implementation of the spin texture and the scattering potential can be found in Appendix A. The resulting spin-dependent scattering probability maps can be directly compared to the experimental FT-QPI patterns.

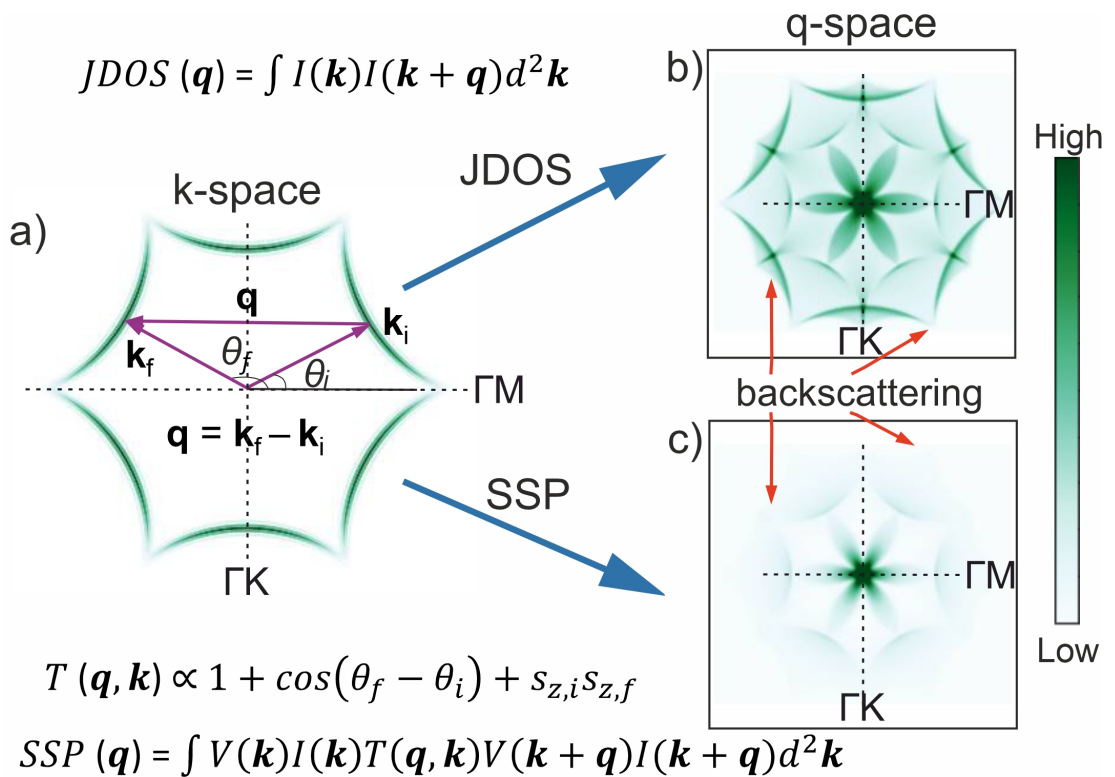


**Fig. 4.1.15** a) Idealized sketch of the constant-energy contour in the shape of a warped hexagon. Scattering vector  $\mathbf{q}$  is a difference between the final (scattered) and the initial states with wavevectors  $\mathbf{k}_f$  and  $\mathbf{k}_i$ . b) JDOS pattern in the  $\mathbf{q}$ -space obtained from the autocorrelation of the constant-energy contour plotted in a). c) Spin-dependent scattering probability pattern calculated for the constant-energy contour in a). Red arrows highlight the suppression of the backscattering. The high-symmetry directions are marked for all the presented figures.

To make the analysis more clear, different constant-energy contours in the  $\mathbf{k}$ -

space for  $\text{Bi}_2\text{Te}_3$  were approximately derived from the ARPES data [8, 53]. The schematic illustration of the scattering geometry for the constant-energy contour of the warped hexagonal shape in  $\text{Bi}_2\text{Te}_3$  is shown in Fig. 4.1.16, where the QPI is mainly determined by six scattering vectors  $\mathbf{q}_1$ – $\mathbf{q}_6$  connecting points on the constant-energy contour with extremal curvatures, according to [49]. Coming back to Fig. 4.1.15, the outer contour in Fig. 4.1.15b stems from backscattering with vectors  $\mathbf{q}_1$ ,  $\mathbf{q}_4$  (there is also a contribution of the vector  $\mathbf{q}_6$  which is parallel to  $\mathbf{q}_4$ ), since all these vectors are the longest scattering vectors in this geometry. The middle contour in Fig. 4.1.15b corresponds to the scattering between two neighbouring sides of the warped hexagon and has maximal intensities at the vectors  $\mathbf{q}_2$  and  $\mathbf{q}_5$  (both are in the  $\Gamma$ -M direction). The vectors  $\mathbf{q}_3$  and  $\mathbf{q}_6$  contribute to the JDOS pattern as well (both are in the  $\Gamma$ -K direction), and their weight can be enhanced by making the DOS distribution on the constant-energy contour more abrupt than in Fig. 4.1.15a. In the spin-dependent scattering probability pattern plotted in Fig. 4.1.15c, as mentioned above, the outer structure related to the backscattering ( $\mathbf{q}_1$  and  $\mathbf{q}_4$ ) is suppressed due to the spin-momentum locking. In addition, the vector  $\mathbf{q}_3$  becomes almost invisible due to the three-fold symmetric scattering potential and the out-of-plane spin texture. Thus, only  $\mathbf{q}_2$  and  $\mathbf{q}_5$  scattering vectors are dominant in the spin-dependent scattering probability pattern.

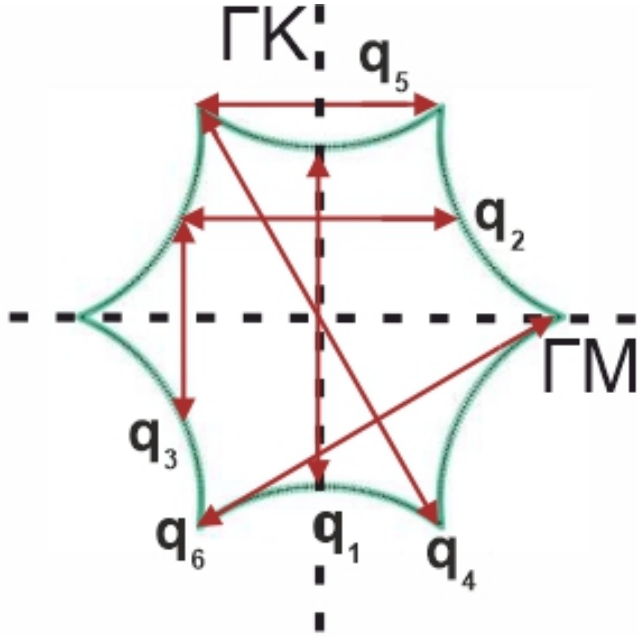


**Fig. 4.1.16** Scattering geometry for the hexagonally warped surface state constant-energy contour in  $\text{Bi}_2\text{Te}_3$ . The main scattering vectors  $\mathbf{q}_1$ – $\mathbf{q}_6$  connect points of the extremal curvature on the constant-energy contour.

In order to implement spin-dependent scattering probability calculations, one should note that the DOS distribution on the constant-energy contours could not

be unambiguously derived from the ARPES data in [8, 53] (see also Fig. 4.1.17 for surface states). For this reason, the DOS variation on each of the constant-energy contours was qualitatively modeled with a Gaussian distribution, considering the DOS distribution experimentally determined by ARPES. Thereby, the width of the gaussians was chosen as to obtain reasonable simulation results. For more details see Appendix A and one example of the program code with a brief description in Appendix C.

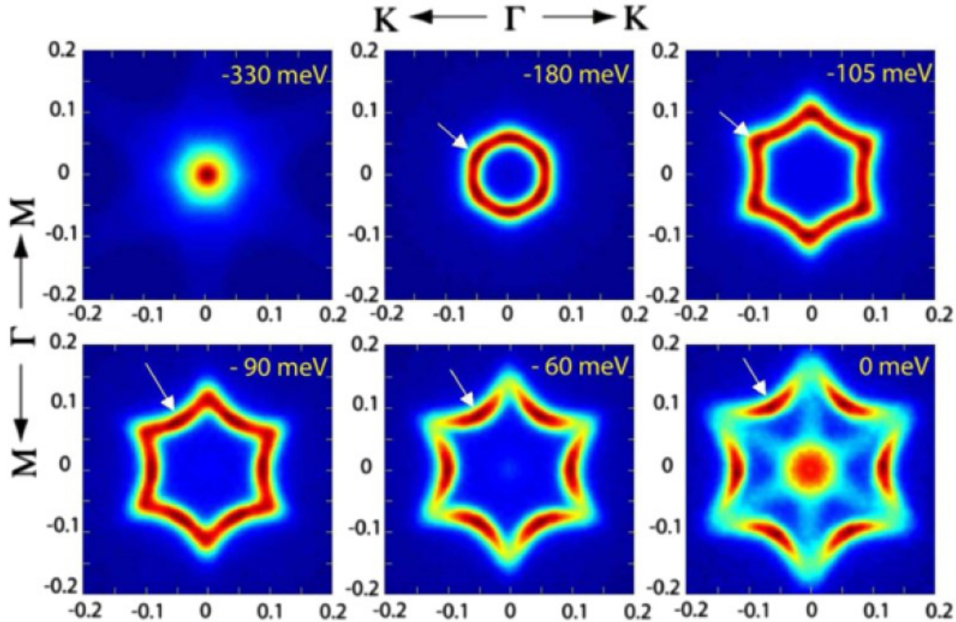


**Fig. 4.1.17** Constant-energy contours of the surface state band in  $\text{Bi}_2\text{Te}_3$  measured by ARPES. Strength of DOS increases from blue (no DOS) to dark red (strong contribution to DOS). Both horizontal and vertical axes are in units of  $1/\text{\AA}$ , the edge of the hexagonal Brillouin zone in the  $\Gamma$ -M direction is at  $\sim 0.8 1/\text{\AA}$ . White arrows point to the position of maximum in DOS (note six-fold symmetry). Adapted from [53].

Since the electronic band structure of  $\text{Bi}_2\text{Te}_3$  is known at large [8, 52, 55], the aim of the present work is to interpret the QPI data based on that and find some additional details in the band structure of the measured samples. As shown in Fig. 4.1.18, the comparison of the experimental data with the spin-dependent scattering probability calculations begins with the case when there is only surface constant-energy contour (in the bulk energy gap range) which is distorted due to the strong hexagonal warping. According to the ARPES data, the maximal DOS is on the warped hexagon, in the  $\Gamma$ -K direction [8, 53]. This leads to the six-fold symmetric spin-dependent scattering probability pattern in Fig. 4.1.18b, where the outer structure arising from backscattering (marked as  $\mathbf{q}_1, \mathbf{q}_4$ ) is strongly weakened. The arc-shaped six-fold symmetric intensity spots in the  $\Gamma$ -M direction in Fig. 4.1.18b are in a reasonable agreement with the QPI data measured at  $U_{bias} = [-70; 100]$  mV shown in Fig. 4.1.18c, thus, they are related to  $\mathbf{q}_5$  or  $\mathbf{q}_2$  scattering processes forming the  $\mathbf{q}_{ss}$

mentioned above. However, it is difficult to disentangle which of those vectors ( $\mathbf{q}_5$  or  $\mathbf{q}_2$ ) dominates. On the one hand, according to [42, 180], the scattering matrix element for  $\mathbf{q}_5$  is three times larger than that for  $\mathbf{q}_2$ , which is favorable for  $\mathbf{q}_5$  to be the dominant scattering vector. On the other hand,  $\mathbf{q}_2$  connects points with the maximal DOS, and, in addition, the out-of-plane spin component enhances the weight of  $\mathbf{q}_2$  with respect to  $\mathbf{q}_5$  [46]. For these reasons, the observed six-fold symmetric pattern can not be unambiguously associated with one of the two vectors  $\mathbf{q}_5$  or  $\mathbf{q}_2$ , but rather with their combination dubbed  $\mathbf{q}_{ss}$ . It is important to note that the QPI simulation result exhibits a flower-like shaped pattern in the  $\Gamma$ -M direction at scattering vectors shorter than  $\mathbf{q}_5$  (see Fig. 4.1.18b and Figs. 4.1.15b,c). The origin of this pattern comes from scattering within a single arc on the hexagonally warped constant-energy contour, thus, it cannot be totally suppressed. However, by calculating the spin-dependent scattering probability with optimized resolution in the  $\mathbf{q}$ -space, leading to the intensity suppression at its lobes and intensity enhancement at its center, the flower-like pattern can become consistent with the experimental data presented in Fig. 4.1.18c.

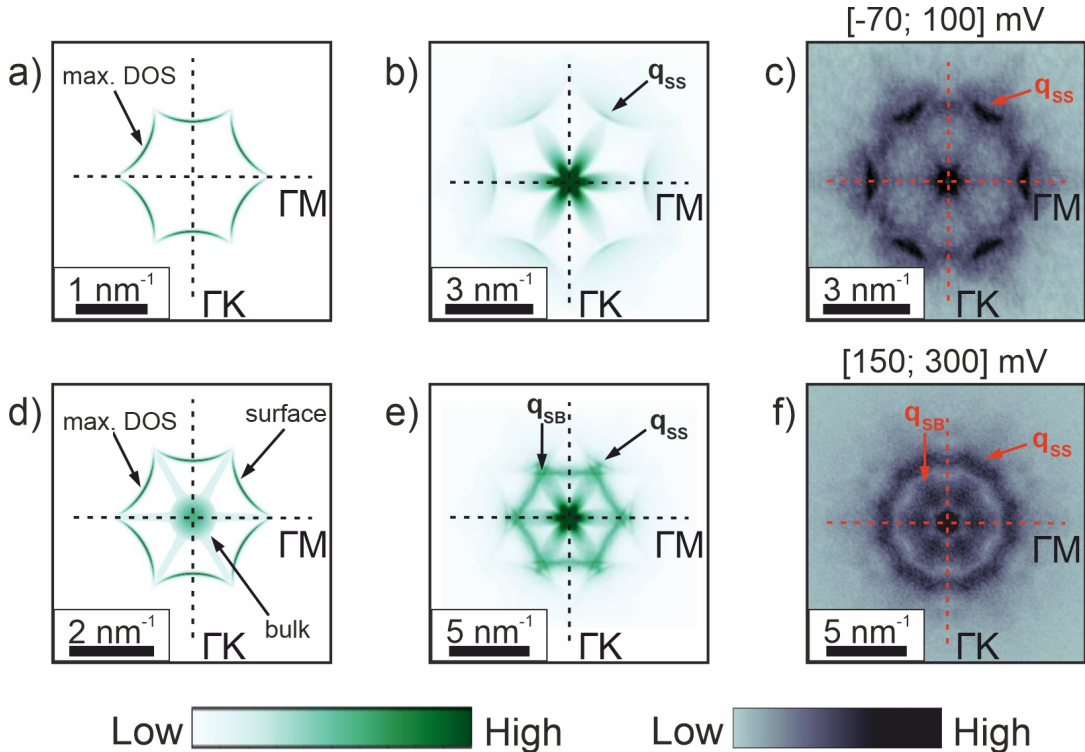


**Fig. 4.1.18** a), d) Constant-energy contours considered for different energy ranges according to the ARPES data [8, 53]. b), e) Spin-dependent scattering probability calculations corresponding to the constant-energy contours in a), d), respectively. c), f) QPI patterns measured in the current work with the energy ranges indicated on top of each figure. The high-symmetry directions and the scalebars are marked for all the presented figures. The left and the right colorbars correspond to the data in the two columns on the left side and the right column, respectively.

At higher energies with respect to the Dirac point, from 150 meV to 300 meV, the experimental FT-QPI patterns cannot be interpreted by the surface state constant-energy contour alone (see more details in Appendix A). For this reason, the bulk conduction band was considered in the QPI simulation as a circular continuum centered at the  $\Gamma$ -point with the DOS smoothly decaying away from  $\Gamma$  and extending in the  $\Gamma$ -M direction (see Fig. 4.1.18d). In the experimental QPI data presented in Fig. 4.1.18f, the arc-shaped structures  $\mathbf{q}_{SS}$  appear slightly less well defined than those at lower energies in Fig. 4.1.18c. This is in a good agreement with the spin-dependent scattering probability calculations involving bulk states (see Fig. 4.1.18e). Apart from that, in the considered energy range the QPI shown in Fig. 4.1.18f exhibits an enhanced non-dispersive intensity in the  $\Gamma$ -M direction at scattering vectors even shorter than  $\mathbf{q}_{SS}$  (the inner ring-like structure). Therefore, the origin of these peaks can not be explained in terms of only surface state contributions to the constant-energy contour and comes from scattering involving bulk states. In particular, the inner ring-like structure  $\mathbf{q}_{SB}$  originates from the bulk-to-surface scattering in the bulk conduction band (see Appendix A for more details). This surface-bulk scattering scenario was previously proposed to interpret the experimental QPI data of  $\text{Bi}_2\text{Se}_3$  [181].

Unlike the linear energy dispersion of the Dirac surface states, the dispersion of the QPI features in the experimental data acquired in the present work deviates from the linear one below 50 mV and cannot be observed below  $-70$  mV (see Fig. 4.1.13). Due to the inconsistency between the linearly dispersing surface state bands and the experimentally observed lack of dispersion in the QPI data, bulk (in particular, helical so-called bulk-surface hybridized [52, 182, 183]) states can be involved in scattering processes for energies below  $-70$  mV, too. Within this scenario, the two observed non-dispersive scattering modes (above 100 mV and below  $-70$  mV) allow to roughly estimate the bulk energy gap range in the measured samples as  $[-70; 100] \pm 25$  mV, and the gap size is consistent with the literature data on  $\text{Bi}_2\text{Te}_3$  [8]).

As mentioned before, the QPI data measured in the current work at  $U_{bias} = [-320; -120]$  mV (see Fig. 4.1.9) exhibit double intensity peaks in the  $\Gamma$ -M direction at  $q \approx 0.16$  1/ $\text{\AA}$  and  $0.22$  1/ $\text{\AA}$ . In order to interpret this experimental finding, the surface constant-energy contour in the bulk valence band energy regime (so-called bulk-surface hybridized states) and the DOS distribution can be modeled according to the known surface band structure of  $\text{Bi}_2\text{Te}_3$  [8, 52, 53, 55] (see Fig. 4.1.19a). Apart from the non-warped Dirac cone, the constant-energy contour consists of six-fold symmetrical pockets of elliptical shape extending in the  $\Gamma$ -M direction and representing the bulk-surface hybridized states. The maximal DOS is set in the  $\Gamma$ -M direction for all the parts of the constant-energy contour, and the

spin texture is modeled according to [34]. The calculation of the spin-dependent scattering probability results in two scattering peaks in the  $\Gamma$ -M direction consistent with the experimental data acquired in the present work in the corresponding energy range. Fig. 4.1.19b illustrates the corresponding spin-dependent scattering probability pattern with two six-fold symmetric structures in the  $\Gamma$ -M direction, resembling the experimental QPI patterns shown in Fig. 4.1.19c. However, there is a strong difference in the shape of the abovementioned six-fold symmetric structures (see Figs. 4.1.19b and 4.1.19c), and, in the model, they exhibit an energy dispersion, in contrast to the experimental data measured in this work. Therefore, either a different dispersion of the bulk-surface hybridized states as described in Ref. 52 or another, unknown, mechanism behind the non-dispersive modes should be considered<sup>1</sup>.

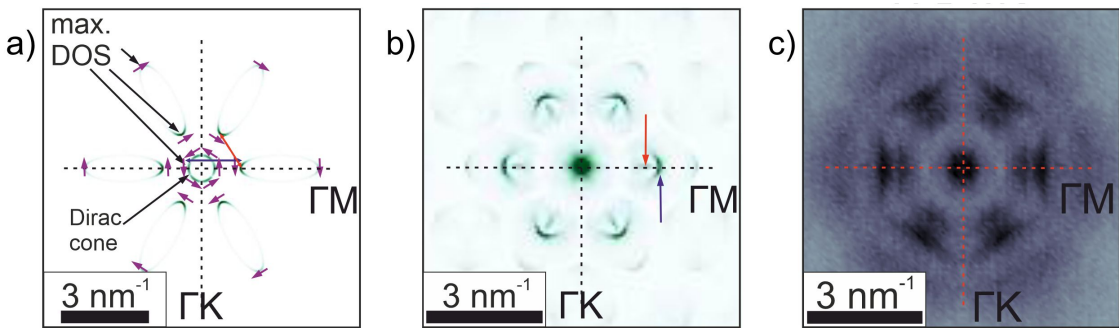


**Fig. 4.1.19** a) Constant-energy contour for the Dirac surface state shown as the circle and the surface state band merging with the bulk valence band as six-fold symmetric elliptically shaped pockets. All the states are spin-polarized, the spin texture is represented by magenta arrows. Maximal DOS is set in the  $\Gamma$ -M direction for all the parts of the constant-energy contour. Two dominant scattering vectors are indicated by red and blue arrows. b) Spin-dependent scattering probability pattern for the constant-energy contour plotted in a). Two scattering peaks coming from scattering processes shown in a) are denoted by red and blue arrows. c) Exemplary FT-QPI pattern exhibiting the double structure measured at  $U_{bias} = -170$  mV.

At yet lower energies, in particular, at  $U_{bias} = -370$  mV, the splitting of the scattering vector vanishes, and a single scattering vector is detected in the  $\Gamma$ -M direction (see Fig. 4.1.11d). In the scenario presented for  $U_{bias} = [-320; -120]$  mV which involves the bulk-surface hybridized states, this indicates an accidental match of the length of the involved scattering vectors.

Finally, the very faint FT-QPI patterns observed at  $U_{bias} = [-600; -420]$  mV exhibiting a star-like shape in the  $\Gamma$ -M direction can be interpreted by scattering

<sup>1</sup>A double QPI structure in the  $\Gamma$ -M direction at different energies has also been recently reported in Ref. 55. It was observed there at a completely different energy range, where a significant warping of the Dirac constant-energy contour is known, and the splitting naturally results from that warping. Note that in the energy range considered in the present work, there is practically no warping, according to ARPES [8,53]. Thus, the splitting observed in the current work must be of different origin.

within the bulk valence band at the energies significantly below the Dirac point.

To further prove the absence of backscattering in the presented experimental QPI data one has to note that backscattering would imply that there should be at least 2 structures in the FT-QPI pattern related to backscattering itself and the scattering with smaller vectors inside the constant-energy contour at all the energies. However, the STM data in this work reveal only one dominant scattering vector at most of the energies. Furthermore, as Fig. 4.1.20 illustrates, the energy dispersion obtained from the QPI can be plotted with the ARPES extracted dispersions from [8] for all possible scattering processes in the  $\Gamma$ -M direction which are  $\mathbf{q}_2$ ,  $\mathbf{q}_4$ ,  $\mathbf{q}_5$  in the notation of Fig. 4.1.16. The energy scale is set to start from the Dirac point for both QPI and ARPES data. In particular,  $\mathbf{q}_4$ , which is the backscattering vector, has values significantly larger than that measured by STM, so it is not expected to appear in the QPI data. At the same time, the one can not unambiguously claim which of the QPI scattering vectors  $\mathbf{q}_2$  or  $\mathbf{q}_5$  dominates as was mentioned above as well.

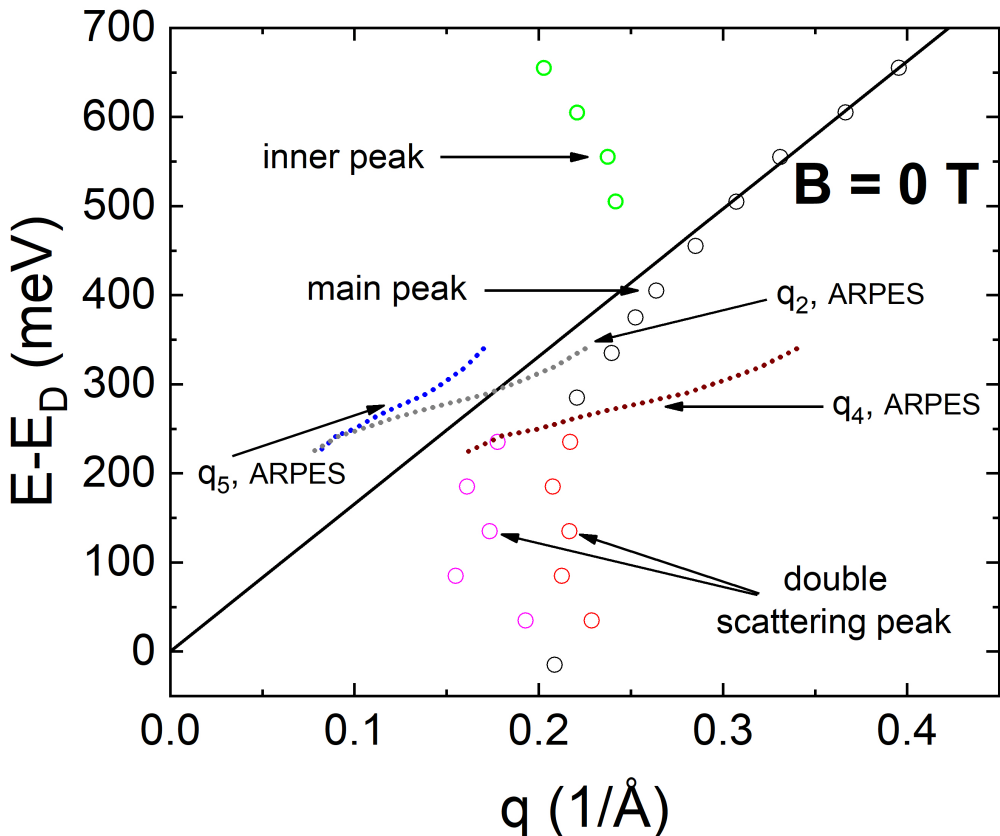


**Fig. 4.1.20** a) QPI and ARPES energy dispersion for  $\Gamma$ -M direction. The energies are counted from the Dirac point for both datasets.

It is also important to note that, according to the ARPES data [8,53] for  $\text{Bi}_2\text{Te}_3$ ,

when the constant-energy contour is evolving from the circle to the warped hexagon, it shows a hexagonal shape at some energy as illustrated in Fig. 4.1.21a. However, the spin-dependent scattering probability calculated for this constant-energy contour gives the pattern plotted in Fig. 4.1.21b which looks totally different from any FT-QPI patterns observed in the present work. Therefore, given that the  $dI/dU$  maps were measured with 50 mV step, it is very likely, that the FT-QPI pattern corresponding to the hexagonal shape of the constant-energy contour was missed in the experiment and was not detected.

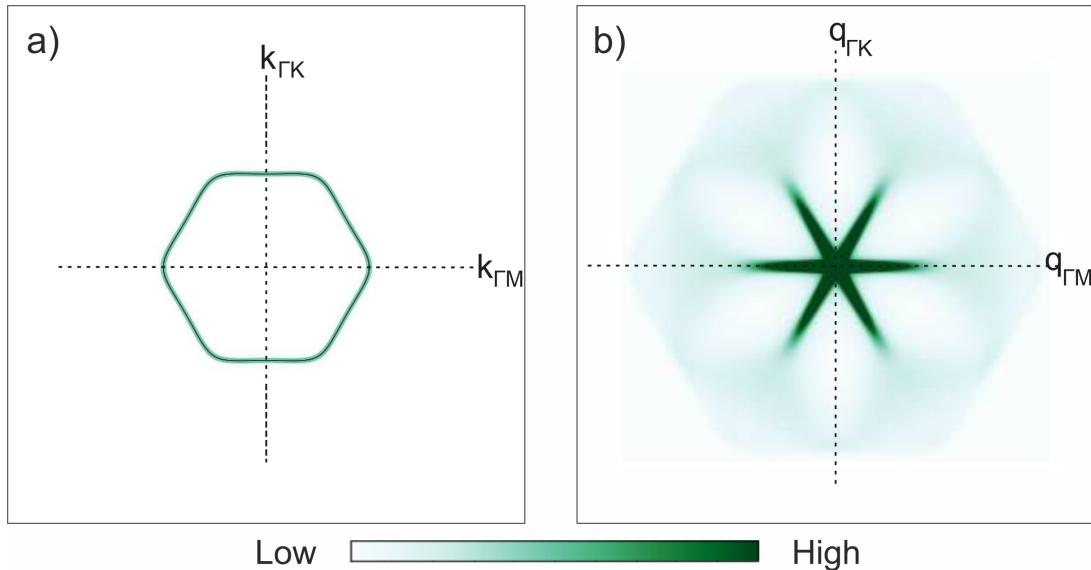


**Fig. 4.1.21** a) Constant-energy contour in the shape of the hexagon. b) Spin-dependent scattering probability calculation for the constant-energy contour shown in a).

Comparing the energy scales from the QPI data acquired in the present work with the former QPI and ARPES studies in  $\text{Bi}_2\text{Te}_3$  [8, 50, 52, 53, 55–57], it is clear that there is a significant difference in the bulk energy gap location with respect to the Dirac point which are separated by around 250 meV (counting distance between the Dirac point and the top of the bulk valence band) in the current work unlike 100–200 meV in the literature. The reason for this discrepancy is unknown. This might be caused by the material disorder which may result in a modification of the electronic band structure of the compound. Note that the altered Dirac cone dispersion with respect to the bulk states naturally implies different bulk-surface hybridized states as commonly considered [52] (see discussion of the non-dispersive double QPI structure above).

#### 4.1.5. Magnetic field measurements

The next aim was to measure the  $dI/dU$  maps in a magnetic field provided by the magnet cryostat (the maximal possible field  $B = 15$  T) in order to compare the

QPI data measured in the zero field, which were discussed in sections 4.1.3 and 4.1.4, with the in-field QPI features caused by the presence of the magnetic field, which could break the time-reversal symmetry and the topological protection of the surface states. There are no differential conductance maps measured in a magnetic field in  $\text{Bi}_2\text{Te}_3$  available in the literature to date which encourages this kind of experiment. Additionally, the energy quantization of the Dirac surface electrons with possible occurrence of the Landau levels was explored by STS which could help with a more precise estimation of the Dirac point location.

The  $dI/dU$  maps in the magnetic field of 12 T were measured on the same 60 nm  $\times$  60 nm area at 9 bias voltages from 300 mV to  $-50$  mV keeping the tunneling resistance constant at each bias voltage and the same as in the zero-field measurements. The samples used for the in-field measurements were different from that where the zero-field data were obtained. Figs. 4.1.22a,c show the topography of the scanning area at  $U_{bias} = 150$  mV at  $B = 12$  T with its Fourier transform which look qualitatively the same as the data measured at 0 T (see section 4.1.3). The corresponding  $dI/dU$  map acquired at  $U_{bias} = 150$  mV is depicted in Fig. 4.1.22b. In general, the  $dI/dU$  maps measured in this experiment under the magnetic field (see all the real space data in Fig. 4.1.23) turned out to be of somewhat reduced quality compared to the zero-field  $dI/dU$  maps in section 4.1.3 which could be explained by not only different samples and tips but also by the lower momentum resolution (i.e. smaller scanning area size) as well as a stronger experimental noise in the in-field measurements. However, it is still possible to define the most pronounced features in the FFT patterns of the  $dI/dU$  maps as shown in Fig. 4.1.22d which represents a zoomed-in view of the hexagonally symmetrized FFT of the map in Fig. 4.1.22c following the same procedure for scattering vectors extraction as described in section 4.1.4. The Bragg peaks in Fig. 4.1.22c are clearly visible and, hence, allow to match the orientation of the QPI intensity peaks with the crystallographic directions. The six-fold symmetric scattering vector pointing in the same  $\Gamma$ -M direction with the scattering vectors in the zero-field maps exhibits a continuous decrease upon the bias voltage decreases. This scattering vector exists at all the data measured with the bias voltage varying from 300 mV to  $-50$  mV (only at 20 mV it is hardly visible) at  $B = 12$  T. It was previously observed in the zero-field data discussed in sections 4.1.3 and 4.1.4 and can be assigned to  $\mathbf{q}_{ss}$ , i.e. some combination of scattering vectors  $\mathbf{q}_2$  and  $\mathbf{q}_5$ .

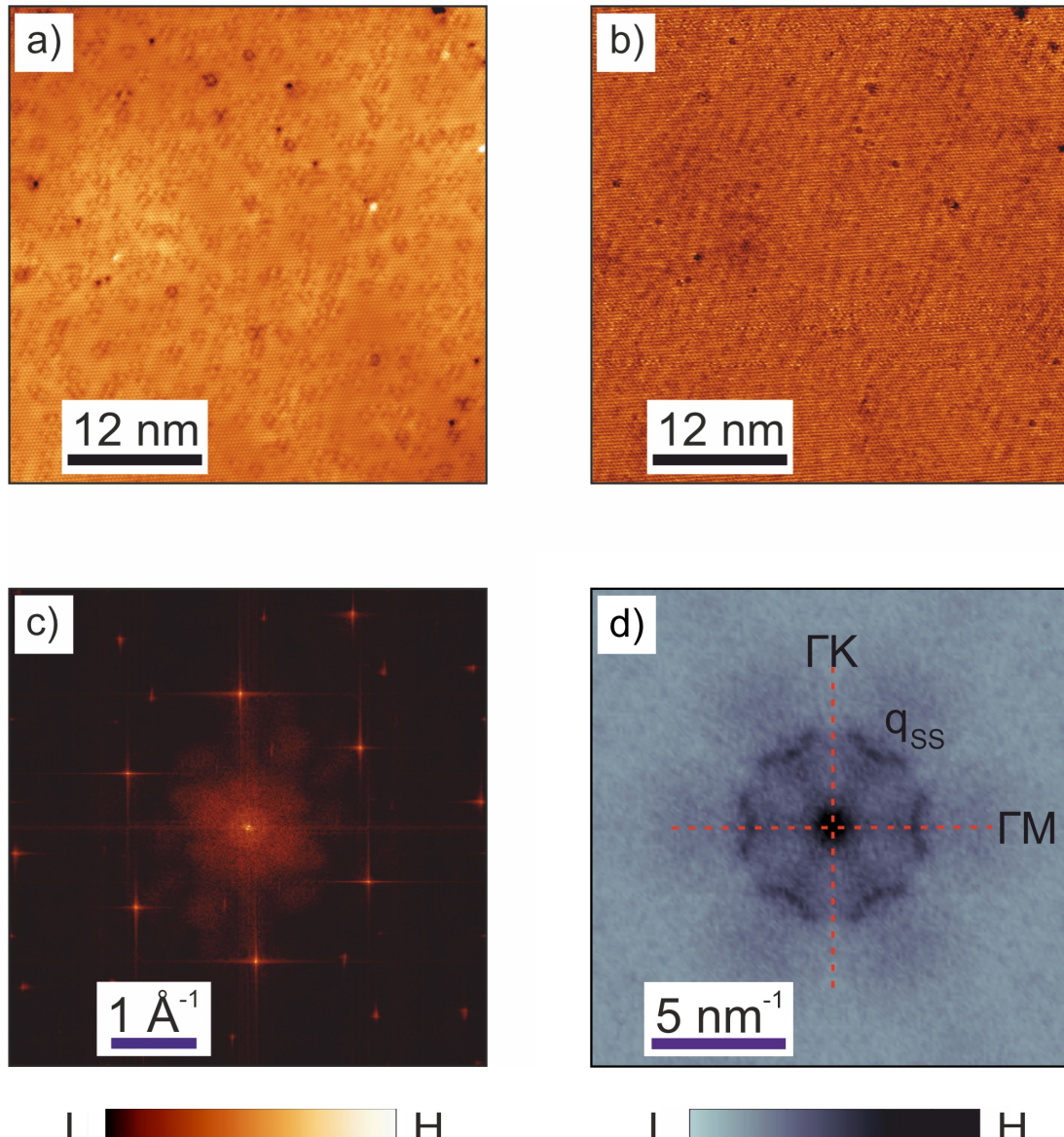


**Fig. 4.1.22** Example of the  $dI/dU$  map measured at  $U_{bias} = 150$  mV at  $B = 12$  T: a)  $60\text{ nm} \times 60\text{ nm}$  topography scan with its FFT in c); b)  $dI/dU$  map of the area shown in a) with its symmetrized and zoomed-in FT-QPI pattern in d). High-symmetry directions  $\Gamma$ -M and  $\Gamma$ -K are indicated by red dashed lines in d).

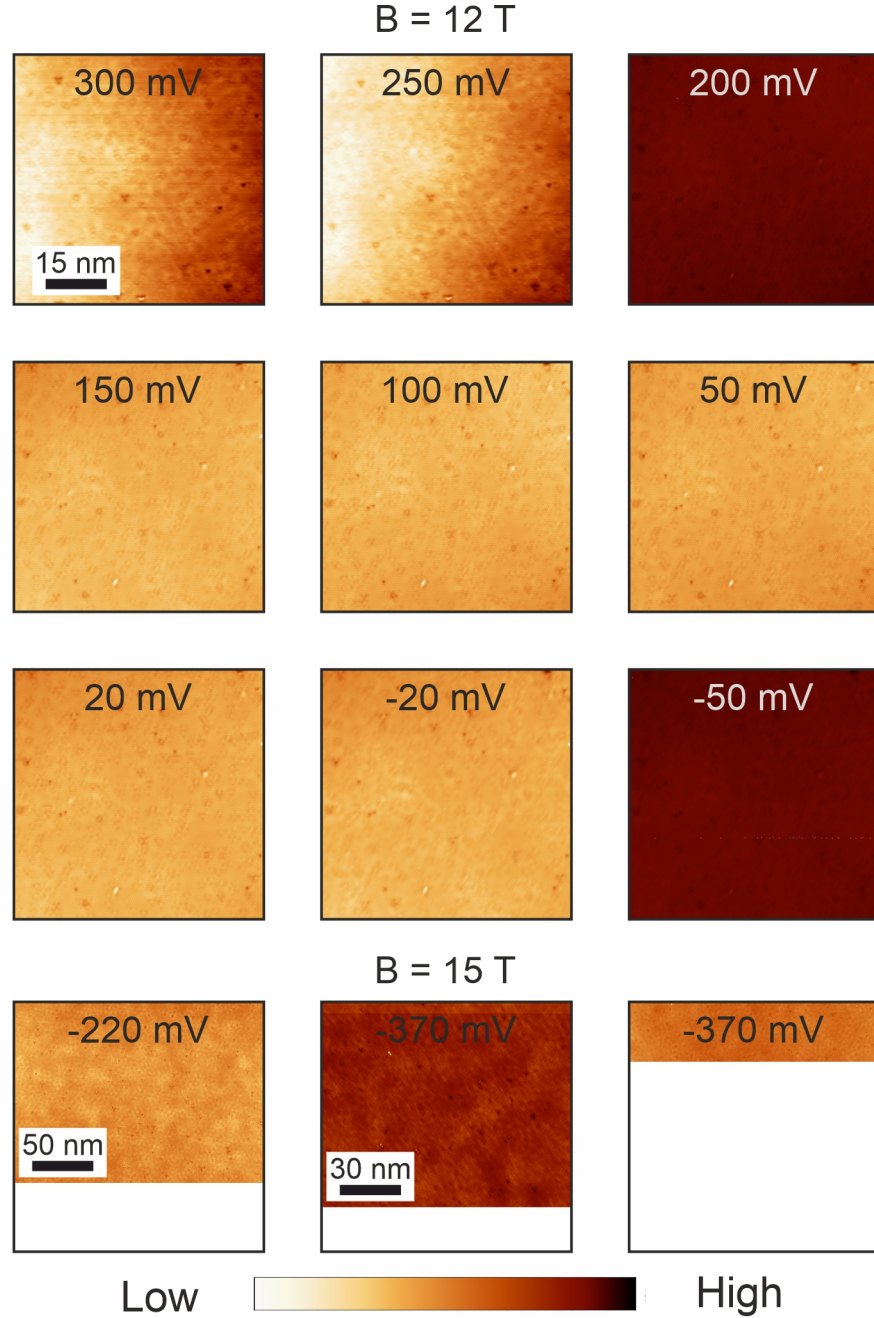


**Fig. 4.1.23** Series of the  $dI/dU$  maps measured at  $B = 12$  T and  $B = 15$  T at the energies from 300 mV to  $-50$  mV at  $B = 12$  T and at  $-220$  mV and  $-370$  mV at  $B = 15$  T. The scalebar is the same for each of the maps at  $B = 12$  T. The scalebar for the map measured at  $-370$  mV (shown in the right-bottom corner) is the same as that at  $-220$  mV.

All the FT-QPI patterns measured at  $B = 12$  T are presented in Fig. 4.1.24 in comparison with the corresponding data obtained at  $B = 0$  T. One can notice slight differences in the FT-QPI intensity distributions which could be caused by different tunneling junctions in the zero-field and the in-field experiments. Apart from the dominant scattering vector, another scattering channel in the magnetic field with a vector even shorter than  $\mathbf{q}_5$  in the  $\Gamma$ -M direction appears at  $U_{bias} = 300$  mV, 250 mV and 200 mV (see Fig. 4.1.24). This vector demonstrates a different but unclear

dispersion in comparison with that at  $B = 0$  T as shown in Fig. 4.1.24. It was already found in the zero-field data, where this scattering vector also extends down to 150 mV and is supposed to be associated with the bulk-surface scattering mode (see section 4.1.4). Again, as in the zero-field data at  $-50$  mV and  $-20$  mV, the QPI peaks are more distinct than those observed at higher energies implying the bulk energy gap, at least, at the bias voltages of  $-50$  mV,  $-20$  mV.

The linear fit of the energy dispersion of the dominant scattering vector (see Fig. 4.1.25) gives the estimation of the Dirac point situated at  $U_{bias} = (-384 \pm 37)$  mV with the Dirac velocity  $v_D = (4.5 \pm 0.3) \times 10^5$  m/s which are both consistent with the corresponding values at  $B = 0$  T being within the error of the measurements. No backscattering peaks were observed in the QPI data which may reinforce the assumption that even the external field of  $B = 12$  T was not sufficient to lift the topological protection of the surface state. Overall, no significant changes in the FT-QPI patterns at  $B = 12$  T with respect to that at  $B = 0$  T were found as can be seen in Fig. 4.1.24. Note that the Zeeman interaction at  $B = 15$  T is around 0.87 meV which is significantly weaker than the spin-orbit interaction in  $\text{Bi}_2\text{Te}_3$  (the SOC constant  $\lambda = 1.25$  eV for Bi and 0.49 eV for Te, respectively [6, 184]). Thus, only a very small effect  $\sim 0.001$  of the external field could be expected. Besides that, the Zeeman energy at  $B = 15$  T is even smaller than the energy resolution of the STM at  $T = (6-7)$  K which further complicates the search for signs of the influence of the external magnetic field on the STM experiment.

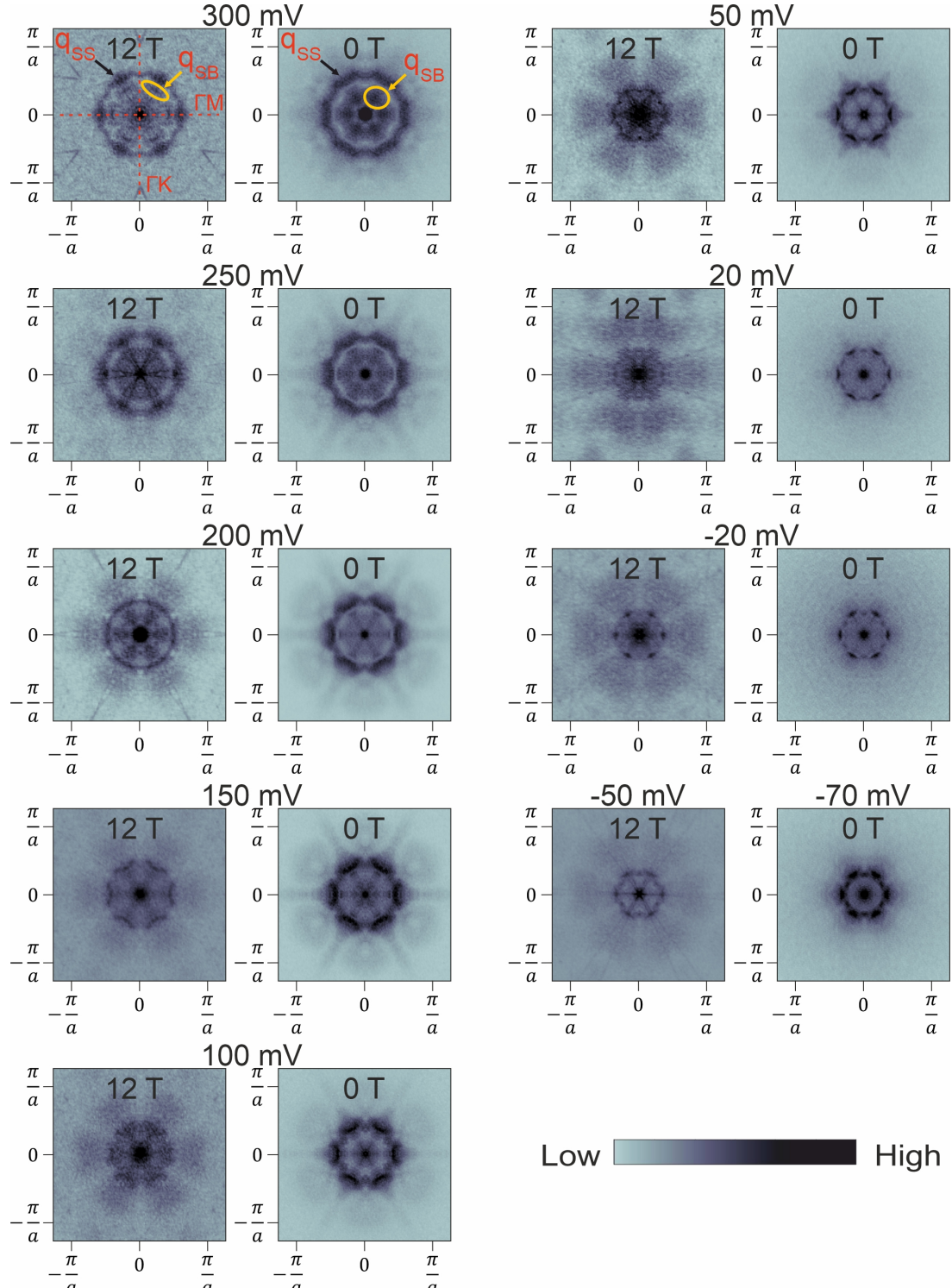


**Fig. 4.1.24** Series of the symmetrized FT-QPI patterns measured at the energies from 300 mV to  $-50$  mV at  $B = 12$  T and from 300 mV to  $-70$  mV at  $B = 0$  T. The outer intensity spots correspond to the vector  $\mathbf{q}_{SS}$  for each of the patterns. The inner intensity spot ( $\mathbf{q}_{SB}$ ) is visible only at 300 mV, 250 mV and 200 mV which is indicated by the yellow ellipse. High-symmetry directions and the colorbar are the same for each of the patterns. The lattice constant value  $a = 4.7$  Å as mentioned in section 4.1.1.

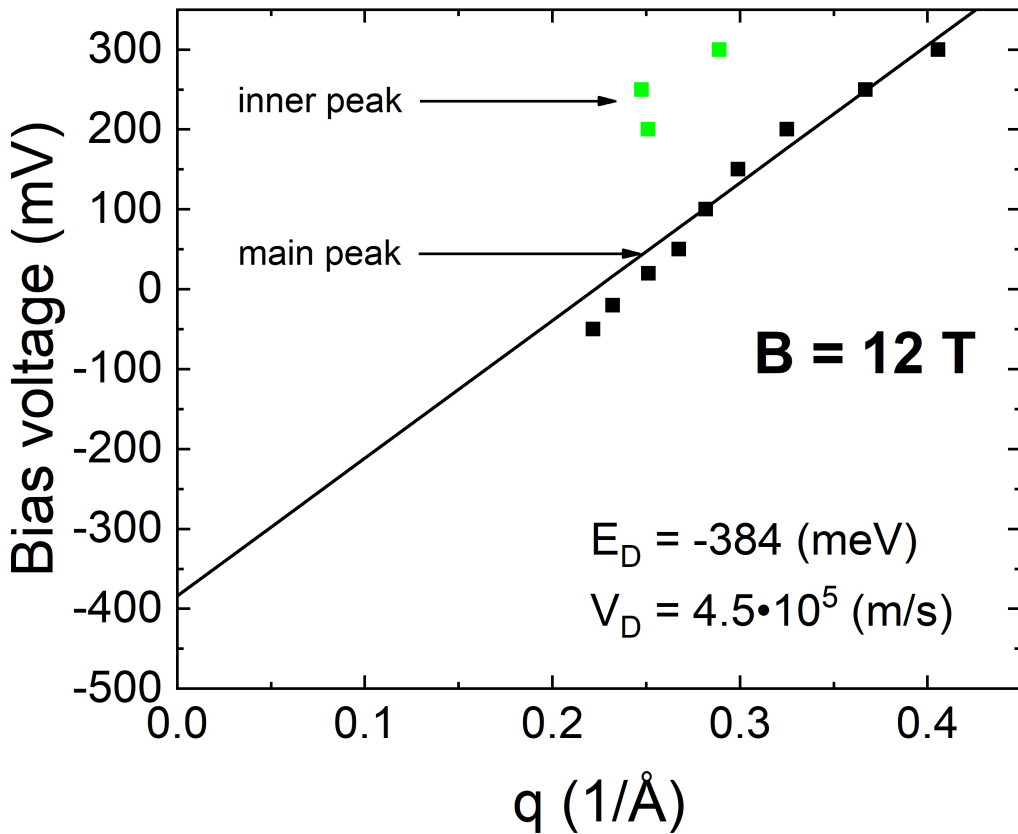


**Fig. 4.1.25** QPI energy dispersion measured at  $B = 12$  T.

The  $dI/dU$  maps were also measured at the maximal achievable field of 15 T at the bias voltages of  $-220$  mV and  $-370$  mV. The corresponding FT-QPI patterns are presented in Fig. 4.1.26 with the data measured at  $B = 0$  T at respective energies. However, even with a better momentum resolution provided by  $200$  nm  $\times$   $200$  nm surface areas which were different in each of the presented data on the same sample, no substantial differences with respect to the zero-field data at those energies were found. In particular, the symmetrized FT-QPI patterns obtained at  $U_{bias} = -220$  mV and  $U_{bias} = -370$  mV (see Fig. 4.1.26) demonstrate six-fold symmetric peaks that split into doublets and single (not splitted) peaks, respectively, in agreement with the corresponding zero-field data. The only difference is that an inner structure appears in the 15 T FT-QPI pattern (see Fig. 4.1.26) which could be related to the bulk scattering processes in the valence band. However, this is not a unique FT-QPI pattern at  $U_{bias} = -370$  mV since it was found to be totally different in the other measurement at  $B = 15$  T (see Fig. 4.1.26), where, in particular, the QPI peaks become splitted into doublets with no visible other scattering channels. This ambiguous appearance of the FT-QPI patterns at  $-370$  mV which were measured on the same surface but at different locations might indicate possible spatial variations

of the Dirac point energy. One can also not rule out that the more noisy FT-QPI pattern at this energy, where only one scattering vector was found, smears out two scattering vectors making them appear as a single vector. Nevertheless, there is not enough data measured at  $B = 15$  T for making strict conclusions. The energy dispersion  $E(q)$  obtained at  $B = 15$  T is presented in Fig. 4.1.27 and is also shown in Fig. 4.1.28 along with the QPI dispersion measured at  $B = 12$  T and  $B = 0$  T.

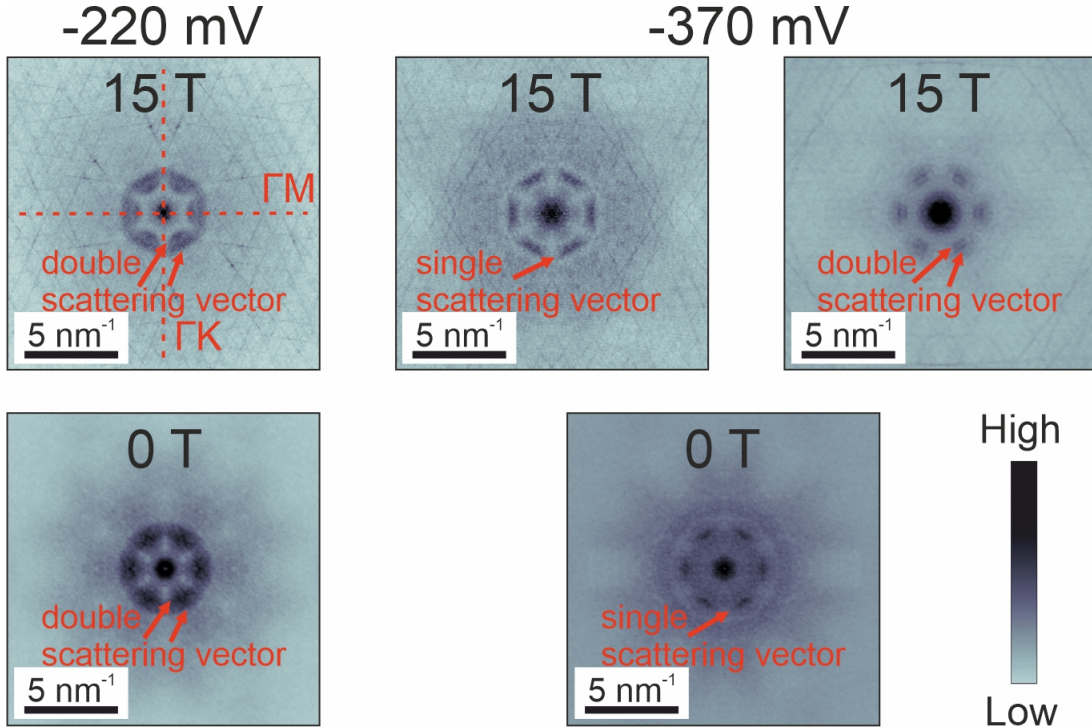


**Fig. 4.1.26** Symmetrized FT-QPI patterns measured at  $U_{bias} = -220$  mV and  $U_{bias} = -370$  mV at  $B = 15$  T in comparison with the data measured at  $B = 0$  T at the same energies. Two different FT-QPI patterns at  $U_{bias} = -370$  mV at  $B = 15$  T were measured on the same cleavage but at different surface areas. The colorbar is the same for each of the patterns.

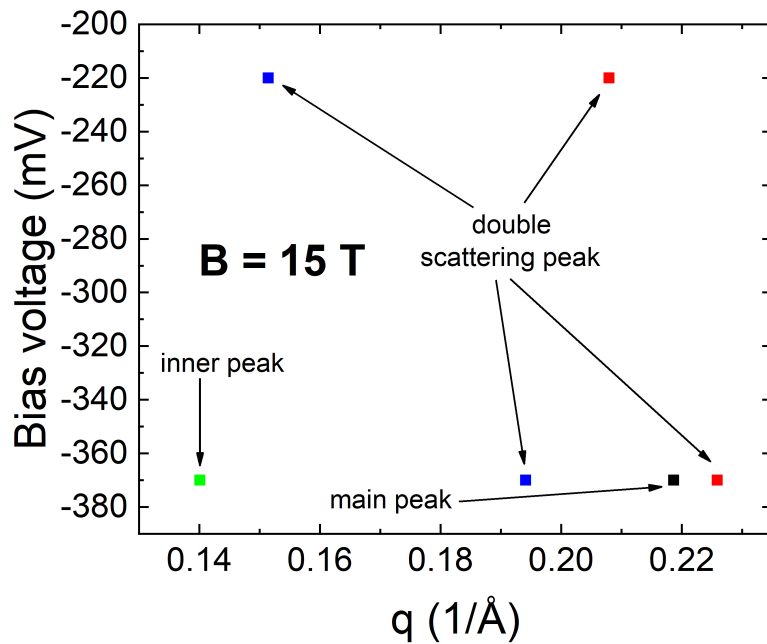


Fig. 4.1.27 QPI energy dispersion measured at  $B = 15$  T.

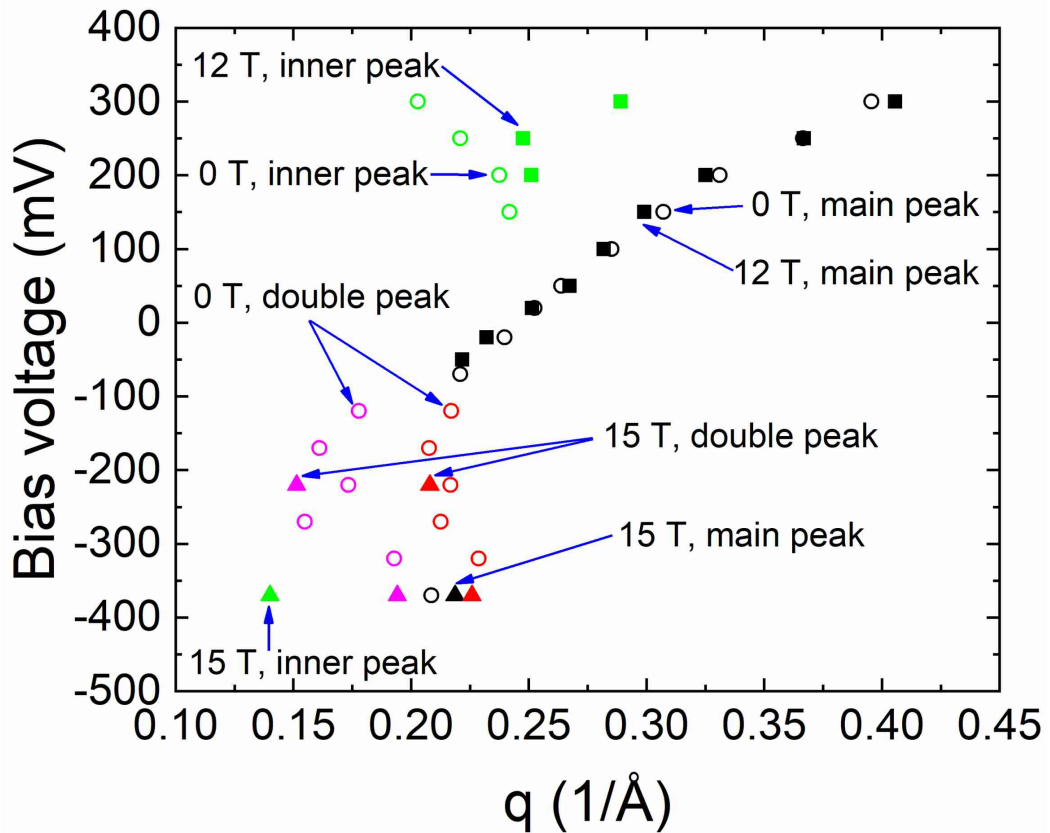


Fig. 4.1.28 QPI energy dispersion measured at  $B = 0$  T, 12 T and 15 T.

Apart from that, since the investigated surface of  $\text{Bi}_2\text{Te}_3$  manifests itself as a two-dimensional electron system which in the presence of a perpendicular magnetic field

experiences the quantization of the energy spectrum with the occurrence of Landau levels which allow to determine the Dirac point energy, the tunneling spectra of  $\text{Bi}_2\text{Te}_3$  were also measured in the field  $B = 15$  T. The quantized energy spectrum of the massless Dirac fermions can be derived from both the semiclassical approach and the relativistic Dirac equation resulting in the following expression [185]:

$$E_n = E_D + \text{sgn}(n)v_D\sqrt{2e\hbar|n|B}, \quad (4.1.4)$$

where  $E_n$  is the energy of the  $n^{\text{th}}$  Landau level ( $n = 0, \pm 1, \pm 2, \dots$ ),  $\hbar$  is the Plank constant and  $e$  is the elementary charge. Therefore, unlike the Landau levels in a parabolic dispersion two-dimensional electron system, the levels are not equidistant with  $E_n \propto \sqrt{|n|B}$ . Besides, the Landau level with  $n = 0$  ( $E_0 = E_D$ ) is independent on the magnetic field  $B$  as shown in Fig. 4.1.29, thus, it could be used for a more precise than the QPI energy dispersion estimation of  $E_D$ . The Landau levels were successfully measured by means of STS on various two-dimensional electron systems [186–192], including the topological insulators as  $\text{Bi}_2\text{Se}_3$ ,  $\text{Sb}_2\text{Te}_3$  [179, 193, 194] and only on a structurally deformed surface of  $\text{Bi}_2\text{Te}_3$  [57]. The latter one further motivates the search of the Landau levels on the atomically flat surface of  $\text{Bi}_2\text{Te}_3$  in the present work.

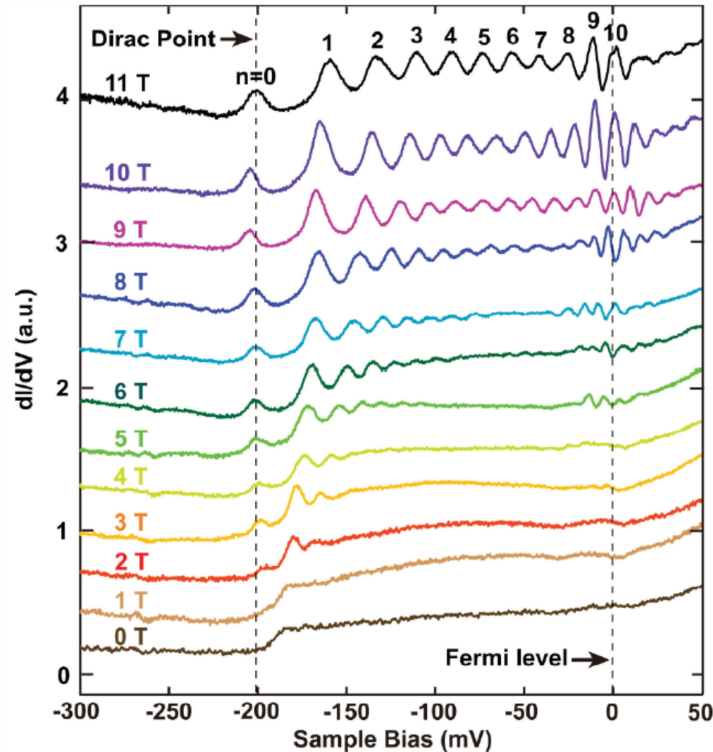


**Fig. 4.1.29** Landau quantization of the topological surface states obtained by STS in  $\text{Bi}_2\text{Se}_3$ . Adapted from [179].

However, as it is clearly seen from the representative  $dI/dU$  spectrum measured

at  $B = 15$  T with 1.2 mV step in Fig. 4.1.30, no signatures of the Landau levels which are expected to appear as LDOS oscillations at the energies indicated with dashed lines were found. The presented spectrum was measured at the energies both below and above  $E_D$ . Its value along with the Dirac velocity were taken from the linear fit of the energy dispersion of the QPI peaks at  $B = 12$  T (see Fig. 4.1.25). The calculated distances between the neighbouring  $n = 0$  and  $n = 1$ ,  $n = 1$  and  $n = 2$  Landau levels at  $B = 15$  T are around 61 meV and 25 meV, respectively, which further decrease with increasing  $n$  as illustrated in Fig. 4.1.30. Given that there is no exact shape of the background, since no spectra at  $B = 0$  T were measured with the same tip on the same surface, no anomalies found in the in-field spectra point towards the conclusion that the Landau levels peaks in the in-field spectra could not be resolved. The most plausible reason of the absence of the Landau levels in the STS is the intrinsic material disorder mentioned in section 4.1.1 which leads to broadening of the Landau levels and, less likely, bulk contribution to the spectra and the experimental rather low signal-to-noise ratio. The former is also supported by the Landau levels suppression in  $\text{Bi}_2\text{Se}_3$  [179] where it occurred at magnetic lengths comparable with the average distance between the defects. Indeed, the magnetic length even at the highest possible field  $B = 15$  T  $l_B = \sqrt{\frac{\hbar}{eB}} \approx 6.6$  nm exceeds the average distance between the observed dominant defects in  $\text{Bi}_2\text{Te}_3$  which is in the range of 2–4 nm as found from the topography data (see section 4.1.1).

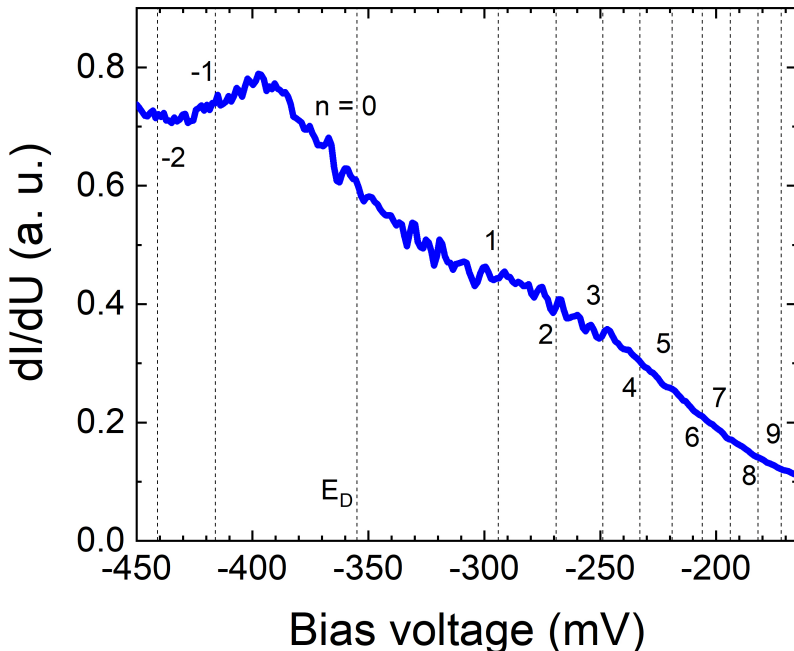


**Fig. 4.1.30** The measured tunneling spectrum at  $B = 15$  T,  $U_{bias} = -450$  mV,  $I_T = 1.5$  nA with the marked positions of the expected Landau levels. The numbers are the Landau levels numbers  $n$ .

#### 4.1.6. Conclusions

Topography measurements on  $\text{Bi}_2\text{Te}_3$  single crystals demonstrate atomically corrugated Te-terminated surface with the presence of numerous defects of different origin generally consistent with the literature data. The XPS data on the used samples reveals no extrinsic doping and no deviation from the stoichiometry but the indication of possible material disorder in comparison to former studies performed on this compound by other groups. The QPI data were taken in a wide energy range  $[-600; 300]$  mV and provide different kinds of the interference patterns which were interpreted based on the spin-dependent scattering probability and JDOS calculations (for both surface and bulk states) according to the scattering geometry for each of the considered energy ranges. The linear energy-momentum dispersion and the absence of the backscattering were clearly demonstrated proving the helical spin texture of the material. The QPI data allowed to roughly compare the electronic band structure of the material with its known band structure based on the experimental and simulated QPI data. In particular, the observed non-dispersive scattering was detected and associated with the bulk-involved scattering from which the bulk energy gap range was identified, and its value is consistent with the known value. The QPI data are not only reliable and reproducible but are of even better quality than the existing QPI data on  $\text{Bi}_2\text{Te}_3$  as evidenced by rather sharp structures in the FT-QPI patterns even in the presence of the chemical disorder in the material. QPI data were measured, probably, for the first time in the magnetic field in  $\text{Bi}_2\text{Te}_3$ . However, their comparison with the zero-field QPI data shows no substantial differences in the FT-QPI patterns with the scattering vectors amplitudes showing very similar linear energy dispersion. No backscattering peaks were found in the FT-QPI patterns in the magnetic field data, thus, the topological protection of the surface state survives even at  $B = 12$  T due to the strong spin-orbit coupling in  $\text{Bi}_2\text{Te}_3$ . The chemical disorder of the material impedes the observation of the Landau levels as demonstrated by the STS data measured at the maximal field  $B = 15$  T.

## 4.2. $\text{MnBi}_2\text{Te}_4$

All the STM/STS measurements on  $\text{Mn}_2\text{Bi}_2\text{Te}_4$  single crystals presented in this section were performed at the base temperature of 5 K with the RHK R9 and Nanonis Specs STM-controllers.

### 4.2.1. Topography

The topography data shown in Fig. 4.2.1a reveal the typical Te-terminated (since the topmost layer in the crystal structure of  $\text{MnBi}_2\text{Te}_4$  consists of Te-atoms) surface of 50 nm squared size. Its FFT (see Fig. 4.2.1b) exhibits not only six-fold symmetric Bragg spots corresponding to the hexagonal crystal lattice (providing the lattice constant  $a \approx 4.3 \pm 0.2 \text{ \AA}$  which is consistent with the literature value of 4.33  $\text{\AA}$ ) but other ordered structures inside which can be better understood from the zoom-in area of Fig. 4.2.1a (see Fig. 4.2.1c). In particular, the atomic corrugation is superimposed by an electronic modulation which manifests itself as a weakly ordered hexagonal structure (superstructure 1, further in the text) in the FFT with rather broad and blurred spots oriented along the Bragg peaks. The superstructure 1 in the FFT appears at all the bias voltages from  $-500 \text{ mV}$  to  $500 \text{ mV}$  used in the experiment (see Fig. 4.2.2) and has a period of approximately double lattice constant in the real space as can be seen from the topography image in Fig. 4.2.1c where there are some bright spots separated by around 8  $\text{\AA}$  on top of the atomic corrugation. This unusual modulated atomic corrugation is demonstrated on the representative topographic line profile (see Fig. 4.2.1d) and is larger than that for a pure atomic corrugation as in the parent compound  $\text{Bi}_2\text{Te}_3$  in Fig. 4.1.1, for example. The peaks with the average period of  $\sim 4.3 \text{ \AA}$  are distinguished on the right side of Fig. 4.2.1d and, thus, correspond to the atomic corrugation, while on the left their period is around 8  $\text{\AA}$ , nearly the same as found for the superstructure 1 from the FFT. At the same time, in most of the plotted FFT patterns in Fig. 4.2.2 one can also find spots of slightly lower intensity in the  $\Gamma$ -K direction compared to the spots in the  $\Gamma$ -M direction which is collinear with the Bragg peaks. The observed electronic modulations could be caused by possible strain in the lattice and might be also associated with a charge (spin) density wave which, however, has never been reported in the literature on this compound.

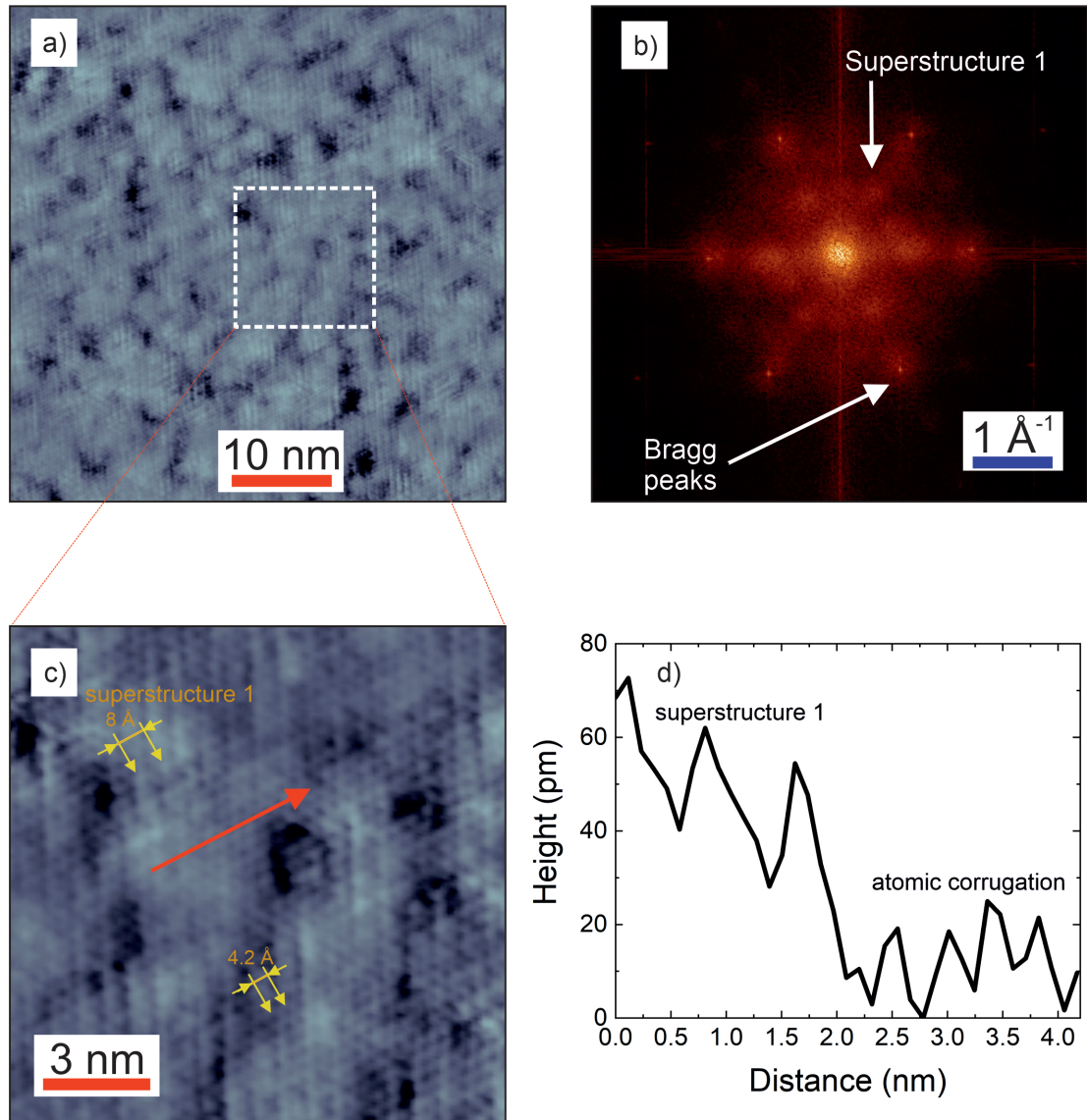


**Fig. 4.2.1** a) Topography at  $U_{bias} = -100$  mV,  $I_T = 100$  pA. b) FFT of the image in a). c) 14 nm x 14 nm zoom-in of the image a). d) Line profile marked with the red arrow in c), the yellow arrows indicate the characteristic period of the superstructure 1 and the lattice constant in real space. The superstructure 2 is not resolved in these data.

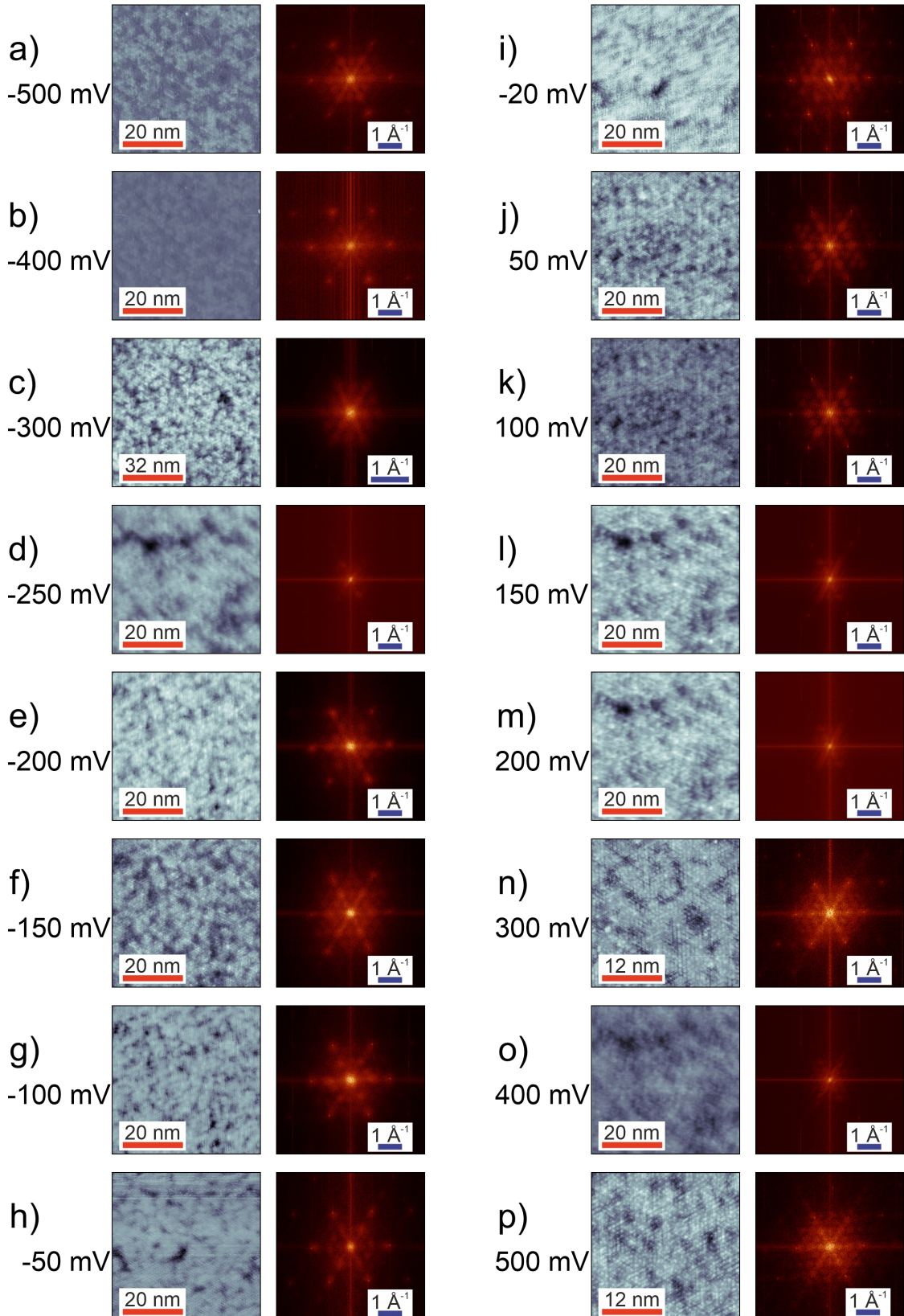


**Fig. 4.2.2** a)–o) Topography scans (on the left sides) at different bias voltages from  $-500$  mV to  $500$  mV with corresponding FFTs shown on the right sides. Images a), b), d)–m), o) were measured on  $50$  nm  $\times$   $50$  nm areas, while n) and p) correspond to  $30$  nm  $\times$   $30$  nm areas and c) was obtained on  $80$  nm  $\times$   $80$  nm surface spot. The superstructure 1 persists at each of the plotted images at nearly the same positions as inferred the FFTs. Note that the resolution of the images d), l), m), o) was not high enough to clearly resolve the superstructure 1.

Apart from that, another hexagonal structure (superstructure 2, further in the text) in the FFT of topography of the  $80 \text{ nm} \times 80 \text{ nm}$  field of view (i.e. better momentum resolution compared to Fig. 4.2.1) shown in Fig. 4.2.3 appeared with a larger period corresponding to the long-wavelength modulation which is less pronounced in Fig. 4.2.1b but it is better seen in the FFT of the  $dI/dU$  maps (see section 4.2.3). It is worth to note that the superstructure 2 can be also found in the FFTs of Figs. 4.2.2j,k. The superstructure 2 has a period of a few nanometers (could not be determined with higher precision) which, probably, arises from the distances between the electronic clouds (areas of bright or dark contrast) in topography.

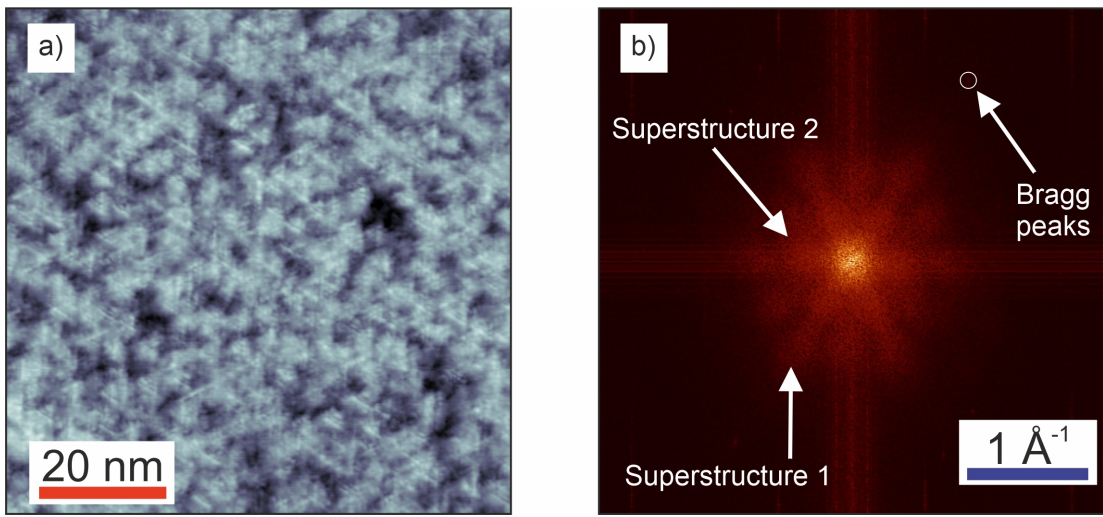


**Fig. 4.2.3** a) Topography at  $U_{bias} = -300 \text{ mV}$ ,  $I_T = 50 \text{ pA}$ . b) FFT of the image in a). Both superstructures 1 and 2 are indicated with white arrows and aligned in the same direction with the Bragg spots.

According to the recent STM studies of  $\text{MnBi}_2\text{Te}_4$  crystals [139–142], the topography of this material reveals several kinds of defects, in particular, dark triangular depressions and, more rarely, bright circular protrusions which were assigned to Mn/Bi antisites in the second Bi layer and Bi substitution of the topmost Te atoms, respectively, as, also, observed in the current work (see section 4.1.1) and in the literature on  $\text{Bi}_2\text{Te}_3$  [50, 51]. The representative topographies from [139–142] are depicted in Fig. 4.2.4. The Bi/Mn antisite defect was also identified in [141] which appears as bright spot in Fig. 4.2.4. However, according to [140, 142], all those defects are especially pronounced at bias voltages larger than 0.6 V for both polarities at which there is no data in the present work. On the other hand, at lower bias voltages within  $\pm 0.5 \text{ V}$  with respect to  $E_F$  instead of the abovementioned defects, there are areas of bright and dark contrast (see Figs. 4.2.4b,d) resembling that shown in Fig. 4.2.1. It is worth to note, that the bright areas in Fig. 4.2.4b were interpreted in [140] as another kind of defects, presumably, in the Mn layer, inducing resonance states at the Dirac point energy  $E_D$ . However, it is difficult to define the bright

clouds as a defect with corresponding chemical species in the data measured in the present work. The absence of three-fold symmetric defects typical for  $\text{Bi}_2\text{Te}_3$  (see Fig. 2.1.13 and Fig. 4.1.1), the presence of the electronic modulations with almost bias-independent positions of the superstructure 1, and the Mn origin of the defects found by other STM studies [139–142] on this compound lead to a speculation that in the current work the superstructures arise from the structural defects in the Mn-consisting septuple layers. To be more precise, relatively high influence of randomly distributed Mn and Bi atoms known as the Mn/Bi antisite disorder reported ubiquitously in the MnBiTe-compounds with the concentration varying from 3 to 17.5 % [11, 103, 109, 115, 116, 123, 139–141, 195] may result in such an unusual topography (superstructures 1 and 2) observed in the present work.

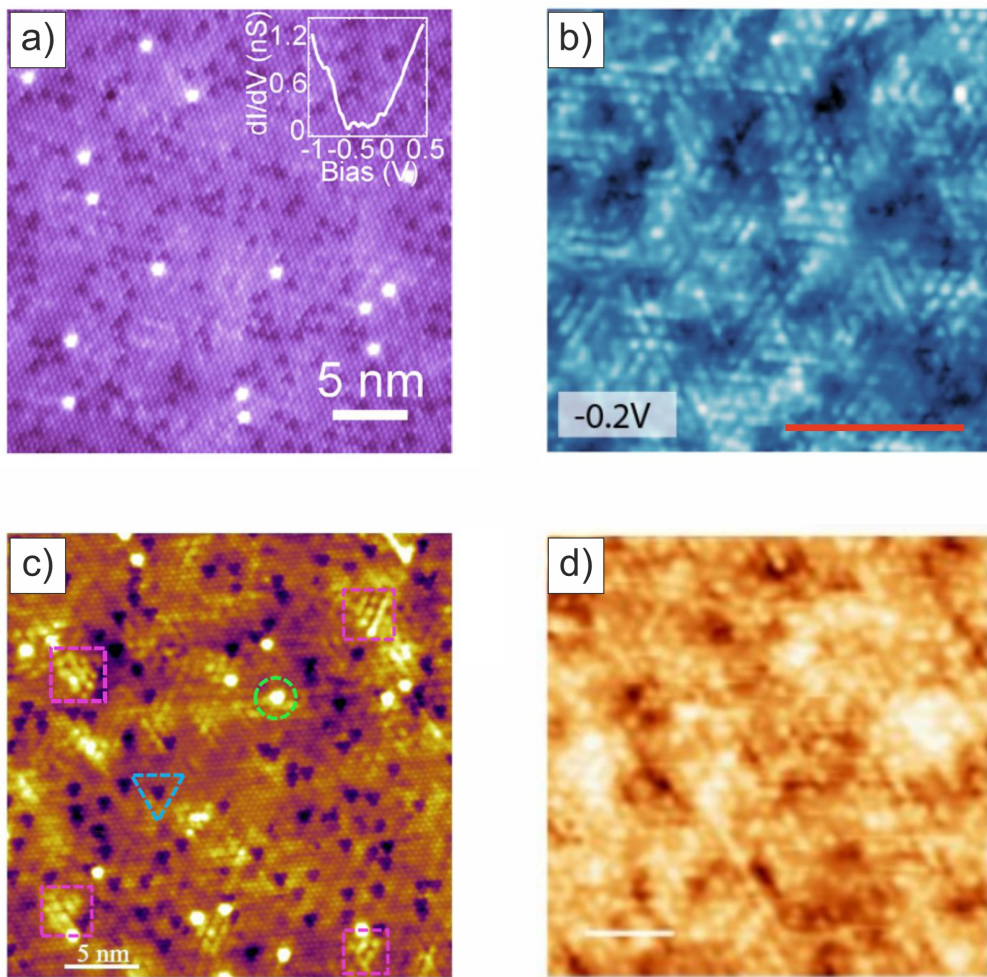


**Fig. 4.2.4** a)–d) STM topography images at  $U_{bias} = -1.2$  V,  $-0.2$  V,  $-0.8$  V,  $0.3$  V, from [139–142], respectively. Images a) and c) are taken in the field of view of  $30\text{ nm} \times 30\text{ nm}$ . The scalebars in b) and d) correspond to  $7\text{ nm}$  and  $4\text{ nm}$ , respectively.

### 4.2.2. STS

Spectroscopic data of these crystals were acquired by the standard lock-in technique with a sinusoidal modulation signal of 2 mV RMS amplitude at a frequency of 1.111 kHz. For instance, the differential conductance tunneling spectra with the corresponding  $I(U)$  curves averaged over 20 repetitions are presented in Fig. 4.2.5 and were measured with the set point of  $I_T = 100$  pA in a voltage range of  $\pm 100$  mV as well as  $\pm 400$  mV.

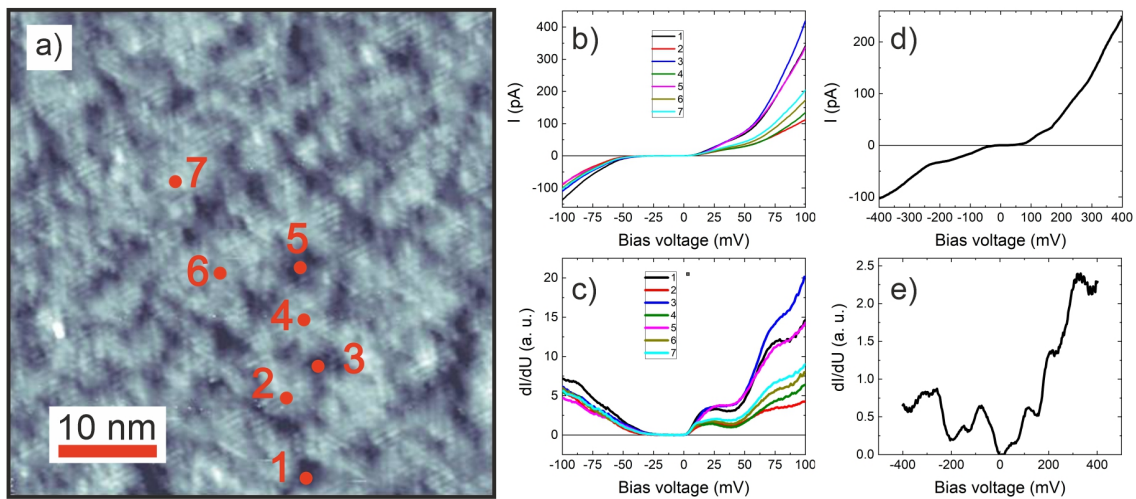


**Fig. 4.2.5** a) Topography at  $U_{bias} = -100$  mV,  $I_T = 100$  pA. b), c)  $I(U)$  and  $dI/dU$  spectra taken on 7 surface points marked in red color within  $\pm 100$  mV. d), e)  $I(U)$  and  $dI/dU$  spectrum measured within  $\pm 400$  mV.

The spectra taken from  $-100$  mV to  $100$  mV on seven different positions on the surface shown as red circles in Fig. 4.2.5a illustrate a very important finding in this experiment which is the detection of an energy gap in the  $dI/dU$  spectra. All these spectra show a distinct gap at the bias voltages from  $-25$  mV to  $0$  mV which is supported by the zero tunneling current in the same range as shown in Figs. 4.2.5b,d. It is worth to say that there is a noticeable difference in the spectra taken on the spots with bright and dark contrast reflecting a strong influence of the chemical inhomogeneity of the material on its electronic DOS similar to the bulk disorder in Mn-doped topological insulators [88]. Meanwhile, the spectrum taken at a larger  $[-400; 400]$  mV bias voltage range (see Figs. 4.2.5d,e) shows a small shift of the gap towards positive bias. One can not argue on the type of charge carriers doping (which is expected to be of the n-type as reported in [9,117,123,128] with the Dirac point located at around 300 meV below  $E_F$ ) since the edges of bulk conduction and valence bands are not prominent in the tunneling spectra. However, one can conclude that the samples used in this STM studies are more p-doped than that used in the ARPES experiments (taking into account the relative position of the observed energy gap and  $E_F$ ) even though produced by the same group [9,109,116].

The comparison of the acquired spectra with the spectra measured by other groups [139–141] shows no clear agreement but from the comparison of the regions with the suppressed DOS (see Fig. 4.2.6a) it appears to be an energy band shifts of the samples used in the current work of around 400 mV with respect to the spectra from [139, 141] and around 200 mV [140] towards the valence band. This implies a different charge carriers doping of the samples resulting in the shift of the bulk energy gap and the Dirac point closer to  $E_F$  in the measured samples in this work.

Despite the strong discrepancy in the STS data most of the rest spectra (see Fig. 4.2.6b) measured at the bias voltages  $\sim[-100; 100]$  mV (at which the gap was found) on different samples (4 of them marked with black, red, blue and magenta colors were obtained on the same cleaving but on different surface areas) with topography similar to that plotted in Fig. 4.2.1a show a common feature. In particular, a dip-like DOS suppression at around  $E_F$  but not a true gap which could be ascribed to the spatially inhomogeneous surface magnetic and electronic structures of the material and will be discussed further. In addition, no systematic changes in the measured DOS on bright and dark regions were found which does not allow to associate the electronic clouds in topography with the defects which induce resonance states near  $E_D$  as reported in [140].

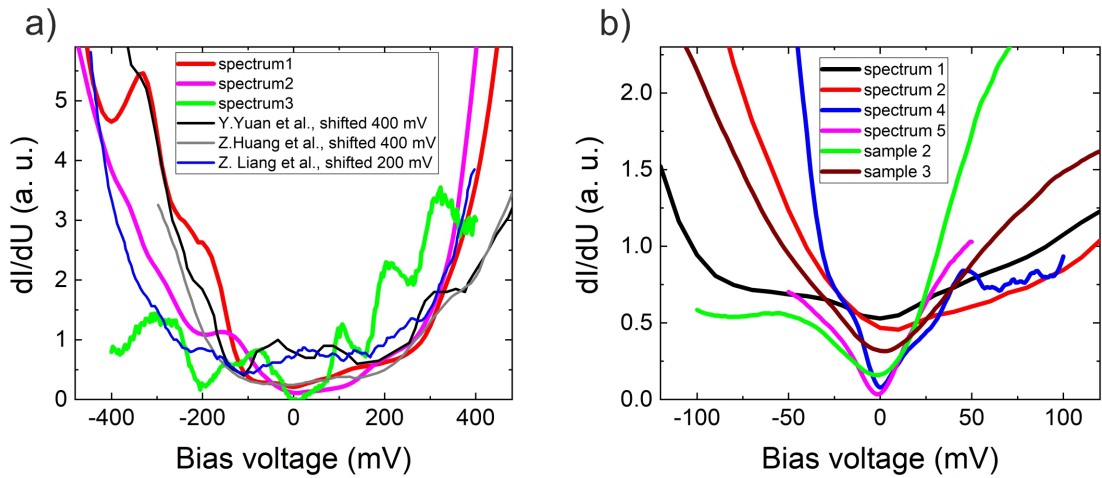


**Fig. 4.2.6** Different examples of the  $dI/dU$  spectra taken on the  $\text{MnBi}_2\text{Te}_4$  surface. a) Comparison with the literature. b) Spectra measured on 3 different samples in the current work. Black, red, blue and magenta were obtained from the same sample (sample 1).  $I_T$  was set to the values in the range 150–500 pA. Each of the plotted spectra represents an average of 140–200 spectra taken at different surface points within  $50 \text{ nm} \times 50 \text{ nm}$  investigated surface areas.

It should be pointed out that the tip-induced band bending phenomenon mentioned in section 4.1.2 and occurring in some topological insulators as, for example, in  $\text{Bi}_2\text{Se}_3$  [179], most probably, does not appear in the measured samples since there are no strong deviations between the spectra acquired with different bias voltage set

point values as illustrated by Fig. 4.2.7. One of these spectra is shown in Fig. 4.2.6a with the red color. Because of the chosen lower energy resolution in the wide energy range spectra the dip-like DOS suppression near  $E_F$  is not as pronounced in Fig. 4.2.7 as that in Fig. 4.2.6.

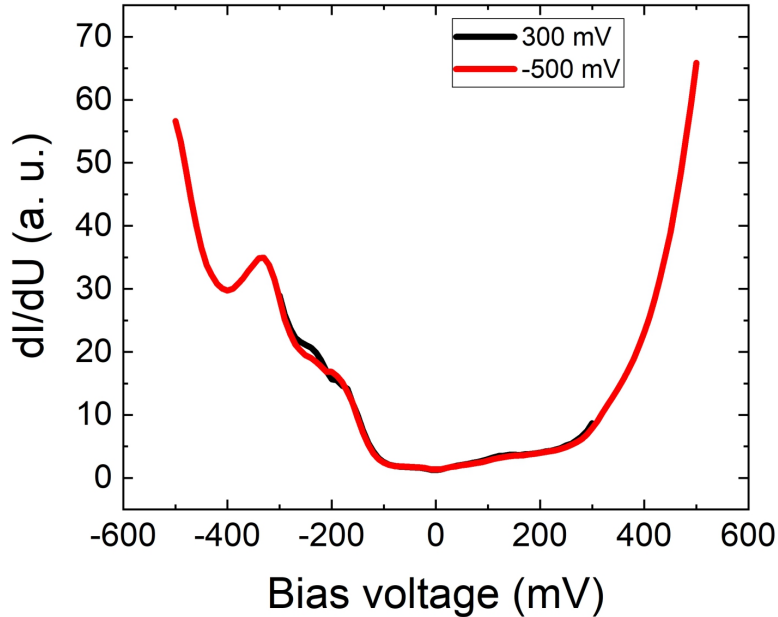


**Fig. 4.2.7**  $dI/dU$  spectra measured at 300 mV and  $-500$  mV bias voltages at  $I_T = 200$  pA.

The observed energy gap size is around 25 meV which is one order of magnitude smaller than the bulk band gap predicted in calculations and measured by ARPES [9, 111–113, 116, 134, 135]. As an example, Figs. 4.2.8a,b show the band structure calculations and ARPES measurements, respectively, on  $\text{MnBi}_2\text{Te}_4$  with the bulk gap size of  $\sim 200$  meV. One could also assume that the gap observed in the current work could be related to the charge (spin) density wave coming from possible periodic lattice distortions. However, until now there are no any evidences of this revealed by other experimental techniques even measured on the same crystals [9, 109, 116, 148]. Therefore, the gap measured in this work is, apparently, the surface state gap which width was experimentally found to be in the range (15–90) meV [9, 109, 111, 112, 116, 117, 119, 134, 196–199] and seems to be one of the first manifestation of the magnetic exchange gap in magnetic topological insulators detected by local STS to date [200–202].

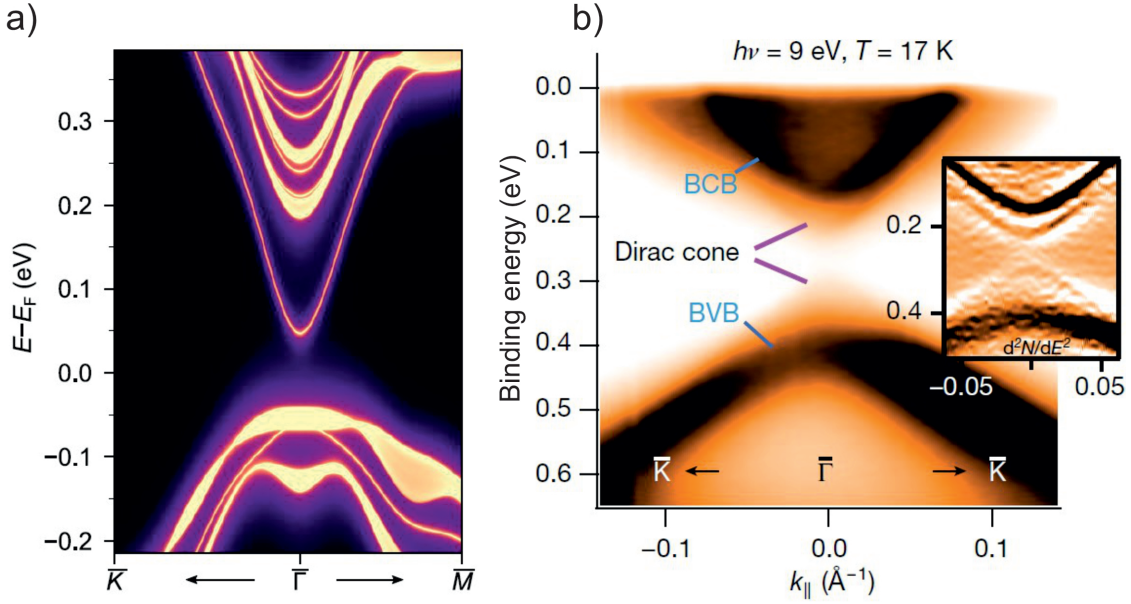


**Fig. 4.2.8** a) Electronic band structure calculations on the (0001) surface. Regions with a continuous spectrum correspond to the bulk states. b) ARPES measured band structure at  $T = 17$  K,  $h\nu = 9$  eV. Adapted from [9].

For the interpretation of the difference in the surface states gap size with respect to that expected from theoretical calculations one should note that the surface magnetism is supposed to be a valid reason of the contradiction in both ARPES and STM data on this compound. For example, according to the band structure calculations for the out-of-plane A-type antiferromagnetic order which is realized in the bulk  $\text{MnBi}_2\text{Te}_4$  a surface state gap of around 90 meV [9, 112, 142] should appear, but the other possible surface magnetic structures (spin disorder or, less likely, G-type antiferromagnetic order – both interlayer and intralayer antiferromagnetic coupling, A-type antiferromagnetism with in-plane magnetic moments) which have not been experimentally proved lead to gapless surface states [112, 122, 137]. Therefore, the characteristic energy scale of the observed gap of 25 meV implies that the expected gap [9] is diminished by possible rearrangement of magnetic moments on the surface, unlike A-type antiferromagnetism in the bulk, with a formation of surface magnetic domains with parallel or antiparallel directions of magnetization as proposed in [9, 113, 135]. Moreover, magnetic domains with sizes of hundreds of nanometers have been experimentally visualized in  $\text{MnBi}_2\text{Te}_4$  by cryogenic magnetic force microscopy [203, 204]. Other considerations might be reasonable as well such as impurity-induced resonance states reported in [140], the cleavage process in the STM and ARPES experiments [122, 134, 139] along with the ubiquitous Mn/Bi antisite intermixing in  $\text{MnBi}_2\text{Te}_4$  [103, 109, 115, 116, 123, 134, 139, 140, 195] which may strongly modify the surface's magnetic and crystal structures. This can result in a surface reconstruction, so the Dirac surface states may be shifted deeper, to the second septuple layer and, thereby, experience a compensated magnetic moment of the

two topmost septuple layers [134]. The diminished magnetic gap size in  $\text{MnBi}_2\text{Te}_4$  which was observed in the STS data in the present work might be also caused by negative surface charge emerging from structural defects on the surface which was proposed by DFT calculations [196, 198, 199].

However, according to the very recent studies [142], it seems that the most plausible factor which affects the magnetic exchange gap size is the Mn/Bi intermixing which was indeed found in the crystals used in the present work [109]. Due to the antiferromagnetic coupling between the main Mn-layer and the Mn/Sb atoms in the isostructural compound  $\text{MnSb}_2\text{Te}_4$  inferred from neutron diffraction experiments [205, 206] the real magnetic structure turns out to be ferrimagnetic which leads to a reduction of the magnetic exchange gap size. Fig. 4.2.9 illustrates the shrinking of the Dirac point gap from 90 meV for the ideal defectless surface of  $\text{MnBi}_2\text{Te}_4$  to 37 meV for Mn/Bi exchange in the second atomic layer and even to 3.5 meV (almost gapless surface states) when it appears in the sixth layer as obtained by DFT calculations [142]. This fact is proposed to explain the differences of the Dirac point gap size for different samples and sample cleavages observed by ARPES and STS [142]. Therefore, the spatial inhomogeneous cation intermixing in  $\text{MnBi}_2\text{Te}_4$  seems to be a reasonable scenario for the surface state magnetic gap variations on the surface for different samples, while the other aforementioned explanations may also affect the gap size. The STS results obtained in the current work point to the intrinsic structural disorder in the crystals which has a strong impact on the electronic structure of this material. To achieve a homogeneity of the electronic properties, one needs more efforts in tuning the crystal growth process.

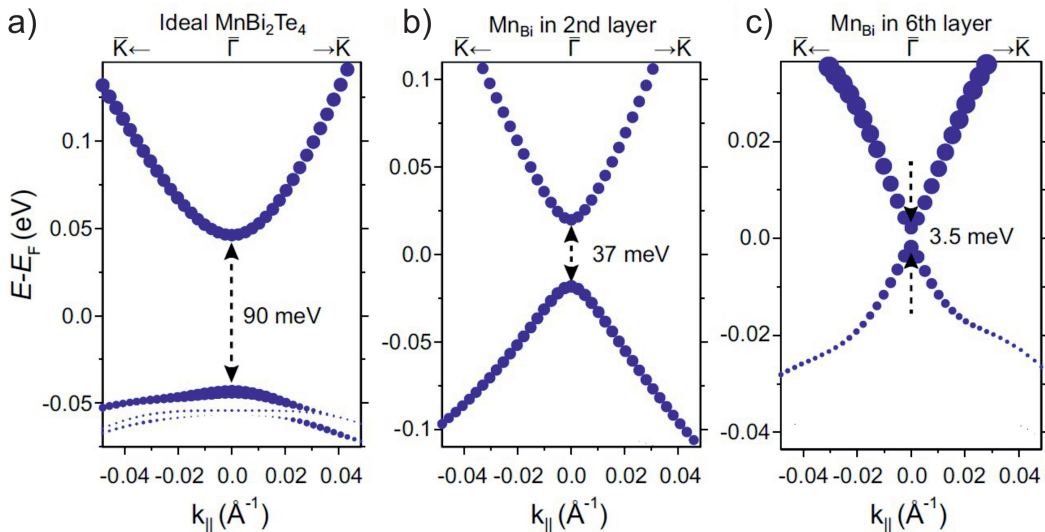


**Fig. 4.2.9** DFT surface electronic structure calculations of a) ideal and defective  $\text{MnBi}_2\text{Te}_4$  with Mn/Bi defect located in the b) second and c) sixth atomic layers counting from top of the surface septuple layer. Adapted from [142].

### 4.2.3. $dI/dU$ mapping

In order to elucidate the origin of the hexagonally ordered superstructures which appear in the FFT of topographic images,  $dI/dU$  maps were measured at 11 values of the bias voltage in the ranges from  $-400$  mV to  $-50$  mV and from  $150$  mV to  $400$  mV. These data were taken on a  $50$  nm squared area (see Fig. 4.2.10) with the set point  $I_T = 150$  pA and the internal lock-in of the RHK R9 controller. The bias voltage modulation parameters  $U_{mod} = 14$  mV RMS,  $f_{mod} = 1.111$  kHz were kept the same at each energy except for  $U_{bias} = \pm 20$  mV where the modulation amplitude was set to 4 mV RMS.

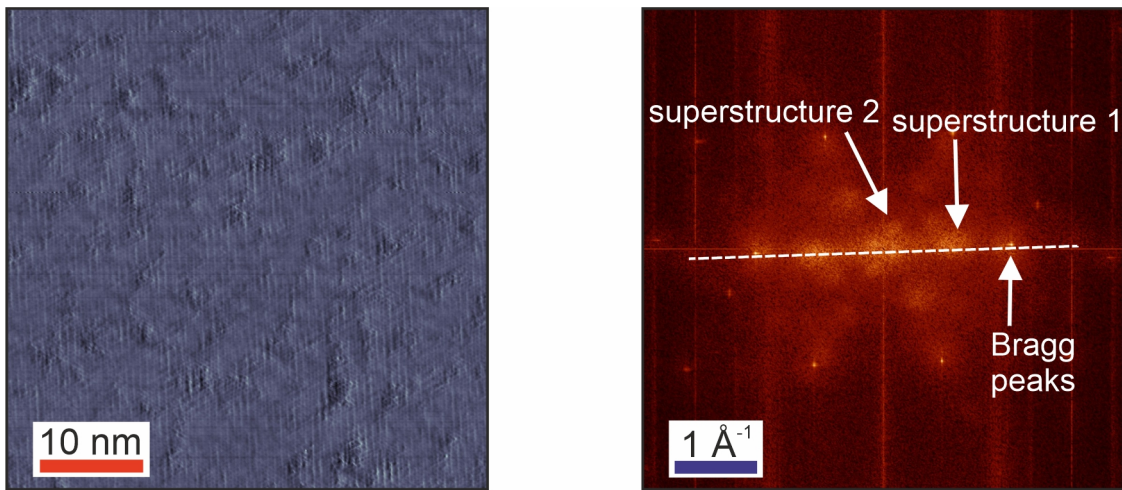


**Fig. 4.2.10**  $dI/dU$  map measured at  $U_{bias} = -100$  mV and  $I_T = 150$  pA with its Fourier transformation. The white line (in the  $\Gamma$ -M direction) indicates the direction of the Bragg spots and the inner spots related to the superstructures 1 and 2.

Fig. 4.2.10 depicts one example of the  $dI/dU$  map at  $U_{bias} = -100$  mV where one can notice two kinds of the inner six-fold symmetric spots similar to those observed in the topographic data in section 4.2.1 (superstructures 1 and 2) which are unidirectional with the Bragg peaks ( $\Gamma$ -M direction). The spots with the real space period related to the superstructure 1 are rather diffuse and persist at most of the energies as observed in the topography presented in Fig. 4.2.2. The others (superstructure 2) are hardly visible and could be clearly distinguishable only at  $200$  mV and  $300$  mV. All the measured  $dI/dU$  maps are plotted in Fig. 4.2.11 for different bias voltages and reveal LDOS modulations which is a signature of the QPI.

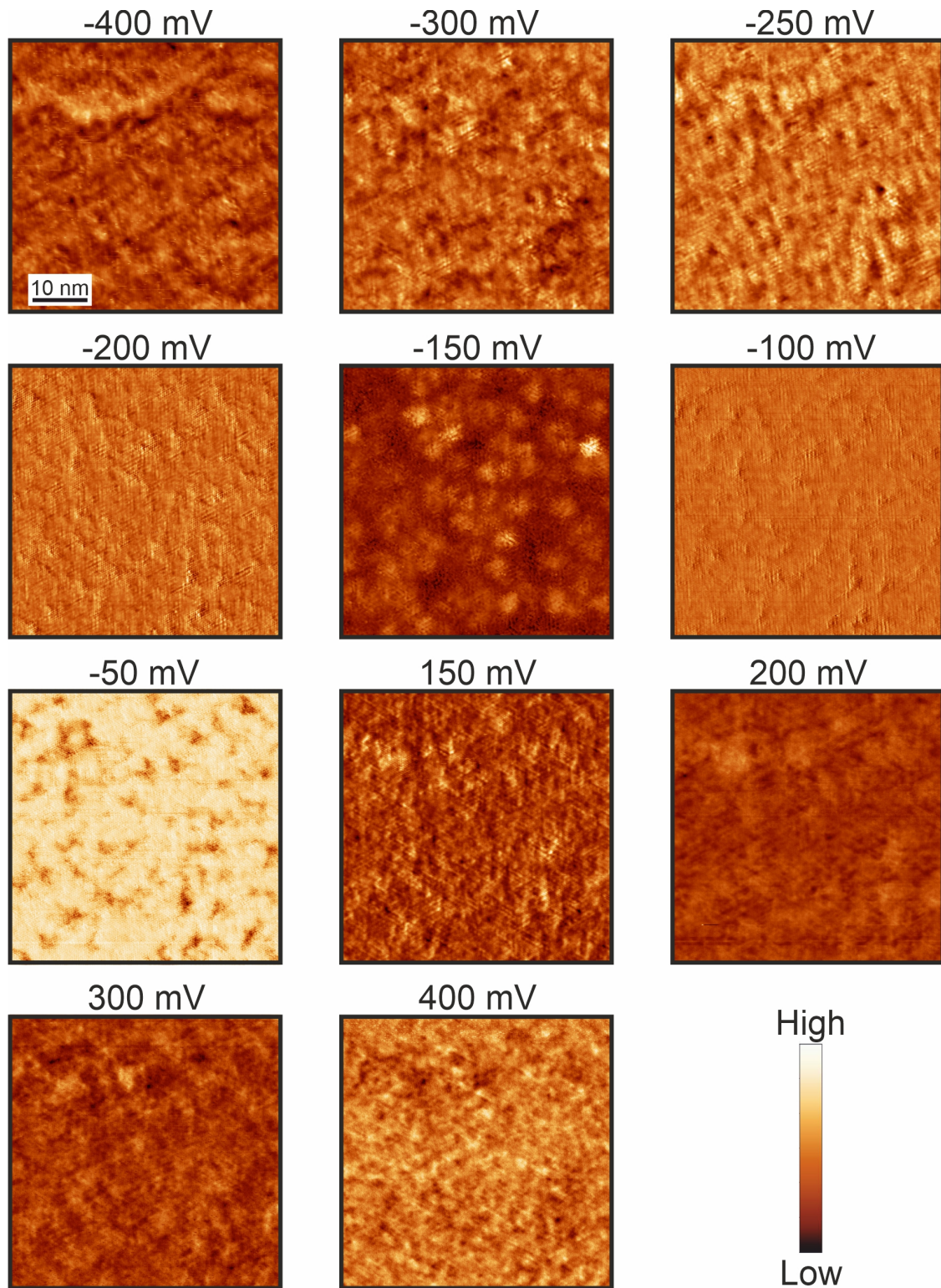


**Fig. 4.2.11** Real space  $dI/dU$  maps measured with the corresponding bias voltages from  $-400$  mV to  $400$  mV,  $I_T = 150$  pA. The length scalebar is the same for each image.

The series of the FFT patterns of the  $dI/dU$  maps in Fig. 4.2.12 shows the energy evolution of the intensity peaks related to the superstructure 1. For instance, one can notice its enhanced intensity at the bias voltages of  $-200$  mV,  $-150$  mV, and  $-100$  mV where additional peaks pointing at the  $\Gamma$ -K direction also appear (see

Fig. 4.2.12). Meanwhile, only two of the maps which were measured at 200 mV and 300 mV exhibit the additional long-wavelength feature (superstructure 2) in the FFT. This superstructure as the other one (superstructure 1) consists of six-fold symmetric spots pointing in the  $\Gamma$ -M direction which are rather blurred in contrast to  $\text{Bi}_2\text{Te}_3$  (see Fig. 4.1.12), which could be caused by material chemical inhomogeneity in  $\text{MnBi}_2\text{Te}_4$  as also observed in [139, 140]. The line profiles of the FFT of each of the  $dI/dU$  maps taken along the spots were fitted by Gaussian functions which allowed to extract the peak positions with the corresponding errors as illustrated in Fig. 4.2.13 and Fig. 4.2.14.

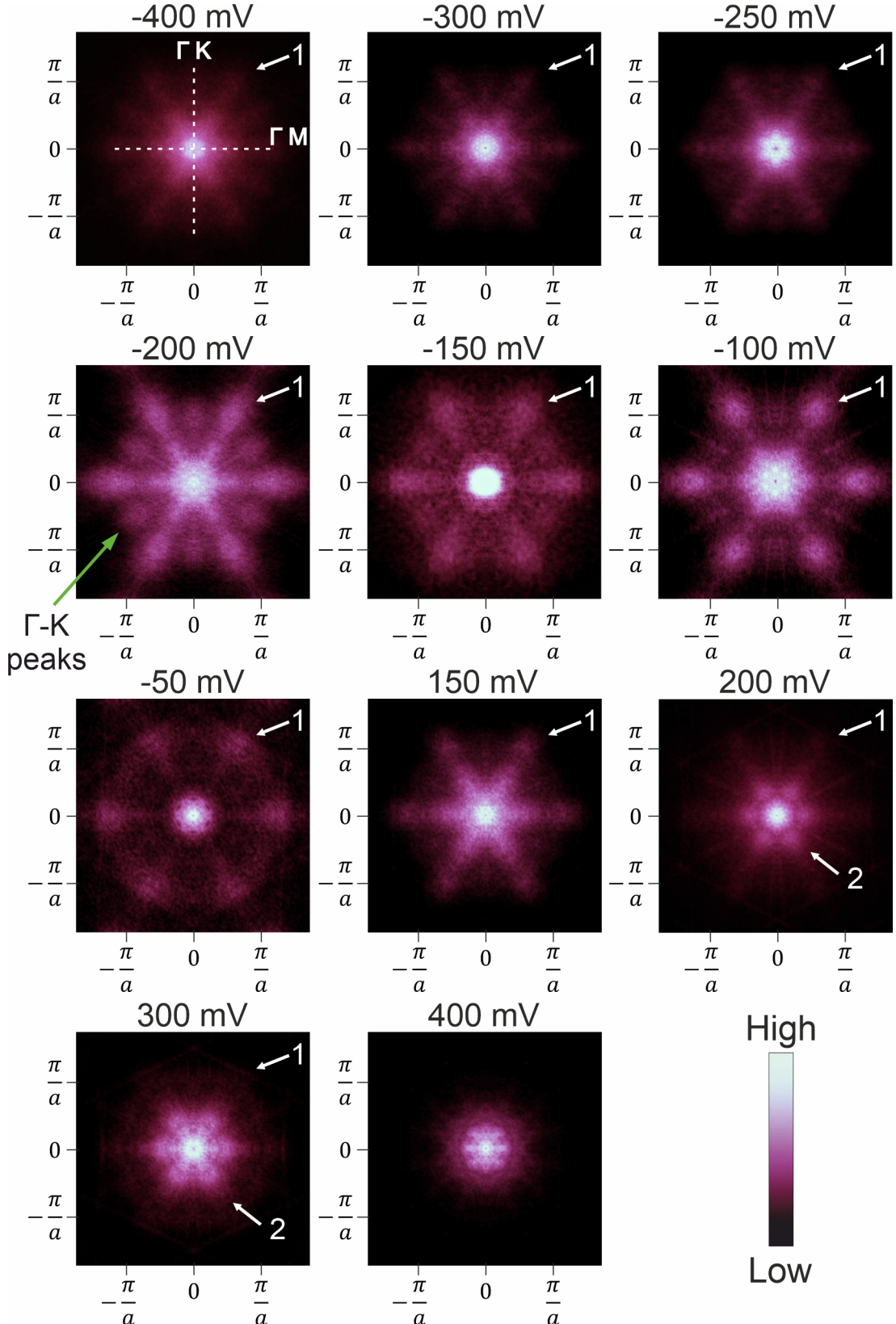


**Fig. 4.2.12** Symmetrized FFTs (see more details on the procedure in Appendix B) of the  $dI/dU$  maps plotted in Fig. 4.2.11 with the corresponding bias voltages from  $-400$  mV to  $400$  mV,  $I_T = 150$  pA. Numbers 1 and 2 indicate the superstructures 1 and 2, respectively. High-symmetry directions are labelled in the FT-QPI at  $U_{bias} = -400$  mV and are the same for each of the patterns. The lattice constant  $a = 4.27$  Å was inferred from the position of the Bragg peaks. Note that both superstructures were not resolved at  $U_{bias} = 400$  mV.

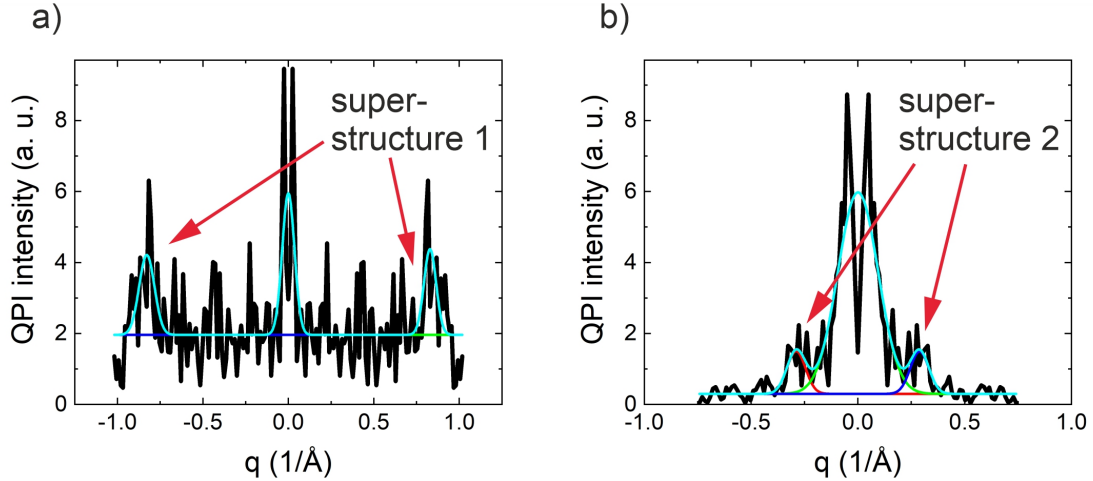


**Fig. 4.2.13** Examples of the QPI intensity profiles taken along the  $\Gamma$ -M direction at bias voltages of  $-200$  mV in a) and  $200$  mV in b) with corresponding Gaussian fits.

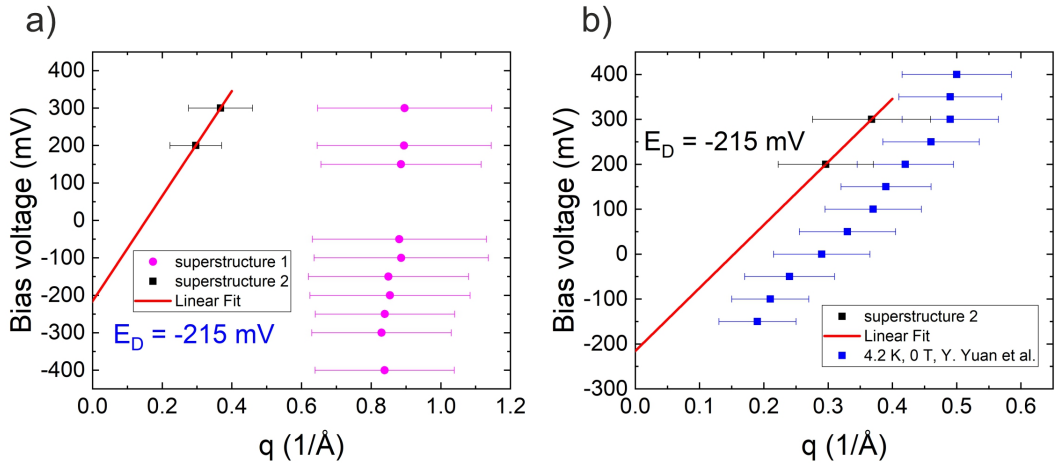


**Fig. 4.2.14** a) Energy dispersion for the observed superstructures 1 and 2 in FT-QPI. b) Comparison of the derived QPI dispersion with [139].

As mentioned above, the superstructure 1 shows no energy dependence, at least, within the error of the measurements and roughly corresponds to  $(1.9 \pm 0.5)$  of the lattice parameter in real space. This might be a signature of the antiferromagnetic order if the superstructure 1 corresponds to a spin density wave arising from possible lattice distortions or electronic modulations. On the other hand, the superstructure 2 at two energies  $200$  mV and  $300$  mV have different scattering vector lengths. Moreover, unlike for the superstructure 1, the lengths of this QPI scattering vector are in the same order of magnitude with the ones shown in [139, 140] as illustrated in Fig. 4.2.14b which corroborates their origin from the QPI of the Dirac surface electrons in  $\text{MnBi}_2\text{Te}_4$ . The linear fit of the QPI peaks made for only  $200$  mV and  $300$  mV results in the Dirac point energy located at  $215$  meV below the  $E_F$  (see Fig. 4.2.14a) which is not in agreement with the observed energy gap (see Fig. 4.2.5b) in the range  $(-25; 0)$  meV measured on a different area of the same cleaved surface.

However, taking into account the error of the Dirac point energy estimation from only 2 points as well as a possible deviation from the linear dispersion of the surface states band as evidenced by ARPES [113, 119, 134, 135, 207], the given value of 215 meV might be significantly different from the real one. Given this considerable inconsistency one can speculate that the surface chemical inhomogeneity (Mn/Bi antisite disorder) could be a reason of the substantial spatial variations in the surface electronic structure. Most of the ARPES data on this compound reported on the Dirac point positioned at  $\sim(300 \pm 50)$  meV below the  $E_F$  but these values are spatially averaged on a few (or even larger) micrometers scale areas depending on the beam spot size. Considering the possible energy band shifts (due to different doping) towards the valence band with respect to the data in [139–141] mentioned in section 4.2.2, it would result in the Dirac point located at the bias voltages of  $-80$  or  $130$  mV which is also not consistent with neither the QPI nor the STS data in the present work. Thus, the idea that the electronic structure at the nanometer scale might be strongly modified can be viable.

The obtained QPI scattering vector related to the superstructure 2 is oriented along the  $\Gamma$ -M direction and has comparable values with the existing QPI data on this material [139, 140] keeping in mind possible energy band shifts. However, according to the QPI calculations based on the constant-energy contour with an out-of-plane A-type antiferromagnetic, in-plane A-type antiferromagnetic and out-of-plane ferromagnetic orders [139], the length (and the direction in some cases) of the simulated QPI scattering vector for the out-of-plane A-type AFM at  $0.4$  eV,  $0.5$  eV and  $0.6$  eV above the Dirac point energy, for example, is not consistent with the experimental data in [139, 140]. This appears to be also inconsistent with the data measured in the present work since the QPI vector observed in the  $\Gamma$ -M direction is not as much (more than two times) different from the experimental QPI vector in [139]. Moreover, in those calculations the scattering vector in the  $\Gamma$ -K direction exists at the energies of  $0.4$  eV,  $0.5$  eV and  $0.6$  eV above the Dirac point energy for the out-of-plane A-type antiferromagnetic order (see Fig. 4.2.15) but there are  $\Gamma$ -K scattering intensity peaks only at the bias voltages of  $-200$  mV,  $-150$  mV, and  $-100$  mV in the current work which are, most probably, much closer to the Dirac point. This has already considered the possible energy band shifts, although the energy scale can not be compared precisely based on the data obtained in this work. In this regard, there could be no A-type AFM on the surface area where the  $dI/dU$  maps were measured, therefore, no energy gap in tunneling spectra can be expected. This fact refers to the explanation of the observed STS gap (see section 4.2.2), which is smaller than that expected from the calculations, in that sense that the magnetic order on the surface is different from its bulk with possible spin disorder or occurrence of different magnetic domains with a short-range

$\sim (10\text{--}100)$  nm magnetic order. Another essential reason could be a chemically and, thus, magnetically inhomogeneous surface. In particular, there may be areas on the sample surface with higher concentration of Mn/Bi-antisites leading to the deviation from the A-type antiferromagnetism and, therefore, the Dirac point gap reduction, while there may be areas with lower concentration of the Mn/Bi-antisites implying nearly intact short-range A-type antiferromagnetic order and larger Dirac point gap size.

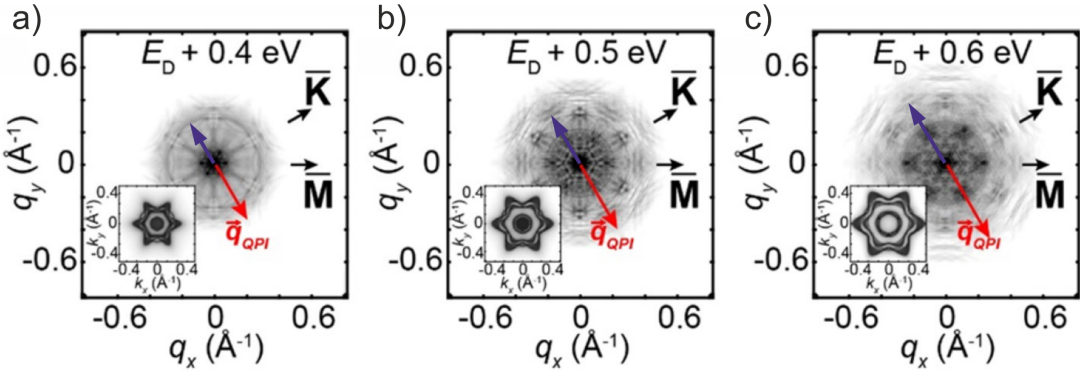


**Fig. 4.2.15** a)–c) Simulated QPI patterns based on constant-energy contours with out-of-plane A-type antiferromagnetic order at  $E_D + 0.4$  eV,  $E_D + 0.5$  eV,  $E_D + 0.6$  eV, respectively. The red arrows indicate the QPI scattering vectors measured in [139]. The blue arrows show the QPI scattering vectors obtained in the current work assuming that  $E_D = -215$  meV as inferred from Fig. 4.2.14a. The corresponding calculated constant-energy contours are plotted in the insets.

#### 4.2.4. Conclusions

Within the presented low-temperature ( $T = 5$  K) STM data on  $\text{MnBi}_2\text{Te}_4$  an atomically corrugated hexagonal surface with appreciable electronic modulation that reveals two superstructures in the FFT were obtained. The origin of the superstructures formation is potentially associated with the Mn structural defects, most probably, Mn/Bi antisite intermixing. The noticeable energy gap of approximately 25 meV width was detected by STS on the  $50\text{ nm} \times 50\text{ nm}$  surface area which is, conceivably, a magnetic exchange gap but with significantly smaller width than that expected from calculations for the ideal compound without the cation intermixing. According to the recent studies of  $\text{MnBi}_2\text{Te}_4$ , the Mn/Bi intermixing is considered as the crucial factor affecting the surface state gap size. Most probably, the measured surfaces are chemically inhomogeneous with different concentrations of Mn/Bi and Bi/Mn defects resulting in the regions with higher (smaller) influence on the electronic structure of the material with gapless (gapped) tunneling spectra. Other scenarios proposed in the literature such as altered surface magnetism (not A-type antiferromagnetism as in the bulk), magnetic domains, resonance states, surface states relocation to deeper layers are also reasonable and can not be neglected.

## 4.3. $\text{MnBi}_4\text{Te}_7$

The STM/STS measurements on  $\text{MnBi}_4\text{Te}_7$  single crystals were performed with the Nanonis SPM controller and the external SR 830 lock-in amplifier operated at  $U_{mod} = 14$  mV RMS and  $f_{mod} = 1.111$  kHz. The measurements were done, also, at different temperatures in the range (5–20) K aiming to track the evolution of the electronic structure crossing  $T_N = 13$  K.

### 4.3.1. Topography

Since  $\text{MnBi}_4\text{Te}_7$  is supposed to be built up of the alternate sequence of the quintuple layer and septuple layer blocks, the natural important question is at which layer the sample is cleaved. Two obviously different surfaces were observed on different samples at  $T = 5$  K which may be a signature of two possible surface terminations as illustrated in Fig. 4.3.1.

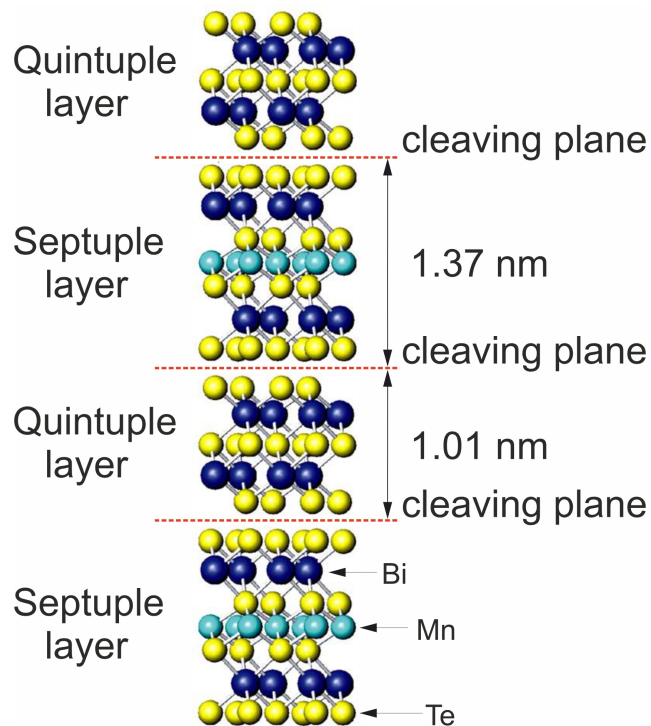


**Fig. 4.3.1** Crystal structure of  $\text{MnBi}_4\text{Te}_7$ . Mn, Bi and Te atoms are marked with green, blue and yellow colors, respectively. Adapted from [102].

Most of the obtained data on  $\text{MnBi}_4\text{Te}_7$  demonstrate atomically resolved surface with the hexagonally symmetric Bragg peaks in FFT corresponding to the lattice constant value  $a \approx 4.3 \pm 0.2$  Å which is consistent with the literature value of 4.36 Å. An exemplary topography image is shown Fig. 4.3.2. It reveals a distinct atomic corrugation with the three-fold symmetric defects which were already observed on pristine  $\text{Bi}_2\text{Te}_3$  in the present work (see section 4.1.1) and in the literature [50–52,58].

According to these studies, the dark circular and the bright clover-shaped defects are Te-vacancies in the first Te-layer and Te/Bi-antisite defects residing on the first Bi-layer from top, respectively. This fact points towards the conclusion that this was indeed the quintuple layer surface termination.

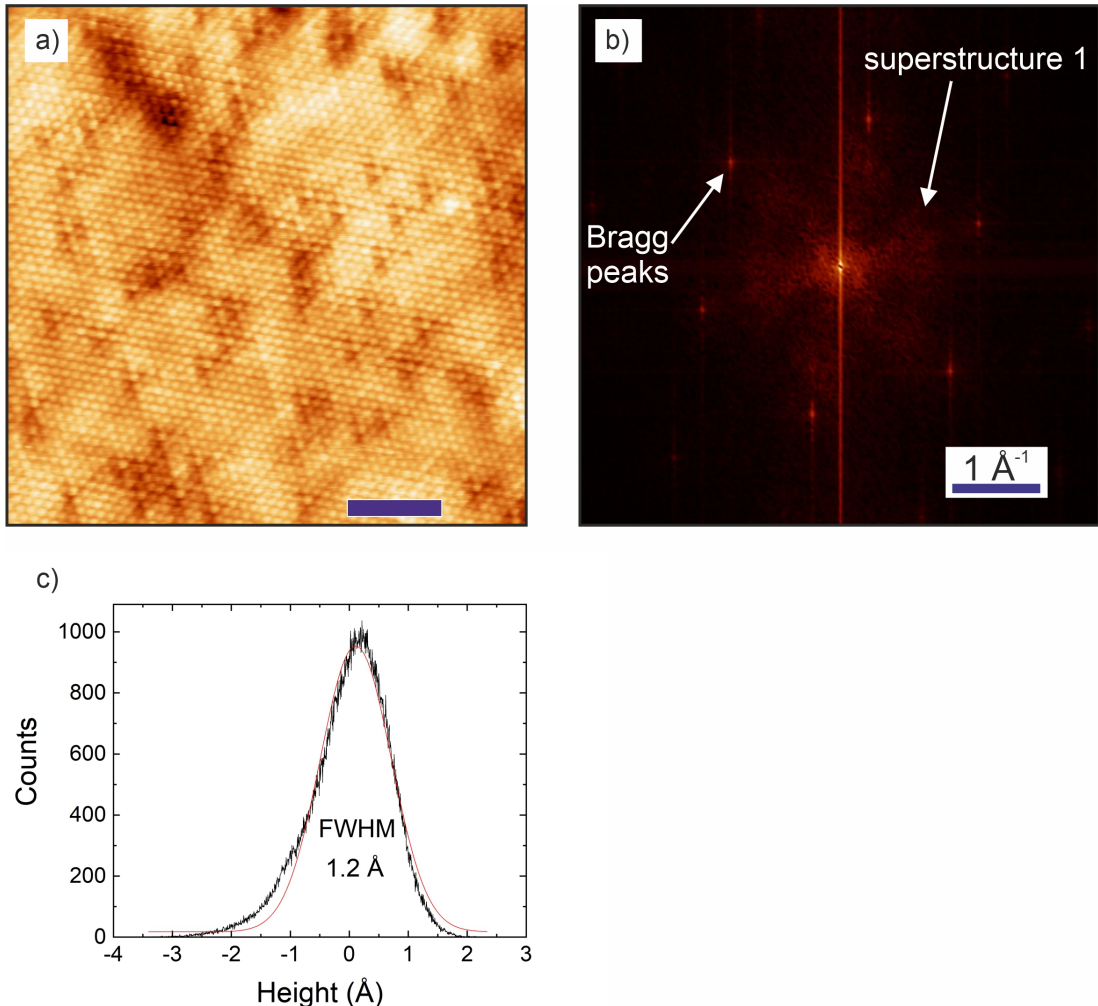


**Fig. 4.3.2** a) 22 nm  $\times$  22 nm topography at  $U_{bias} = 100$  mV,  $I_T = 70$  pA,  $T = 5$  K. b) FFT of the image in a) with the indication of the superstructure 1 and Bragg peaks. c) Height distribution of the surface shown in a) with the Gaussian fit indicated as the red curve. The blue scalebar in a) is equal to 4 nm.

Fig. 4.3.3 shows the topography scans with atomic defects detected at  $T = 14$  K and at  $T = 20$  K, i.e. above  $T_N$ , on the area where full STS maps (which will be discussed in section 4.3.2) were measured as well.

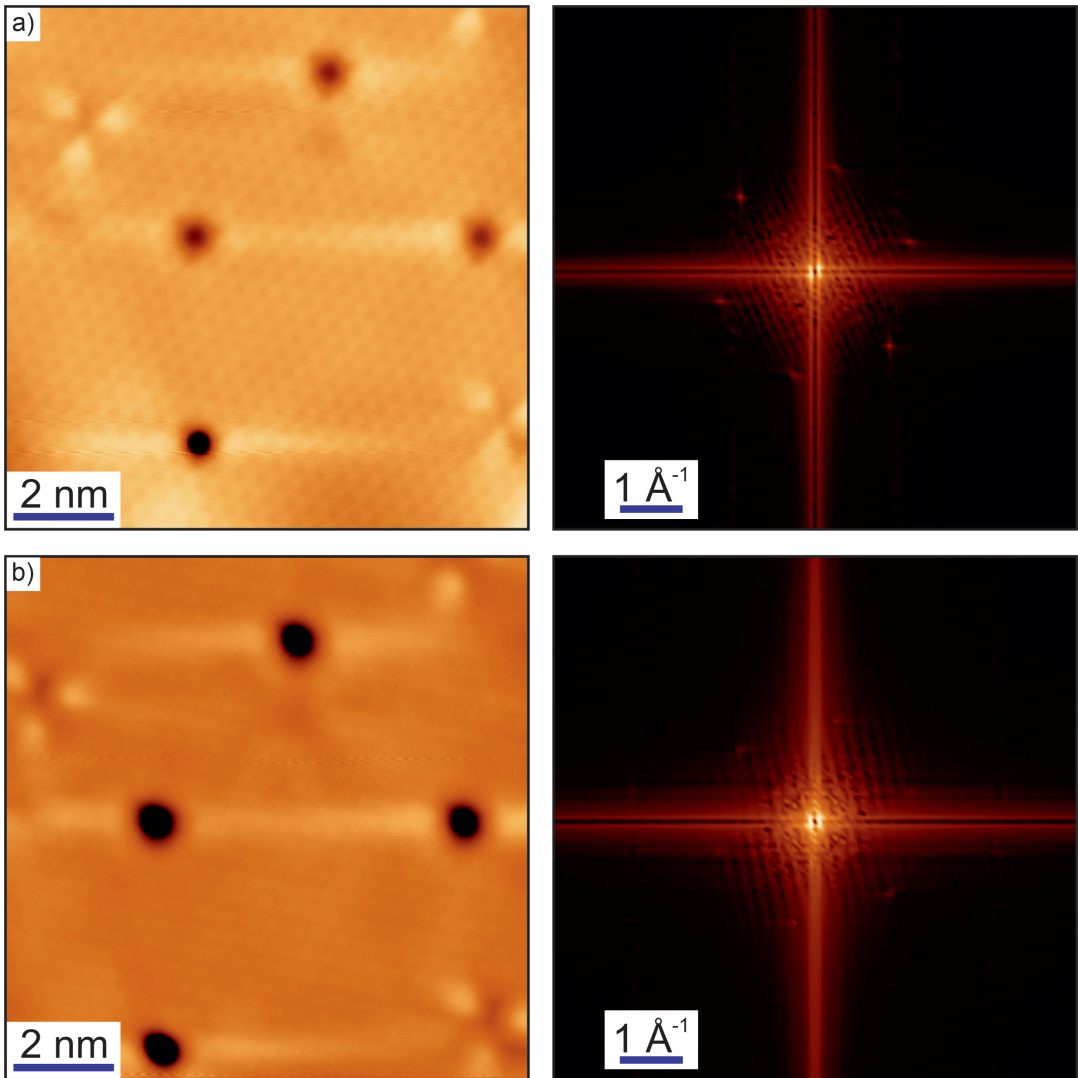


**Fig. 4.3.3** Topographies at 20 K (a) and 14 K (b) on the left with the corresponding FFT on the right,  $U_{bias} = 500$  mV,  $I_T = 150$  pA.

The other kind of surface shown in Fig. 4.3.4 has no intrinsic  $\text{Bi}_2\text{Te}_3$  defects and looks similar to the topography of  $\text{MnBi}_2\text{Te}_4$  shown in Fig. 4.2.1 and measured in this work (note that both crystals were produced by the same group in a similar way). In addition, the surface illustrated in Fig. 4.3.4 looks more rough as can be inferred from the height distribution of this surface in Fig. 4.3.4d with the broader Gaussian fit compared to that for the other surface in Fig. 4.3.2c (both surfaces are of the same size and the number of pixels). Although the FFT of both surfaces in Fig. 4.3.2b and Fig. 4.3.4b reveal superstructures similar to that observed in  $\text{MnBi}_2\text{Te}_4$  (superstructure 1 as seen from Fig. 4.2.1), the surface in Fig. 4.3.4 exhibits pronounced local electronic modulations resulting in the additional superstructure in the FFT (see Fig. 4.3.4b). This superstructure is reminiscent of that resolvable in some topography of  $\text{MnBi}_2\text{Te}_4$  (superstructure 2) with high enough momentum resolution (see Fig. 4.2.3) and signal-to-noise ratio (see Figs. 4.2.2j,k) but has never

been found on  $\text{Bi}_2\text{Te}_3$ . Therefore, it allows to identify the surface in Fig. 4.3.4 as the septuple layer terminated surface. It is worth to note, that the blurry superstructure 1 in the FFT exists on both surfaces highlighting the influence of the Mn layer even when it is beneath the topmost quintuple layer and, thus, indicating a surface-bulk hybridization as mentioned in the literature for this compound [115] as well as for  $\text{MnBi}_2\text{Te}_4$  [120].

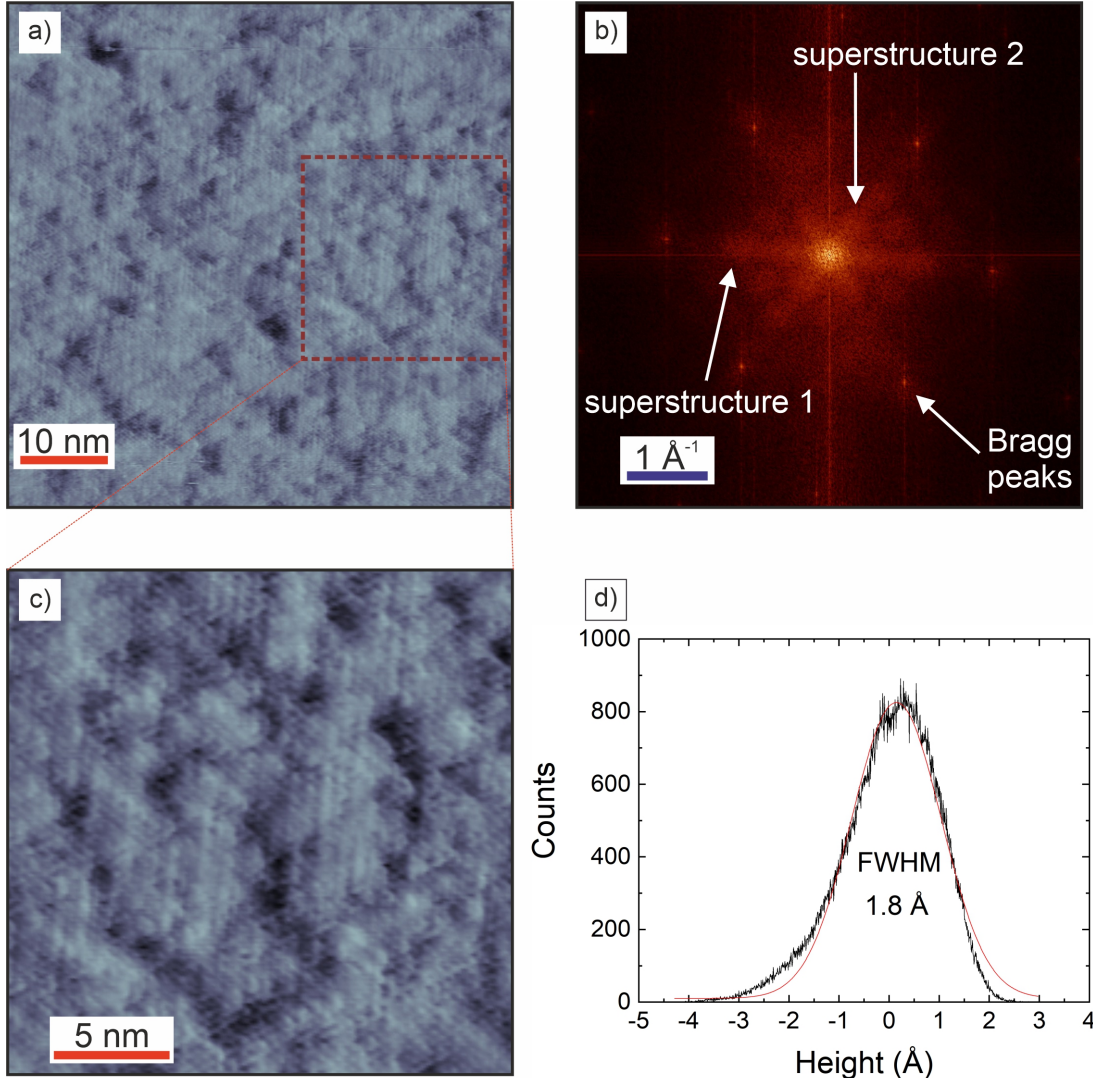


**Fig. 4.3.4** a) 50 nm  $\times$  50 nm topography at  $U_{bias} = 100$  mV,  $I_T = 50$  pA,  $T = 5$  K. b) FFT of the image in a) with the indication of the superstructures 1 and 2 and Bragg peaks. Note that here the superstructure 1 consists of intensity spots not only in the  $\Gamma$ -M direction (which is collinear with the Bragg peaks) but also in the  $\Gamma$ -K direction as was also found in  $\text{MnBi}_2\text{Te}_4$  (see section 4.2.1). c) 22 nm  $\times$  22 nm zoom-in view of the image a). d) Height distribution of the field of view shown in c) with the Gaussian fit (red curve).

Multiple atomic steps with very different heights varying from 0.2 nm to more than 2 nm were observed in one of the measured samples. Fig. 4.3.5 represents different sequences of atomic steps, for example, repetitions of, most likely, two septuple layers (Fig. 4.3.5a) and two quintuple layers (Fig. 4.3.5b), the expected

alternation of quintuple and septuple layers in Fig. 4.3.5c or even unusual heights of the steps which can not be attributed neither to quintuple nor septuple layers (Fig. 4.3.5d).

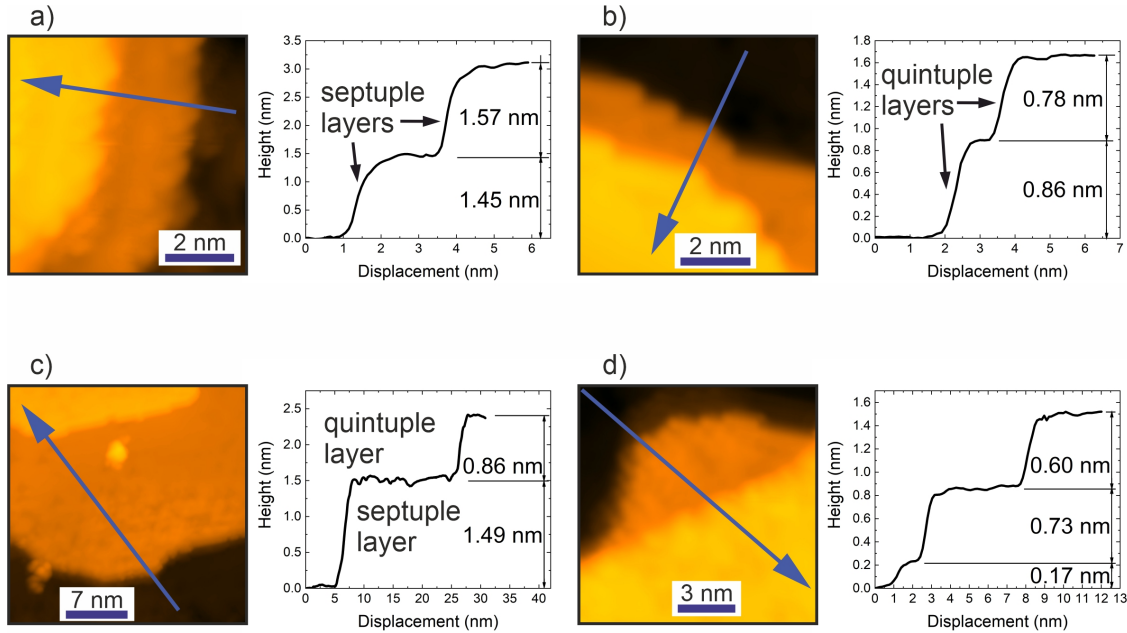


**Fig. 4.3.5** Different examples of step heights observed on  $\text{MnBi}_4\text{Te}_7$  crystals.

In order to estimate the step heights, statistical analysis of the roughness was performed for the topographic scans with steps. In total 57 steps were taken into account. The obtained height distribution illustrates distinct peaks in the number of counts which indicate the heights of the terraces, while the differences between each of adjacent peaks are the step heights (see Fig. 4.3.6 and Fig. 4.3.5). The error of the heights values estimated in this way is determined by the standard deviation of the Gaussian fit which amounts to 0.1–0.2 nm. The plotted height histogram in Fig. 4.3.7 shows the dominating step height which is very close to that of the quintuple layer ( $\approx 10 \text{ \AA}$ ) (this is consistent with the ARPES data on  $\text{MnBi}_4\text{Te}_7$  [11] which indicates an abundance of the quintuple layer terminated surface) and contradicts the reasonable expectation to observe quintuple layer and septuple layer steps on this compound with nearly equal probability.

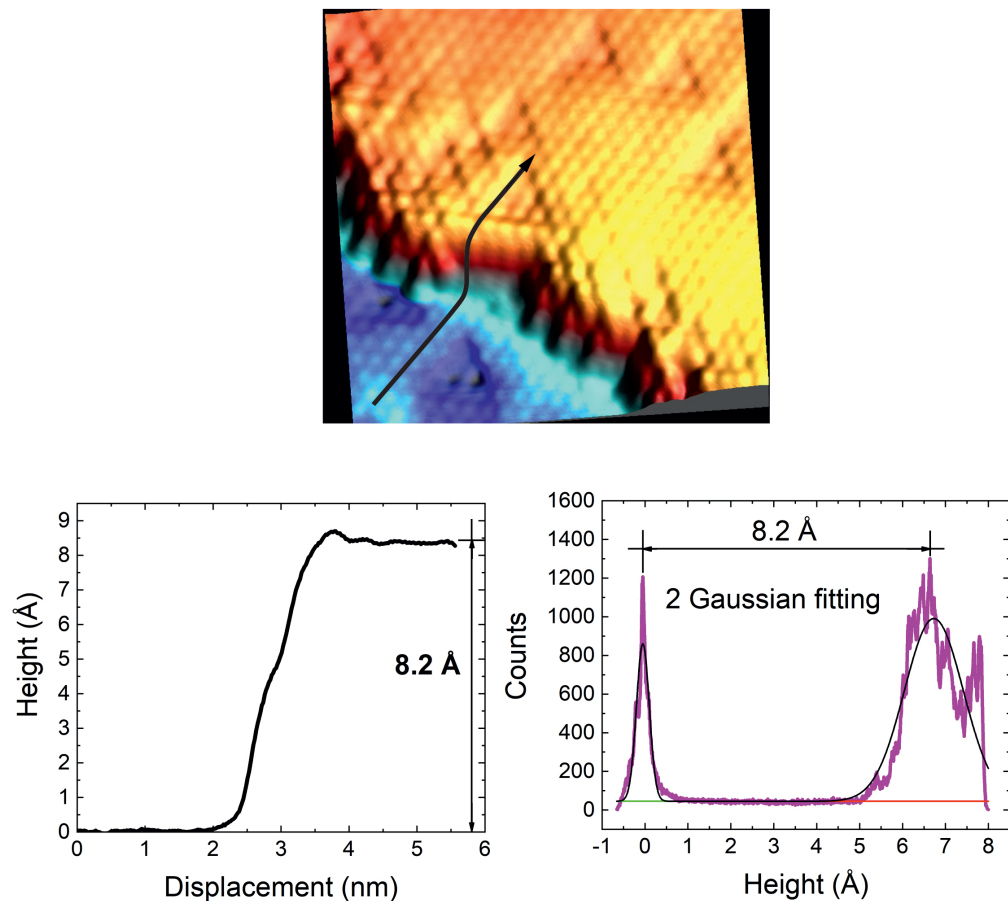


**Fig. 4.3.6** Single quintuple layer atomic step: topographic line profile and the height distribution,  $U_{bias} = 400$  mV,  $I_T = 70$  pA,  $T = 12$  K.

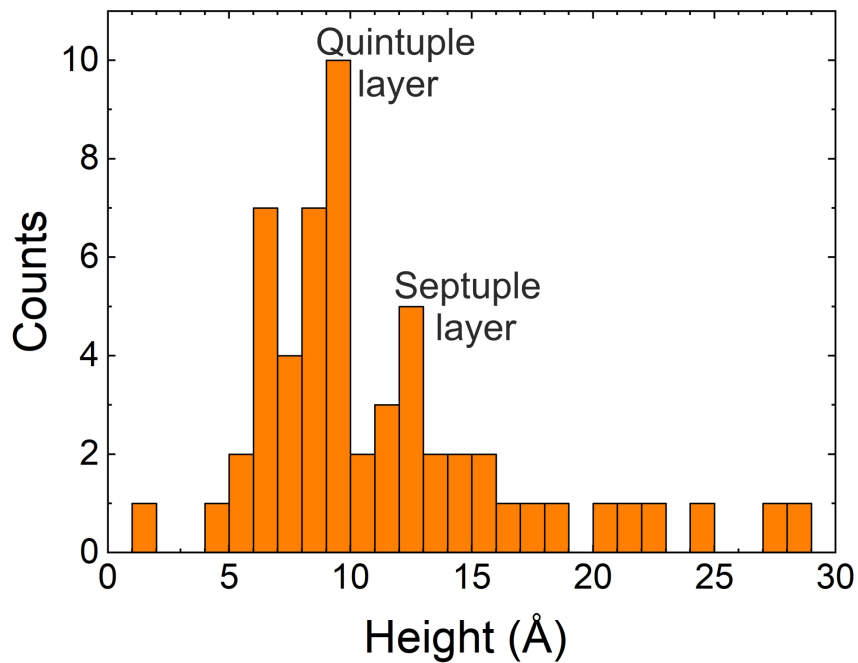


**Fig. 4.3.7** Height histogram of all the steps heights observed on  $\text{MnBi}_4\text{Te}_7$ .

The single step in Fig. 4.3.6 which height is close to that for the quintuple layer within the error of the measurement reveals similar hexagonal atomic corrugation with triangular shaped defects on both sides of the step. For a spectroscopic characterization of this kind of step a full STS map was measured on both terraces of another quintuple layer step from which a similar electronic structure ( $dI/dU$  spectra) on both sides of the step was inferred (see Fig. 4.3.8). It is worth to mention that the spectra exhibit some change near the step edge. However, one can not claim on the magnetic origin of this step edge state which was found in [149], since there are no analogous STS data measured on other surfaces and at higher temperatures. Given the noticeable difference between two observed surfaces of this compound (see Figs. 4.3.2 and 4.3.4), similar spectra along with the similar topographies on both sides of the step edge lead to the assumption that, most probably, this sample had sequences of quintuple layers as illustrated in Fig. 4.3.9.

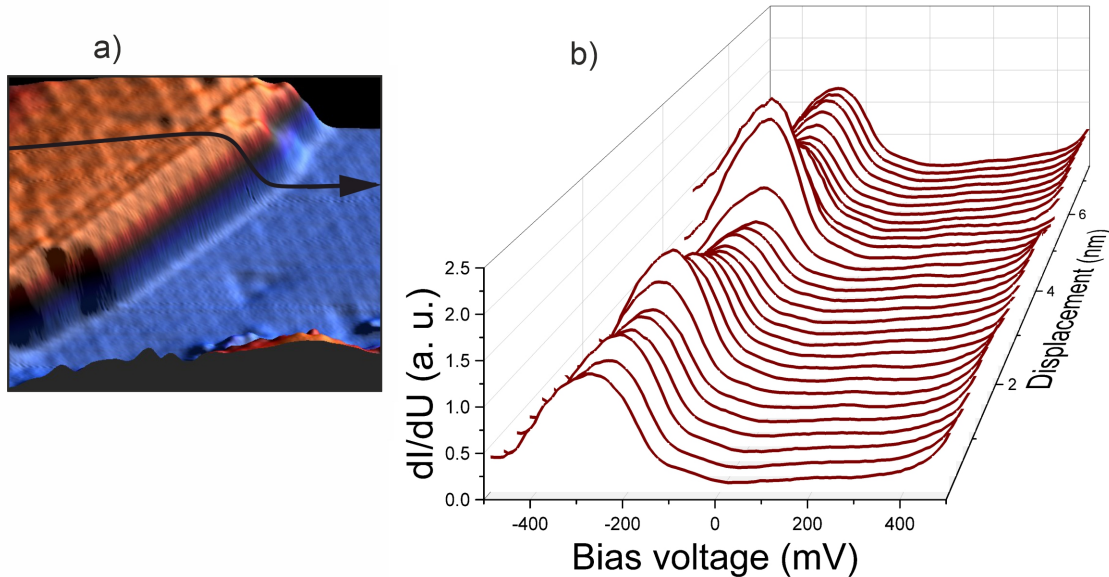


**Fig. 4.3.8** a) Quintuple layer step edge,  $U_{bias} = 500$  mV,  $I_T = 150$  pA,  $T = 12$  K. b)  $dI/dU$  spectroscopic line profile across the step edge shown along the line indicated in a).

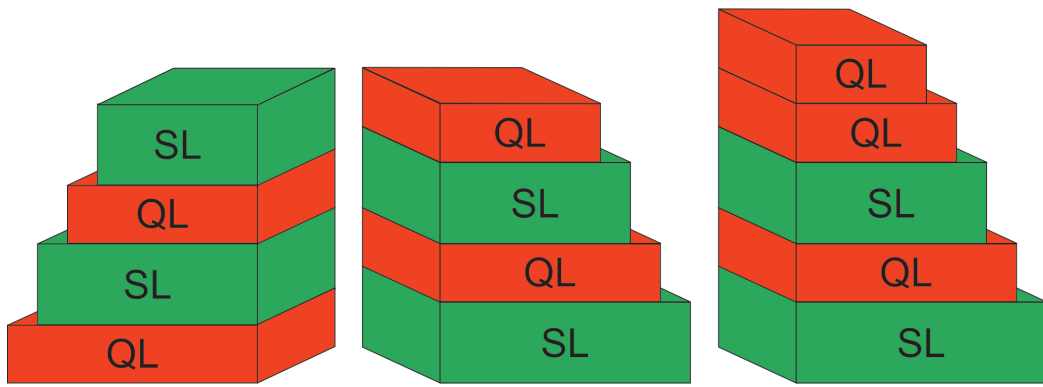


**Fig. 4.3.9** Two ideal cleaving situations and the one (on the right) apparently realized in the  $\text{MnBi}_4\text{Te}_7$  STM-experiment. Here QL and SL are abbreviations of "quintuple layer" and "septuple layer", respectively.

### 4.3.2. Temperature-dependent STS

As mentioned above, one of the most intriguing STM experiment on  $\text{MnBi}_4\text{Te}_7$  compound could be temperature-dependent spectroscopy measurements across  $T_N = 13$  K in order to reveal changes of the DOS of the sample driven by the magnetic phase transitions.

At first, Fig. 4.3.10 shows spatially averaged spectra taken at 12 K, 14 K and 20 K on defect-free regions of the surface shown in Fig. 4.3.3.

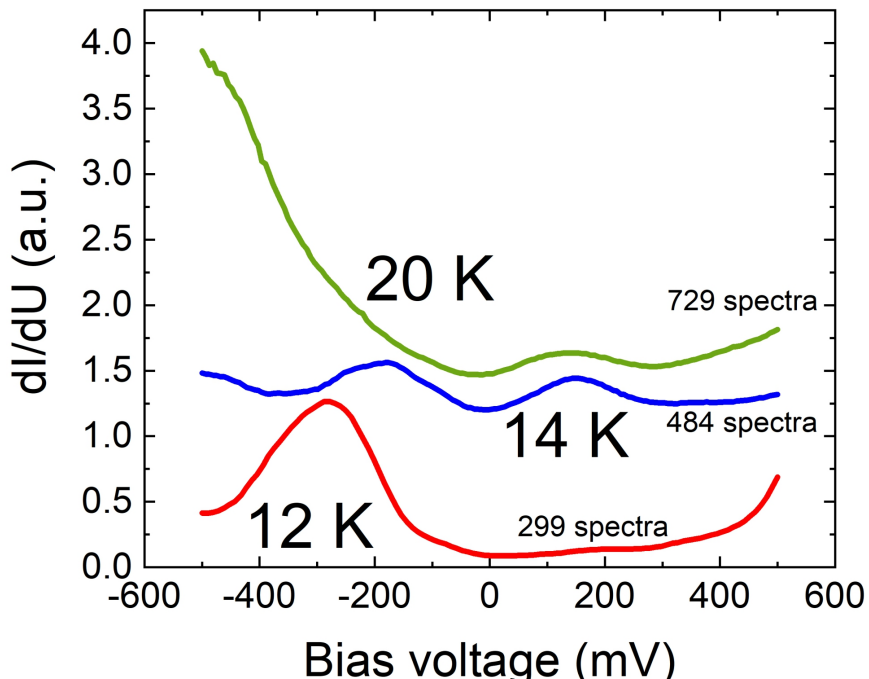


**Fig. 4.3.10** Spatially averaged tunneling spectra measured at 12 K, 14 K, 20 K,  $U_{bias} = 500$  mV,  $I_T = 150$  pA. Numbers of the averaged spectra are indicated next to the corresponding curves.

From Fig. 4.3.10 it is clear that there is no systematic evolution of the DOS spectra as a function of temperature. There is an enhanced DOS at  $T = 12$  K near  $U_{bias} = -300$  mV, which is, presumably, very close to the Dirac point energy found by ARPES [11, 110, 114, 115, 121, 122, 147, 148]. Similar increase of DOS at the Dirac point was observed in the STM experiment on  $\text{MnBi}_2\text{Te}_4$  crystals and was attributed to resonance states caused by defects in Mn atomic layers [140]. However, the data displayed in Fig. 4.3.10 were measured, most probably, on the  $\text{Bi}_2\text{Te}_3$ -terminated surface (see Fig. 4.3.3). At the same time, it is worth to note that the spectroscopic map at  $T = 12$  K was taken on a different region, not on that where the maps at 14 K and 20 K were measured. Therefore, one can not rule out that due to the observed inhomogeneities of the samples the measured local electronic structure could vary by changing the measurement position on the surface. In other words, the presence of the cationic intermixing and, also, the stepping faults in the crystal stacking can be reasonable factors which affect the measured tunneling spectra (see Appendix D with more data as well).

With this in mind, point spectroscopy measurements at  $T = 5$ – $20$  K were also carried out while keeping the same defect-free surface spot of 15 nm  $\times$  15 nm of a different cleave (at  $T = 5$  K) which shows clearly triangular shaped defects as in pure  $\text{Bi}_2\text{Te}_3$ . It was repeated on 2 different surfaces of the same cleavage (see Fig. 4.3.11a and Fig. 4.3.11b). The measurements were done on 10 selected points both on defects and on defect-free regions at different temperatures from 5 K to 20 K. These STS experiments were rather stable since at each of the measured point 20 sweeps of the bias voltage within the error provided the same spectra. The tip-induced band bending mentioned in sections 4.1.2 and 4.2.2 is also excluded for  $\text{MnBi}_4\text{Te}_7$  (see Fig. 4.3.12) because the spectra measured at different bias voltages lie on top of each other. Besides, there was no strong variation of the spectra with the position on the surface. Therefore, the averaged over 200 spectra at a certain temperature are plotted as a function of temperature as shown on Fig. 4.3.11 where  $dI/dU$  spectra show almost no temperature dependence as expected for  $\text{Bi}_2\text{Te}_3$ , but not for  $\text{MnBi}_2\text{Te}_4$ , at least, in its bulk. One should also note that the change in the spectral shape from 12.0 K to 8.2 K in Fig. 4.3.11b was due to the tip-state change in the experiment. Since the measured surfaces in Fig. 4.3.11a and Fig. 4.3.11b are supposed to be of the quintuple layer-type, the fact that they do not reveal striking changes in the temperature-dependent STS below and above  $T_N$  could be related to possible crystal imperfections and/or the idea of a reduced magnetization across the topmost quintuple layer which is not strong enough to open the surface states gap [121] as supported by the gapless spectra in Fig. 4.3.11.

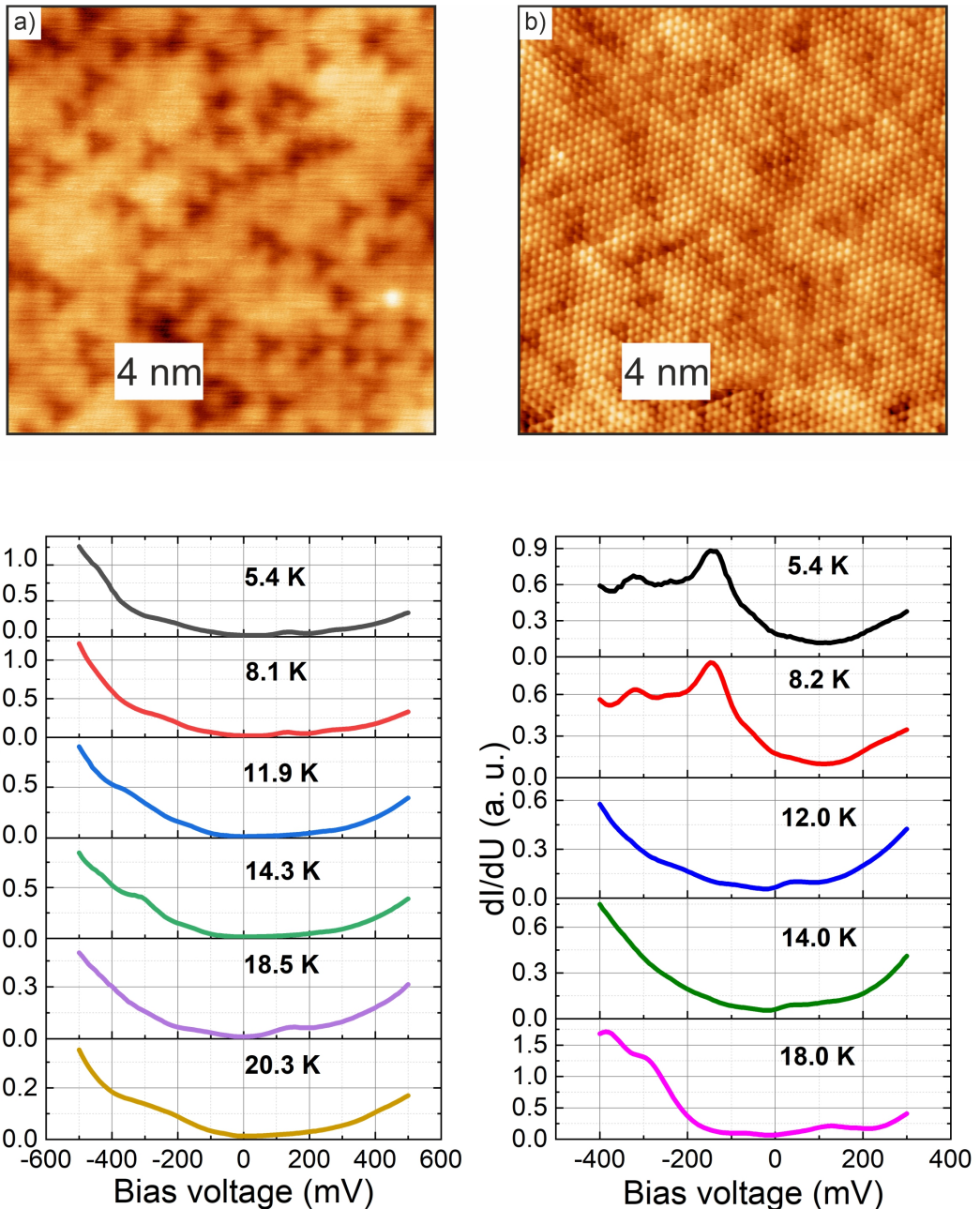


**Fig. 4.3.11** STS at different temperatures for 2 experiments a) and b) with the corresponding topographies, 20 nm x 20 nm,  $U_{bias} = 500$  mV,  $I_T = 200$  pA.

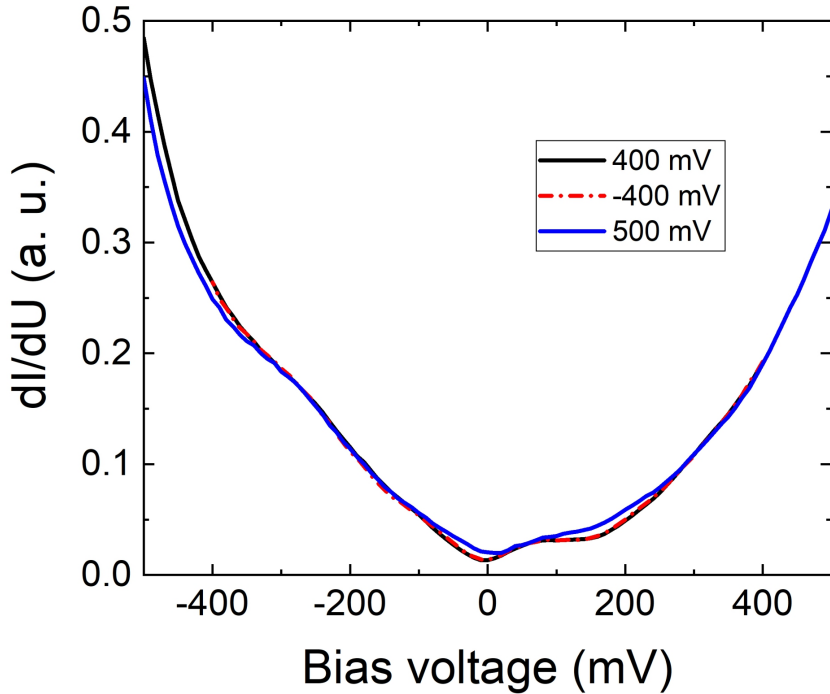


**Fig. 4.3.12**  $dI/dU$  spectra measured at the same surface position at 400 mV,  $-400$  mV and 500 mV bias voltages with  $I_T = 200$  pA,  $T = 5$  K.

### 4.3.3. Conclusions

To summarize, two kinds of surfaces corresponding to two different cleavage ( $\text{Bi}_2\text{Te}_3$ - and  $\text{MnBi}_2\text{Te}_4$ -terminations) possibilities were identified by the topographic measurements. However, the existence of very different atomic step edges evidences a relatively poor quality of the crystals. This inhomogeneous crystal structure with possible repetitions of quintuple layers may result in different cleaving, unlike two ideal cases to cleave either on quintuple layer or on septuple layer. The STS data are sample-dependent and, very likely, tip-state dependent. It is noteworthy that the obtained spectra bear no clear similarities with the STS spectra in [115, 140, 149]. Presumably, the discrepancy of the spectroscopy data is related to the cation exchange as well as the abovementioned imperfection of the crystal stacking. Nevertheless, the reliable temperature-dependent STS data on the quintuple layer surface termination show no signatures of both the antiferromagnetic phase transition and the surface state gap opening.

# Chapter 5

## Summary

In this work two material classes were investigated at the atomic scale by means of low-temperature STM. Namely, they are conventional topological insulators ( $\text{Bi}_2\text{Te}_3$ ) and intrinsic magnetic topological insulators ( $\text{MnBi}_2\text{Te}_4$  and  $\text{MnBi}_4\text{Te}_7$ ). All the experimental results are shown in Chapter 4.

Measurements on  $\text{Bi}_2\text{Te}_3$  single crystals reveal atomically flat surfaces with densely distributed defects of various origin consistent with the literature data. High resolution QPI data were measured in a relatively large energy range  $[-600; 300]$  mV and provide energy dependent interference patterns as expected for dispersive electronic structures. For their comparison with the existing ARPES band structure data the calculations of the spin-selective JDOS (including the intricate three-dimensional spin texture of the material) were performed, which show a considerable agreement with the experimental data. Topological properties of the investigated compound were clearly demonstrated by the absence of the backscattering along with the linear energy dispersion of the dominant QPI vector. In addition, non-dispersive scattering was observed at some energies and associated with the bulk-to-surface scattering. This allowed to give a rough estimation of the bulk energy gap width in the measured samples. To the best knowledge, the QPI data were measured for the first time in the magnetic field on this compound. It was found that there are no significant changes in the QPI caused by magnetic fields up to 15 T. The backscattering processes do not manifest themselves even at such a strong field proving that the strong spin-orbit coupling in  $\text{Bi}_2\text{Te}_3$  prevents the lifting of the topological protection of the surface states in this material.

Single crystals of  $\text{MnBi}_2\text{Te}_4$  show atomically corrugated surface with pronounced electronic modulations revealing two superstructures in the Fourier transform which appear due to the ubiquitous Mn/Bi antisite intermixing in these crystals. The STS data provide an example of the  $dI/dU$  spectra with a zero DOS region below the Fermi energy. This is, most probably, one of the very first magnetic exchange gap in magnetic topological insulators measured by STS. The gap width of 25 meV is

in a reasonable agreement with the surface band structure calculations of  $\text{MnBi}_2\text{Te}_4$  including the cation intermixing. From the topographic, point spectroscopic and QPI data one can conclude that the measured surfaces are chemically inhomogeneous with different concentrations of Mn/Bi defects which lead to the regions with their higher (smaller) influence on the electronic structure of the compound, thus exhibiting ungapped (gapped) tunneling spectra. Meanwhile, other proposed scenarios (altered surface magnetism different from that in the bulk, magnetic domains formation, resonance states, surface states relocation to deeper layers) are also viable and can not be neglected.

The STM data obtained on the other example of the intrinsic magnetic topological insulators,  $\text{MnBi}_4\text{Te}_7$  allow to distinguish two kinds of surfaces since the material has two cleaving options (quintuple layer and septuple layer terminations). Different atomic step heights were found and possible repetitions of quintuple layers point towards a poor (but improvable) quality of the crystals. Besides that, the obtained  $dI/dU$  spectra show no clear similarities with the literature data on this compound. The cation exchange and the quality of the crystals are supposed to affect the STS data. Although, no signatures of the antiferromagnetic phase transition and the surface states gap opening were found from some reliable temperature-dependent STS data on the quintuple layer surface termination.

It is also worth to highlight that on high quality crystals of  $\text{Bi}_2\text{Te}_3$  even with strong intrinsic disorder the quality of the obtained data turned out to be fairly good. As for  $\text{MnBi}_2\text{Te}_4$  and  $\text{MnBi}_4\text{Te}_7$ , the crystals which were measured in this work are of a pioneering stage of research, and, first of all, the existing crystal growth techniques need to be improved to reduce the cation disorder which is also still reported in the most recent literature [208, 209]. This explains the abovementioned difficulties to reliably obtain the data on these materials, and, therefore, this should be readdressed to a future work.

# Appendix A

## Additional experimental and simulated QPI data on $\text{Bi}_2\text{Te}_3$

More QPI data measured on the  $\text{Bi}_2\text{Te}_3$  samples are presented in this section. The data were acquired on 5 different cleaved samples of the same crystal in total. In general, no significant differences in the FT-QPI patterns measured at different conditions (sample, surface spot location and size,  $I_T$ ,  $T$ ) were found. There are some changes in the intensity distributions (see Fig. A.0.1a) which could stem from different sample-tip combinations used in the experiments or slightly different stoichiometry of the samples. One representative example for comparison is shown in Fig. A.0.1a, where 2 FT-QPI patterns measured on different samples at  $U_{bias} = 300$  mV are presented. Both FT-QPI patterns demonstrate almost identical two six-fold symmetric scattering vectors oriented in the  $\Gamma$ -M direction. Note that their length-scales are nearly the same for both data. The  $dI/dU$  maps were also measured at the energies higher than those mentioned in section 4.1.3. In particular, the data obtained at  $U_{bias} = 350, 400, 450$ , and  $500$  mV (see Fig. A.0.1b) show a little increase of the dominant scattering vector's length. The extracted energy dispersion in the  $\Gamma$ -M direction (where the intensity is the most pronounced) of all the FT-QPI patterns was shown in Fig. 4.1.14. The main trend in the data is a clear linear energy dispersion confirmed by several measurements. The inner QPI intensity peaks were found only at high energies and have no certain energy dispersion, thus, they are, most likely, of the bulk origin as mentioned in section 4.1.4. The scattering vector splitting observed in the current work (see section 4.1.4) on "sample 1" was not resolved on another sample ("sample 2") due to likely higher noise in the experiment on that sample. In addition, the  $dI/dU$  maps were also measured at the bias voltages from  $-600$  mV down to  $-800$  mV but at those energies the FT-QPI patterns remain rather ill-defined.

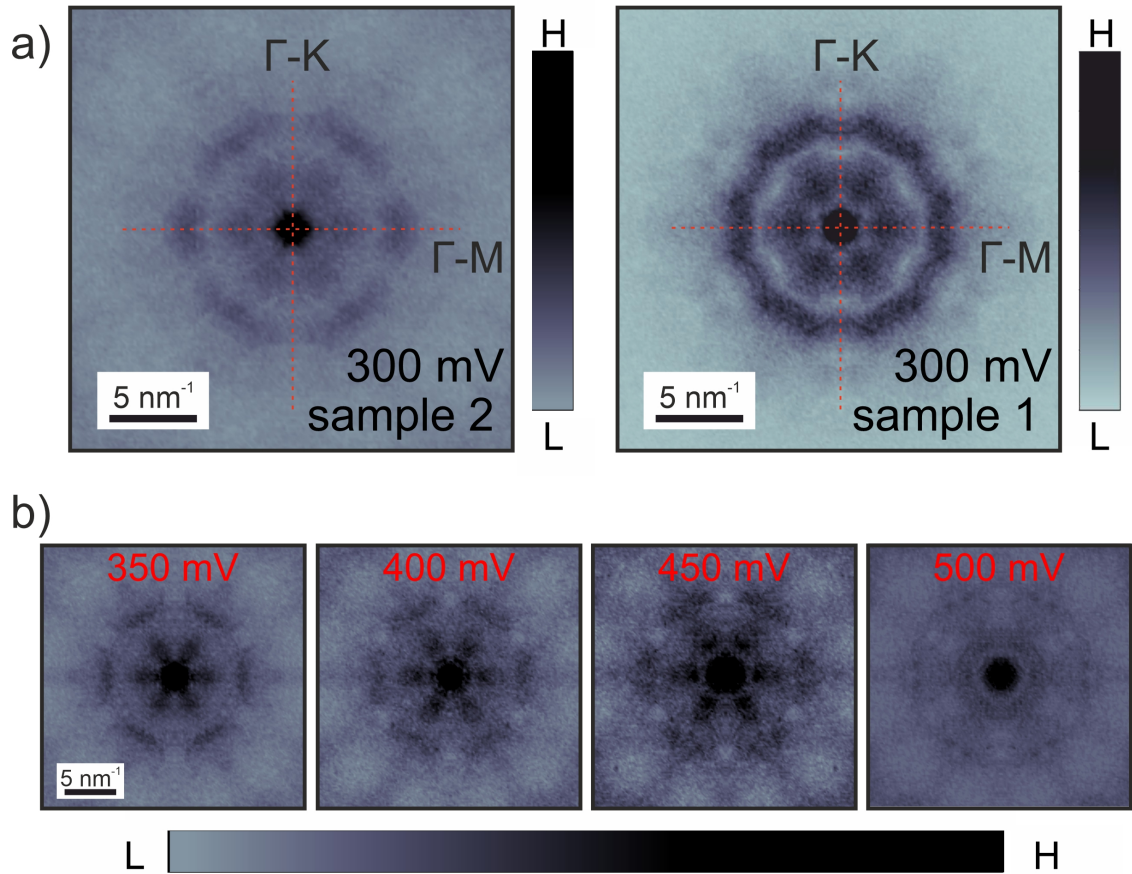


**Fig. A.0.1** a) Representative symmetrized FT-QPI patterns measured on different samples at the same  $U_{bias} = 300$  mV. The data obtained on the "sample 1" were presented in sections 4.1.3 and 4.1.4. The high-symmetry directions are indicated with red lines. b) FT-QPI patterns (after the symmetrization) measured on the same  $60 \text{ nm} \times 60 \text{ nm}$  surface spot of the "sample 2" at  $U_{bias} = 350, 400, 450$ , and  $500$  mV. The scalebar is indicated on the left image and is the same for all the patterns.

As mentioned in section 4.1.4, the FT-QPI patterns of the  $dI/dU$  maps discussed there exhibit intensity variations not only in the  $\Gamma$ -M direction, but also in the  $\Gamma$ -K direction. In general, the QPI peak intensities are weaker in the  $\Gamma$ -K direction compared to the  $\Gamma$ -M direction as illustrated in Fig. A.0.2b for  $U_{bias} = 200$  mV, for example. The QPI intensity profiles in the  $\Gamma$ -K direction were analyzed in the same way as for the  $\Gamma$ -M direction using Gaussian fit of the peaks. The resulting energy dispersion in both high-symmetry directions is shown in Fig. A.0.2c, where ARPES extracted dispersions for all possible scattering vectors  $\mathbf{q}_1$ – $\mathbf{q}_6$  are plotted on top for comparison. The dominant QPI scattering vector in the  $\Gamma$ -K direction has values which are very close to that for the  $\Gamma$ -M direction (mainly associated with  $\mathbf{q}_{SS}$ , i.e. some combination of  $\mathbf{q}_2$  and  $\mathbf{q}_5$ ). The linear fit of the energy dispersion in the  $\Gamma$ -K direction provides the Dirac point energy value of around  $-372$  mV with the Dirac velocity of around  $4.6 \times 10^5$  m/s similar to the values derived from the  $\Gamma$ -M dispersion. There is also the second peak (dubbed  $\mathbf{q}_{SB}$  in section 4.1.4) in the

---

## APPENDIX A. ADDITIONAL EXPERIMENTAL AND SIMULATED QPI DATA ON $\text{Bi}_2\text{Te}_3$

---

QPI intensity profiles in the  $\Gamma$ -K direction at the bias voltages 100–250 mV with no certain dispersion as was found in section 4.1.4 for the  $\Gamma$ -M direction. Unlike for the  $\Gamma$ -M direction, it was not possible to find a splitting of the scattering vector in the  $\Gamma$ -K direction because of less pronounced intensity peaks. The dominant scattering vector in the  $\Gamma$ -K direction in the QPI data (see Fig. A.0.2c) has significantly different dispersion compared to the vectors  $\mathbf{q}_3$ ,  $\mathbf{q}_6$  and  $\mathbf{q}_1$  (the backscattering vector which must not exist). Given that, one could assume that the intensity peaks in the  $\Gamma$ -K direction might arise from the  $\mathbf{q}_3$  or  $\mathbf{q}_6$  scattering process if the shape of constant-energy contour and/or the DOS variations are different from that one which was measured by ARPES [8,53]. Possible deviations of the electronic structure could occur due to the material disorder.

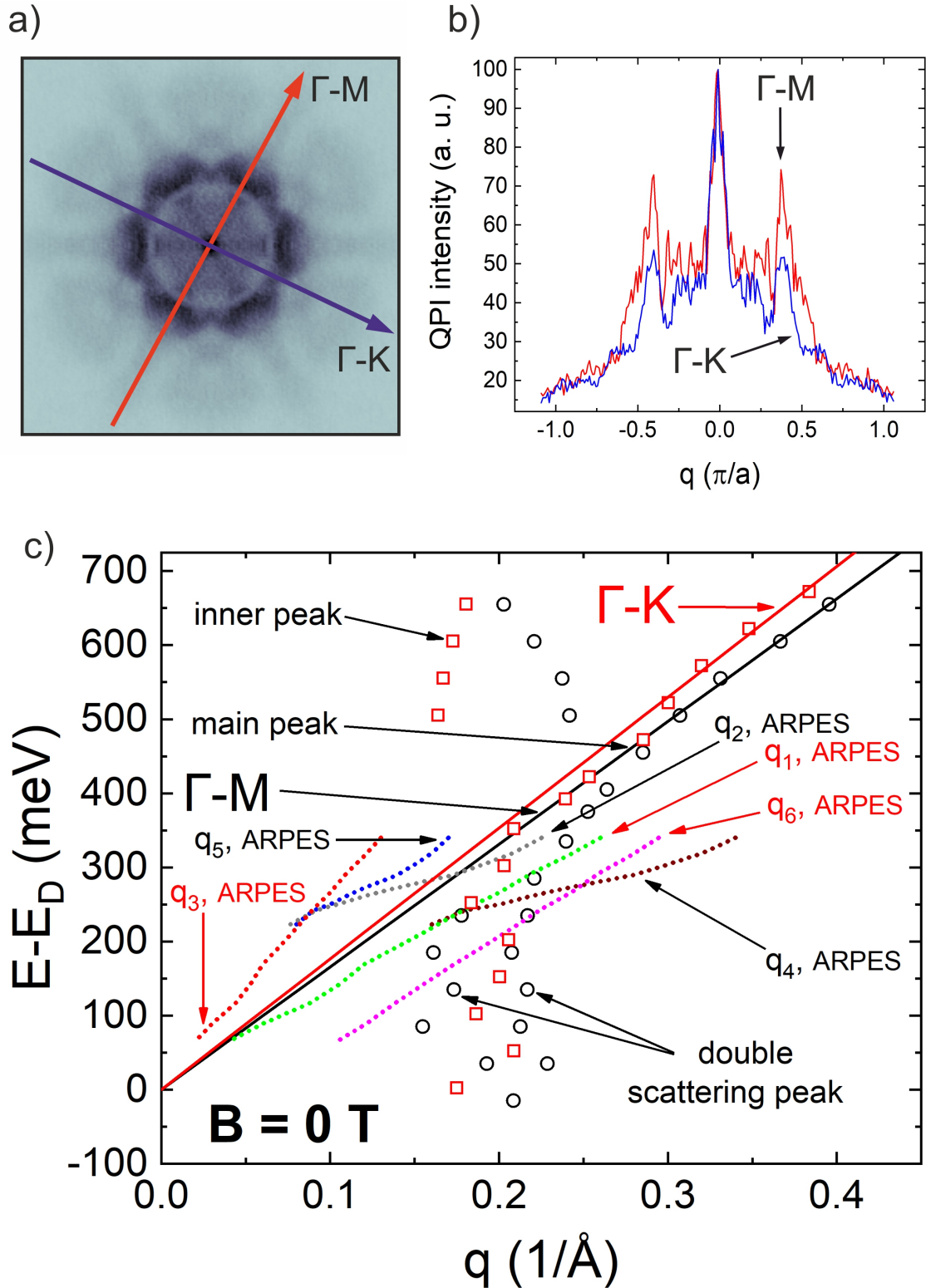


**Fig. A.0.2** a) Symmetrized FT-QPI pattern obtained at  $U_{bias} = 200$  mV. b) Intensity profiles of the FT-QPI pattern in a) taken along the  $\Gamma$ -M and  $\Gamma$ -K directions marked with the red and blue arrows in a), respectively. c) QPI and ARPES energy dispersion for both  $\Gamma$ -M and  $\Gamma$ -K directions. The energies are counted from the Dirac point estimated from the linear dispersion in the  $\Gamma$ -M direction.

As mentioned in section 4.1.3, the symmetrized FT-QPI patterns presented there

were cut at the edges for better demonstration of the QPI features. This led to the fact that, in particular, the Bragg peaks were also cut out. One example of raw FT-QPI patterns with visible Bragg peaks is presented in Fig. A.0.3.

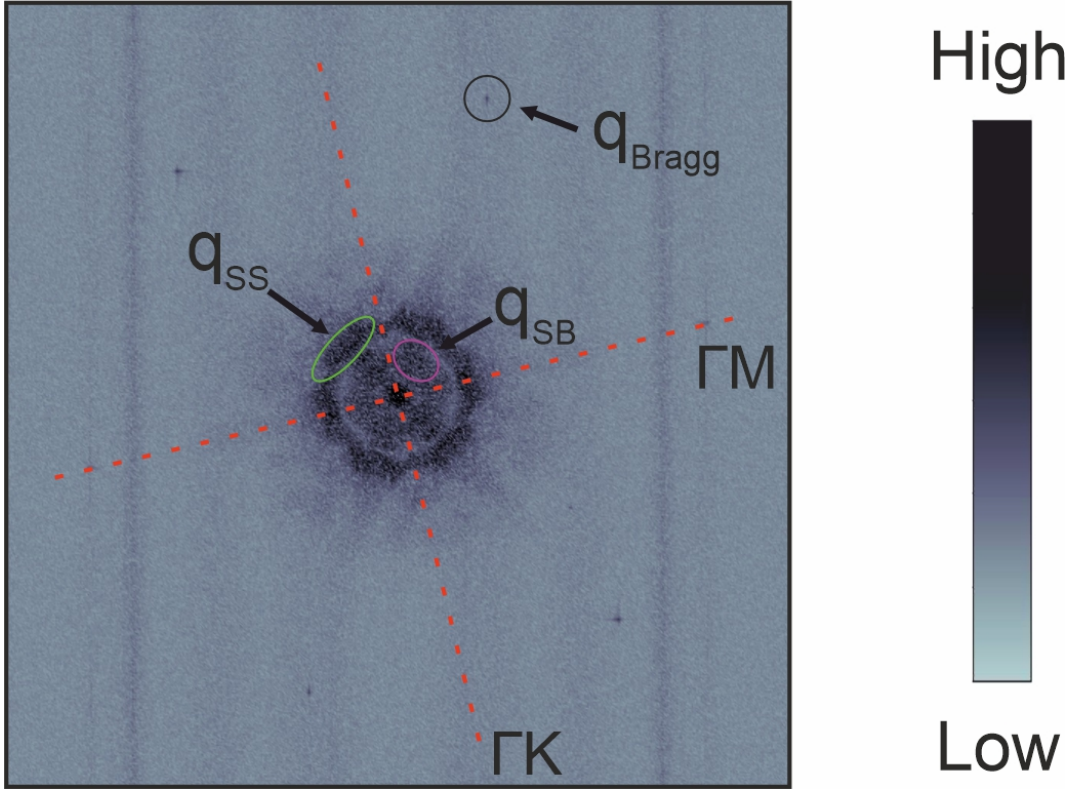


**Fig. A.0.3** a) Example of a raw FT-QPI pattern measured at  $U_{bias} = 250$  mV. The intensity spots in the  $\Gamma$ -M direction  $q_{SS}$  and  $q_{SB}$  discussed in Chapter 4 are marked by green and magenta ellipses, respectively, while one of the six-fold symmetric Bragg peaks is indicated by the black circle. High-symmetry crystallographic directions are labelled.

Concerning the QPI simulations, as mentioned in section 4.1.4, the three-fold symmetric scattering potential was used in the QPI simulations. It comes from the dominant defect type in the measured STM data. The scattering potential was modeled as follows:

$$V = \text{const} \times \begin{cases} \exp\left(-\frac{|\theta - \pi/6|}{\pi/48}\right), & \theta = \left[-\frac{\pi}{6}; \frac{\pi}{2}\right], \\ \exp\left(-\frac{|\theta - 5\pi/6|}{\pi/48}\right), & \theta = \left[\frac{\pi}{2}; \frac{7\pi}{6}\right], \\ \exp\left(-\frac{|\theta - 3\pi/2|}{\pi/48}\right), & \theta = \left[\frac{7\pi}{6}; \frac{11\pi}{6}\right], \end{cases} \quad (\text{A.0.1})$$

where the angle  $\theta$  defines the vector  $\mathbf{k}$  in reciprocal space and was introduced in section 4.1.4.

Fig. A.0.4 represents an example of the effect of the influence of the scattering potential and the out-of-plane spin component on the spin-dependent scattering probability pattern for the hexagonally warped constant-energy contour. Fig. A.0.4a

shows the result, when both are not taken into account. Fig. A.0.4b corresponds to the case, when only the scattering potential is considered, and results in the suppressed spin-dependent scattering probability intensity of the inner flower-like shaped pattern. Fig. A.0.4c illustrates a weaker suppression of this inner pattern which is caused by including the out-of-plane spin component. The final result is plotted in Fig. A.0.4d and was obtained taking into account both the scattering potential and the out-of-plane spin component, and the inner flower-like pattern becomes significantly suppressed compared to Fig. A.0.4a.

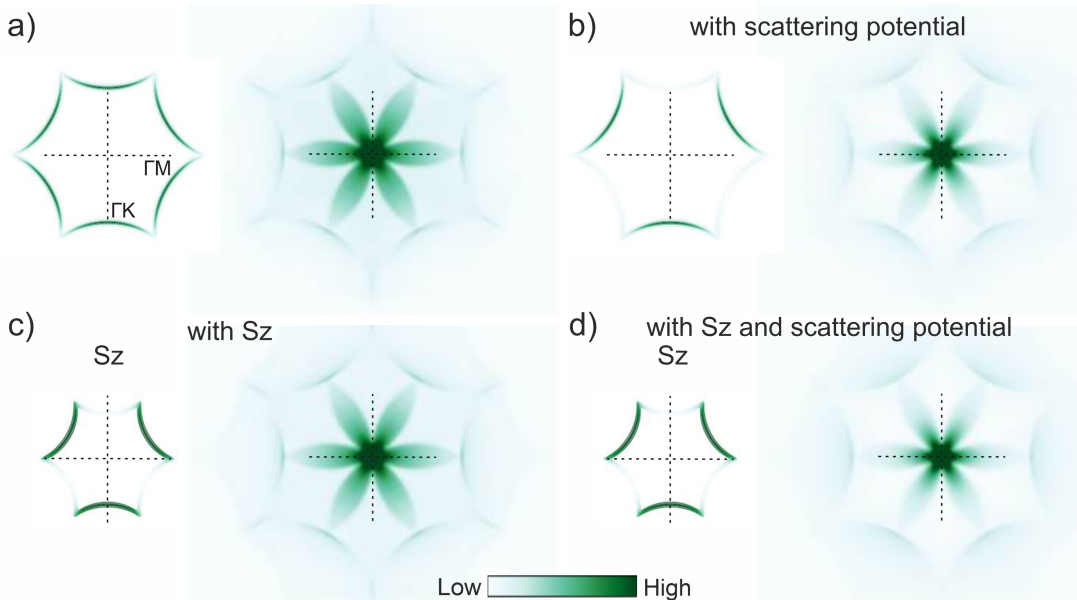


**Fig. A.0.4** Schematic illustration of the spin-dependent scattering probability calculations with the out-of-plane spin component and the scattering potential. The constant-energy contour is shown on the left sides in a) and b) before and after the three-fold scattering potential was implemented, respectively. The out-of-plane spin texture is plotted on the left sides in c) and d). The high-symmetry directions and the scalebars are the same for all the presented figures.

The DOS was modeled by the Gaussian distribution on each of the six arcs of the constant-energy contour, e.g., for  $\theta = [0; \pi/3]$  it is proportional to  $\exp\left(-\frac{(i - n/12)^2}{2\sigma^2}\right)$ , where  $i$  and  $n = 1000$  are the index of a certain point and the total number of points on the modeled constant-energy contour. Fig. A.0.5 shows the evolution of the spin-dependent scattering probability patterns for the hexagonally warped surface constant-energy contour when the width  $\sigma$  of the Gaussian distribution of the DOS is changing from 10 to 80. The best match to the measured QPI data was found at  $\sigma = 40$ , which corresponds to the DOS ratio of about 10:1 in the middle of the arc of the constant-energy contour and at the corner. In particular, at lower  $\sigma$  values the shape of the spin-dependent scattering probability scattering peaks differs from that obtained in the experiment, and at higher values of  $\sigma$  the inner flower-like shaped pattern becomes more intense (because it results from scattering within a

single arc, which has a larger DOS at the corners at higher  $\sigma$  values).

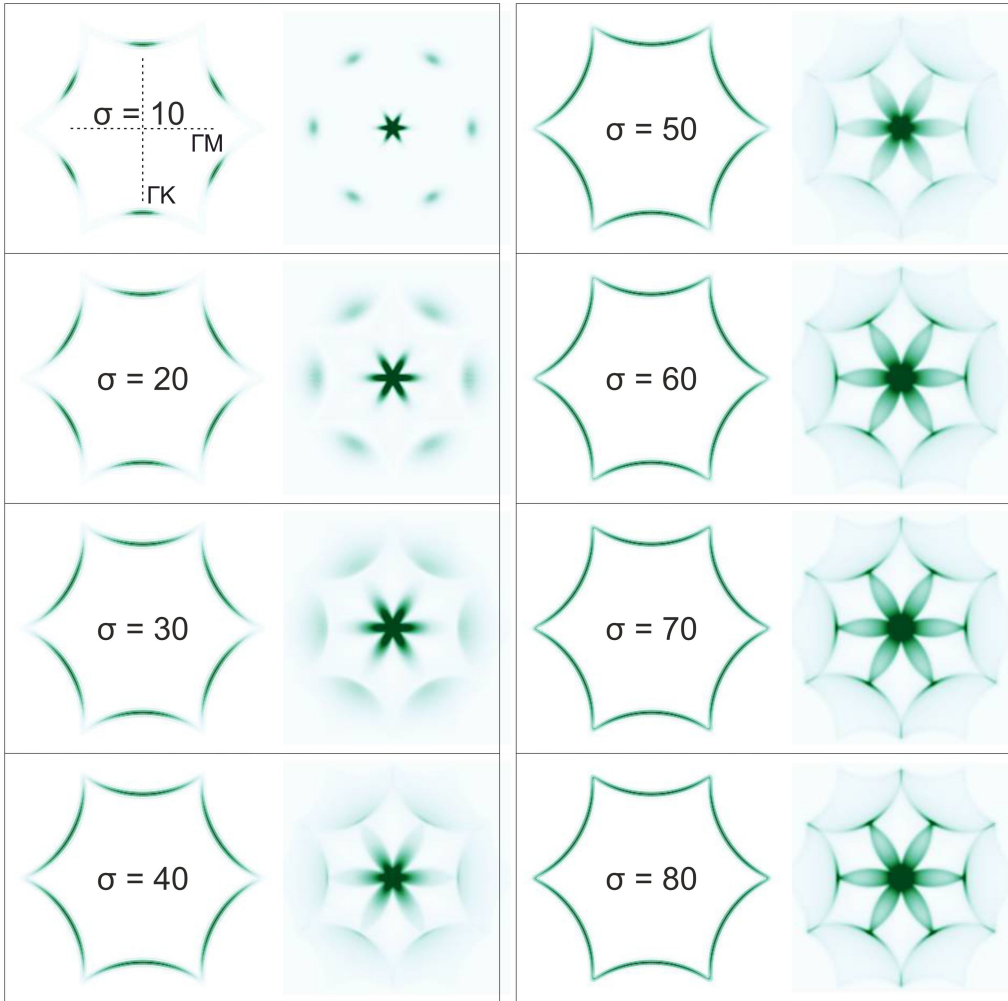


**Fig. A.0.5** Hexagonally warped constant-energy contours (on the left sides) with different widths  $\sigma$  of the Gaussian distribution of the DOS and the corresponding spin-dependent scattering probability patterns (on the right sides). The high-symmetry directions and the scales are the same for all the presented figures. The color scale is the same as that in Fig. A.0.4.

By analyzing the FT-QPI data measured in the energy range at which the bulk conduction band appears, it is important to distinguish contributions of the surface states and the bulk states into the spin-dependent scattering probability pattern (see the constant-energy contour in Fig. A.0.6a). Fig. A.0.6b represents a superposition of 3 spin-dependent scattering probability patterns arising from scattering only within the surface constant-energy contour, bulk-to-surface scattering and scattering only within the bulk conduction band, which are plotted separately in Figs. A.0.6c-e, respectively.

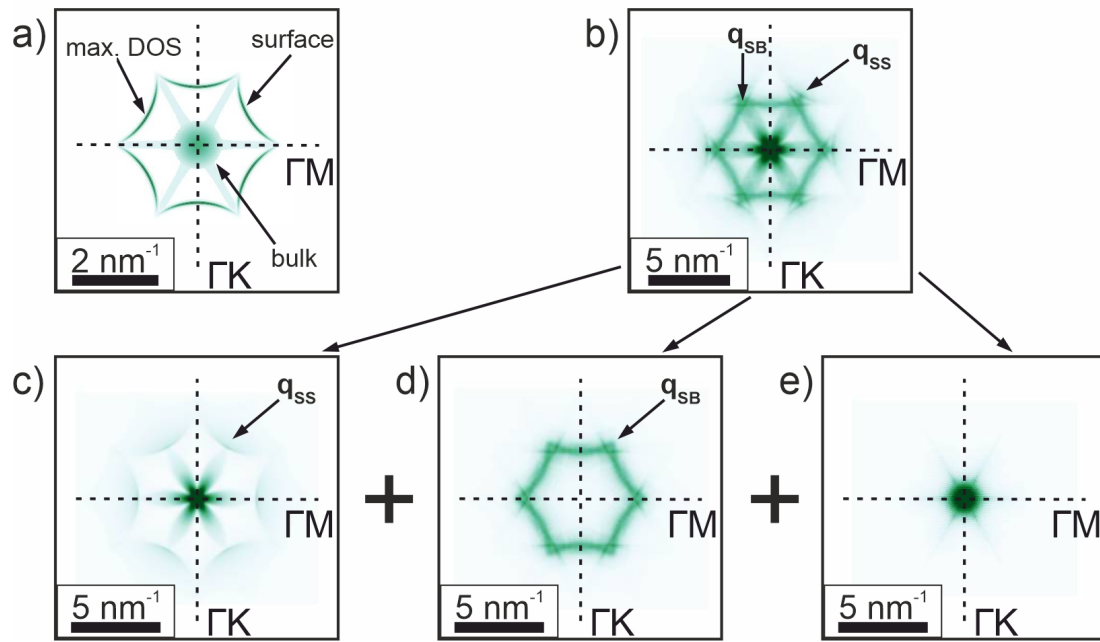


**Fig. A.0.6** Different contributions to the total spin-dependent scattering probability pattern in b) for the constant-energy contour plotted in a) corresponding to the bulk conduction band. In particular, spin-dependent scattering probability calculations results for the surface-to-surface, bulk-to-surface and bulk-to-bulk scattering are presented in c), d) and e), respectively. The color scale is the same as that in Fig. A.0.4.

## Appendix B

# Symmetrization procedure of the FT-QPI patterns

All the FT-QPI patterns presented in this work on both  $\text{Bi}_2\text{Te}_3$  and  $\text{MnBi}_2\text{Te}_4$  compounds were symmetrized according to the six-fold symmetric crystal structure. The aim was to increase the signal-to-noise ratio for a more accurate analysis of the QPI features. The symmetrization procedure was performed with the use of WSxM software [175] in the following way. As an example, the  $dI/dU$  map measured at  $U_{bias} = 300$  mV at  $B = 0$  T on  $\text{Bi}_2\text{Te}_3$  with its Fourier transformation are presented in Figs. B.0.1a,b. For the symmetrization of the FT-QPI pattern shown in Fig. B.0.1b one needs to take in WSxM QPI intensity profiles across two opposite QPI spots (the most pronounced spots are in the  $\Gamma$ -M direction) unless the line profile looks the most symmetrical. Using the option "Rotate angle" in WSxM one can rotate the FT-QPI pattern in the way that those two opposite spots become aligned horizontally (or vertically). Note that by doing this the number of pixels in the pattern becomes larger, and the new pixels at the edges acquire the average intensity of the entire image. Further, one can take one of the directions 1, 2 or 3 in Fig. B.0.1b (for example, the direction 1 shown in Fig. B.0.1c) to mirror the pattern vertically (see Fig. B.0.1d) and horizontally (see Fig. B.0.1e) and mirror the last one again vertically (see Fig. B.0.1f). All these 4 patterns shown in Figs. B.0.1c-f can be averaged providing one pattern plotted in Fig. B.0.2a.

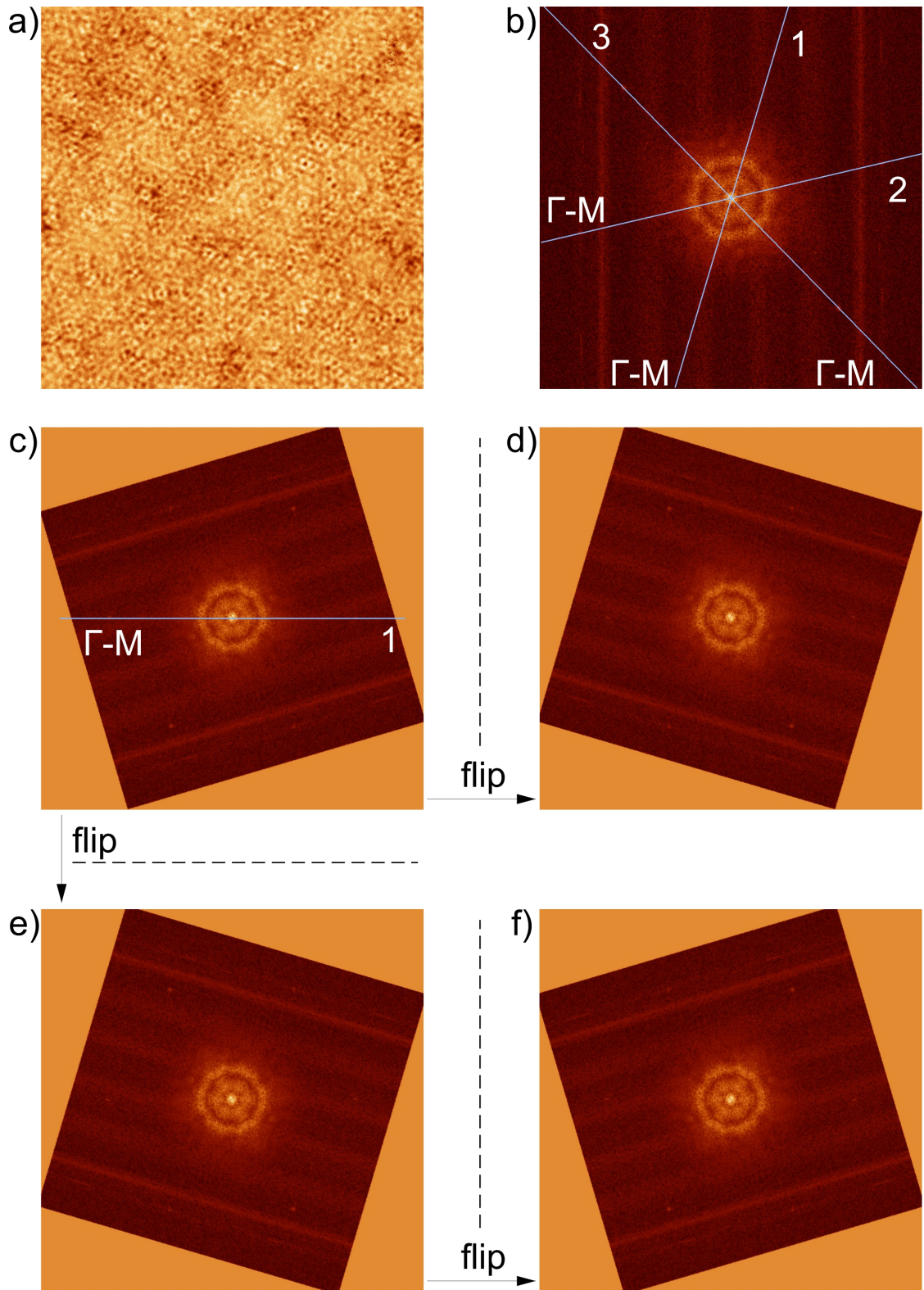


**Fig. B.0.1** a)  $dI/dU$  map measured at  $U_{bias} = 300$  mV at  $B = 0$  T on  $\text{Bi}_2\text{Te}_3$  in the present work. b) FT-QPI pattern of the data shown in a). c) FT-QPI pattern obtained by a rotation of the image b) making the direction 1 horizontal. d) The FT-QPI pattern shown in c) flipped around the vertical axis. e) The FT-QPI pattern shown in c) flipped around the horizontal axis. f) The FT-QPI pattern shown in e) flipped around the vertical axis.

## APPENDIX B. SYMMETRIZATION PROCEDURE OF THE FT-QPI PATTERNS

The same procedure has to be done for two other equivalent directions 2 and 3 in the initial FT-QPI pattern shown in Fig. B.0.1b. Finally, 3 patterns of different pixels numbers (see Figs. B.0.2a-c) have to be averaged. For that, the pattern with the lowest number of pixels remains unchanged, while the two others have to be cut at the edges in order to have the same number of pixels with the first one. All the three patterns are averaged and provide the final symmetrized FT-QPI pattern plotted in Fig. B.0.2d. Comparing the raw FT-QPI pattern (see Fig. B.0.1b) with the final one (see Fig. B.0.2d), it can be seen with the naked eye that the latter one looks less noisy than the former one. The signal-to-noise ratio is enhanced with respect to the initial data in Fig. B.0.1b because the signal was averaged while the noise in different directions was suppressed. It should be noted that one needs to take care of the symmetry of the patterns (i.e. they have to be symmetrical with respect to the center of the image) at each step of the symmetrization procedure in order not to lose the signal-to-noise ratio.

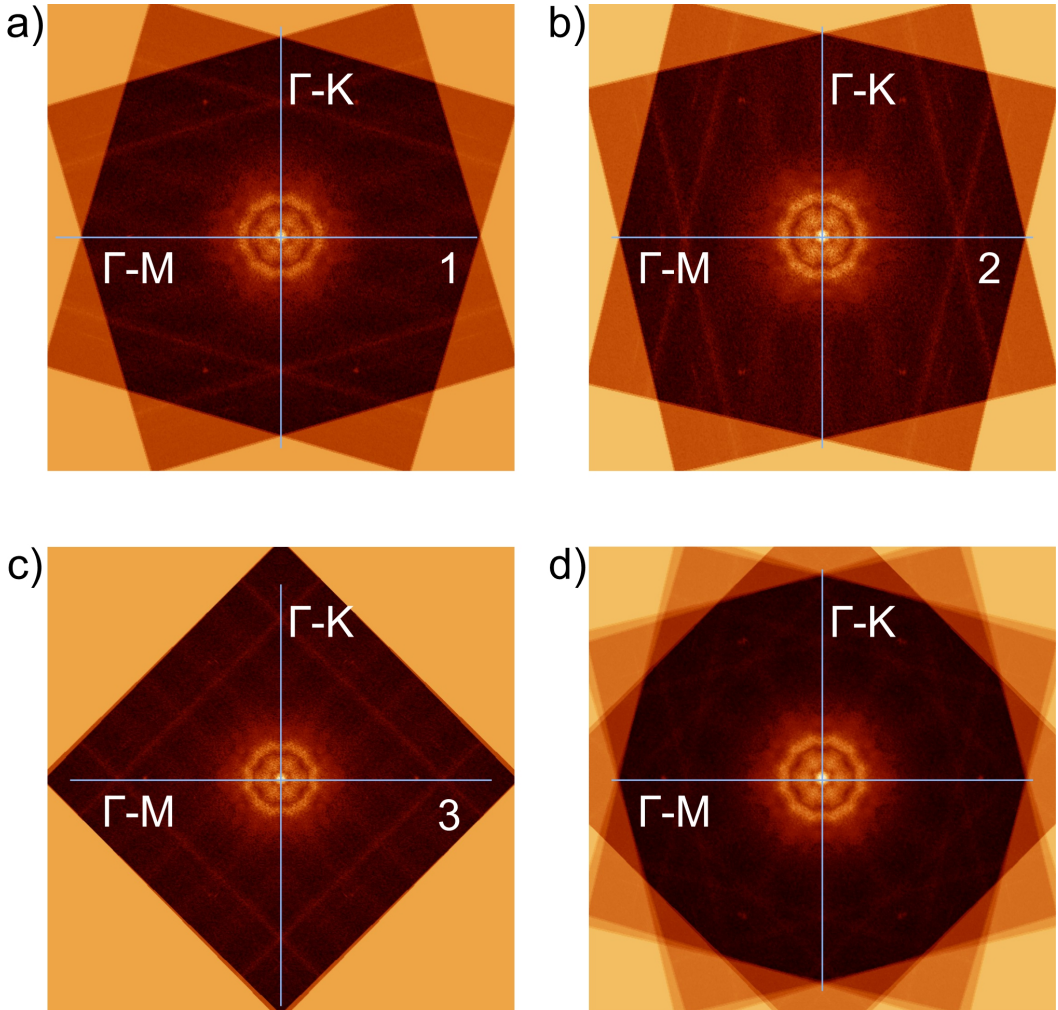


**Fig. B.0.2** a) FT-QPI pattern obtained by averaging of Figs. B.0.1c-f. b-c) FT-QPI patterns obtained by the procedure described for a) but for the directions 2 and 3 in Fig. B.0.1b, respectively. d) The final symmetrized FT-QPI pattern.



# Appendix C

## Program codes

One example of the Python program code for JDOS and spin-dependent scattering probability calculations discussed in section 4.1.4 is presented below. This corresponds to the constant-energy contour including both warped hexagon for surface states and bulk conduction states as shown in Fig. 4.1.18d. In this case, one warped hexagon with maximal DOS on the arcs was considered with two inner and two outer warped hexagons of lower DOS and bulk conduction states inside. The DOS variation on the warped hexagons and the bulk conduction band was modeled using the Gaussian distribution with maximal DOS in the middle on the arcs of the warped hexagon and also in the  $\Gamma$ -point, respectively. Since the DOS distribution on the constant-energy contour could not be explicitly extracted from the existing ARPES data on  $\text{Bi}_2\text{Te}_3$  [8,53], the parameters of the Gaussians were adjusted as to obtain reasonable simulation results.

```
#####
# Author: Vladislav Nagorkin
# Created: 29.08.2022
#####

import numpy as np
import matplotlib.pyplot as plt
from matplotlib import cm

X = [] #array for qx
Y = [] #array for qy
Z = [] #array for JDOS
Z1 = [] #array for spin-dependent scattering probability

#number of points on one warped hexagonal constant-energy contour
n = 1000

t = np.arange(0, 1, 1/n)
#define the middle warped hexagon(which has the maximal DOS)
```

```
def kxmiddle(t):
    return 5*np.cos(2*np.pi*t) + 0.8*np.cos(10*np.pi*t)
def kymiddle(t):
    return 5*np.sin(2*np.pi*t) - 0.8*np.sin(10*np.pi*t)
plt.plot(kxmiddle(t), kymiddle(t), color = 'red')
plt.axis('scaled')
plt.show()

#define the inner warped hexagon
def kxinner(t):
    return 0.95*(5*np.cos(2*np.pi*t) + 0.8*np.cos(10*np.pi*t))
def kyinner(t):
    return 0.95*(5*np.sin(2*np.pi*t) - 0.8*np.sin(10*np.pi*t))
plt.plot(kxinner(t), kyinner(t), color = 'black')
plt.axis('scaled')
plt.show()

#define the outer warped hexagon
def kxouter(t):
    return 1.05*(5*np.cos(2*np.pi*t) + 0.8*np.cos(10*np.pi*t))
def kyouter(t):
    return 1.05*(5*np.sin(2*np.pi*t) - 0.8*np.sin(10*np.pi*t))
plt.plot(kxouter(t), kyouter(t), color = 'black')
plt.axis('scaled')
plt.show()

#define the inner inner warped hexagon
def kxinnerinner(t):
    return 0.98*(5*np.cos(2*np.pi*t) + 0.8*np.cos(10*np.pi*t))
def kyinnerinner(t):
    return 0.98*(5*np.sin(2*np.pi*t) - 0.8*np.sin(10*np.pi*t))
plt.plot(kxinnerinner(t), kyinnerinner(t), color = 'black')
plt.axis('scaled')
plt.show()

#define the outer outer warped hexagon
def kxouterouter(t):
    return 1.02*(5*np.cos(2*np.pi*t) + 0.8*np.cos(10*np.pi*t))
def kyouterouter(t):
    return 1.02*(5*np.sin(2*np.pi*t) - 0.8*np.sin(10*np.pi*t))
plt.plot(kxouterouter(t), kyouterouter(t), color = 'black')
plt.axis('scaled')
plt.show()

kax = np.zeros(5*n+414+312)
kay = np.zeros(5*n+414+312)
```

```
#define an array of DOS
intensity = np.zeros(5*n+414+312)

#define Gaussian function
def gaussian(x,amp=1,mean=0,sigma=1):
    return amp*np.exp(-(x-mean)**2/(2*sigma**2))

sz = np.zeros(5*n+0)                      #out-of-plane spin component
sp = np.zeros(5*n+0)                      #scattering potential

sigma1 = 40

#modeling the DOS distribution for the middle hexagon
for i in np.arange (0, n//6, 1):
    t = i/n
    kax[i] = kxmiddle(t)
    kay[i] = kymiddle(t)
    intensity[i] = gaussian(i,5,n//12,sigma1)
for i in np.arange (n//6, n//3, 1):
    t = i/n
    kax[i] = kxmiddle(t)
    kay[i] = kymiddle(t)
    intensity[i] = gaussian(i,5,n//4,sigma1)
for i in np.arange (n//3, n//2, 1):
    t = i/n
    kax[i] = kxmiddle(t)
    kay[i] = kymiddle(t)
    intensity[i] = gaussian(i,5,5*n//12,sigma1)
for i in np.arange (n//2, 2*n//3, 1):
    t = i/n
    kax[i] = kxmiddle(t)
    kay[i] = kymiddle(t)
    intensity[i] = gaussian(i,5,7*n//12,sigma1)
for i in np.arange (2*n//3, 5*n//6, 1):
    t = i/n
    kax[i] = kxmiddle(t)
    kay[i] = kymiddle(t)
    intensity[i] = gaussian(i,5,3*n//4,sigma1)
for i in np.arange (5*n//6, n, 1):
    t = i/n
    kax[i] = kxmiddle(t)
    kay[i] = kymiddle(t)
    intensity[i] = gaussian(i,5,11*n//12,sigma1)

#modeling the DOS distribution for the inner hexagon
for i in np.arange (n, n + n//6, 1):
    tprime = (i-n)/n
    kax[i] = kxinner(tprime)
```

```
    kay[i] = kyinner(tprime)
    intensity[i] = gaussian(i,1,n + n//12,sigma1)
for i in np.arange (n + n//6, n + n//3, 1):
    tprime = (i-n)/n
    kax[i] = kxinner(tprime)
    kay[i] = kyinner(tprime)
    intensity[i] = gaussian(i,1,n + n//4,sigma1)
for i in np.arange (n + n//3, n + n//2, 1):
    tprime = (i-n)/n
    kax[i] = kxinner(tprime)
    kay[i] = kyinner(tprime)
    intensity[i] = gaussian(i,1,n + 5*n//12,sigma1)
for i in np.arange (n + n//2, n + 2*n//3, 1):
    tprime = (i-n)/n
    kax[i] = kxinner(tprime)
    kay[i] = kyinner(tprime)
    intensity[i] = gaussian(i,1,n + 7*n//12,sigma1)
for i in np.arange (n + 2*n//3, n + 5*n//6, 1):
    tprime = (i-n)/n
    kax[i] = kxinner(tprime)
    kay[i] = kyinner(tprime)
    intensity[i] = gaussian(i,1,n + 3*n//4,sigma1)
for i in np.arange (n + 5*n//6, 2*n, 1):
    tprime = (i-n)/n
    kax[i] = kxinner(tprime)
    kay[i] = kyinner(tprime)
    intensity[i] = gaussian(i,1,n + 11*n//12,sigma1)

#modeling the DOS distribution for the outer hexagon
for i in np.arange (2*n, 2*n + n//6, 1):
    tprime = (i-2*n)/n
    kax[i] = kxouter(tprime)
    kay[i] = kyouter(tprime)
    intensity[i] = gaussian(i,1,2*n + n//12,sigma1)
for i in np.arange (2*n + n//6, 2*n + n//3, 1):
    tprime = (i-2*n)/n
    kax[i] = kxouter(tprime)
    kay[i] = kyouter(tprime)
    intensity[i] = gaussian(i,1,2*n + n//4,sigma1)
for i in np.arange (2*n + n//3, 2*n + n//2, 1):
    tprime = (i-2*n)/n
    kax[i] = kxouter(tprime)
    kay[i] = kyouter(tprime)
    intensity[i] = gaussian(i,1,2*n + 5*n//12,sigma1)
for i in np.arange (2*n + n//2, 2*n + 2*n//3, 1):
    tprime = (i-2*n)/n
    kax[i] = kxouter(tprime)
```

```
    kay[i] = kyouter(tprime)
    intensity[i] = gaussian(i,1,2*n + 7*n//12,sigma1)
for i in np.arange (2*n + 2*n//3, 2*n + 5*n//6, 1):
    tprime = (i-2*n)/n
    kax[i] = kxouter(tprime)
    kay[i] = kyouter(tprime)
    intensity[i] = gaussian(i,1,2*n + 3*n//4,sigma1)
for i in np.arange (2*n + 5*n//6, 3*n, 1):
    tprime = (i-2*n)/n
    kax[i] = kxouter(tprime)
    kay[i] = kyouter(tprime)
    intensity[i] = gaussian(i,1,2*n + 11*n//12,sigma1)

#modeling the DOS distribution for the inner inner hexagon
for i in np.arange (3*n, 3*n + n//6, 1):
    tprime = (i-3*n)/n
    kax[i] = kxinnerinner(tprime)
    kay[i] = kyinnerinner(tprime)
    intensity[i] = gaussian(i,3,3*n + n//12,sigma1)
for i in np.arange (3*n + n//6, 3*n + n//3, 1):
    tprime = (i-3*n)/n
    kax[i] = kxinnerinner(tprime)
    kay[i] = kyinnerinner(tprime)
    intensity[i] = gaussian(i,3,3*n + n//4,sigma1)
for i in np.arange (3*n + n//3, 3*n + n//2, 1):
    tprime = (i-3*n)/n
    kax[i] = kxinnerinner(tprime)
    kay[i] = kyinnerinner(tprime)
    intensity[i] = gaussian(i,3,3*n + 5*n//12,sigma1)
for i in np.arange (3*n + n//2, 3*n + 2*n//3, 1):
    tprime = (i-3*n)/n
    kax[i] = kxinnerinner(tprime)
    kay[i] = kyinnerinner(tprime)
    intensity[i] = gaussian(i,3,3*n + 7*n//12,sigma1)
for i in np.arange (3*n + 2*n//3, 3*n + 5*n//6, 1):
    tprime = (i-3*n)/n
    kax[i] = kxinnerinner(tprime)
    kay[i] = kyinnerinner(tprime)
    intensity[i] = gaussian(i,3,3*n + 3*n//4,sigma1)
for i in np.arange (3*n + 5*n//6, 4*n, 1):
    tprime = (i-3*n)/n
    kax[i] = kxinnerinner(tprime)
    kay[i] = kyinnerinner(tprime)
    intensity[i] = gaussian(i,3,3*n + 11*n//12,sigma1)

#modeling the DOS distribution for the outer outer hexagon
for i in np.arange (4*n, 4*n + n//6, 1):
```

```
tprime = (i-4*n)/n
kax[i] = kxouterouter(tprime)
kay[i] = kyouterouter(tprime)
intensity[i] = gaussian(i,3,4*n + n//12,sigma1)
for i in np.arange (4*n + n//6, 4*n + n//3, 1):
    tprime = (i-4*n)/n
    kax[i] = kxouterouter(tprime)
    kay[i] = kyouterouter(tprime)
    intensity[i] = gaussian(i,3,4*n + n//4,sigma1)
for i in np.arange (4*n + n//3, 4*n + n//2, 1):
    tprime = (i-4*n)/n
    kax[i] = kxouterouter(tprime)
    kay[i] = kyouterouter(tprime)
    intensity[i] = gaussian(i,3,4*n + 5*n//12,sigma1)
for i in np.arange (4*n + n//2, 4*n + 2*n//3, 1):
    tprime = (i-4*n)/n
    kax[i] = kxouterouter(tprime)
    kay[i] = kyouterouter(tprime)
    intensity[i] = gaussian(i,3,4*n + 7*n//12,sigma1)
for i in np.arange (4*n + 2*n//3, 4*n + 5*n//6, 1):
    tprime = (i-4*n)/n
    kax[i] = kxouterouter(tprime)
    kay[i] = kyouterouter(tprime)
    intensity[i] = gaussian(i,3,4*n + 3*n//4,sigma1)
for i in np.arange (4*n + 5*n//6, 5*n, 1):
    tprime = (i-4*n)/n
    kax[i] = kxouterouter(tprime)
    kay[i] = kyouterouter(tprime)
    intensity[i] = gaussian(i,3,4*n + 11*n//12,sigma1)

#define bulk conduction band points
sigma2 = 1
for i in np.arange (5*n, 5*n+40, 1):
    kax[i] = 1.6*np.cos((i-5*n)*np.pi/20)
    kay[i] = 1.6*np.sin((i-5*n)*np.pi/20)
    intensity[i] = gaussian(1.1,3, 0, sigma2)
for i in np.arange (5*n+40, 5*n+78, 1):
    kax[i] = 1.5*np.cos((i-5*n-40)*np.pi/19)
    kay[i] = 1.5*np.sin((i-5*n-40)*np.pi/19)
    intensity[i] = gaussian(1.04,3, 0, sigma2)
for i in np.arange (5*n+78, 5*n+114, 1):
    kax[i] = 1.4*np.cos((i-5*n-78)*np.pi/18)
    kay[i] = 1.4*np.sin((i-5*n-78)*np.pi/18)
    intensity[i] = gaussian(0.98,3, 0, sigma2)
for i in np.arange (5*n+114, 5*n+148, 1):
    kax[i] = 1.3*np.cos((i-5*n-114)*np.pi/17)
    kay[i] = 1.3*np.sin((i-5*n-114)*np.pi/17)
```

```
intensity[i] = gaussian(0.92,3, 0, sigma2)
for i in np.arange (5*n+148, 5*n+180, 1):
    kax[i] = 1.2*np.cos((i-5*n-148)*np.pi/16)
    kay[i] = 1.2*np.sin((i-5*n-148)*np.pi/16)
    intensity[i] = gaussian(0.86,3, 0, sigma2)
for i in np.arange (5*n+180, 5*n+210, 1):
    kax[i] = 1.1*np.cos((i-5*n-180)*np.pi/15)
    kay[i] = 1.1*np.sin((i-5*n-180)*np.pi/15)
    intensity[i] = gaussian(0.8,3, 0, sigma2)
for i in np.arange (5*n+210, 5*n+238, 1):
    kax[i] = 1*np.cos((i-5*n-210)*np.pi/14)
    kay[i] = 1*np.sin((i-5*n-210)*np.pi/14)
    intensity[i] = gaussian(0.74,3, 0, sigma2)
for i in np.arange (5*n+238, 5*n+264, 1):
    kax[i] = 0.9*np.cos((i-5*n-238)*np.pi/13)
    kay[i] = 0.9*np.sin((i-5*n-238)*np.pi/13)
    intensity[i] = gaussian(0.68,3, 0, sigma2)
for i in np.arange (5*n+264, 5*n+288, 1):
    kax[i] = 0.8*np.cos((i-5*n-264)*np.pi/12)
    kay[i] = 0.8*np.sin((i-5*n-264)*np.pi/12)
    intensity[i] = gaussian(0.62,3, 0, sigma2)
for i in np.arange (5*n+288, 5*n+310, 1):
    kax[i] = 0.7*np.cos((i-5*n-288)*np.pi/11)
    kay[i] = 0.7*np.sin((i-5*n-288)*np.pi/11)
    intensity[i] = gaussian(0.56,3, 0, sigma2)
for i in np.arange (5*n+310, 5*n+330, 1):
    kax[i] = 0.6*np.cos((i-5*n-310)*np.pi/10)
    kay[i] = 0.6*np.sin((i-5*n-310)*np.pi/10)
    intensity[i] = gaussian(0.5,3, 0, sigma2)
for i in np.arange (5*n+330, 5*n+348, 1):
    kax[i] = 0.5*np.cos((i-5*n-330)*np.pi/9)
    kay[i] = 0.5*np.sin((i-5*n-330)*np.pi/9)
    intensity[i] = gaussian(0.44,3, 0, sigma2)
for i in np.arange (5*n+348, 5*n+364, 1):
    kax[i] = 0.4*np.cos((i-5*n-348)*np.pi/8)
    kay[i] = 0.4*np.sin((i-5*n-348)*np.pi/8)
    intensity[i] = gaussian(0.38,3, 0, sigma2)
for i in np.arange (5*n+364, 5*n+378, 1):
    kax[i] = 0.33*np.cos((i-5*n-364)*np.pi/7)
    kay[i] = 0.33*np.sin((i-5*n-364)*np.pi/7)
    intensity[i] = gaussian(0.32,3, 0, sigma2)
for i in np.arange (5*n+378, 5*n+390, 1):
    kax[i] = 0.26*np.cos((i-5*n-378)*np.pi/6)
    kay[i] = 0.26*np.sin((i-5*n-378)*np.pi/6)
    intensity[i] = gaussian(0.26,3, 0, sigma2)
for i in np.arange (5*n+390, 5*n+400, 1):
    kax[i] = 0.2*np.cos((i-5*n-390)*np.pi/5)
```

```
    kay[i] = 0.2*np.sin((i-5*n-390)*np.pi/5)
    intensity[i] = gaussian(0.2,3, 0, sigma2)
for i in np.arange (5*n+400, 5*n+408, 1):
    kax[i] = 0.14*np.cos((i-5*n-400)*np.pi/4)
    kay[i] = 0.14*np.sin((i-5*n-400)*np.pi/4)
    intensity[i] = gaussian(0.14,3, 0, sigma2)
for i in np.arange (5*n+408, 5*n+414, 1):
    kax[i] = 0.05*np.cos((i-5*n-408)*np.pi/3)
    kay[i] = 0.05*np.sin((i-5*n-408)*np.pi/3)
    intensity[i] = gaussian(0.05,3, 0, sigma2)

#bulk conduction band points in Gamma-M direction
sigma3 = 2
for i in np.arange (5*n+414, 5*n+414+6, 1):
    kax[i] = 1.9*np.cos((i-5*n-414)*np.pi/3)
    kay[i] = 1.9*np.sin((i-5*n-414)*np.pi/3)
    intensity[i] = gaussian(1.07,2,0,sigma3)
for i in np.arange (5*n+414+6, 5*n+414+12, 1):
    kax[i] = 1.9*np.cos((i-5*n-414-6)*np.pi/3 + 2*np.pi/n)
    kay[i] = 1.9*np.sin((i-5*n-414-6)*np.pi/3 + 2*np.pi/n)
    intensity[i] = gaussian(1.07,2,0,sigma3)
for i in np.arange (5*n+414+12, 5*n+414+18, 1):
    kax[i] = 1.9*np.cos((i-5*n-414-12)*np.pi/3 - 2*np.pi/n)
    kay[i] = 1.9*np.sin((i-5*n-414-12)*np.pi/3 - 2*np.pi/n)
    intensity[i] = gaussian(1.07,2,0,sigma3)
for i in np.arange (5*n+414+18, 5*n+414+24, 1):
    kax[i] = 1.9*np.cos((i-5*n-414-18)*np.pi/3 + 2*2*np.pi/n)
    kay[i] = 1.9*np.sin((i-5*n-414-18)*np.pi/3 + 2*2*np.pi/n)
    intensity[i] = gaussian(1.07,2,0,sigma3)
for i in np.arange (5*n+414+24, 5*n+414+30, 1):
    kax[i] = 1.9*np.cos((i-5*n-414-24)*np.pi/3 - 2*2*np.pi/n)
    kay[i] = 1.9*np.sin((i-5*n-414-24)*np.pi/3 - 2*2*np.pi/n)
    intensity[i] = gaussian(1.07,2,0,sigma3)
for i in np.arange (5*n+414+30, 5*n+414+36, 1):
    kax[i] = 1.9*np.cos((i-5*n-414-30)*np.pi/3 + 9*np.pi/n)
    kay[i] = 1.9*np.sin((i-5*n-414-30)*np.pi/3 + 9*np.pi/n)
    intensity[i] = gaussian(1.07,2,0,sigma3)
for i in np.arange (5*n+414+36, 5*n+414+42, 1):
    kax[i] = 1.9*np.cos((i-5*n-414-36)*np.pi/3 - 9*np.pi/n)
    kay[i] = 1.9*np.sin((i-5*n-414-36)*np.pi/3 - 9*np.pi/n)
    intensity[i] = gaussian(1.07,2,0,sigma3)
for i in np.arange (5*n+414+42, 5*n+414+48, 1):
    kax[i] = 1.7*np.cos((i-5*n-414-42)*np.pi/3 + 6*2*np.pi/n)
    kay[i] = 1.7*np.sin((i-5*n-414-42)*np.pi/3 + 6*2*np.pi/n)
    intensity[i] = gaussian(1.065,2,0,sigma3)
for i in np.arange (5*n+414+48, 5*n+414+54, 1):
    kax[i] = 1.7*np.cos((i-5*n-414-48)*np.pi/3 - 6*2*np.pi/n)
```

```
    kay[i] = 1.7*np.sin((i-5*n-414-48)*np.pi/3 - 6*2*np.pi/n)
    intensity[i] = gaussian(1.065,2,0,sigma3)
for i in np.arange (5*n+414+54, 5*n+414+60, 1):
    kax[i] = 2.1*np.cos((i-5*n-414-54)*np.pi/3)
    kay[i] = 2.1*np.sin((i-5*n-414-54)*np.pi/3)
    intensity[i] = gaussian(1.11,2,0,sigma3)
for i in np.arange (5*n+414+60, 5*n+414+66, 1):
    kax[i] = 2.1*np.cos((i-5*n-414-60)*np.pi/3 + 2*np.pi/n)
    kay[i] = 2.1*np.sin((i-5*n-414-60)*np.pi/3 + 2*np.pi/n)
    intensity[i] = gaussian(1.11,2,0,sigma3)
for i in np.arange (5*n+414+66, 5*n+414+72, 1):
    kax[i] = 2.1*np.cos((i-5*n-414-66)*np.pi/3 - 2*np.pi/n)
    kay[i] = 2.1*np.sin((i-5*n-414-66)*np.pi/3 - 2*np.pi/n)
    intensity[i] = gaussian(1.11,2,0,sigma3)
for i in np.arange (5*n+414+72, 5*n+414+78, 1):
    kax[i] = 2.1*np.cos((i-5*n-414-72)*np.pi/3 + 2*2*np.pi/n)
    kay[i] = 2.1*np.sin((i-5*n-414-72)*np.pi/3 + 2*2*np.pi/n)
    intensity[i] = gaussian(1.11,2,0,sigma3)
for i in np.arange (5*n+414+78, 5*n+414+84, 1):
    kax[i] = 2.1*np.cos((i-5*n-414-78)*np.pi/3 - 2*2*np.pi/n)
    kay[i] = 2.1*np.sin((i-5*n-414-78)*np.pi/3 - 2*2*np.pi/n)
    intensity[i] = gaussian(1.11,2,0,sigma3)
for i in np.arange (5*n+414+84, 5*n+414+90, 1):
    kax[i] = 2.1*np.cos((i-5*n-414-84)*np.pi/3 + 6*np.pi/n)
    kay[i] = 2.1*np.sin((i-5*n-414-84)*np.pi/3 + 6*np.pi/n)
    intensity[i] = gaussian(1.11,2,0,sigma3)
for i in np.arange (5*n+414+90, 5*n+414+96, 1):
    kax[i] = 2.1*np.cos((i-5*n-414-90)*np.pi/3 - 6*np.pi/n)
    kay[i] = 2.1*np.sin((i-5*n-414-90)*np.pi/3 - 6*np.pi/n)
    intensity[i] = gaussian(1.11,2,0,sigma3)
for i in np.arange (5*n+414+96, 5*n+414+102, 1):
    kax[i] = 2.4*np.cos((i-5*n-414-96)*np.pi/3)
    kay[i] = 2.4*np.sin((i-5*n-414-96)*np.pi/3)
    intensity[i] = gaussian(1.15,2,0,sigma3)
for i in np.arange (5*n+414+102, 5*n+414+108, 1):
    kax[i] = 2.4*np.cos((i-5*n-414-102)*np.pi/3 + 2*np.pi/n)
    kay[i] = 2.4*np.sin((i-5*n-414-102)*np.pi/3 + 2*np.pi/n)
    intensity[i] = gaussian(1.15,2,0,sigma3)
for i in np.arange (5*n+414+108, 5*n+414+114, 1):
    kax[i] = 2.4*np.cos((i-5*n-414-108)*np.pi/3 - 2*np.pi/n)
    kay[i] = 2.4*np.sin((i-5*n-414-108)*np.pi/3 - 2*np.pi/n)
    intensity[i] = gaussian(1.15,2,0,sigma3)
for i in np.arange (5*n+414+114, 5*n+414+120, 1):
    kax[i] = 2.4*np.cos((i-5*n-414-114)*np.pi/3 + 5.5*np.pi/n)
    kay[i] = 2.4*np.sin((i-5*n-414-114)*np.pi/3 + 5.5*np.pi/n)
    intensity[i] = gaussian(1.15,2,0,sigma3)
for i in np.arange (5*n+414+120, 5*n+414+126, 1):
```

```
kax[i] = 2.4*np.cos((i-5*n-414-120)*np.pi/3 - 5.5*np.pi/n)
kay[i] = 2.4*np.sin((i-5*n-414-120)*np.pi/3 - 5.5*np.pi/n)
intensity[i] = gaussian(1.15,2,0,sigma3)
for i in np.arange (5*n+414+126, 5*n+414+132, 1):
    kax[i] = 2.6*np.cos((i-5*n-414-126)*np.pi/3)
    kay[i] = 2.6*np.sin((i-5*n-414-126)*np.pi/3)
    intensity[i] = gaussian(1.19,2,0,sigma3)
for i in np.arange (5*n+414+132, 5*n+414+138, 1):
    kax[i] = 2.6*np.cos((i-5*n-414-132)*np.pi/3 + 2*np.pi/n)
    kay[i] = 2.6*np.sin((i-5*n-414-132)*np.pi/3 + 2*np.pi/n)
    intensity[i] = gaussian(1.19,2,0,sigma3)
for i in np.arange (5*n+414+138, 5*n+414+144, 1):
    kax[i] = 2.6*np.cos((i-5*n-414-138)*np.pi/3 - 2*np.pi/n)
    kay[i] = 2.6*np.sin((i-5*n-414-138)*np.pi/3 - 2*np.pi/n)
    intensity[i] = gaussian(1.19,2,0,sigma3)
for i in np.arange (5*n+414+144, 5*n+414+150, 1):
    kax[i] = 2.6*np.cos((i-5*n-414-144)*np.pi/3 + 4.5*np.pi/n)
    kay[i] = 2.6*np.sin((i-5*n-414-144)*np.pi/3 + 4.5*np.pi/n)
    intensity[i] = gaussian(1.19,2,0,sigma3)
for i in np.arange (5*n+414+150, 5*n+414+156, 1):
    kax[i] = 2.6*np.cos((i-5*n-414-150)*np.pi/3 - 4.5*np.pi/n)
    kay[i] = 2.6*np.sin((i-5*n-414-150)*np.pi/3 - 4.5*np.pi/n)
    intensity[i] = gaussian(1.19,2,0,sigma3)
for i in np.arange (5*n+414+156, 5*n+414+162, 1):
    kax[i] = 2.9*np.cos((i-5*n-414-156)*np.pi/3)
    kay[i] = 2.9*np.sin((i-5*n-414-156)*np.pi/3)
    intensity[i] = gaussian(1.23,2,0,sigma3)
for i in np.arange (5*n+414+162, 5*n+414+168, 1):
    kax[i] = 2.9*np.cos((i-5*n-414-162)*np.pi/3 + 2*np.pi/n)
    kay[i] = 2.9*np.sin((i-5*n-414-162)*np.pi/3 + 2*np.pi/n)
    intensity[i] = gaussian(1.23,2,0,sigma3)
for i in np.arange (5*n+414+168, 5*n+414+174, 1):
    kax[i] = 2.9*np.cos((i-5*n-414-168)*np.pi/3 - 2*np.pi/n)
    kay[i] = 2.9*np.sin((i-5*n-414-168)*np.pi/3 - 2*np.pi/n)
    intensity[i] = gaussian(1.23,2,0,sigma3)
for i in np.arange (5*n+414+174, 5*n+414+180, 1):
    kax[i] = 2.9*np.cos((i-5*n-414-174)*np.pi/3 + 3.5*np.pi/n)
    kay[i] = 2.9*np.sin((i-5*n-414-174)*np.pi/3 + 3.5*np.pi/n)
    intensity[i] = gaussian(1.23,2,0,sigma3)
for i in np.arange (5*n+414+180, 5*n+414+186, 1):
    kax[i] = 2.9*np.cos((i-5*n-414-180)*np.pi/3 - 3.5*np.pi/n)
    kay[i] = 2.9*np.sin((i-5*n-414-180)*np.pi/3 - 3.5*np.pi/n)
    intensity[i] = gaussian(1.23,2,0,sigma3)
for i in np.arange (5*n+414+186, 5*n+414+192, 1):
    kax[i] = 3.1*np.cos((i-5*n-414-186)*np.pi/3)
    kay[i] = 3.1*np.sin((i-5*n-414-186)*np.pi/3)
    intensity[i] = gaussian(1.23,2,0,sigma3)
```

```
for i in np.arange (5*n+414+192, 5*n+414+198, 1):
    kax[i] = 3.1*np.cos((i-5*n-414-192)*np.pi/3 + 3*np.pi/n)
    kay[i] = 3.1*np.sin((i-5*n-414-192)*np.pi/3 + 3*np.pi/n)
    intensity[i] = gaussian(1.23,2,0,sigma3)
for i in np.arange (5*n+414+198, 5*n+414+204, 1):
    kax[i] = 3.1*np.cos((i-5*n-414-198)*np.pi/3 - 3*np.pi/n)
    kay[i] = 3.1*np.sin((i-5*n-414-198)*np.pi/3 - 3*np.pi/n)
    intensity[i] = gaussian(1.23,2,0,sigma3)
for i in np.arange (5*n+414+204, 5*n+414+210, 1):
    kax[i] = 3.4*np.cos((i-5*n-414-204)*np.pi/3)
    kay[i] = 3.4*np.sin((i-5*n-414-204)*np.pi/3)
    intensity[i] = gaussian(1.27,2,0,sigma3)
for i in np.arange (5*n+414+210, 5*n+414+216, 1):
    kax[i] = 3.4*np.cos((i-5*n-414-210)*np.pi/3 + 2.5*np.pi/n)
    kay[i] = 3.4*np.sin((i-5*n-414-210)*np.pi/3 + 2.5*np.pi/n)
    intensity[i] = gaussian(1.27,2,0,sigma3)
for i in np.arange (5*n+414+216, 5*n+414+222, 1):
    kax[i] = 3.4*np.cos((i-5*n-414-216)*np.pi/3 - 2.5*np.pi/n)
    kay[i] = 3.4*np.sin((i-5*n-414-216)*np.pi/3 - 2.5*np.pi/n)
    intensity[i] = gaussian(1.27,2,0,sigma3)
for i in np.arange (5*n+414+222, 5*n+414+228, 1):
    kax[i] = 3.7*np.cos((i-5*n-414-222)*np.pi/3)
    kay[i] = 3.7*np.sin((i-5*n-414-222)*np.pi/3)
    intensity[i] = gaussian(1.31,2,0,sigma3)
for i in np.arange (5*n+414+228, 5*n+414+234, 1):
    kax[i] = 3.7*np.cos((i-5*n-414-228)*np.pi/3 + 2*np.pi/n)
    kay[i] = 3.7*np.sin((i-5*n-414-228)*np.pi/3 + 2*np.pi/n)
    intensity[i] = gaussian(1.31,2,0,sigma3)
for i in np.arange (5*n+414+234, 5*n+414+240, 1):
    kax[i] = 3.7*np.cos((i-5*n-414-234)*np.pi/3 - 2*np.pi/n)
    kay[i] = 3.7*np.sin((i-5*n-414-234)*np.pi/3 - 2*np.pi/n)
    intensity[i] = gaussian(1.31,2,0,sigma3)
for i in np.arange (5*n+414+240, 5*n+414+246, 1):
    kax[i] = 4*np.cos((i-5*n-414-240)*np.pi/3)
    kay[i] = 4*np.sin((i-5*n-414-240)*np.pi/3)
    intensity[i] = gaussian(1.35,2,0,sigma3)
for i in np.arange (5*n+414+246, 5*n+414+252, 1):
    kax[i] = 4*np.cos((i-5*n-414-246)*np.pi/3 + 1.5*np.pi/n)
    kay[i] = 4*np.sin((i-5*n-414-246)*np.pi/3 + 1.5*np.pi/n)
    intensity[i] = gaussian(1.35,2,0,sigma3)
for i in np.arange (5*n+414+252, 5*n+414+258, 1):
    kax[i] = 4*np.cos((i-5*n-414-252)*np.pi/3 - 1.5*np.pi/n)
    kay[i] = 4*np.sin((i-5*n-414-252)*np.pi/3 - 1.5*np.pi/n)
    intensity[i] = gaussian(1.35,2,0,sigma3)
for i in np.arange (5*n+414+258, 5*n+414+264, 1):
    kax[i] = 4.3*np.cos((i-5*n-414-258)*np.pi/3)
    kay[i] = 4.3*np.sin((i-5*n-414-258)*np.pi/3)
```

```
intensity[i] = gaussian(1.39,2,0,sigma3)
for i in np.arange (5*n+414+264, 5*n+414+270, 1):
    kax[i] = 4.3*np.cos((i-5*n-414-264)*np.pi/3 + 1.1*np.pi/n)
    kay[i] = 4.3*np.sin((i-5*n-414-264)*np.pi/3 + 1.1*np.pi/n)
    intensity[i] = gaussian(1.39,2,0,sigma3)
for i in np.arange (5*n+414+270, 5*n+414+276, 1):
    kax[i] = 4.3*np.cos((i-5*n-414-270)*np.pi/3 - 1.1*np.pi/n)
    kay[i] = 4.3*np.sin((i-5*n-414-270)*np.pi/3 - 1.1*np.pi/n)
    intensity[i] = gaussian(1.39,2,0,sigma3)
for i in np.arange (5*n+414+276, 5*n+414+282, 1):
    kax[i] = 4.6*np.cos((i-5*n-414-276)*np.pi/3)
    kay[i] = 4.6*np.sin((i-5*n-414-276)*np.pi/3)
    intensity[i] = gaussian(1.43,2,0,sigma3)
for i in np.arange (5*n+414+282, 5*n+414+288, 1):
    kax[i] = 4.6*np.cos((i-5*n-414-282)*np.pi/3 + 0.7*np.pi/n)
    kay[i] = 4.6*np.sin((i-5*n-414-282)*np.pi/3 + 0.7*np.pi/n)
    intensity[i] = gaussian(1.43,2,0,sigma3)
for i in np.arange (5*n+414+288, 5*n+414+294, 1):
    kax[i] = 4.6*np.cos((i-5*n-414-288)*np.pi/3 - 0.7*np.pi/n)
    kay[i] = 4.6*np.sin((i-5*n-414-288)*np.pi/3 - 0.7*np.pi/n)
    intensity[i] = gaussian(1.43,2,0,sigma3)
for i in np.arange (5*n+414+294, 5*n+414+300, 1):
    kax[i] = 4.9*np.cos((i-5*n-414-294)*np.pi/3)
    kay[i] = 4.9*np.sin((i-5*n-414-294)*np.pi/3)
    intensity[i] = gaussian(1.46,2,0,sigma3)
for i in np.arange (5*n+414+300, 5*n+414+306, 1):
    kax[i] = 5.2*np.cos((i-5*n-414-300)*np.pi/3)
    kay[i] = 5.2*np.sin((i-5*n-414-300)*np.pi/3)
    intensity[i] = gaussian(1.48,2,0,sigma3)
for i in np.arange (5*n+414+306, 5*n+414+312, 1):
    kax[i] = 5.5*np.cos((i-5*n-414-306)*np.pi/3)
    kay[i] = 5.5*np.sin((i-5*n-414-306)*np.pi/3)
    intensity[i] = gaussian(1.5,2,0,sigma3)

a = 0.6
def cosine(x,mean=0):
    return a*np.cos((x-mean)*np.pi/(n//6))
def expon(x,mean=0):
    return np.exp(-np.abs((x-mean))/(n//12))
#modeling the scattering potential
for i in np.arange (0, n//4, 1):
    sp[i] = expon(i,n//12)
for i in np.arange (n//4, 7*n//12, 1):
    sp[i] = expon(i,5*n//12)
for i in np.arange (7*n//12, 11*n//12, 1):
    sp[i] = expon(i,3*n//4)
```

## APPENDIX C. PROGRAM CODES

---

```

for i in np.arange (11*n//12, n+n//4, 1):
    sp[i] = expon(i,n+n//12)
for i in np.arange (n+n//4, n+7*n//12, 1):
    sp[i] = expon(i,n+5*n//12)
for i in np.arange (n+7*n//12, n+11*n//12, 1):
    sp[i] = expon(i,n+3*n//4)

for i in np.arange (n+11*n//12, 2*n+n//4, 1):
    sp[i] = expon(i,2*n+n//12)
for i in np.arange (2*n+n//4, 2*n+7*n//12, 1):
    sp[i] = expon(i,2*n+5*n//12)
for i in np.arange (2*n+7*n//12, 2*n+11*n//12, 1):
    sp[i] = expon(i,2*n+3*n//4)

for i in np.arange (2*n+11*n//12, 3*n+n//4, 1):
    sp[i] = expon(i,3*n+n//12)
for i in np.arange (3*n+n//4, 3*n+7*n//12, 1):
    sp[i] = expon(i,3*n+5*n//12)
for i in np.arange (3*n+7*n//12, 3*n+11*n//12, 1):
    sp[i] = expon(i,3*n+3*n//4)

for i in np.arange (3*n+11*n//12, 4*n+n//4, 1):
    sp[i] = expon(i,4*n+n//12)
for i in np.arange (4*n+n//4, 4*n+7*n//12, 1):
    sp[i] = expon(i,4*n+5*n//12)
for i in np.arange (4*n+7*n//12, 4*n+11*n//12, 1):
    sp[i] = expon(i,4*n+3*n//4)
for i in np.arange (4*n+11*n//12, 5*n, 1):
    sp[i] = expon(i,5*n+n//12)

#modeling the out-of-plane spin texture for the middle hexagon
for i in np.arange (0, n//6, 1):
    sz[i] = cosine(i,n//12)
for i in np.arange (n//6, n//3, 1):
    sz[i] = -cosine(i,n//4)
for i in np.arange (n//3, n//2, 1):
    sz[i] = cosine(i,5*n//12)
for i in np.arange (n//2, 2*n//3, 1):
    sz[i] = -cosine(i,7*n//12)
for i in np.arange (2*n//3, 5*n//6, 1):
    sz[i] = cosine(i,3*n//4)
for i in np.arange (5*n//6, n, 1):
    sz[i] = -cosine(i,11*n//12)

#modeling the out-of-plane spin texture for the inner hexagon
for i in np.arange (n, n+n//6, 1):
    sz[i] = cosine(i,n+n//12)
for i in np.arange (n+n//6, n+n//3, 1):

```

```
sz[i] = -cosine(i,n+n//4)
for i in np.arange (n+n//3,n+n//2, 1):
    sz[i] = cosine(i,n+5*n//12)
for i in np.arange (n+n//2, n+2*n//3, 1):
    sz[i] = -cosine(i,n+7*n//12)
for i in np.arange (n+2*n//3, n+5*n//6, 1):
    sz[i] = cosine(i,n+3*n//4)
for i in np.arange (n+5*n//6, 2*n, 1):
    sz[i] = -cosine(i,n+11*n//12)
#modeling the out-of-plane spin texture for the outer hexagon
for i in np.arange (2*n, 2*n+n//6, 1):
    sz[i] = cosine(i,2*n+n//12)
for i in np.arange (2*n+n//6, 2*n+n//3, 1):
    sz[i] = -cosine(i,2*n+n//4)
for i in np.arange (2*n+n//3, 2*n+n//2, 1):
    sz[i] = cosine(i,2*n+5*n//12)
for i in np.arange (2*n+n//2, 2*n+2*n//3, 1):
    sz[i] = -cosine(i,2*n+7*n//12)
for i in np.arange (2*n+2*n//3, 2*n+5*n//6, 1):
    sz[i] = cosine(i,2*n+3*n//4)
for i in np.arange (2*n+5*n//6, 3*n, 1):
    sz[i] = -cosine(i,2*n+11*n//12)
#modeling the out-of-plane spin texture for the inner inner hexagon
for i in np.arange (3*n, 3*n+n//6, 1):
    sz[i] = cosine(i,3*n+n//12)
for i in np.arange (3*n+n//6, 3*n+n//3, 1):
    sz[i] = -cosine(i,3*n+n//4)
for i in np.arange (3*n+n//3, 3*n+n//2, 1):
    sz[i] = cosine(i,3*n+5*n//12)
for i in np.arange (3*n+n//2, 3*n+2*n//3, 1):
    sz[i] = -cosine(i,3*n+7*n//12)
for i in np.arange (3*n+2*n//3, 3*n+5*n//6, 1):
    sz[i] = cosine(i,3*n+3*n//4)
for i in np.arange (3*n+5*n//6, 4*n, 1):
    sz[i] = -cosine(i,3*n+11*n//12)
#modeling the out-of-plane spin texture for the outer outer hexagon
for i in np.arange (4*n, 4*n+n//6, 1):
    sz[i] = cosine(i,4*n+n//12)
for i in np.arange (4*n+n//6, 4*n+n//3, 1):
    sz[i] = -cosine(i,4*n+n//4)
for i in np.arange (4*n+n//3, 4*n+n//2, 1):
    sz[i] = cosine(i,4*n+5*n//12)
for i in np.arange (4*n+n//2, 4*n+2*n//3, 1):
    sz[i] = -cosine(i,4*n+7*n//12)
for i in np.arange (4*n+2*n//3, 4*n+5*n//6, 1):
    sz[i] = cosine(i,4*n+3*n//4)
for i in np.arange (4*n+5*n//6, 5*n, 1):
```

## APPENDIX C. PROGRAM CODES

---

```

sz[i] = -cosine(i,4*n+11*n//12)

#plot the constant-energy contour
fig = plt.figure(figsize=(6,6))
ax1 = fig.add_subplot(111)
ax1.set_aspect('equal')
sc = plt.scatter(kax[:5*n],kay[:5*n], c=intensity[:5*n], cmap='BuGn',
                 marker='o', s=1)
sc1 = plt.scatter(kax[5*n+414:5*n+414+312],kay[5*n+414:5*n
+414+312],c=intensity[5*n+414:5*n+414+312], cmap='BuGn', vmin=0,
vmax=5, marker='o', s=40)
sc2 = plt.scatter(kax[5*n:5*n+414],kay[5*n:5*n+414], c=intensity[5*n
:5*n+414], cmap='BuGn', vmin=0, vmax=5, marker='o', s=50)
plt.axis('off')
plt.show()

#JDOS and SSP calculations

#applying the scattering potential
for i in np.arange (0, 5*n+0, 1):
    intensity[i] = intensity[i]*sp[i]*5

#only surface state scattering
for i in np.arange (0, 5*n+0, 1):
    kx1 = kax[i]
    ky1 = kay[i]
    sz1 = sz[i]
    intensity1 = intensity[i]
    if kx1 > 0:
        theta1 = np.arctan(ky1/kx1)
    else:
        theta1 = np.pi + np.arctan(ky1/kx1)
    for j in np.arange (0, 5*n, 1):
        kx2 = kax[j]
        ky2 = kay[j]
        sz2 = sz[j]
        intensity2 = intensity[j]
        qx = kx2 - kx1
        qy = ky2 - ky1
        if kx2 > 0:
            theta2 = np.arctan(ky2/kx2)
        else:
            theta2 = np.pi + np.arctan(ky2/kx2)
        for_jdos = 1

#suppressed backscattering

```

```
    for_ssp = 0.5*(1/2*(1 + np.cos(theta2-theta1)) + 1/2*a*a*(1
+ np.cos(3*theta2)*np.cos(3*theta1) + sz1*sz2/a/a))/(1+a*a)*2

    z = intensity1*for_jdos*intensity2
    z1 = intensity1*for_ssp*intensity2
    X.append(qx)
    Y.append(qy)
    Z.append(z)
    Z1.append(z1)

#surface-to-bulk scattering
for i in np.arange (0, 5*n, 1):
    kx1 = kax[i]
    ky1 = kay[i]
    intensity1 = intensity[i]
    if kx1 > 0:
        theta1 = np.arctan(ky1/kx1)
    else:
        theta1 = np.pi + np.arctan(ky1/kx1)
    for j in np.arange (5*n, 5*n+414+312, 1):
        kx2 = kax[j]
        ky2 = kay[j]
        intensity2 = intensity[j]
        qx = kx2 - kx1
        qy = ky2 - ky1
        if kx2 > 0:
            theta2 = np.arctan(ky2/kx2)
        else:
            theta2 = np.pi + np.arctan(ky2/kx2)

        for_jdos = 1

#allowed backscattering
for_ssp = 1

    z = intensity1*for_jdos*intensity2
    z1 = intensity1*for_ssp*intensity2
    X.append(qx)
    Y.append(qy)
    Z.append(z)
    Z1.append(z1)

#surface-to-bulk scattering
for i in np.arange (5*n, 5*n+414+312, 1):
    kx1 = kax[i]
    ky1 = kay[i]
    intensity1 = intensity[i]
```

```
if kx1 > 0:
    theta1 = np.arctan(ky1/kx1)
else:
    theta1 = np.pi + np.arctan(ky1/kx1)
for j in np.arange (0, 5*n, 1):
    kx2 = kax[j]
    ky2 = kay[j]
    intensity2 = intensity[j]
    qx = kx2 - kx1
    qy = ky2 - ky1
    if kx2 > 0:
        theta2 = np.arctan(ky2/kx2)
    else:
        theta2 = np.pi + np.arctan(ky2/kx2)

    for_jdos = 1

    #allowed backscattering
    for_ssp = 1

    z = intensity1*for_jdos*intensity2
    z1 = intensity1*for_ssp*intensity2
    X.append(qx)
    Y.append(qy)
    Z.append(z)
    Z1.append(z1)

#only bulk scattering
for i in np.arange (5*n, 5*n+414+312, 1):
    kx1 = kax[i]
    ky1 = kay[i]
    intensity1 = intensity[i]
    if kx1 > 0:
        theta1 = np.arctan(ky1/kx1)
    else:
        theta1 = np.pi + np.arctan(ky1/kx1)
    for j in np.arange (5*n, 5*n+414+312, 1):
        kx2 = kax[j]
        ky2 = kay[j]
        intensity2 = intensity[j]
        qx = kx2 - kx1
        qy = ky2 - ky1
        if kx2 > 0:
            theta2 = np.arctan(ky2/kx2)
        else:
            theta2 = np.pi + np.arctan(ky2/kx2)
```

```
for_jdos = 1

#allowed backscattering
for_ssp = 1

z = intensity1*for_jdos*intensity2
z1 = intensity1*for_ssp*intensity2
X.append(qx)
Y.append(qy)
Z.append(z)
Z1.append(z1)

#plot the constant-energy contour with 3-fold symmetry
fig = plt.figure(figsize=(6,6))
ax1 = fig.add_subplot(111)
ax1.set_aspect('equal')
sc = plt.scatter(kax[:5*n],kay[:5*n], c=intensity[:5*n], cmap='BuGn',
                 marker='o', s=1)
sc1 = plt.scatter(kax[5*n+414:5*n+414+312],kay[5*n+414:5*n
+414+312], c=intensity[5*n+414:5*n+414+312], cmap='BuGn', vmin
=0, vmax=5, marker='o', s=40)
sc2 = plt.scatter(kax[5*n:5*n+414],kay[5*n:5*n+414], c=intensity[5*
n:5*n+414], cmap='BuGn', vmin=0, vmax=5, marker='o', s=50)
plt.axis('off')
plt.show()

#plot the out-of-plane spin component
fig = plt.figure(figsize=(6,6))
ax1 = fig.add_subplot(111)
ax1.set_aspect('equal')
sc = plt.scatter(kax[:5*n],kay[:5*n], c=sz, cmap='BuGn', marker='o',
                 s=1)
cbar = fig.colorbar(sc, orientation='vertical', fraction=0.046, pad
=0.04)
plt.show()

# create grids for qx und qy
qx_grid = np.linspace(np.min(X), np.max(X), 600)
qy_grid = np.linspace(np.min(Y), np.max(Y), 600)

# create density map (2D-histogram)
density_map, _, _ = np.histogram2d(X, Y, bins=(qx_grid, qy_grid),
                                    weights=Z1)
# plot the density map
fig, ax = plt.subplots()
plt.imshow(density_map.T, origin='lower', extent=(np.min(qx_grid),
np.max(qx_grid), np.min(qy_grid), np.max(qy_grid)), cmap='BuGn',
```

## APPENDIX C. PROGRAM CODES

---

```
vmax=np.max(density_map)/38
ax.axis('off')
plt.show()
```

The code example below was written to open and analyze  $dI/dU$  maps measured at a certain bias voltage with the RHK R9 STM controller. This Python program code allows to load the experimental data which were saved in the ASCII format with further cutting the maps, taking their FFT and FFT linecuts for the data analysis.

```
#####
# Author: Vladislav Nagorkin
# Created: 27.01.2020
#####

import numpy as np
import matplotlib.pyplot as plt
n=512 #number of pixels
with open("1MnBi2Te4_11_11_19__0991 Image LIA Current_ Forward.txt"
) as inp:
    alldata = list(map(float,inp.read().split()))
#create an array of the y-coordinate values of each line
x1=[]
for i in range(0, n*(n+1), n+1):
    x1.append(alldata[i])
#create an array of the dI/dU values of all the pixels
didv=[]
for j in range(0,n,1):
    for i in range(1,n+1,1):
        didv.append(alldata[i+(n+1)*j])
#create a 2D array of the dI/dU values at all the pixels
d2 = [[0 for i in range(n)] for j in range(n)]
for j in range(0,n,1):
    for i in range(0,n,1):
        d2[i][j]=didv[i+n*j]
from matplotlib import cm
# x and y coordinates
#plot a dI/dU map on the (x,y)-grid as a heatmap
x = np.arange(0,n,1)
y = np.arange(0,n,1)
data = np.zeros((len(x),len(y)))

for j, xx in enumerate(x):
    for i, yy in enumerate(y):
        data[i,j] = 10**12*d2[n-1-j][n-1-i] #dI/dU values in pA
#In the beginning of the program I assigned i-indexes while
    changing
```

```
#x-coordinate, j - while changing y-coordinate.
#But matshow sets i-indexes on y-axis, j - on x-axis
#Also, I assign the right-upper pixel which is named (0,0)
#the number (n,n) and the left-bottom pixel (n,n) -
#the number (0,0) in order to have the map corresponding to the
#topography which starts from the right-upper pixel -> n-i, n-j

#create an array of all the dI/dU values
didv_slice=np.zeros([n,n])
for b in range(0,n,1):
    for a in range(0,n,1):
        didv_slice[a,b]=d2[n-1-a][n-1-b]
#show a dI/dU map at a certain bias voltage
img_didv=didv_slice[:, :]
plt.figure(figsize=(12, 12))
plt.subplot(1, 3, 1)
plt.imshow(img_didv, cmap=cm.magma, interpolation='bilinear')
plt.colorbar(fraction=0.046, pad=0.04)
#FFT of the dI/dU map
array_fft = np.zeros([n,n])
x2 = np.arange(n)
w_func_hamm_g = 0.54-0.46*np.cos(2*np.pi*x2/(n-1))+0.0*np.cos(4*np.
    pi*x2/(n-1))-0.0*np.cos(6*np.pi*x2/(n-1))    # Hamming window
w_func_hamm = np.outer(w_func_hamm_g, w_func_hamm_g)
array_fft[:, :] = np.fft.fftshift(np.abs(np.fft.fft2((didv_slice
    [:,:]-1*np.mean(didv_slice[:,:])+0*abs(np.min(didv_slice[:,:])))*
    *w_func_hamm)))
#cut a piece of the dI/dU map for its further FFT
mapcut=np.zeros([n,n])
for b in range(0,n,1):
    for a in range(0,n,1):
        mapcut[a-0,b-0]=didv_slice[a,b]
img_didv_cut=mapcut[:, :]
plt.figure(figsize=(12, 12))
plt.subplot(2, 1, 1)
plt.imshow(img_didv_cut, cmap=cm.gnuplot2, origin='lower',
    interpolation='bilinear')
#FFT of a piece of the dI/dU map
array_fft_cut = np.zeros([n,n])
x2 = np.arange(n)
w_func_hamm_g = 0.54-0.46*np.cos(2*np.pi*x2/(n-1))+0.0*np.cos(4*np.
    pi*x2/(n-1))-0.0*np.cos(6*np.pi*x2/(n-1))    # Hamming window
w_func_hamm = np.outer(w_func_hamm_g, w_func_hamm_g)
array_fft_cut[:, :] = np.fft.fftshift(np.abs(np.fft.fft2((mapcut
    [:,:]-1*np.mean(mapcut[:,:])+0*abs(np.min(mapcut[:,:])))*
    *w_func_hamm)))
img_fft=array_fft_cut[:, :]
```

```
plt.subplot(2, 1, 2)
plt.imshow(img_fft, cmap=cm.gnuplot2, interpolation='none')
#take a linecut of the dI/dU map along a certain direction
x, y = np.mgrid[0:n:1, 0:n:1]
z = array_fft_cut[x,y]
plt.figure(figsize=(12, 12))
plt.imshow(z, cmap=cm.gnuplot2, interpolation='none')

x0, y0 = 409, 0 # these are in pixel coordinates
x1, y1 = 105, 511
num = int(np.hypot(x1-x0, y1-y0))
x, y = np.linspace(x0, x1, num), np.linspace(y0, y1, num)
# extract the values along the line, using cubic interpolation
# swap x and y here in order to show the linecut properly -
#in normal x - horizontal and y - vertical coordinates in the FFT
# image
zi = z[y.astype(np.int), x.astype(np.int)]
plt.figure(figsize=(12, 12))
plt.imshow(z, cmap=cm.gnuplot2, interpolation='none')
plt.plot([x0, x1], [y0, y1], 'ro-')
plt.show()
plt.plot(y,zi)
plt.show()
```

The program code presented below was written also in Python and allows to process full STS maps acquired with the RHK R9 STM controller. Similar to the previous case, the program opens the experimental data saved in the ASCII format and allows analyzing the dI/dU maps with their FFT as well as the differential conductance spectra.

```
#####
# Author: Vladislav Nagorkin
# Created: 13.09.2018
#####

import numpy as np
import matplotlib as mpl
import matplotlib.pyplot as plt
#n - number of pixels, p - number of points in each spectrum,
#m - number which counts forward and backward lines
n=256; p=126; m=2
with open("1MnBi2Te4_11_11_19_0783_LIA Current.txt") as inp:
    alldata = list(map(float,inp.read().split()))
#create an array of the y-coordinate values of each line
x1=[]
for i in range(0, m*n, m):
    x1.append(alldata[i])
```

```
print(x1)
y1=[]
for i in range(m*n*n, 2*m*n*n, m*n):
    y1.append(alldata[i])
print(y1)

x=[10**9*x1[j] for j in range(0,n)]      #x-coordinate in nm
y=[10**9*y1[j] for j in range(0,n)]      #y-coordinate in nm
plt.plot(x,y)
plt.xlabel('x (nm)')
plt.ylabel('y (nm)')
plt.show()

#create an array of the bias voltages
v=[]
for i in range(2*m*n*n, 2*m*n*n+(p-1)*(m*n*n+1)+1, m*n*n+1):
    v.append(alldata[i])
print(v)

#create an array of dI/dU values of the pixel #10 as an example
didv10=[]
for u in range(2*m*n*n+1+m*10, 2*m*n*n+1+m*10+(p-1)*(m*n*n+1)+1, m*n*n+1):
    didv10.append(alldata[u])

x=[1000*v[j] for j in range(0,p)]
y=[didv10[q] for q in range(0,p)]
plt.plot(x,y)
plt.xlabel('Bias voltage (mV)', fontsize=18)
plt.ylabel('dI/dU (a.u.)', fontsize=18)
plt.show()

#create an array of the dI/dU values of all the pixels
didv=[]
for k in range(0,p,1):
    for j in range(0,n,1):
        for i in range(0,n,1):
            didv.append(alldata[2*m*n*n+1+m*i+m*n*j+(m*n*n+1)*k])
#create a 3D array of the dI/dU values of all the pixels
d3 = [[[0 for i in range(n)] for j in range(n)] for voltage in
       range(n)]
for voltage in range(0,p,1):
    for j in range(0,n,1):
        for i in range(0,n,1):
            d3[i][j][voltage]=didv[i+n*j+n*n*voltage]

# x and y coordinates
#plot a dI/dU map on the (x,y)-grid as a heatmap
x = np.arange(0,n,1)
y = np.arange(0,n,1)
data = np.zeros((len(x),len(y)))
```

```
for j, xx in enumerate(x):
    for i, yy in enumerate(y):
        data[i,j] = 10**12*d3[n-1-j][n-1-i][4] #dI/dU values in pA
#In the beginning of the program I assigned i-indexes while
#changing x-coordinate, j - while changing y-coordinate.
#But matshow sets i-indexes on y-axis, j - on x-axis
#Also, I want to assign the right-upper pixel which is named (0,0)
#the number (n,n) and the left-bottom pixel (n,n) -
#the number (0,0) in order to have the map corresponding to the
#topography which starts from the right-upper pixel -> n-i, n-j

# Use matshow to create a heatmap
fig, ax = plt.subplots()
ms = ax.matshow(data, cmap = cm.jet, vmin=data.min() - 0.0,
                 vmax=data.max() + 0.0, origin = 'lower')
# x and y axis ticks
ax.set_xticklabels([str(xx) for xx in x])
ax.set_yticklabels([str(yy) for yy in y])
ax.xaxis.tick_bottom()
# Put the x- and y-axis ticks at the middle of each cell
#ax.set_xticks(np.arange(data.shape[1]), minor = False)
#ax.set_yticks(np.arange(data.shape[0]), minor = False)
# Set custom ticks and ticklabels for colorbar
cbar = fig.colorbar(ms,ticks = np.arange(0,1.5,0.5))
plt.show()
#create an array of all the dI/dU values
didv_slice=np.zeros([n,n,p])
for c in range(0,p,1):
    for b in range(0,n,1):
        for a in range(0,n,1):
            didv_slice[a,b,c]=d3[n-1-b][n-1-a][c]
#show a dI/dU map at a certain bias voltage
img_didv=didv_slice[:, :, 0]
plt.figure(figsize=(5, 5))
plt.imshow(img_didv, cmap=cm.gnuplot2, origin='lower',
           interpolation='none')
plt.colorbar()

#show the dI/dU maps at all the energies
vs=-0.05           #initial bias voltage in volts
ve=0               #final bias voltage in volts
for t in range(0,p,1):
    img=didv_slice[:, :, t]
    img_ = plt.figure(figsize=(12, 12))
    fig = plt.imshow(img, cmap=cm.jet)
    plt.xlabel('Bias voltage (mV)', fontsize=18)
    plt.ylabel('dI/dU averaged (a.u.)', fontsize=18)
```

```
plt.imshow(img, cmap=cm.gnuplot2, origin='lower', interpolation
          ='none')
plt.colorbar()
print(vs*1000 - t*1000*(vs-ve)/(p-1))
print('mV')
plt.close(img_)

#FFT of the dI/dU maps
array_fft = np.zeros([n,n,p])
x2 = np.arange(n)
w_func_hamm_g = 0.54-0.46*np.cos(2*np.pi*x2/(n-1))+0.0*np.cos(4*np.
    pi*x2/(n-1))-0.0*np.cos(6*np.pi*x2/(n-1)) # Hamming window
w_func_hamm = np.outer(w_func_hamm_g, w_func_hamm_g)
for ii in range(p):
    array_fft[:, :, ii] = np.fft.fftshift(np.abs(np.fft.fft2(
        didv_slice[:, :, ii]-1*np.mean(didv_slice[:, :, ii])+0*np.min(
            didv_slice[:, :, ii])))*w_func_hamm))
img_fft=array_fft[:, :, 11]
plt.figure(figsize=(12, 12))
plt.subplot(1, 3, 1)
plt.imshow(img_fft, cmap=cm.gnuplot2, origin='lower', interpolation
          ='bilinear')

#show the FFT of dI/dU maps at all energies
for t in range(0,p, 1):
    imge1=array_fft[:, :, t]
    imge1_ = plt.figure(figsize=(12, 12))
    f1 = plt.imshow(imge1, cmap =cm.jet)
    plt.imshow(imge1, cmap=cm.gnuplot2, origin='lower',
               interpolation='bilinear')
    print(vs*1000 - t*1000*(vs-ve)/(p-1))
    print('mV')
    plt.close(imge1_)

#plot an averaged dI/dU spectrum of the whole map
fig = plt.figure()
q=np.zeros(p)
xx=[1000*v[j] for j in range(0,p,1)]
for sp in range (0,p,1):
    for bb in range (0,n,1):
        for aa in range (0,n,1):
            q[sp]=np.mean(didv_slice[aa,bb,sp])
plt.plot(xx,q)
plt.xlabel('Bias voltage (mV)', fontsize=18)
plt.ylabel('dI/dU averaged (a.u.)', fontsize=18)
plt.show()

#choose some area of the map and show dI/dU spectra from all the
#points there
fig = plt.figure()
for b in range (0,n,1):
```

```
for a in range (0,n,1):
    plt.plot(xx,didv_slice[a,b,:])
    plt.axhline(y=0,color='k')
    plt.xlabel('Bias voltage (mV)', fontsize=18)
    plt.ylabel('dI/dU (a. u.)', fontsize=18)
plt.plot(xx,q, color='black', linewidth=5)
plt.show()
#cut a piece of the dI/dU map for its further FFT
mapcut=np.zeros([35,35,p])
for c in range(0,p,1):
    for b in range(12,47,1):
        for a in range(12,47,1):
            mapcut[a-12,b-12,c]=didv_slice[a,b,c]
img_didv_cut=mapcut[:, :, 4]
#show a piece of the dI/dU map at a certain bias voltage
plt.figure(figsize=(12, 12))
plt.subplot(1, 3, 1)
plt.imshow(img_didv_cut, cmap=cm.gnuplot2, origin='lower',
           interpolation='none')
array_fftcut = np.zeros([35,35,p])
#FFT of the piece of the dI/dU map at a certain bias voltage
x2 = np.arange(35)
w_func_hamm_g = 0.54-0.46*np.cos(2*np.pi*x2/(n-1))+0.0*np.cos(4*np.
    pi*x2/(n-1))-0.0*np.cos(6*np.pi*x2/(n-1))    # Hamming window
w_func_hamm = np.outer(w_func_hamm_g, w_func_hamm_g)
for ii in range(p):
    array_fftcut[:, :, ii] = np.fft.fftshift(np.abs(np.fft.fft2((
        mapcut[:, :, ii]-1*np.mean(mapcut[:, :, ii])+0*abs(np.min(mapcut
        [:, :, ii])))*w_func_hamm)))
img_fft=array_fftcut[:, :, 4]
plt.figure(figsize=(12, 12))
plt.subplot(1, 3, 1)
plt.imshow(img_fft, cmap=cm.gnuplot2, origin='lower', interpolation
           ='bilinear')
```



## Appendix D

### Additional STS data on $\text{MnBi}_4\text{Te}_7$

In addition, temperature-dependent full STS maps on a presumably quintuple layer surface termination were taken on very small defect-free  $2 \text{ nm} \times 2 \text{ nm}$  spots. Although the tip did not give atomic resolution all the time, it was stable enough for STS providing negligibly small variations in all 288 spectra on each map. Started from  $T = 5.4 \text{ K}$ , the STS maps were measured at  $7.7 \text{ K}$ ,  $11.1 \text{ K}$ ,  $12.9 \text{ K}$  and  $16.6 \text{ K}$  as well. However, these measurements were strongly influenced by accidental tip changes and were surface dependent as inferred from totally different spectra shape at a certain temperature (e.g. at  $7.7 \text{ K}$ ,  $12.9 \text{ K}$ ) (see Fig. D.0.1). Therefore, no strict conclusion from this dataset can be derived.

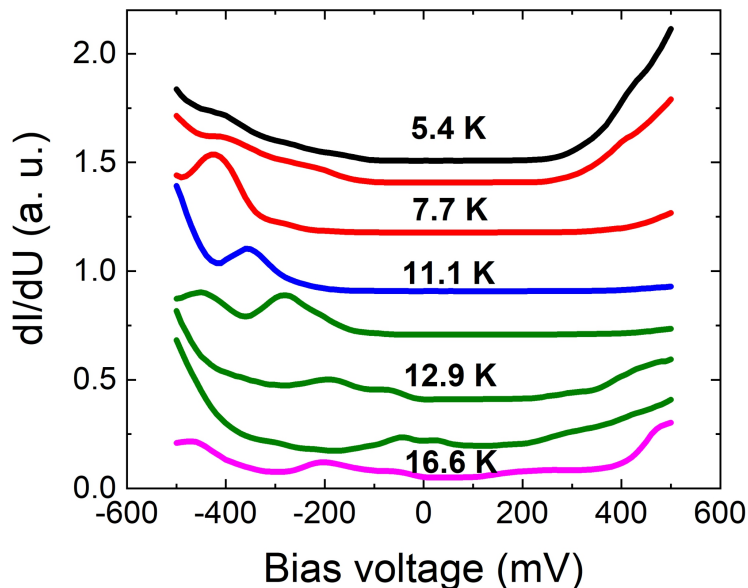


**Fig. D.0.1** Averaged temperature-dependent spectra taken on  $2 \text{ nm} \times 2 \text{ nm}$  areas,  $U_{bias} = -500 \text{ mV}$ ,  $I_T = 200 \text{ pA}$ . Black, red, blue, green and magenta colors correspond to spectra measured  $5.4 \text{ K}$ ,  $7.7 \text{ K}$ ,  $11.1 \text{ K}$ ,  $12.9 \text{ K}$  and  $16.6 \text{ K}$ , respectively. Each curve represents an averaged of 288 spectra taken on a grid. Different spectra at  $7.7 \text{ K}$  were recorded with different tip state, the spectra at  $12.9 \text{ K}$  were obtained on different surface areas.



# Bibliography

- [1] Liang Fu, C. L. Kane, and E. J. Mele. Topological Insulators in Three Dimensions. *Phys. Rev. Lett.*, 98:106803, Mar 2007.
- [2] J. E. Moore and L. Balents. Topological invariants of time-reversal-invariant band structures. *Phys. Rev. B*, 75:121306, Mar 2007.
- [3] Rahul Roy. Topological phases and the quantum spin Hall effect in three dimensions. *Phys. Rev. B*, 79:195322, May 2009.
- [4] Liang Fu and C. L. Kane. Topological insulators with inversion symmetry. *Phys. Rev. B*, 76:045302, Jul 2007.
- [5] Joel Moore. The next generation. *Nature Physics*, 5(6):378–380, 2009.
- [6] Haijun Zhang, Chao-Xing Liu, Xiao-Liang Qi, Xi Dai, Zhong Fang, and Shou-Cheng Zhang. Topological insulators in  $\text{Bi}_2\text{Se}_3$ ,  $\text{Bi}_2\text{Te}_3$  and  $\text{Sb}_2\text{Te}_3$  with a single Dirac cone on the surface. *Nature Physics*, 5(6):438–442, 2009.
- [7] Y. Xia, D. Qian, D. Hsieh, L. Wray, A. Pal, H. Lin, A. Bansil, D. Grauer, Y. S. Hor, R. J. Cava, and M. Z. Hasan. Observation of a large-gap topological-insulator class with a single Dirac cone on the surface. *Nature Physics*, 5(6):398–402, 2009.
- [8] Y. L. Chen, J. G. Analytis, J.-H. Chu, Z. K. Liu, S.-K. Mo, X. L. Qi, H. J. Zhang, D. H. Lu, X. Dai, Z. Fang, S. C. Zhang, I. R. Fisher, Z. Hussain, and Z.-X. Shen. Experimental Realization of a Three-Dimensional Topological Insulator,  $\text{Bi}_2\text{Te}_3$ . *Science*, 325(5937):178–181, 2009.
- [9] M. M. Otrokov, I. I. Klimovskikh, H. Bentmann, D. Estyunin, A. Zeugner, Z. S. Aliev, S. Gaß, A. U. B. Wolter, A. V. Koroleva, A. M. Shikin, M. Blanco-Rey, M. Hoffmann, I. P. Rusinov, A. Yu. Vyazovskaya, S. V. Eremeev, Yu. M. Koroteev, V. M. Kuznetsov, F. Freyse, J. Sánchez-Barriga, I. R. Amiraslanov, M. B. Babanly, N. T. Mamedov, N. A. Abdullayev, V. N. Zverev, A. Alfonsov, V. Kataev, B. Büchner, E. F. Schwier, S. Kumar, A. Kimura, L. Petaccia,

G. Di Santo, R. C. Vidal, S. Schatz, K. Kißner, M. Ünzelmann, C. H. Min, Simon Moser, T. R. F. Peixoto, F. Reinert, A. Ernst, P. M. Echenique, A. Isaeva, and E. V. Chulkov. Prediction and observation of an antiferromagnetic topological insulator. *Nature*, 576(7787):416–422, 2019.

[10] Yan Gong, Jingwen Guo, Jiaheng Li, Kejing Zhu, Menghan Liao, Xiaozhi Liu, Qinghua Zhang, Lin Gu, Lin Tang, Xiao Feng, Ding Zhang, Wei Li, Canli Song, Lili Wang, Pu Yu, Xi Chen, Yayu Wang, Hong Yao, Wenhui Duan, Yong Xu, Shou-Cheng Zhang, Xucun Ma, Qi-Kun Xue, and Ke He. Experimental Realization of an Intrinsic Magnetic Topological Insulator. *Chinese Physics Letters*, 36(7):076801, 2019.

[11] Raphael C. Vidal, Alexander Zeugner, Jorge I. Facio, Rajyavardhan Ray, M. Hossein Haghghi, Anja U. B. Wolter, Laura T. Corredor Bohorquez, Federico Caglieris, Simon Moser, Tim Figgemeier, Thiago R. F. Peixoto, Hari Babu Vasili, Manuel Valvidares, Sungwon Jung, Cephise Cacho, Alexey Alfonsov, Kavita Mehlawat, Vladislav Kataev, Christian Hess, Manuel Richter, Bernd Büchner, Jeroen van den Brink, Michael Ruck, Friedrich Reinert, Hendrik Bentmann, and Anna Isaeva. Topological Electronic Structure and Intrinsic Magnetization in  $\text{MnBi}_4\text{Te}_7$ : A  $\text{Bi}_2\text{Te}_3$  Derivative with a Periodic Mn Sublattice. *Phys. Rev. X*, 9:041065, Dec 2019.

[12] Yoshinori Tokura, Kenji Yasuda, and Atsushi Tsukazaki. Magnetic topological insulators. *Nature Reviews Physics*, 1(2):126–143, 2019.

[13] Y. L. Chen, J.-H. Chu, J. G. Analytis, Z. K. Liu, K. Igarashi, H.-H. Kuo, X. L. Qi, S. K. Mo, R. G. Moore, D. H. Lu, M. Hashimoto, T. Sasagawa, S. C. Zhang, I. R. Fisher, Z. Hussain, and Z. X. Shen. Massive Dirac Fermion on the Surface of a Magnetically Doped Topological Insulator. *Science*, 329(5992):659–662, 2010.

[14] Roland Wiesendanger. *Scanning Probe Microscopy and Spectroscopy: Methods and Applications*. Cambridge University Press, 2001.

[15] C. Julian Chen. *Introduction to Scanning Tunneling Microscopy*. Monographs on the Physics and Chemistry of Materials. Oxford University Press, 2 edition, 2007.

[16] R. Wiesendanger, H.-J. Güntherodt, G. Güntherodt, R. J. Gambino, and R. Ruf. Observation of vacuum tunneling of spin-polarized electrons with the scanning tunneling microscope. *Phys. Rev. Lett.*, 65:247–250, Jul 1990.

## BIBLIOGRAPHY

---

- [17] K. v. Klitzing, G. Dorda, and M. Pepper. New Method for High-Accuracy Determination of the Fine-Structure Constant Based on Quantized Hall Resistance. *Phys. Rev. Lett.*, 45:494–497, Aug 1980.
- [18] D. C. Tsui, H. L. Stormer, and A. C. Gossard. Two-Dimensional Magnetotransport in the Extreme Quantum Limit. *Phys. Rev. Lett.*, 48:1559–1562, May 1982.
- [19] J M Kosterlitz and D J Thouless. Long range order and metastability in two dimensional solids and superfluids. (Application of dislocation theory). *Journal of Physics C: Solid State Physics*, 5(11):L124, jun 1972.
- [20] J M Kosterlitz and D J Thouless. Ordering, metastability and phase transitions in two-dimensional systems. *Journal of Physics C: Solid State Physics*, 6(7):1181, apr 1973.
- [21] C. L. Kane and E. J. Mele.  $Z_2$  Topological Order and the Quantum Spin Hall Effect. *Phys. Rev. Lett.*, 95:146802, Sep 2005.
- [22] Klaus von Klitzing. Developments in the quantum Hall effect. *Philosophical Transactions of the Royal Society A: Mathematical, Physical and Engineering Sciences*, 363(1834):2203–2219, 2005.
- [23] D. J. Thouless, M. Kohmoto, M. P. Nightingale, and M. den Nijs. Quantized Hall Conductance in a Two-Dimensional Periodic Potential. *Phys. Rev. Lett.*, 49:405–408, Aug 1982.
- [24] Charles Kane and Joel Moore. Topological insulators. *Physics World*, 24(02):32–36, feb 2011.
- [25] M. Z. Hasan and C. L. Kane. Colloquium: Topological insulators. *Rev. Mod. Phys.*, 82:3045–3067, Nov 2010.
- [26] C. L. Kane and E. J. Mele. Quantum Spin Hall Effect in Graphene. *Phys. Rev. Lett.*, 95:226801, Nov 2005.
- [27] B. Andrei Bernevig and Shou-Cheng Zhang. Quantum Spin Hall Effect. *Phys. Rev. Lett.*, 96:106802, Mar 2006.
- [28] Paul Adrien Maurice Dirac and Ralph Howard Fowler. The quantum theory of the electron. *Proceedings of the Royal Society of London. Series A, Containing Papers of a Mathematical and Physical Character*, 117(778):610–624, 1928.

## BIBLIOGRAPHY

---

- [29] Kentaro Nomura, Mikito Koshino, and Shinsei Ryu. Topological Delocalization of Two-Dimensional Massless Dirac Fermions. *Phys. Rev. Lett.*, 99:146806, Oct 2007.
- [30] Liang Fu and C. L. Kane. Time reversal polarization and a  $Z_2$  adiabatic spin pump. *Phys. Rev. B*, 74:195312, Nov 2006.
- [31] Xiao-Liang Qi, Taylor L. Hughes, and Shou-Cheng Zhang. Topological field theory of time-reversal invariant insulators. *Phys. Rev. B*, 78:195424, Nov 2008.
- [32] Rahul Roy.  $Z_2$  classification of quantum spin Hall systems: An approach using time-reversal invariance. *Phys. Rev. B*, 79:195321, May 2009.
- [33] Ying Ran, Yi Zhang, and Ashvin Vishwanath. One-dimensional topologically protected modes in topological insulators with lattice dislocations. *Nature Physics*, 5(4):298–303, 2009.
- [34] D. Hsieh, Y. Xia, D. Qian, L. Wray, J. H. Dil, F. Meier, J. Osterwalder, L. Patthey, J. G. Checkelsky, N. P. Ong, A. V. Fedorov, H. Lin, A. Bansil, D. Grauer, Y. S. Hor, R. J. Cava, and M. Z. Hasan. A tunable topological insulator in the spin helical Dirac transport regime. *Nature*, 460(7259):1101–1105, 2009.
- [35] D. Hsieh, Y. Xia, D. Qian, L. Wray, F. Meier, J. H. Dil, J. Osterwalder, L. Patthey, A. V. Fedorov, H. Lin, A. Bansil, D. Grauer, Y. S. Hor, R. J. Cava, and M. Z. Hasan. Observation of Time-Reversal-Protected Single-Dirac-Cone Topological-Insulator States in  $\text{Bi}_2\text{Te}_3$  and  $\text{Sb}_2\text{Te}_3$ . *Phys. Rev. Lett.*, 103:146401, Sep 2009.
- [36] B. Andrei Bernevig, Taylor L. Hughes, and Shou-Cheng Zhang. Quantum Spin Hall Effect and Topological Phase Transition in HgTe Quantum Wells. *Science*, 314(5806):1757–1761, 2006.
- [37] Markus König, Steffen Wiedmann, Christoph Brüne, Andreas Roth, Hartmut Buhmann, Laurens W. Molenkamp, Xiao-Liang Qi, and Shou-Cheng Zhang. Quantum Spin Hall Insulator State in HgTe Quantum Wells. *Science*, 318(5851):766–770, 2007.
- [38] Yi Liu and Roland E. Allen. Electronic structure of the semimetals Bi and Sb. *Phys. Rev. B*, 52:1566–1577, Jul 1995.
- [39] P.A. Wolff. Matrix elements and selection rules for the two-band model of bismuth. *Journal of Physics and Chemistry of Solids*, 25(10):1057–1068, 1964.

## BIBLIOGRAPHY

---

[40] D. Hsieh, D. Qian, L. Wray, Y. Xia, Y. S. Hor, R. J. Cava, and M. Z. Hasan. A topological Dirac insulator in a quantum spin Hall phase. *Nature*, 452(7190):970–974, 2008.

[41] D. Hsieh, Y. Xia, L. Wray, D. Qian, A. Pal, J. H. Dil, J. Osterwalder, F. Meier, G. Bihlmayer, C. L. Kane, Y. S. Hor, R. J. Cava, and M. Z. Hasan. Observation of Unconventional Quantum Spin Textures in Topological Insulators. *Science*, 323(5916):919–922, 2009.

[42] Pedram Roushan, Jungpil Seo, Colin V. Parker, Y. S. Hor, D. Hsieh, Dong Qian, Anthony Richardella, M. Z. Hasan, R. J. Cava, and Ali Yazdani. Topological surface states protected from backscattering by chiral spin texture. *Nature*, 460(7259):1106–1109, 2009.

[43] J. Heremans, D. L. Partin, C. M. Thrush, G. Karczewski, M. S. Richardson, and J. K. Furdyna. Cyclotron resonance in epitaxial  $\text{Bi}_{1-x}\text{Sb}_x$  films grown by molecular-beam epitaxy. *Phys. Rev. B*, 48:11329–11335, Oct 1993.

[44] J. Zemann. Crystal structures, 2nd edition, Vol. 2 by R. W. G. Wyckoff. *Acta Crystallographica*, 19(3):490–490, 1965.

[45] S K Mishra, S Satpathy, and O Jepsen. Electronic structure and thermoelectric properties of bismuth telluride and bismuth selenide. *Journal of Physics: Condensed Matter*, 9(2):461–470, jan 1997.

[46] Liang Fu. Hexagonal Warping Effects in the Surface States of the Topological Insulator  $\text{Bi}_2\text{Te}_3$ . *Phys. Rev. Lett.*, 103:266801, Dec 2009.

[47] M. Z. Hasan, H. Lin, and A. Bansil. Warping the cone on a Topological Insulator. *Physics*, 108(2), 2009.

[48] S. Souma, K. Kosaka, T. Sato, M. Komatsu, A. Takayama, T. Takahashi, M. Kriener, Kouji Segawa, and Yoichi Ando. Direct Measurement of the Out-of-Plane Spin Texture in the Dirac-Cone Surface State of a Topological Insulator. *Phys. Rev. Lett.*, 106:216803, May 2011.

[49] Wei-Cheng Lee, Congjun Wu, Daniel P. Arovas, and Shou-Cheng Zhang. Quasiparticle interference on the surface of the topological insulator  $\text{Bi}_2\text{Te}_3$ . *Phys. Rev. B*, 80:245439, Dec 2009.

[50] Asteriona-Maria Netsou, Dmitry A. Muzychko, Heleen Dausy, Taishi Chen, Fengqi Song, Koen Schouteden, Margriet J. Van Bael, and Chris Van Haezendonck. Identifying Native Point Defects in the Topological Insulator  $\text{Bi}_2\text{Te}_3$ . *ACS Nano*, 14(10):13172–13179, October 2020.

## BIBLIOGRAPHY

---

- [51] Thomas Bathon, Simona Achilli, Paolo Sessi, Vladimir Andreevich Golyashov, Konstantin Aleksandrovich Kokh, Oleg Evgenievich Tereshchenko, and Matthias Bode. Experimental Realization of a Topological p–n Junction by Intrinsic Defect Grading. *Advanced Materials*, 28(11):2183–2188, 2016.
- [52] P. Sessi, M. M. Otrokov, T. Bathon, M. G. Vergniory, S. S. Tsirkin, K. A. Kokh, O. E. Tereshchenko, E. V. Chulkov, and M. Bode. Visualizing spin-dependent bulk scattering and breakdown of the linear dispersion relation in  $\text{Bi}_2\text{Te}_3$ . *Phys. Rev. B*, 88:161407, Oct 2013.
- [53] Zhanybek Alpichshev, J. G. Analytis, J.-H. Chu, I. R. Fisher, Y. L. Chen, Z. X. Shen, A. Fang, and A. Kapitulnik. STM Imaging of Electronic Waves on the Surface of  $\text{Bi}_2\text{Te}_3$ : Topologically Protected Surface States and Hexagonal Warping Effects. *Phys. Rev. Lett.*, 104:016401, Jan 2010.
- [54] S. Urazhdin, D. Bilc, S. D. Mahanti, S. H. Tessmer, Theodora Kyratsi, and M. G. Kanatzidis. Surface effects in layered semiconductors  $\text{Bi}_2\text{Se}_3$  and  $\text{Bi}_2\text{Te}_3$ . *Phys. Rev. B*, 69:085313, Feb 2004.
- [55] V. S. Stolyarov, V. A. Sheina, D. A. Khokhlov, S. Vlaic, S. Pons, H. Aubin, R. S. Akzyanov, A. S. Vasenko, T. V. Menshchikova, E. V. Chulkov, A. A. Golubov, T. Cren, and D. Roditchev. Disorder-Promoted Splitting in Quasiparticle Interference at Nesting Vectors. *The Journal of Physical Chemistry Letters*, 12(12):3127–3134, 2021. PMID: 33755482.
- [56] Tong Zhang, Peng Cheng, Xi Chen, Jin-Feng Jia, Xucun Ma, Ke He, Lili Wang, Haijun Zhang, Xi Dai, Zhong Fang, Xincheng Xie, and Qi-Kun Xue. Experimental Demonstration of Topological Surface States Protected by Time-Reversal Symmetry. *Phys. Rev. Lett.*, 103:266803, Dec 2009.
- [57] Yoshinori Okada, Wenwen Zhou, Chetan Dhital, D. Walkup, Ying Ran, Z. Wang, Stephen D. Wilson, and V. Madhavan. Visualizing Landau Levels of Dirac Electrons in a One-Dimensional Potential. *Phys. Rev. Lett.*, 109:166407, Oct 2012.
- [58] Paolo Sessi, Felix Reis, Thomas Bathon, Konstantin A Kokh, Oleg E Tereshchenko, and Matthias Bode. Signatures of Dirac fermion-mediated magnetic order. *Nature communications*, 5(1):1–8, 2014.
- [59] Roger S. K. Mong, Andrew M. Essin, and Joel E. Moore. Antiferromagnetic topological insulators. *Phys. Rev. B*, 81:245209, Jun 2010.

## BIBLIOGRAPHY

---

- [60] Rui Yu, Wei Zhang, Hai-Jun Zhang, Shou-Cheng Zhang, Xi Dai, and Zhong Fang. Quantized Anomalous Hall Effect in Magnetic Topological Insulators. *Science*, 329(5987):61–64, 2010.
- [61] Andrew M. Essin, Joel E. Moore, and David Vanderbilt. Magnetoelectric Polarizability and Axion Electrodynamics in Crystalline Insulators. *Phys. Rev. Lett.*, 102:146805, Apr 2009.
- [62] Xiao-Liang Qi and Shou-Cheng Zhang. Topological insulators and superconductors. *Rev. Mod. Phys.*, 83:1057–1110, Oct 2011.
- [63] F. Wilczek. Problem of Strong  $P$  and  $T$  Invariance in the Presence of Instantons. *Phys. Rev. Lett.*, 40:279–282, Jan 1978.
- [64] Steven Weinberg. A New Light Boson? *Phys. Rev. Lett.*, 40:223–226, Jan 1978.
- [65] Masataka Mogi, Minoru Kawamura, Atsushi Tsukazaki, Ryutaro Yoshimi, Kei S. Takahashi, Masashi Kawasaki, and Yoshinori Tokura. Tailoring tricolor structure of magnetic topological insulator for robust axion insulator. *Science Advances*, 3(10):eaao1669, 2017.
- [66] Cui-Zu Chang, Weiwei Zhao, Duk Y. Kim, Peng Wei, J. K. Jain, Chaoxing Liu, Moses H. W. Chan, and Jagadeesh S. Moodera. Zero-Field Dissipationless Chiral Edge Transport and the Nature of Dissipation in the Quantum Anomalous Hall State. *Phys. Rev. Lett.*, 115:057206, Jul 2015.
- [67] A. J. Bestwick, E. J. Fox, Xufeng Kou, Lei Pan, Kang L. Wang, and D. Goldhaber-Gordon. Precise Quantization of the Anomalous Hall Effect near Zero Magnetic Field. *Phys. Rev. Lett.*, 114:187201, May 2015.
- [68] Y. S. Hor, P. Roushan, H. Beidenkopf, J. Seo, D. Qu, J. G. Checkelsky, L. A. Wray, D. Hsieh, Y. Xia, S.-Y. Xu, D. Qian, M. Z. Hasan, N. P. Ong, A. Yazdani, and R. J. Cava. Development of ferromagnetism in the doped topological insulator  $\text{Bi}_{2-x}\text{Mn}_x\text{Te}_3$ . *Phys. Rev. B*, 81:195203, May 2010.
- [69] M. Mogi, R. Yoshimi, A. Tsukazaki, K. Yasuda, Y. Kozuka, K. S. Takahashi, M. Kawasaki, and Y. Tokura. Magnetic modulation doping in topological insulators toward higher-temperature quantum anomalous Hall effect. *Applied Physics Letters*, 107(18):182401, 2015.
- [70] Joseph G. Checkelsky, Jianting Ye, Yoshinori Onose, Yoshihiro Iwasa, and Yoshinori Tokura. Dirac-fermion-mediated ferromagnetism in a topological insulator. *Nature Physics*, 8(10):729–733, 2012.

[71] Su-Yang Xu, Madhab Neupane, Chang Liu, Duming Zhang, Anthony Richardella, L. Andrew Wray, Nasser Alidoust, Mats Leandersson, Thiagarajan Balasubramanian, Jaime Sánchez-Barriga, Oliver Rader, Gabriel Landolt, Bartosz Slomski, Jan Hugo Dil, Jürg Osterwalder, Tay-Rong Chang, Horng-Tay Jeng, Hsin Lin, Arun Bansil, Nitin Samarth, and M. Zahid Hasan. Hedgehog spin texture and Berry's phase tuning in a magnetic topological insulator. *Nature Physics*, 8(8):616–622, 2012.

[72] J. Henk, A. Ernst, S. V. Eremeev, E. V. Chulkov, I. V. Maznichenko, and I. Mertig. Complex Spin Texture in the Pure and Mn-Doped Topological Insulator  $\text{Bi}_2\text{Te}_3$ . *Phys. Rev. Lett.*, 108:206801, May 2012.

[73] A. M. Shikin, A. A. Rybkina, D. A. Estyunin, D. M. Sostina, V. Yu. Voroshnin, I. I. Klimovskikh, A. G. Rybkin, Yu. A. Surnin, K. A. Kokh, O. E. Tereshchenko, L. Petaccia, G. Di Santo, P. N. Skirdkov, K. A. Zvezdin, A. K. Zvezdin, A. Kimura, E. V. Chulkov, and E. E. Krasovskii. Signatures of in-plane and out-of-plane magnetization generated by synchrotron radiation in magnetically doped and pristine topological insulators. *Phys. Rev. B*, 97:245407, Jun 2018.

[74] Jing Teng, Nan Liu, and Yongqing Li. Mn-doped topological insulators: a review. *Journal of Semiconductors*, 40(8):081507, Aug 2019.

[75] Peng Wei, Ferhat Katmis, Badih A. Assaf, Hadar Steinberg, Pablo Jarillo-Herrero, Donald Heiman, and Jagadeesh S. Moodera. Exchange-Coupling-Induced Symmetry Breaking in Topological Insulators. *Phys. Rev. Lett.*, 110:186807, Apr 2013.

[76] Ivana Vobornik, Unnikrishnan Manju, Jun Fujii, Francesco Borgatti, Piero Torelli, Damjan Krizmancic, Yew San Hor, Robert J. Cava, and Giancarlo Panaccione. Magnetic Proximity Effect as a Pathway to Spintronic Applications of Topological Insulators. *Nano Lett.*, 11(10):4079–4082, October 2011.

[77] S. V. Eremeev, V. N. Men'shov, V. V. Tugushev, P. M. Echenique, and E. V. Chulkov. Magnetic proximity effect at the three-dimensional topological insulator/magnetic insulator interface. *Phys. Rev. B*, 88:144430, Oct 2013.

[78] Ferhat Katmis, Valeria Lauter, Flavio S. Nogueira, Badih A. Assaf, Michelle E. Jamer, Peng Wei, Biswarup Satpati, John W. Freeland, Ilya Eremin, Don Heiman, Pablo Jarillo-Herrero, and Jagadeesh S. Moodera. A high-temperature ferromagnetic topological insulating phase by proximity coupling. *Nature*, 533(7604):513–516, 2016.

[79] Zilong Jiang, Cui-Zu Chang, Chi Tang, Peng Wei, Jagadeesh S. Moodera, and Jing Shi. Independent Tuning of Electronic Properties and Induced Ferromagnetism in Topological Insulators with Heterostructure Approach. *Nano Lett.*, 15(9):5835–5840, September 2015.

[80] Zilong Jiang, Cui-Zu Chang, Massoud Ramezani Masir, Chi Tang, Yadong Xu, Jagadeesh S. Moodera, Allan H. MacDonald, and Jing Shi. Enhanced spin Seebeck effect signal due to spin-momentum locked topological surface states. *Nature Communications*, 7(1):11458, 2016.

[81] Hailong Wang, James Kally, Joon Sue Lee, Tao Liu, Houchen Chang, Danielle Reifsnnyder Hickey, K. Andre Mkhoyan, Mingzhong Wu, Anthony Richardella, and Nitin Samarth. Surface-State-Dominated Spin-Charge Current Conversion in Topological-Insulator–Ferromagnetic-Insulator Heterostructures. *Phys. Rev. Lett.*, 117:076601, Aug 2016.

[82] Chi Tang, Cui-Zu Chang, Gejian Zhao, Yawen Liu, Zilong Jiang, Chao-Xing Liu, Martha R. McCartney, David J. Smith, Tingyong Chen, Jagadeesh S. Moodera, and Jing Shi. Above 400-K robust perpendicular ferromagnetic phase in a topological insulator. *Science Advances*, 3(6):e1700307, 2017.

[83] M. M. Otkrov, T. V. Menshchikova, I. P. Rusinov, M. G. Vergniory, V. M. Kuznetsov, and E. V. Chulkov. Magnetic extension as an efficient method for realizing the quantum anomalous Hall state in topological insulators. *JETP Letters*, 105(5):297–302, 2017.

[84] M M Otkrov, T V Menshchikova, M G Vergniory, I P Rusinov, A Yu Vayzovskaya, Yu M Koroteev, G Bihlmayer, A Ernst, P M Echenique, A Arnaud, and E V Chulkov. Highly-ordered wide bandgap materials for quantized anomalous Hall and magnetoelectric effects. *2D Materials*, 4(2):025082, apr 2017.

[85] Toru Hirahara, Sergey V. Eremeev, Tetsuroh Shirasawa, Yuma Okuyama, Takayuki Kubo, Ryosuke Nakanishi, Ryota Akiyama, Akari Takayama, Tetsuya Hajiri, Shin-ichiro Ieda, Masaharu Matsunami, Kazuki Sumida, Koji Miyamoto, Yasumasa Takagi, Kiyoisa Tanaka, Taichi Okuda, Toshihiko Yokoyama, Shin-ichi Kimura, Shuji Hasegawa, and Evgueni V. Chulkov. Large-Gap Magnetic Topological Heterostructure formed by Subsurface incorporation of a Ferromagnetic Layer. *Nano Lett.*, 17(6):3493–3500, June 2017.

[86] Sergey V. Eremeev, Mikhail M. Otrokov, and Evgueni V. Chulkov. New Universal Type of Interface in the Magnetic Insulator/Topological Insulator Heterostructures. *Nano Lett.*, 18(10):6521–6529, October 2018.

[87] Inhee Lee, Chung Koo Kim, Jinho Lee, Simon J. L. Billinge, Ruidan Zhong, John A. Schneeloch, Tiansheng Liu, Tonica Valla, John M. Tranquada, Genda Gu, and J. C. Séamus Davis. Imaging Dirac-mass disorder from magnetic dopant atoms in the ferromagnetic topological insulator  $\text{Cr}_x(\text{Bi}_{0.1}\text{Sb}_{0.9})_{2-x}\text{Te}_3$ . *Proceedings of the National Academy of Sciences*, 112(5):1316–1321, 2015.

[88] Haim Beidenkopf, Pedram Roushan, Jungpil Seo, Lindsay Gorman, Ilya Drozdov, Yew San Hor, R. J. Cava, and Ali Yazdani. Spatial fluctuations of helical Dirac fermions on the surface of topological insulators. *Nature Physics*, 7(12):939–943, 2011.

[89] Yoshinori Okada, Chetan Dhalal, Wenwen Zhou, Erik D. Huemiller, Hsin Lin, S. Basak, A. Bansil, Y.-B. Huang, H. Ding, Z. Wang, Stephen D. Wilson, and V. Madhavan. Direct Observation of Broken Time-Reversal Symmetry on the Surface of a Magnetically Doped Topological Insulator. *Phys. Rev. Lett.*, 106:206805, May 2011.

[90] Cui-Zu Chang, Jinsong Zhang, Xiao Feng, Jie Shen, Zuocheng Zhang, Minghua Guo, Kang Li, Yunbo Ou, Pang Wei, Li-Li Wang, Zhong-Qing Ji, Yang Feng, Shuaihua Ji, Xi Chen, Jinfeng Jia, Xi Dai, Zhong Fang, Shou-Cheng Zhang, Ke He, Yayu Wang, Li Lu, Xu-Cun Ma, and Qi-Kun Xue. Experimental Observation of the Quantum Anomalous Hall Effect in a Magnetic Topological Insulator. *Science*, 340(6129):167–170, 2013.

[91] J. G. Checkelsky, R. Yoshimi, A. Tsukazaki, K. S. Takahashi, Y. Kozuka, J. Falson, M. Kawasaki, and Y. Tokura. Trajectory of the anomalous Hall effect towards the quantized state in a ferromagnetic topological insulator. *Nature Physics*, 10(10):731–736, 2014.

[92] Xufeng Kou, Shih-Ting Guo, Yabin Fan, Lei Pan, Murong Lang, Ying Jiang, Qiming Shao, Tianxiao Nie, Koichi Murata, Jianshi Tang, Yong Wang, Liang He, Ting-Kuo Lee, Wei-Li Lee, and Kang L. Wang. Scale-Invariant Quantum Anomalous Hall Effect in Magnetic Topological Insulators beyond the Two-Dimensional Limit. *Phys. Rev. Lett.*, 113:137201, Sep 2014.

[93] S. Grauer, S. Schreyeck, M. Winnerlein, K. Brunner, C. Gould, and L. W. Molenkamp. Coincidence of superparamagnetism and perfect quantization in the quantum anomalous Hall state. *Phys. Rev. B*, 92:201304, Nov 2015.

## BIBLIOGRAPHY

---

[94] Xufeng Kou, Lei Pan, Jing Wang, Yabin Fan, Eun Sang Choi, Wei-Li Lee, Tianxiao Nie, Koichi Murata, Qiming Shao, Shou-Cheng Zhang, and Kang L. Wang. Metal-to-insulator switching in quantum anomalous Hall states. *Nature Communications*, 6(1):8474, 2015.

[95] Abhinav Kandala, Anthony Richardella, Susan Kempinger, Chao-Xing Liu, and Nitin Samarth. Giant anisotropic magnetoresistance in a quantum anomalous Hall insulator. *Nature Communications*, 6(1):7434, 2015.

[96] Cui-Zu Chang, Weiwei Zhao, Duk Y. Kim, Haijun Zhang, Badih A. Assaf, Don Heiman, Shou-Cheng Zhang, Chaoxing Liu, Moses H. W. Chan, and Jagadeesh S. Moodera. High-precision realization of robust quantum anomalous Hall state in a hard ferromagnetic topological insulator. *Nature Materials*, 14(5):473–477, 2015.

[97] Yang Feng, Xiao Feng, Yunbo Ou, Jing Wang, Chang Liu, Liguo Zhang, Dongyang Zhao, Gaoyuan Jiang, Shou-Cheng Zhang, Ke He, Xucun Ma, Qi-Kun Xue, and Yayu Wang. Observation of the Zero all Plateau in a Quantum Anomalous Hall Insulator. *Phys. Rev. Lett.*, 115:126801, Sep 2015.

[98] M. Mogi, M. Kawamura, R. Yoshimi, A. Tsukazaki, Y. Kozuka, N. Shirakawa, K. S. Takahashi, M. Kawasaki, and Y. Tokura. A magnetic heterostructure of topological insulators as a candidate for an axion insulator. *Nature Materials*, 16(5):516–521, 2017.

[99] Yujun Deng, Yijun Yu, Meng Zhu Shi, Zhongxun Guo, Zihan Xu, Jing Wang, Xian Hui Chen, and Yuanbo Zhang. Quantum anomalous Hall effect in intrinsic magnetic topological insulator  $\text{MnBi}_2\text{Te}_4$ . *Science*, 367(6480):895–900, 2020.

[100] Chang Liu, Yongchao Wang, Hao Li, Yang Wu, Yaoxin Li, Jiaheng Li, Ke He, Yong Xu, Jinsong Zhang, and Yayu Wang. Robust axion insulator and Chern insulator phases in a two-dimensional antiferromagnetic topological insulator. *Nature Materials*, 19(5):522–527, 2020.

[101] Dong Sun Lee, Tae-Hoon Kim, Cheol-Hee Park, Chan-Yeup Chung, Young Soo Lim, Won-Seon Seo, and Hyung-Ho Park. Crystal structure, properties and nanostructuring of a new layered chalcogenide semiconductor,  $\text{Bi}_2\text{MnTe}_4$ . *CrystEngComm*, 15:5532–5538, 2013.

[102] Ziya S. Aliev, Imamaddin R. Amiraslanov, Daria I. Nasonova, Andrei V. Shevelkov, Nadir A. Abdullayev, Zakir A. Jahangirli, Elnur N. Orujlu, Mikhail M. Otrokov, Nazim T. Mamedov, Mahammad B. Babanly, and

## BIBLIOGRAPHY

---

Evgueni V. Chulkov. Novel ternary layered manganese bismuth tellurides of the MnTe-Bi<sub>2</sub>Te<sub>3</sub> system: Synthesis and crystal structure. *Journal of Alloys and Compounds*, 789:443–450, 2019.

[103] Daniel Souchay, Markus Nentwig, Daniel Günther, Simon Keilholz, Johannes de Boor, Alexander Zeugner, Anna Isaeva, Michael Ruck, Anja UB Wolter, Bernd Büchner, et al. Layered manganese bismuth tellurides with GeBi<sub>4</sub>Te<sub>7</sub>- and GeBi<sub>6</sub>Te<sub>10</sub>-type structures: towards multifunctional materials. *Journal of Materials Chemistry C*, 7(32):9939–9953, 2019.

[104] Chenhui Yan, Yanglin Zhu, Leixin Miao, Sebastian Fernandez-Mulligan, Emanuel Green, Ruobing Mei, Hengxin Tan, Binghai Yan, Chao-Xing Liu, Nasim Alem, Zhiqiang Mao, and Shuolong Yang. Delicate Ferromagnetism in MnBi<sub>6</sub>Te<sub>10</sub>. *Nano Lett.*, 22(24):9815–9822, December 2022.

[105] Abdul-Vakhab Tcakaev, Bastian Rubrecht, Jorge I. Facio, Volodymyr B. Zabolotnyy, Laura T. Corredor, Laura C. Folkers, Ekaterina Kochetkova, Thiago R. F. Peixoto, Philipp Kagerer, Simon Heinze, Hendrik Bentmann, Robert J. Green, Pierluigi Gargiani, Manuel Valvidares, Eugen Weschke, Mau- rits W. Haverkort, Friedrich Reinert, Jeroen van den Brink, Bernd Büchner, Anja U. B. Wolter, Anna Isaeva, and Vladimir Hinkov. Intermixing-Driven Surface and Bulk Ferromagnetism in the Quantum Anomalous Hall Candidate MnBi<sub>6</sub>Te<sub>10</sub>. *Advanced Science*, 2203239, 2023.

[106] Dmitry Ovchinnikov, Xiong Huang, Zhong Lin, Zaiyao Fei, Jiaqi Cai, Tiancheng Song, Minhao He, Qianni Jiang, Chong Wang, Hao Li, Yayu Wang, Yang Wu, Di Xiao, Jiun-Haw Chu, Jiaqiang Yan, Cui-Zu Chang, Yong-Tao Cui, and Xiaodong Xu. Intertwined Topological and Magnetic Orders in Atomically Thin Chern Insulator MnBi<sub>2</sub>Te<sub>4</sub>. *Nano Lett.*, 21(6):2544–2550, March 2021.

[107] Chaowei Hu, Lei Ding, Kyle N. Gordon, Barun Ghosh, Hung-Ju Tien, Haoxiang Li, A. Garrison Linn, Shang-Wei Lien, Cheng-Yi Huang, Scott Mackey, Jinyu Liu, P. V. Sreenivasa Reddy, Bahadur Singh, Amit Agarwal, Arun Bansil, Miao Song, Dongsheng Li, Su-Yang Xu, Hsin Lin, Huibo Cao, Tay-Rong Chang, Dan Dessau, and Ni Ni. Realization of an intrinsic ferromagnetic topological state in MnBi<sub>8</sub>Te<sub>13</sub>. *Science Advances*, 6(30):eaba4275, 2020.

[108] Jiazen Wu, Fucai Liu, Can Liu, Yong Wang, Changcun Li, Yangfan Lu, Satoru Matsuishi, and Hideo Hosono. Toward 2D Magnets in the (MnBi<sub>2</sub>Te<sub>4</sub>)(Bi<sub>2</sub>Te<sub>3</sub>)<sub>n</sub> Bulk Crystal. *Advanced Materials*, 32(23):2001815, 2020.

[109] Alexander Zeugner, Frederik Nietschke, Anja U. B. Wolter, Sebastian Gaß, Raphael C. Vidal, Thiago R. F. Peixoto, Darius Pohl, Christine Damm, Axel Lubk, Richard Henrich, Simon K. Moser, Celso Fornari, Chul Hee Min, Sonja Schatz, Katharina Kißner, Maximilian Ünzelmann, Martin Kaiser, Francesco Scaravaggi, Bernd Rellinghaus, Kornelius Nielsch, Christian Hess, Bernd Büchner, Friedrich Reinert, Hendrik Bentmann, Oliver Oeckler, Thomas Doert, Michael Ruck, and Anna Isaeva. Chemical Aspects of the Candidate Antiferromagnetic Topological Insulator  $\text{MnBi}_2\text{Te}_4$ . *Chemistry of Materials*, 31(8):2795–2806, 2019.

[110] Jiazen Wu, Fucai Liu, Masato Sasase, Koichiro Ienaga, Yukiko Obata, Ryu Yukawa, Koji Horiba, Hiroshi Kumigashira, Satoshi Okuma, Takeshi Inoshita, et al. Natural van der Waals heterostructural single crystals with both magnetic and topological properties. *Science advances*, 5(11):eaax9989, 2019.

[111] Jiaheng Li, Chong Wang, Zetao Zhang, Bing-Lin Gu, Wenhui Duan, and Yong Xu. Magnetically controllable topological quantum phase transitions in the antiferromagnetic topological insulator  $\text{MnBi}_2\text{Te}_4$ . *Phys. Rev. B*, 100:121103, Sep 2019.

[112] Dongqin Zhang, Minji Shi, Tongshuai Zhu, Dingyu Xing, Haijun Zhang, and Jing Wang. Topological Axion States in the Magnetic Insulator  $\text{MnBi}_2\text{Te}_4$  with the Quantized Magnetoelectric Effect. *Phys. Rev. Lett.*, 122:206401, May 2019.

[113] Yu-Jie Hao, Pengfei Liu, Yue Feng, Xiao-Ming Ma, Eike F. Schwier, Masashi Arita, Shiv Kumar, Chaowei Hu, Rui'e Lu, Meng Zeng, Yuan Wang, Zhanyang Hao, Hong-Yi Sun, Ke Zhang, Jiawei Mei, Ni Ni, Liusuo Wu, Kenya Shimada, Chaoyu Chen, Qihang Liu, and Chang Liu. Gapless Surface Dirac Cone in Antiferromagnetic Topological Insulator  $\text{MnBi}_2\text{Te}_4$ . *Phys. Rev. X*, 9:041038, Nov 2019.

[114] Chaowei Hu, Kyle N Gordon, Pengfei Liu, Jinyu Liu, Xiaoqing Zhou, Peipei Hao, Dushyant Narayan, Eve Emmanouilidou, Hongyi Sun, Yuntian Liu, et al. A van der Waals antiferromagnetic topological insulator with weak interlayer magnetic coupling. *Nature communications*, 11(1):1–8, 2020.

[115] Xuefeng Wu, Jiayu Li, Xiao-Ming Ma, Yu Zhang, Yuntian Liu, Chun-Sheng Zhou, Jifeng Shao, Qiaoming Wang, Yu-Jie Hao, Yue Feng, et al. Distinct topological surface states on the two terminations of  $\text{MnBi}_4\text{Te}_7$ . *Physical Review X*, 10(3):031013, 2020.

[116] RC Vidal, Hendrik Bentmann, TRF Peixoto, Alexander Zeugner, S Moser, C-H Min, S Schatz, K Kißner, M Ünzelmann, CI Fornari, et al. Surface states and Rashba-type spin polarization in antiferromagnetic  $\text{MnBi}_2\text{Te}_4$  (0001). *Physical Review B*, 100(12):121104, 2019.

[117] Seng Huat Lee, Yanglin Zhu, Yu Wang, Leixin Miao, Timothy Pillsbury, Hemian Yi, Susan Kempinger, Jin Hu, Colin A. Heikes, P. Quarterman, William Ratcliff, Julie A. Borchers, Heda Zhang, Xianglin Ke, David Graf, Nasim Alem, Cui-Zu Chang, Nitin Samarth, and Zhiqiang Mao. Spin scattering and noncollinear spin structure-induced intrinsic anomalous Hall effect in antiferromagnetic topological insulator  $\text{MnBi}_2\text{Te}_4$ . *Phys. Rev. Research*, 1:012011, Aug 2019.

[118] Bo Chen, Fucong Fei, Dongqin Zhang, Bo Zhang, Wanling Liu, Shuai Zhang, Pengdong Wang, Boyuan Wei, Yong Zhang, Zewen Zuo, Jingwen Guo, Qianqian Liu, Zilu Wang, Xuchuan Wu, Junyu Zong, Xuedong Xie, Wang Chen, Zhe Sun, Shancai Wang, Yi Zhang, Minhao Zhang, Xuefeng Wang, Fengqi Song, Haijun Zhang, Dawei Shen, and Baigeng Wang. Intrinsic magnetic topological insulator phases in the Sb doped  $\text{MnBi}_2\text{Te}_4$  bulks and thin flakes. *Nature Communications*, 10(1):4469, 2019.

[119] D. A. Estyunin, I. I. Klimovskikh, A. M. Shikin, E. F. Schwier, M. M. Otrokov, A. Kimura, S. Kumar, S. O. Filnov, Z. S. Aliev, M. B. Babanly, and E. V. Chulkov. Signatures of temperature driven antiferromagnetic transition in the electronic structure of topological insulator  $\text{MnBi}_2\text{Te}_4$ . *APL Materials*, 8(2):021105, 2020.

[120] Xiao-Ming Ma, Zhongjia Chen, Eike F. Schwier, Yang Zhang, Yu-Jie Hao, Shiv Kumar, Ruie Lu, Jifeng Shao, Yuanjun Jin, Meng Zeng, Xiang-Rui Liu, Zhanyang Hao, Ke Zhang, Wumiti Mansuer, Chunyao Song, Yuan Wang, Boyan Zhao, Cai Liu, Ke Deng, Jiawei Mei, Kenya Shimada, Yue Zhao, Xingjiang Zhou, Bing Shen, Wen Huang, Chang Liu, Hu Xu, and Chaoyu Chen. Hybridization-induced gapped and gapless states on the surface of magnetic topological insulators. *Phys. Rev. B*, 102:245136, Dec 2020.

[121] Lixuan Xu, Yuanhao Mao, Hongyuan Wang, Jiaheng Li, Yujie Chen, Yunyouyou Xia, Yiwei Li, Ding Pei, Jing Zhang, Huijun Zheng, Kui Huang, Chaofan Zhang, Shengtao Cui, Aiji Liang, Wei Xia, Hao Su, Sungwon Jung, Cephise Cacho, Meixiao Wang, Gang Li, Yong Xu, Yanfeng Guo, Lexian Yang, Zhongkai Liu, Yulin Chen, and Mianheng Jiang. Persistent surface states with diminishing gap in  $\text{MnBi}_2\text{Te}_4/\text{Bi}_2\text{Te}_3$  superlattice antiferromagnetic topological insulator. *Science Bulletin*, 65(24):2086–2093, 2020.

## BIBLIOGRAPHY

---

[122] Yong Hu, Lixuan Xu, Mengzhu Shi, Aiyun Luo, Shuting Peng, Z. Y. Wang, J. J. Ying, T. Wu, Z. K. Liu, C. F. Zhang, Y. L. Chen, G. Xu, X.-H. Chen, and J.-F. He. Universal gapless Dirac cone and tunable topological states in  $(\text{MnBi}_2\text{Te}_4)_m(\text{Bi}_2\text{Te}_3)_n$  heterostructures. *Phys. Rev. B*, 101:161113, Apr 2020.

[123] J.-Q. Yan, Q. Zhang, T. Heitmann, Zengle Huang, K. Y. Chen, J.-G. Cheng, Weida Wu, D. Vaknin, B. C. Sales, and R. J. McQueeney. Crystal growth and magnetic structure of  $\text{MnBi}_2\text{Te}_4$ . *Phys. Rev. Materials*, 3:064202, Jun 2019.

[124] Jiaheng Li, Yang Li, Shiqiao Du, Zun Wang, Bing-Lin Gu, Shou-Cheng Zhang, Ke He, Wenhui Duan, and Yong Xu. Intrinsic magnetic topological insulators in van der Waals layered  $\text{MnBi}_2\text{Te}_4$ -family materials. *Science Advances*, 5(6):eaaw5685, 2019.

[125] E. D. L. Rienks, S. Wimmer, J. Sánchez-Barriga, O. Caha, P. S. Mandal, J. Růžička, A. Ney, H. Steiner, V. V. Volobuev, H. Groiss, M. Albu, G. Kothleitner, J. Michalička, S. A. Khan, J. Minár, H. Ebert, G. Bauer, F. Freyse, A. Varykhalov, O. Rader, and G. Springholz. Large magnetic gap at the Dirac point in  $\text{Bi}_2\text{Te}_3/\text{MnBi}_2\text{Te}_4$  heterostructures. *Nature*, 576(7787):423–428, 2019.

[126] J.-Q. Yan, S. Okamoto, M. A. McGuire, A. F. May, R. J. McQueeney, and B. C. Sales. Evolution of structural, magnetic, and transport properties in  $\text{MnBi}_{2-x}\text{Sb}_x\text{Te}_4$ . *Phys. Rev. B*, 100:104409, Sep 2019.

[127] Lei Ding, Chaowei Hu, Feng Ye, Erxi Feng, Ni Ni, and Huibo Cao. Crystal and magnetic structures of magnetic topological insulators  $\text{MnBi}_4\text{Te}_7$ . *Phys. Rev. B*, 101:020412, Jan 2020.

[128] Jianhua Cui, Mengzhu Shi, Honghui Wang, Fanghang Yu, Tao Wu, Xiangang Luo, Jianjun Ying, and Xianhui Chen. Transport properties of thin flakes of the antiferromagnetic topological insulator  $\text{MnBi}_2\text{Te}_4$ . *Phys. Rev. B*, 99:155125, Apr 2019.

[129] Bing Li, J.-Q. Yan, D. M. Pajerowski, Elijah Gordon, A.-M. Nedić, Y. Sizuk, Liqin Ke, P. P. Orth, D. Vaknin, and R. J. McQueeney. Competing Magnetic Interactions in the Antiferromagnetic Topological Insulator  $\text{MnBi}_2\text{Te}_4$ . *Phys. Rev. Lett.*, 124:167204, Apr 2020.

[130] L.A. Kuznetsova, V.L. Kuznetsov, and D.M. Rowe. Thermoelectric properties and crystal structure of ternary compounds in the  $\text{Ge}(\text{Sn},\text{Pb})\text{Te}-\text{Bi}_2\text{Te}_3$  systems. *Journal of Physics and Chemistry of Solids*, 61(8):1269–1274, 2000.

## BIBLIOGRAPHY

---

- [131] You Lai, Liqin Ke, Jiaqiang Yan, Ross D. McDonald, and Robert J. McQueeney. Defect-driven ferrimagnetism and hidden magnetization in  $\text{MnBi}_2\text{Te}_4$ . *Phys. Rev. B*, 103:184429, May 2021.
- [132] Bing Li, D. M. Pajerowski, S. X. M. Riberolles, Liqin Ke, J.-Q. Yan, and R. J. McQueeney. Quasi-two-dimensional ferromagnetism and anisotropic interlayer couplings in the magnetic topological insulator  $\text{MnBi}_2\text{Te}_4$ . *Phys. Rev. B*, 104:L220402, Dec 2021.
- [133] J.-Q. Yan. Perspective-The Elusive Quantum Anomalous Hall Effect in  $\text{MnBi}_2\text{Te}_4$ : Materials. *ECS Journal of Solid State Science and Technology*, 11(6):063007, 2022.
- [134] A. M. Shikin, D. A. Estyunin, I. I. Klimovskikh, S. O. Filnov, E. F. Schwier, S. Kumar, K. Miyamoto, T. Okuda, A. Kimura, K. Kuroda, K. Yaji, S. Shin, Y. Takeda, Y. Saitoh, Z. S. Aliev, N. T. Mamedov, I. R. Amiraslanov, M. B. Babanly, M. M. Otrokov, S. V. Eremeev, and E. V. Chulkov. Nature of the Dirac gap modulation and surface magnetic interaction in axion antiferromagnetic topological insulator  $\text{MnBi}_2\text{Te}_4$ . *Scientific Reports*, 10(1):13226, 2020.
- [135] Y. J. Chen, L. X. Xu, J. H. Li, Y. W. Li, H. Y. Wang, C. F. Zhang, H. Li, Y. Wu, A. J. Liang, C. Chen, S. W. Jung, C. Cacho, Y. H. Mao, S. Liu, M. X. Wang, Y. F. Guo, Y. Xu, Z. K. Liu, L. X. Yang, and Y. L. Chen. Topological Electronic Structure and Its Temperature Evolution in Antiferromagnetic Topological Insulator  $\text{MnBi}_2\text{Te}_4$ . *Phys. Rev. X*, 9:041040, Nov 2019.
- [136] Hang Li, Shun-Ye Gao, Shao-Feng Duan, Yuan-Feng Xu, Ke-Jia Zhu, Shang-Jie Tian, Jia-Cheng Gao, Wen-Hui Fan, Zhi-Cheng Rao, Jie-Rui Huang, Jia-Jun Li, Da-Yu Yan, Zheng-Tai Liu, Wan-Ling Liu, Yao-Bo Huang, Yu-Liang Li, Yi Liu, Guo-Bin Zhang, Peng Zhang, Takeshi Kondo, Shik Shin, He-Chang Lei, You-Guo Shi, Wen-Tao Zhang, Hong-Ming Weng, Tian Qian, and Hong Ding. Dirac Surface States in Intrinsic Magnetic Topological Insulators  $\text{EuSn}_2\text{As}_2$  and  $\text{MnBi}_{2n}\text{Te}_{3n+1}$ . *Phys. Rev. X*, 9:041039, Nov 2019.
- [137] Przemyslaw Swatek, Yun Wu, Lin-Lin Wang, Kyungchan Lee, Benjamin Schrunk, Jiaqiang Yan, and Adam Kaminski. Gapless Dirac surface states in the antiferromagnetic topological insulator  $\text{MnBi}_2\text{Te}_4$ . *Phys. Rev. B*, 101:161109, Apr 2020.
- [138] A. Alfonsov, K. Mehlawat, A. Zeugner, A. Isaeva, B. Büchner, and V. Kataev. Magnetic-field tuning of the spin dynamics in the magnetic topological insulators  $(\text{MnBi}_2\text{Te}_4)(\text{Bi}_2\text{Te}_3)_n$ . *Phys. Rev. B*, 104:195139, Nov 2021.

## BIBLIOGRAPHY

---

[139] Yonghao Yuan, Xintong Wang, Hao Li, Jiaheng Li, Yu Ji, Zhenqi Hao, Yang Wu, Ke He, Yayu Wang, Yong Xu, Wenhui Duan, Wei Li, and Qi-Kun Xue. Electronic States and Magnetic Response of  $\text{MnBi}_2\text{Te}_4$  by Scanning Tunneling Microscopy and Spectroscopy. *Nano Letters*, 20(5):3271–3277, 2020. PMID: 32298117.

[140] Zuowei Liang, Aiyun Luo, Mengzhu Shi, Qiang Zhang, Simin Nie, JJ Ying, J-F He, Tao Wu, Zhijun Wang, Gang Xu, et al. Mapping Dirac fermions in the intrinsic antiferromagnetic topological insulators  $(\text{MnBi}_2\text{Te}_4)(\text{Bi}_2\text{Te}_3)_n$  ( $n = 0, 1$ ). *Physical Review B*, 102(16):161115, 2020.

[141] Zengle Huang, Mao-Hua Du, Jiaqiang Yan, and Weida Wu. Native defects in antiferromagnetic topological insulator  $\text{MnBi}_2\text{Te}_4$ . *Phys. Rev. Materials*, 4:121202, Dec 2020.

[142] Manuela Garnica, Mikhail M. Otrokov, P Casado Aguilar, Ilya I. Klimovskikh, D. A. Estyunin, Ziya S. Aliev, Imamaddin Rajabali Amiraslanov, Nadir A. Abdullayev, Vladimir N Zverev, M. B. Babanly, Nazim T. Mamedov, Alexander Shikin, Andrés Arnau, A. L. Vázquez de Parga, E. V. Chulkov, and Rodolfo Miranda. Native point defects and their implications for the Dirac point gap at  $\text{MnBi}_2\text{Te}_4(0001)$ . *npj Quantum Materials*, 7:1–9, 2022.

[143] M. Z. Shi, B. Lei, C. S. Zhu, D. H. Ma, J. H. Cui, Z. L. Sun, J. J. Ying, and X. H. Chen. Magnetic and transport properties in the magnetic topological insulators  $\text{MnBi}_2\text{Te}_4(\text{Bi}_2\text{Te}_3)_n$  ( $n = 1, 2$ ). *Phys. Rev. B*, 100:155144, Oct 2019.

[144] J.-Q. Yan, Y. H. Liu, D. S. Parker, Y. Wu, A. A. Aczel, M. Matsuda, M. A. McGuire, and B. C. Sales. A-type antiferromagnetic order in  $\text{MnBi}_4\text{Te}_7$  and  $\text{MnBi}_6\text{Te}_{10}$  single crystals. *Phys. Rev. Materials*, 4:054202, May 2020.

[145] M. Ceccardi, A. Zeugner, L. C. Folkers, C. Hess, B. Büchner, D. Marré, A. Isaeva, and F. Caglieris. Anomalous Nernst effect in the topological and magnetic material  $\text{MnBi}_4\text{Te}_7$ . *npj Quantum Materials*, 8(1):76, 2023.

[146] A. Alfonsov, J. I. Facio, K. Mehlawat, A. G. Moghaddam, R. Ray, A. Zeugner, M. Richter, J. van den Brink, A. Isaeva, B. Büchner, and V. Kataev. Strongly anisotropic spin dynamics in magnetic topological insulators. *Phys. Rev. B*, 103:L180403, May 2021.

[147] Ilya I. Klimovskikh, Mikhail M. Otrokov, Dmitry Estyunin, Sergey V. Ere-meev, Sergey O. Filnov, Alexandra Koroleva, Eugene Shevchenko, Vladimir

Voroshnin, Artem G. Rybkin, Igor P. Rusinov, Maria Blanco-Rey, Martin Hoffmann, Ziya S. Aliev, Mahammad B. Babanly, Imamaddin R. Amiraslanov, Nadir A. Abdullayev, Vladimir N. Zverev, Akio Kimura, Oleg E. Tereshchenko, Konstantin A. Kokh, Luca Petaccia, Giovanni Di Santo, Arthur Ernst, Pedro M. Echenique, Nazim T. Mamedov, Alexander M. Shikin, and Eugene V. Chulkov. Tunable 3D/2D magnetism in the  $(\text{MnBi}_2\text{Te}_4)(\text{Bi}_2\text{Te}_3)_m$  topological insulators family. *npj Quantum Materials*, 5(1):54, 2020.

[148] R. C. Vidal, H. Bentmann, J. I. Facio, T. Heider, P. Kagerer, C. I. Fornari, T. R. F. Peixoto, T. Figgemeier, S. Jung, C. Cacho, B. Büchner, J. van den Brink, C. M. Schneider, L. Plucinski, E. F. Schwier, K. Shimada, M. Richter, A. Isaeva, and F. Reinert. Orbital Complexity in Intrinsic Magnetic Topological Insulators  $\text{MnBi}_4\text{Te}_7$  and  $\text{MnBi}_6\text{Te}_{10}$ . *Phys. Rev. Lett.*, 126:176403, Apr 2021.

[149] Hao-Ke Xu, Mingqiang Gu, Fucong Fei, Yi-Sheng Gu, Dang Liu, Qiao-Yan Yu, Sha-Sha Xue, Xu-Hui Ning, Bo Chen, Hangkai Xie, Zhen Zhu, Dandan Guan, Shiyong Wang, Yaoyi Li, Canhua Liu, Qihang Liu, Fengqi Song, Hao Zheng, and Jinfeng Jia. Observation of Magnetism-Induced Topological Edge State in Antiferromagnetic Topological Insulator  $\text{MnBi}_4\text{Te}_7$ . *ACS Nano*, 16(6):9810–9818, 2022. PMID: 35695549.

[150] G. Binnig, H. Rohrer, Ch. Gerber, and E. Weibel. Tunneling through a controllable vacuum gap. *Appl. Phys. Lett.*, 40(2):178–180, January 1982.

[151] G. Binnig and H. Rohrer. Scanning tunneling microscopy. *Surface Science*, 126(1):236–244, 1983.

[152] J. Bardeen. Tunnelling from a Many-Particle Point of View. *Phys. Rev. Lett.*, 6:57–59, Jan 1961.

[153] J. J. Sakurai. *Modern Quantum Mechanics*. Addison Wesley, 1 revised edition, 1993.

[154] J. Tersoff and D. R. Hamann. Theory of the scanning tunneling microscope. *Phys. Rev. B*, 31:805–813, Jan 1985.

[155] Herbert Fröhlich. On the theory of superconductivity: the one-dimensional case. *Proceedings of the Royal Society of London. Series A. Mathematical and Physical Sciences*, 223(1154):296–305, 1954.

[156] R. E. Peierls. *Quantum Theory of Solids*. Oxford classic texts in the physical sciences. Clarendon Press; Oxford University Press, 2001.

## BIBLIOGRAPHY

---

[157] D. Haude. *Rastertunnelspektroskopie auf der InAs(110)-Oberfläche: Untersuchungen an drei-, zwei- und nulldimensionalen Elektronensystemen im Magnetfeld*. Dissertation, Universität Hamburg, 2001.

[158] M. F. Crommie, C. P. Lutz, and D. M. Eigler. Imaging standing waves in a two-dimensional electron gas. *Nature*, 363(6429):524–527, 1993.

[159] Ph. Avouris, I.-W. Lyo, R. E. Walkup, and Y. Hasegawa. Real space imaging of electron scattering phenomena at metal surfaces. *Journal of Vacuum Science & Technology B: Microelectronics and Nanometer Structures Processing, Measurement, and Phenomena*, 12(3):1447–1455, 1994.

[160] J. M. Ziman. *Principles of the Theory of Solids*. Cambridge University Press, 2 edition, 1972.

[161] Y. Hasegawa and Ph. Avouris. Direct observation of standing wave formation at surface steps using scanning tunneling spectroscopy. *Phys. Rev. Lett.*, 71:1071–1074, Aug 1993.

[162] P. T. Sprunger, L. Petersen, E. W. Plummer, E. Laegsgaard, and F. Besenbacher. Giant Friedel Oscillations on the Beryllium(0001) Surface. *Science (New York, N.Y.)*, 275:1764–7, Mar 1997.

[163] L. Petersen, P. T. Sprunger, Ph. Hofmann, E. Lægsgaard, B. G. Briner, M. Doering, H.-P. Rust, A. M. Bradshaw, F. Besenbacher, and E. W. Plummer. Direct imaging of the two-dimensional Fermi contour: Fourier-transform STM. *Phys. Rev. B*, 57:R6858–R6861, Mar 1998.

[164] J. E. Hoffman, K. McElroy, D.-H. Lee, K. M Lang, H. Eisaki, S. Uchida, and J. C. Davis. Imaging quasiparticle interference in  $\text{Bi}_2\text{Sr}_2\text{CaCu}_2\text{O}_{8+\delta}$ . *Science*, 297(5584):1148–1151, 2002.

[165] R. Schlegel, T. Hänke, D. Baumann, M. Kaiser, P. K. Nag, R. Voigtländer, D. Lindackers, B. Büchner, and C. Hess. Design and properties of a cryogenic dip-stick scanning tunneling microscope with capacitive coarse approach control. *Review of Scientific Instruments*, 85(1):013706, 2014.

[166] *Oxford Instruments,  $^4\text{He}$ -Cryostat, Oxford Instruments PLC, Tubney Woods Abingdon, Oxfordshire OX13 5QX, United Kingdom*.

[167] *Specs, Nanonis SPM Controller, SPECS Surface Nano Analysis GmbH, Voltastraße 5, D-13355 Berlin, Germany*.

[168] *RHK, SPM Controller, RHK Technology, Inc., 1050 East Maple Road Troy, Michigan 48083, USA*.

## BIBLIOGRAPHY

---

[169] S. H. Pan. Piezo-electric motor,. *International Patent Publication No. WO 93/19494, International Bureau, World Intellectual Property Organization (30 September 1993).*

[170] *EBL Piezo Electric Ceramics, EBL Products Inc., 91 Prestige Park Circle, East Hartford, Connecticut, 06108, USA.*

[171] *Epotek H20E Epoxy Glue, Epoxy Technology, Inc., 14 Fortune Drive, Billerica, Massachusetts 01821-3972, USA.*

[172] G. Mariotto, M. D'Angelo, and I. V. Shvets. Dynamic behavior of a piezowalker, inertial and frictional configurations. *Review of Scientific Instruments*, 70(9):3651–3655, 1999.

[173] *Macor Corning Incorporated, One Riverfront Plaza Corning, New York 14831, USA.*

[174] *www.cryospares.de.*

[175] I. Horcas, R. Fernández, J. M. Gómez-Rodríguez, J. Colchero, J. Gómez-Herrero, and A. M. Baro. WSxM: A software for scanning probe microscopy and a tool for nanotechnology. *Review of Scientific Instruments*, 78(1):013705, 2007.

[176] S. Schimmel and A. Koitzsch. : *private communication.*

[177] Jeffrey R. Shallenberger, Christopher M. Smyth, Rafik Addou, and Robert M. Wallace. 2D bismuth telluride analyzed by XPS. *Surface Science Spectra*, 26(2):024011, 2019.

[178] Omar Concepción, Miguel Galván-Arellano, Vicente Torres-Costa, Aurelio Climent-Font, Daniel Bahena, Miguel Manso Silván, Arturo Escobosa, and Osvaldo de Melo. Controlling the Epitaxial Growth of  $\text{Bi}_2\text{Te}_3$ ,  $\text{BiTe}$ , and  $\text{Bi}_4\text{Te}_3$  Pure Phases by Physical Vapor Transport. *Inorganic Chemistry*, 57(16):10090–10099, 2018. PMID: 30066565.

[179] Peng Cheng, Canli Song, Tong Zhang, Yanyi Zhang, Yilin Wang, Jin-Feng Jia, Jing Wang, Yayu Wang, Bang-Fen Zhu, Xi Chen, Xucun Ma, Ke He, Lili Wang, Xi Dai, Zhong Fang, Xincheng Xie, Xiao-Liang Qi, Chao-Xing Liu, Shou-Cheng Zhang, and Qi-Kun Xue. Landau Quantization of Topological Surface States in  $\text{Bi}_2\text{Se}_3$ . *Phys. Rev. Lett.*, 105:076801, Aug 2010.

[180] P. Roushan. *Visualizing Surface States of Topological Insulators with Scanning Tunneling Microscopy*. Dissertation, Princeton University, 2011.

## BIBLIOGRAPHY

---

- [181] Sunghun Kim, M. Ye, K. Kuroda, Y. Yamada, E. E. Krasovskii, E. V. Chulkov, K. Miyamoto, M. Nakatake, T. Okuda, Y. Ueda, K. Shimada, H. Namatame, M. Taniguchi, and A. Kimura. Surface Scattering via Bulk Continuum States in the 3D Topological Insulator  $\text{Bi}_2\text{Se}_3$ . *Phys. Rev. Lett.*, 107:056803, Jul 2011.
- [182] Hamoon Hedayat, Davide Bugini, Hemian Yi, Chaoyu Chen, Xingjiang Zhou, Giulio Cerullo, Claudia Dallera, and Ettore Carpene. Ultrafast evolution of bulk, surface and surface resonance states in photoexcited  $\text{Bi}_2\text{Te}_3$ . *Scientific Reports*, 11(1):4924, 2021.
- [183] Yi-Ting Hsu, Mark H. Fischer, Taylor L. Hughes, Kyungwha Park, and Eun-Ah Kim. Effects of surface-bulk hybridization in three-dimensional topological metals. *Phys. Rev. B*, 89:205438, May 2014.
- [184] Klaus Wittel and Rolf Manne. Atomic Spin-Orbit Interaction Parameters from Spectral Data for 19 Elements. *Theoretica chimica acta*, 33(4):347–349, 1974.
- [185] J. W. McClure. Diamagnetism of Graphite. *Phys. Rev.*, 104:666–671, Nov 1956.
- [186] M. Morgenstern, Chr. Wittneven, R. Dombrowski, and R. Wiesendanger. Spatial Fluctuations of the Density of States in Magnetic Fields Observed with Scanning Tunneling Spectroscopy. *Phys. Rev. Lett.*, 84:5588–5591, Jun 2000.
- [187] T. Matsui, H. Kambara, Y. Niimi, K. Tagami, M. Tsukada, and Hiroshi Fukuyama. STS Observations of Landau Levels at Graphite Surfaces. *Phys. Rev. Lett.*, 94:226403, Jun 2005.
- [188] Guohong Li and Eva Y. Andrei. Observation of Landau levels of Dirac fermions in graphite. *Nature Physics*, 3(9):623–627, 2007.
- [189] Guohong Li, Adina Luican, and Eva Y. Andrei. Scanning Tunneling Spectroscopy of Graphene on Graphite. *Phys. Rev. Lett.*, 102:176804, Apr 2009.
- [190] David L. Miller, Kevin D. Kubista, Gregory M. Rutter, Ming Ruan, Walt A. de Heer, Phillip N. First, and Joseph A. Stroscio. Observing the Quantization of Zero Mass Carriers in Graphene. *Science*, 324(5929):924–927, 2009.
- [191] M. Morgenstern, J. Klijn, Chr. Meyer, and R. Wiesendanger. Real-Space Observation of Drift States in a Two-Dimensional Electron System at High Magnetic Fields. *Phys. Rev. Lett.*, 90:056804, Feb 2003.

## BIBLIOGRAPHY

---

[192] K. Hashimoto, C. Sohrmann, J. Wiebe, T. Inaoka, F. Meier, Y. Hirayama, R. A. Römer, R. Wiesendanger, and M. Morgenstern. Quantum Hall Transition in Real Space: From Localized to Extended States. *Phys. Rev. Lett.*, 101:256802, Dec 2008.

[193] T. Hanaguri, K. Igarashi, M. Kawamura, H. Takagi, and T. Sasagawa. Momentum-resolved Landau-level spectroscopy of Dirac surface state in  $\text{Bi}_2\text{Se}_3$ . *Phys. Rev. B*, 82:081305, Aug 2010.

[194] Oliver Storz, Paolo Sessi, Stefan Wilfert, Chris Dirker, Thomas Bathon, Konstantin Kokh, Oleg Tereshchenko, and Matthias Bode. Landau Level Broadening in the Three-Dimensional Topological Insulator  $\text{Sb}_2\text{Te}_3$ . *physica status solidi (RRL) – Rapid Research Letters*, 12(11):1800112, 2018.

[195] Manaswini Sahoo, Ifeanyi John Onuorah, Laura Christina Folkers, Ekaterina Kochetkova, Evgueni V. Chulkov, Mikhail M. Otrokov, Ziya S. Aliev, Ima-maddin R. Amiraslanov, Anja U. B. Wolter, Bernd Büchner, Laura Teresa Corredor, Chennan Wang, Zaher Salman, Anna Isaeva, Roberto De Renzi, and Giuseppe Allodi. Ubiquitous Order-Disorder Transition in the Mn Antisite Sublattice of the  $(\text{MnBi}_2\text{Te}_4)(\text{Bi}_2\text{Te}_3)$  Magnetic Topological Insulators. *Advanced Science*, 11(34):2402753, 2024.

[196] A. M. Shikin, D. A. Estyunin, N. L. Zaitsev, D. Glazkova, I. I. Klimovskikh, S. O. Filnov, A. G. Rybkin, E. F. Schwier, S. Kumar, A. Kimura, N. Mamedov, Z. Aliev, M. B. Babanly, K. Kokh, O. E. Tereshchenko, M. M. Otrokov, E. V. Chulkov, K. A. Zvezdin, and A. K. Zvezdin. Sample-dependent Dirac-point gap in  $\text{MnBi}_2\text{Te}_4$  and its response to applied surface charge: A combined photoemission and *ab initio* study. *Phys. Rev. B*, 104:115168, Sep 2021.

[197] Hao-Ran Ji, Yan-Zhao Liu, He Wang, Jia-Wei Luo, Jia-Heng Li, Hao Li, Yang Wu, Yong Xu, and Jian Wang. Detection of Magnetic Gap in Topological Surface States of  $\text{MnBi}_2\text{Te}_4$ . *Chinese Physics Letters*, 38(10):107404, Nov 2021.

[198] A. M. Shikin, D. A. Estyunin, N. L. Zaitsev, D. A. Glazkova, I. I. Klimovskikh, S. O. Fil'nov, A. G. Rybkin, K. A. Kokh, O. E. Tereshchenko, K. A. Zvezdin, and A. K. Zvezdin. Modulation of the Dirac Point Band Gap in the Antiferromagnetic Topological Insulator  $\text{MnBi}_2\text{Te}_4$  due to the Surface Potential Gradient Change. *Journal of Experimental and Theoretical Physics*, 134(1):103–111, 2022.

[199] A. M. Shikin, D. A. Estyunin, D. A. Glazkova, S. O. Fil'nov, and I. I. Klimovskikh. Electronic and Spin Structures of Intrinsic Antiferromagnetic

Topological Insulators of the  $\text{MnBi}_2\text{Te}_4(\text{Bi}_2\text{Te}_3)_m$  Family and Their Magnetic Properties (Brief Review). *JETP Letters*, 115(4):213–225, 2022.

[200] Wonhee Ko, Marek Kolmer, Jiaqiang Yan, Anh D. Pham, Mingming Fu, Felix Lüpke, Satoshi Okamoto, Zheng Gai, P. Ganesh, and An-Ping Li. Realizing gapped surface states in the magnetic topological insulator  $\text{MnBi}_{2-x}\text{Sb}_x\text{Te}_4$ . *Phys. Rev. B*, 102:115402, Sep 2020.

[201] Stefan Wimmer, Jaime Sánchez-Barriga, Philipp Küppers, Andreas Ney, Enrico Schierle, Friedrich Freyse, Ondrej Caha, Jan Michalička, Marcus Liebmann, Daniel Primetzhofer, Martin Hoffman, Arthur Ernst, Mikhail M. Otrokov, Gustav Bihlmayer, Eugen Weschke, Bella Lake, Evgeni V. Chulkov, Markus Morgenstern, Günther Bauer, Gunther Springholz, and Oliver Rader. Mn-Rich  $\text{MnSb}_2\text{Te}_4$ : A Topological Insulator with Magnetic Gap Closing at High Curie Temperatures of 45–50 K. *Advanced Materials*, 33(42):2102935, 2021.

[202] Mengke Liu, Chao Lei, Hyunsue Kim, Yanxing Li, Lisa Frammolino, Jiaqiang Yan, Allan H. Macdonald, and Chih-Kang Shih. Visualizing the interplay of Dirac mass gap and magnetism at nanoscale in intrinsic magnetic topological insulators. *Proceedings of the National Academy of Sciences*, 119(42):e2207681119, 2022.

[203] Paul M. Sass, Wenbo Ge, Jiaqiang Yan, D. Obeysekera, J. J. Yang, and Weida Wu. Magnetic Imaging of Domain Walls in the Antiferromagnetic Topological Insulator  $\text{MnBi}_2\text{Te}_4$ . *Nano Letters*, 20(4):2609–2614, 2020. PMID: 32119560.

[204] Paul M. Sass, Jinwoong Kim, David Vanderbilt, Jiaqiang Yan, and Weida Wu. Robust A-Type Order and Spin-Flop Transition on the Surface of the Antiferromagnetic Topological Insulator  $\text{MnBi}_2\text{Te}_4$ . *Phys. Rev. Lett.*, 125:037201, Jul 2020.

[205] S. X. M. Riberolles, Q. Zhang, Elijah Gordon, N. P. Butch, Liqin Ke, J.-Q. Yan, and R. J. McQueeney. Evolution of magnetic interactions in Sb-substituted  $\text{MnBi}_2\text{Te}_4$ . *Phys. Rev. B*, 104:064401, Aug 2021.

[206] Yaohua Liu, Lin-Lin Wang, Qiang Zheng, Zengle Huang, Xiaoping Wang, Miaofang Chi, Yan Wu, Bryan C. Chakoumakos, Michael A. McGuire, Brian C. Sales, Weida Wu, and Jiaqiang Yan. Site Mixing for Engineering Magnetic Topological Insulators. *Phys. Rev. X*, 11:021033, May 2021.

[207] Pinyuan Wang, Jun Ge, Jiaheng Li, Yanzhao Liu, Yong Xu, and Jian Wang. Intrinsic magnetic topological insulators. *The Innovation*, 2(2):100098, 2021.

## BIBLIOGRAPHY

---

- [208] Shuai Li, Tianyu Liu, Chang Liu, Yayu Wang, Hai-Zhou Lu, and X C Xie. Progress on antiferromagnetic topological insulator  $\text{MnBi}_2\text{Te}_4$ . *National Science Review*, 01 2023.
- [209] Chaowei Hu, Tiema Qian, and Ni Ni. Recent progress in  $\text{MnBi}_{2n}\text{Te}_{3n+1}$  intrinsic magnetic topological insulators: crystal growth, magnetism and chemical disorder. *National Science Review*, 11(2):nwad282, 11 2023.

# Acknowledgements

First and foremost, I would like to express my gratitude to my PhD supervisor Prof. Dr. Christian Hess for providing me with a very interesting and challenging project to conduct my doctoral research. I deeply appreciate his valuable suggestions, fruitful discussions and critical comments during my work in his group.

I am very thankful to Prof. Dr. Bernd Büchner for giving me the opportunity to carry out my experimental work in the STM lab at the IFW Dresden.

I would also like to thank Prof. Dr. Dirk Lützenkirchen-Hecht for his consent to take on the responsibility of the second reviewer of my thesis.

My special thank goes to Dr. Sebastian Schimmel from whom I received most of my experience in the STM. I especially appreciate all the interesting discussions we have had, his inspiring ideas and invaluable support in various aspects of my work during most of my PhD time.

I would like to thank my colleagues from the STM group at the IFW Dresden: Dr. Christian Salazar, Dr. Jose Guevara, Dr. Zhixiang Sun for guiding and teaching me in the lab at the early stage of my PhD. I express my gratitude to my other groupmates Dr. Sven Hoffmann and Emmanouil Koutsouflakis for their helpful advices and permanently nice hard-working atmosphere in the lab all the time.

I am deeply thankful to Dr. Danny Baumann for his help, especially, in engineering and his assistance in the lab. I acknowledge Tino Schreiner for his permanent willingness to support with the lab-related issues. I also need to thank Falk Sander and his co-workers from the mechanical and electrical workshops for their help in solving various technical problems in the lab.

I am very grateful to Prof. Dr. Anna Isaeva and Dr. Paul Gebauer for providing nice crystals suitable for the STM experiment. I acknowledge Dr. Andreas Koitzsch for the XPS measurements and analysis of the samples that I measured by STM.

I also thank people from the transport group and all other colleagues from the IFW Dresden. I thank everyone from the university of Wuppertal and the IFW Dresden who helped me to solve different problems, both related and unrelated to my work.

Last but not least, I would like to thank my parents and my sister for believing in me, continuous support and patience during this long-running project.



# Erklärung

Hiermit versichere ich, dass ich die vorliegende Arbeit ohne unzulässige Hilfe Dritter und ohne Benutzung anderer als der angegebenen Hilfsmittel angefertigt habe. Die aus fremden Quellen direkt oder indirekt übernommenen Gedanken sind als solche kenntlich gemacht. Die Arbeit wurde bisher weder im Inland noch im Ausland in gleicher oder ähnlicher Form einer anderen Prüfungsbehörde vorgelegt.

Diese Arbeit wurde unter Betreuung von Prof. Dr. Christian Hemker-Heß an der Bergischen Universität Wuppertal und am Instituts für Festkörper- und Werkstoffforschung Dresden e.V. (IFW Dresden) angefertigt. Es haben keine früheren erfolglosen Promotionsverfahren stattgefunden.

Ich erkenne hiermit die Promotionsordnung der Fakultät Mathematik und Naturwissenschaften der Bergischen Universität Wuppertal vom 03.12.2020 an.

Vladislav Nagorkin  
Wuppertal, September 2024